भारतीय प्रौद्योगिकी संस्थान गुवाहाटी
Indian Institute of Technology Guwahati

Strain Gage Based Determination of Stress Intensity Factors in Cracked Orthotropic Materials

A Thesis Submitted
In Partial Fulfillment of the Requirements
for the Degree of

DOCTOR OF PHILOSOPHY

by

Debaleena Chakraborty
(11610307)

Department of Mechanical Engineering
Indian Institute of Technology Guwahati
Guwahati – 781039, India
October, 2016

Certificate

It is certified that the work contained in the Thesis titled **"Strain Gage Based Determination of Stress Intensity Factors in Cracked Orthotropic Materials"** submitted by **Debaleena Chakraborty** to the Indian Institute of Technology Guwahati for the award of the degree of Doctor of Philosophy has been carried out under our supervision in the Department of Mechanical Engineering, Indian Institute of Technology Guwahati. This work has not been submitted elsewhere for the award of any other degree.

5th October, 2016

(D. Chakraborty)
Professor
Department of Mechanical Engineering
Indian Institute of Technology Guwahati
Guwahati – 781039

(K. S. R. K. Murthy)
Associate Professor
Department of Mechanical Engineering
Indian Institute of Technology Guwahati
Guwahati – 781039

Dedicated to my parents

Mr. Hiren Chakraborty

&

Ms. Tinku Chakraborty

Acknowledgements

This thesis is the outcome of five years of research work done in this IIT Guwahati. The exercise was by no means an easy task and during this long period, I have been guided and supported by many people. My grateful thanks are due to all of them for their valuable help at various stages during this tenure. I now have the opportunity to acknowledge my indebtedness to all of them.

At the onset, I would like to express my gratefulness particularly to my supervisors Dr. D. Chakraborty and Dr. K. S. R. K. Murthy, Department of Mechanical Engineering, IIT Guwahati, for their guidance, valuable advice and useful suggestions. I sincerely believe that without their able support, the research work would not have been possible. I would like to offer my heartfelt thanks to my doctoral committee members, Prof. P.S. Robi, Prof. A. Dutta and Dr. A. Banerjee for their valuable suggestions and recommendations.

My particular appreciations are expressed to all the faculty members of Mechanical Engineering Department, IIT Guwahati in general and the Head, Mechanical Engineering Department in particular for providing me a conducive environment for pursuing my research work. I am grateful to the entire technical staff of Central Workshop, IIT Guwahati for their help in preparing some of the experimental specimens. I would like to express my special thanks to Mr. Sanjib Sarma for helping me with his valuable suggestions whicle conducting the experiments. I would also like offer my thanks to Mr. Pranjol Paul, Sajith, Mirzaul, Debabrata and other research scholars with whom I could discuss and share my research related issues. I would like to extend my heartfelt thanks to Vikram Sarabhai Space Centre, ISRO and Mr. Sanjay Singh, Scientist-E, ISRO in particular for providing us with the Carbon-epoxy laminates without which the experimental work would not have been possible.

I wish to express my warm gratitude to all members of my family and my husband who have been pivotal in helping me keep a calm state of mind at all times and to my mother in particular for her constant encouragement and unique capacity of confidence building. Last but not the least I would like to express my sincere thankfulness to Ministry of Human Resource Development, Govt. of India for providing financial assistance during the doctoral program.

5th October

IIT Guwahati Debaleena Chakraborty

Contents

Abstract

In the last few decades considerable attentions have been paid by researchers in extending the concepts of LEFM pertaining to homogenous, isotropic materials to orthotropic composite materials. Stress intensity factor (SIF) being an important parameter in LEFM, accurate determination of SIF of cracked orthotropic materials have been an important area of research. Existence of cracks and notches in laminated composites warrants that SIFs are known to assess whether such cracks grow further during service leading to interlaminar or intralaminar defects in orthotropic laminates. Strain gage technique being one of the simplest experimental method for determination of SIFs could not be successfully used in the case of cracked orthotropic materials. This is due to the fact that unlike isotropic materials, proper theoretical formulations supporting such experimental determination were not reported for orthotropic materials. Even though there were one/two attempts but there were no theoretical guidelines suggesting the number of strain gages and more importantly their locations ensuring accurate determination of SIFs. The present thesis works towards filling these gaps with an objective to facilitate strain gage based accurate determination of SIFs of cracked orthotropic materials. Starting with Westergaard's stress function, and using a three parameter strain series, a single strain gage technique has been developed for accurate determination of K_I in cracked orthotropic materials. A method has also been developed which makes it possible to determine optimal location of the strain gage ensuring accurate estimation of K_I before conducting the experiment. Similarly, using appropriate stress functions and three parameter strain series, theoretical formulations have been developed for a mixed mode problem making it possible to determine K_I and K_{II} accurately by placing four strain gages in the locations and orientations prescribed in the present work. A method has been proposed to determine the optimal locations of strain gages before actual experiments which ensures accurate determination of K_I and K_{II} from the strain gage based experiments. Finally, edge cracked $[90_2/0]_{10S}$ carbon-epoxy laminates have been prepared and the experimental set-up for conducting strain gage based determination of K_I has been designed. Large number of experiments have been performed on laminate specimens of different crack sizes and the experiments are also repeated number of times to ensure repeatability. Results from both numerical simulations and experiments conducted led to some important observations and conclusions. Proposed theoretical formulations, numerical results and experiments show that for cracked orthotropic materials, it is possible to determine K_I using only one strain gage and K_I and K_{II} using four strain gages provided the strain gages are placed within the suggested optimal locations. These optimal locations of strain gages depend upon the crack configuration (size, inclination). More importantly, results show that the procedure put forward for determination of optimal strain gage locations is robust. Experimental and numerical results also show that while highly accurate values of SIFs could be obtained by placing the strain gages within optimal locations, a very high error ($\sim$ 49 %) is incurred if the strain gages are placed at non-optimal locations thus reinforcing the existence and importance of optimal strain gage locations in experimental determination of SIFs in orthotropic materials.

Nomenclature

a	crack length
$b, 2b$	width of the plate
C	constant
e	eccentricity
h	half height of the plate
L, T	principle material directions (Longitudinal and Transverse)
r	radial distance from the crack tip
x, y	x and y coordinates of a point
Z_I, Y_I	complex analytical functions for mode I loading
Z_{II}, Y_{II}	complex analytical functions for mode II loading
z	complex variable
α, β	parameters dependent on material properties
θ	angular coordinate
$+\theta$	orientation of positive gage line with crack axis
$-\theta$	orientation of negative gage line with crack axis
σ	applied stress
ϕ	orientation angle of strain gage
a_{11}, a_{12}	material properties depending on Young's modulus, Poisson's ratio and shear modulus
a_{16}, a_{22}	material properties depending on Young's modulus, Poisson's ratio and shear modulus
A_n, B_m	coefficients of series type complex analytical functions for mode I
C_n, D_m	coefficients of series type complex analytical functions for mode II
E_i	Young's modulus along ith direction $(i = L, T)$
F_I, F_{II}	Airy stress function for mode I and mode II loading for orthotropic composite materials
f_I	non-dimensional mode I stress intensity factors
G_{LT}	shear modulus in $L-T$ plane
K_I, K_{II}, K_{III}	mode I, mode II and mode III stress intensity factor
$r_{\max}$	upper limit for gage locations
$r_{\max}^{+}$	upper limit for gage locations along positive gage line
$r_{\max}^{-}$	upper limit for gage locations along negative gage line

$r_{\min}$	minimum radial distance
$Z_{I,II}, Y_{I,II}$	complex analytical functions for mode I and mode II loading for orthotropic composite materials
ϕ_I, ϕ_{II}	Airy stress function for mode I and mode II loading for isotropic materials
γ_{xy}	shear strain in $x-y$ plane
ε_{aa}	normal strain in the positive direction of θ and ϕ
ε_{bb}	normal strain in the negative direction of θ and ϕ
ε_x	normal strain in x direction
ε_y	normal strain in y direction
$\nu_{i,j}$	Poisson's ratio of orthotropic composite material $(i, j = L, T)$
σ_x	normal stress in x direction
σ_y	normal stress in y direction
τ_{xy}	shear stress in $x-y$ direction
2D	two dimensional
3D	Three dimensional
DS technique	Dally and Sanford single strain gage technique for mode I
DB technique	Dally and Berger multi strain gage mixed mode technique
DECP	Double edge cracked plate
ECCP	Eccentric center cracked plate
FE	Finite element
FEA	Finite element analysis
LEFM	Linear elastic fracture mechanics
QPE	Quarter point element
Q8	Eight noded isoparametric quadrilateral element
SDZ	Singularity dominated zone
SECP	Slant edge cracked plate
SIF	Stress intensity factor

List of Figures

List of Tables

Chapter 1

Introduction

Composite materials are extensively used in large scale applications ranging from engineering and industrial to defense systems. A concise detailing of the importance, application mechanics of such materials is laid out in this chapter. The development of fracture mechanics based analyses and the importance of fracture mechanics based design along with the significance of accurate estimation of fracture parameters like stress intensity factor (SIF) in design of engineering components be it of isotropic or of anisotropic/composite material is also presented in this chapter. Strain gage based estimation of SIFs is discussed and its importance in the fracture mechanics based analyses of orthotropic composites is being presented which forms the outline of the research work.

1.1 Composite materials – A brief insight

Composite materials are created by the combination of two or more materials at a macroscopic level to form a new material with enhanced properties as compared to those of the individual constituents. Composites are conventionally made of two main ingredients – reinforcements and matrix. Examples of composite materials include concrete reinforced with steel and epoxy reinforced with graphite fibers, etc. Composite materials are useful in lowering the overall mass of the system without compromising on its stiffness and strength properties.

Composites are classified by the geometry of the reinforcement or by the type of the matrix. On the basis of reinforcement, the classification may be done as

- *Particulate* composite consisting of particles immersed in matrices such as alloys and ceramics. Typical examples include use of aluminum particles in rubber, silicon carbide particles in aluminum, etc.
- *Flake* composites consisting of flat reinforcements of matrices. Typical flake materials are glass, mica, aluminum and silver.
- *Fiber* composites consisting of matrices reinforced by short (discontinuous) or long (continuous) fibers. Fibers are generally anisotropic and examples include carbon

fiber, glass fiber and aramid fiber. Examples of matrices are resins such as epoxy, metal such as aluminum, etc.

- *Nanocomposites* consist of reinforcement materials that are of the scale of nanometers (10^{-9} m).

Based on the type of matrix, the classification may be done as

- *Polymer Matrix Composites (PMCs)* consisting of polymer matrix (e.g., epoxy, polyster) reinforced by thin diameter fibers (e.g., graphite, aramids, boron, glass).
- *Metal matrix composites (MMCs),* as the name indicates, having metal matrix (e.g., aluminum, magnesium) reinforced with fibers such as carbon, silicon carbide.
- *Ceramic Matrix Composites (CMCs*) having ceramic matrix such as alumina calcium alumino silicate reinforced by fibers such as carbon or silicon carbide.
- *Carbon-carbon composites* using carbon fibers in a carbon matrix.

Continuous fiber composites are emphasized more in the present work and is discussed further. The fibers are generally selected on the basis of qualities like high elasticity modulus and ultimate strength and the fibers must retain their geometrical and mechanical properties during fabrication and handling. The matrix constituent is intended to bind the fibers and transfer stresses to the fibers along with protecting their surface. The stiffness and strength properties of the composite in general respond as per the weighted average of the constituents. However, at times, the constituents may interact mechanically that may cause the composite properties to surpass the expected average of the constituents. In all cases, whatsoever, the composite properties depend on the properties of the individual constituents operating as a continuous structural unit rather than discrete constituent elements.

The use of composites or fibrous reinforcements can be dated back to biblical references of straw-reinforced clay bricks in ancient Egypt. Phenolic resin reinforced asbestos was introduces in the beginning of the last century. The first fiberglass boat was made in the year 1942. The first boron and high-strength carbon fibers were introduced in the early 1960s, followed by applications of advanced composites to aircraft components in 1968.

High specific strength, light-weight, excellent fatigue durability, significant corrosion resistance, chemical and environmental resistance together with the unique possibility of designing the material for desirable mechanical properties make composites an attractive material for a range of engineering and other applications. Applications include aerospace, aircraft, automotive, marine, energy, infrastructure, armor, biomedical and recreational

applications and also in food and chemical processing plants, cooling towers, offshore platforms etc. to name a few. In addition, these materials also possess excellent electromagnetic transparency or electrical insulation.

The high stiffness, high-strength and low-density characteristics make composites highly desirable in primary and secondary structures of both civilian and military aircraft. The Boeing 777, for example, uses composites in fairings, floor beams, wing trailing edge surfaces and the empennage. The hybrid GLARE (glass/ epoxy/ aluminum laminate) constitute substantial portions of the AIRBUS 380. Ship structures incorporate composites in various forms like thick section glass and carbon fiber composites and sandwich construction. Carbon-fiber composites have also been used in the blades of wind turbine generators that significantly improve power output at a reduced cost. Biomedical applications include prosthetic devices and artificial limb parts. Composites are also being used to reinforce structural members against earthquakes.

Composites also come with certain limitations or defects along with their long list of utilities. They suffer from shortcomings such as brittleness, high thermal and residual stresses, low toughness etc. which aid the process of unstable cracking under different loading conditions. These may lead to substantial reduction in stiffness and load bearing capacity causing extensive damage to the structure. Moreover, usage of composites in thin forms makes them more prone to various types of defects. Cracks either in microscopic or macroscopic level is a common defect in these structures and become more prominent with time in concentrated loading conditions like dynamic loading, high velocity impact and explosion. Therefore, the study of crack stability and load bearing capacity of these materials is imperative keeping in mind the safety and durability of structures comprised of such materials.

1.2 Mechanics of fiber reinforced laminated composite materials

The basic building block of a composite structure i.e., the lamina has a fiber-matrix configuration in either of the four ways- continuous fiber, woven, chopped fiber and hybrid. A lamina is a thin layer of a composite material of thickness of the order of 0.125 mm. Fibers in a lamina are oriented in different angles depending upon the strength and stiffness

requirements. These laminae are stacked together to form a laminate (Fig. 1.1), which are then used to build engineering components to take up various loads such as bending, twisting etc. more effectively. The behavior of a laminate is thus dependent on the behavior of individual lamina which constitute a laminate. It is therefore important to understand the stress-strain behavior in a lamina and the stacked laminate.

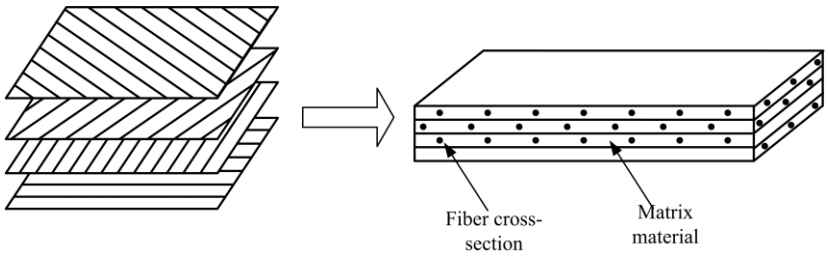

Figure 1.1 A typical four lamina laminate

1.2.1 Stresses and strains in a lamina

The generalized form of the anisotropic Hooke's law may be written as

$$\sigma_{ij} = \mathrm{C}_{ijkl}\varepsilon_{kl} \qquad i, j = 1,2,3 \tag{1.1}$$

A total of 21 constants are required for complete characterization of an anisotropic body. Considering different planes of material symmetry, the number of constants keeps changing for different materials. As for example, a monoclinic material has 13 and an orthotropic material has only 9 independent elastic constants remaining after using proper material symmetry. In laminate analysis, the lamina is often considered to be in plane stress state. Considering a 2D case of a unidirectional lamina (Fig. 1.2) which falls under the orthotropic material category with no out of the plane stress, the stress-strain relations in Eq. (1.1) may be written as

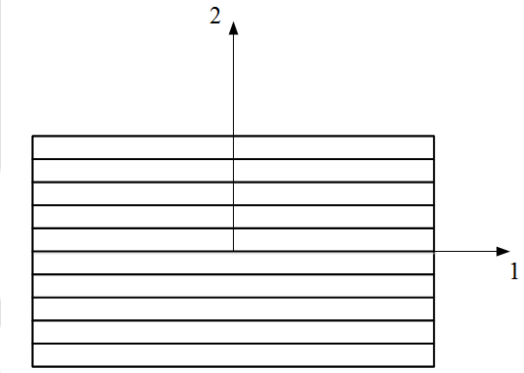

Figure 1.2 A typical unidirectional lamina

$$\begin{Bmatrix} \varepsilon_1 \\ \varepsilon_2 \\ \gamma_{12} \end{Bmatrix} = \begin{pmatrix} S_{11} & S_{12} & 0 \\ S_{21} & S_{22} & 0 \\ 0 & 0 & S_{66} \end{pmatrix} \begin{Bmatrix} \sigma_1 \\ \sigma_2 \\ \tau_{12} \end{Bmatrix} \tag{1.2}$$

where the compliances S_{ij} and the engineering constants are related by the equations

$$S_{11} = \frac{1}{E_1},\ S_{22} = \frac{1}{E_2}$$
$$S_{12} = S_{21} = -\frac{\nu_{21}}{E_2} = -\frac{\nu_{12}}{E_1},\ S_{66} = \frac{1}{G_{12}} \tag{1.3}$$

Thus, there are only four independent compliances for the specially orthotropic lamina. The lamina stresses and corresponding strains are related as

$$\begin{Bmatrix} \sigma_1 \\ \sigma_2 \\ \tau_{12} \end{Bmatrix} = \begin{pmatrix} Q_{11} & Q_{12} & 0 \\ Q_{21} & Q_{22} & 0 \\ 0 & 0 & Q_{66} \end{pmatrix} \begin{Bmatrix} \varepsilon_1 \\ \varepsilon_2 \\ \gamma_{12} \end{Bmatrix} \tag{1.4}$$

where Q_{ij} are the components of the lamina stiffness matrix, which are related to the engineering constants as

$$Q_{11} = \frac{E_1}{1-\nu_{12}\nu_{21}},\quad Q_{22} = \frac{E_2}{1-\nu_{12}\nu_{21}},$$
$$Q_{12} = \frac{\nu_{12}E_2}{1-\nu_{12}\nu_{21}} = Q_{21},\quad Q_{66} = G_{12} \tag{1.5}$$

Since, most laminates consist of some laminae placed at an angle (Fig. 1.3), the transformation of lamina stress/strain from $1-2$ axis to rotated $x-y$ axis is given as

$$\begin{Bmatrix} \sigma_x \\ \sigma_y \\ \tau_{xy} \end{Bmatrix} = [T]^{-1} \begin{Bmatrix} \sigma_1 \\ \sigma_2 \\ \tau_{12} \end{Bmatrix} \tag{1.6}$$

where $[T]$ is called the transformation matrix and in defined as

$$[T] = \begin{pmatrix} \cos^2\theta & \sin^2\theta & 2\cos\theta\sin\theta \\ \sin^2\theta & \cos^2\theta & -2\cos\theta\sin\theta \\ -\cos\theta\sin\theta & \cos\theta\sin\theta & \cos^2\theta-\sin^2\theta \end{pmatrix} \tag{1.7}$$

The lamina stress-strain relation in the rotated $x-y$ co-ordinates is given by

$$\begin{Bmatrix} \sigma_x \\ \sigma_y \\ \tau_{xy} \end{Bmatrix} = \begin{pmatrix} \overline{Q_{11}} & \overline{Q_{12}} & \overline{Q_{16}} \\ \overline{Q_{21}} & \overline{Q_{22}} & \overline{Q_{26}} \\ \overline{Q_{16}} & \overline{Q_{26}} & \overline{Q_{66}} \end{pmatrix} \begin{Bmatrix} \varepsilon_x \\ \varepsilon_y \\ \gamma_{xy} \end{Bmatrix} \tag{1.8}$$

Where

$$\left[\overline{Q}\right]=[T]^{-1}[Q][R][T][R]^{-1} \tag{1.9}$$

where, $[R]=\begin{pmatrix}1 & 0 & 0\\ 0 & 1 & 0\\ 0 & 0 & 2\end{pmatrix}$ is the Reuter matrix

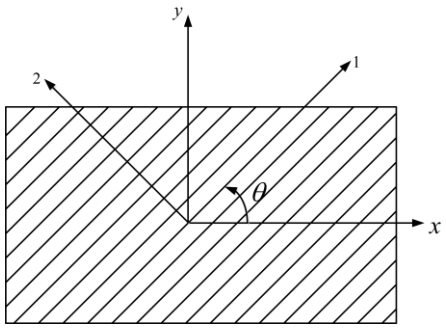

Figure 1.3 Local and global axes of an angle lamina

1.2.2 Macromechanical analysis of a laminate

A laminate is made of a group of single layer lamina bonded to each other. Each layer is identified by its location in the laminate, material and angle of orientation with a reference axis. $[0/-45/90/60/30]$ illustrates a typical example of coding a laminate which consists of five laminae/plies and the numbers indicate the angles of each ply. The 'classical lamination theory' which has evolved from the investigations of various researchers in the years between 1950 and 1979 [1-5] is used to develop the behavioral stress-strain relations for a laminate plate under in-plane loads such as shear and axial forces and bending and twisting moments and is based on certain assumptions for the static analysis which are as follows

- Each layer is orthotropic and homogenous.
- The lamina is thin and its lateral dimensions are much larger compared to the thickness and is loaded in its plane only.
- Displacements are continuous and in-plane displacements (u,v) vary linearly with z.
- Strain-displacement and stress-strain relations are linear.
- ε_z is negligible compared to $\varepsilon_x, \varepsilon_y$.

Considering a laminated plate in the Cartesian co-ordinate system, the origin of which is considered at $z=0$ (Fig. 1.4), the laminate strains at any location may be written as

$$\begin{Bmatrix} \varepsilon_x \\ \varepsilon_y \\ \gamma_{xy} \end{Bmatrix} = \begin{Bmatrix} \varepsilon_x^0 \\ \varepsilon_y^0 \\ \gamma_{xy}^0 \end{Bmatrix} + z_k \begin{Bmatrix} \kappa_x \\ \kappa_y \\ \kappa_{xy} \end{Bmatrix} \tag{1.10}$$

where $\begin{Bmatrix} \varepsilon_x^0 \\ \varepsilon_y^0 \\ \gamma_{xy}^0 \end{Bmatrix}$ and $\begin{Bmatrix} \kappa_x \\ \kappa_y \\ \kappa_{xy} \end{Bmatrix}$ are the mid-plane strains and curvatures and z is the distance from the mid-plane.

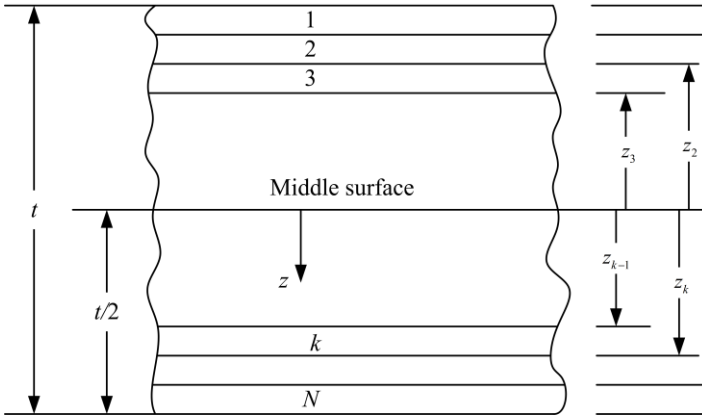

Figure 1.4 Locations of plies in a laminate

Substituting Eq. (1.10) into Eq. (1.8) gives the generalized stress-strain relation for the k^{th} lamina as

$$\begin{Bmatrix} \sigma_x \\ \sigma_y \\ \tau_{xy} \end{Bmatrix} = \begin{pmatrix} \overline{Q_{11}} & \overline{Q_{12}} & \overline{Q_{16}} \\ \overline{Q_{21}} & \overline{Q_{22}} & \overline{Q_{26}} \\ \overline{Q_{16}} & \overline{Q_{26}} & \overline{Q_{66}} \end{pmatrix} \left\{ \begin{Bmatrix} \varepsilon_x^0 \\ \varepsilon_y^0 \\ \gamma_{xy}^0 \end{Bmatrix} + z_k \begin{Bmatrix} \kappa_x \\ \kappa_y \\ \kappa_{xy} \end{Bmatrix} \right\} \tag{1.11}$$

With stresses defined in terms of z-coordinate, integrating these expressions give the in-plane loads $\left(N_x, N_y, N_{xy}\right)$ and moments $\left(M_x, M_y, M_{xy}\right)$ (Fig. 1.5) as

$$\begin{Bmatrix} N_x \\ N_y \\ N_{xy} \end{Bmatrix} = \int_{-\frac{t}{2}}^{\frac{t}{2}} \begin{Bmatrix} \sigma_x \\ \sigma_y \\ \tau_{xy} \end{Bmatrix} dz = \sum_{k=1}^{N} \int_{-z_{k-1}}^{z_k} \begin{Bmatrix} \sigma_x \\ \sigma_y \\ \tau_{xy} \end{Bmatrix}_k dz \tag{1.12}$$

$$\begin{Bmatrix} M_x \\ M_y \\ M_{xy} \end{Bmatrix} = \int_{-\frac{t}{2}}^{\frac{t}{2}} \begin{Bmatrix} \sigma_x \\ \sigma_y \\ \tau_{xy} \end{Bmatrix} z dz = \sum_{k=1}^{N} \int_{-z_{k-1}}^{z_k} \begin{Bmatrix} \sigma_x \\ \sigma_y \\ \tau_{xy} \end{Bmatrix}_k z dz$$

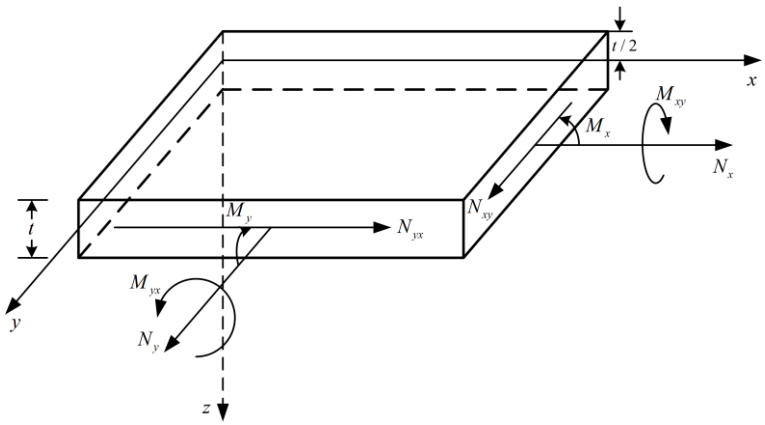

Figure 1.5 In-plane loads and moments in a laminated plate

Using Eq. (1.11), Eq. (1.12) can be simplified as

$$\begin{bmatrix} N_x \\ N_y \\ N_{xy} \\ M_x \\ M_y \\ M_{xy} \end{bmatrix} = \begin{bmatrix} \begin{pmatrix} A_{11} & A_{12} & A_{16} \\ A_{21} & A_{22} & A_{26} \\ A_{16} & A_{26} & A_{66} \end{pmatrix} & \begin{pmatrix} B_{11} & B_{12} & B_{16} \\ B_{21} & B_{22} & B_{26} \\ B_{16} & B_{26} & B_{66} \end{pmatrix} \\ \begin{pmatrix} B_{11} & B_{12} & B_{16} \\ B_{21} & B_{22} & B_{26} \\ B_{16} & B_{26} & B_{66} \end{pmatrix} & \begin{pmatrix} D_{11} & D_{12} & D_{16} \\ D_{21} & D_{22} & D_{26} \\ D_{16} & D_{26} & D_{66} \end{pmatrix} \end{bmatrix} \begin{bmatrix} \varepsilon_x^0 \\ \varepsilon_y^0 \\ \gamma_{xy}^0 \\ \kappa_x \\ \kappa_y \\ \kappa_{xy} \end{bmatrix} \tag{1.13}$$

where

$$\begin{aligned} A_{ij} &= \sum_{k=1}^{n} \left[\left(\overline{Q}_{ij} \right) \right]_k \left(z_k - z_{k-1} \right), \quad i, j = 1, 2, 6 \\ B_{ij} &= \frac{1}{2} \sum_{k=1}^{n} \left[\left(\overline{Q}_{ij} \right) \right]_k \left(z_k^2 - z_{k-1}^2 \right), \quad i, j = 1, 2, 6 \\ D_{ij} &= \frac{1}{3} \sum_{k=1}^{n} \left[\left(\overline{Q}_{ij} \right) \right]_k \left(z_k^3 - z_{k-1}^3 \right), \quad i, j = 1, 2, 6 \end{aligned} \tag{1.14}$$

The $[A],[B]$ and $[D]$ matrices are called the extensional, coupling and bending stiffness matrices respectively. For a symmetric laminate $[B]=0$ and in such a laminate, in-plane loads (N) only produce in-plane strains and in-plane moments produce only curvature. Thereby, the effective longitudinal modulus (E_L), in-plane transverse modulus (E_T), shear modulus (G_{LT}) and in-plane Poisson's ratio $(\nu_{LT}$ and $\nu_{TL})$ are given by

$$E_L = \frac{1}{tA_{11}^*},\ E_T = \frac{1}{tA_{22}^*}$$
$$G_{LT} = \frac{1}{tA_{66}^*},\ \nu_{LT} = -\frac{A_{12}^*}{A_{11}^*},\ \nu_{TL} = -\frac{A_{12}^*}{A_{22}^*} \tag{1.15}$$

where t is the laminate thickness and $\left[A^*\right]$ is the extensional compliance matrix given by

$$\left[A^*\right] = [A]^{-1} \tag{1.16}$$

In a specially orthotropic laminate, the stress-strain relations under conditions of plane stress may be written as

$$\begin{Bmatrix} \varepsilon_x \\ \varepsilon_y \\ \gamma_{xy} \end{Bmatrix} = \begin{pmatrix} \frac{1}{E_L} & \frac{-\nu_{TL}}{E_T} & 0 \\ \frac{-\nu_{LT}}{E_L} & \frac{1}{E_T} & 0 \\ 0 & 0 & \frac{1}{G_{LT}} \end{pmatrix} \begin{Bmatrix} \sigma_x \\ \sigma_y \\ \tau_{xy} \end{Bmatrix} \tag{1.17}$$

1.3 Fracture mechanics – Introduction and importance

Failure of man-made structures may ensue from various factors, the common causes being yielding, buckling, fatigue, fracture, creep, impact, wear etc. Amongst them, fracture is the form of structural failure that often happens without any prior warning, of which history stands witness to. Fracture of engineering components is usually caused by a flaw or a crack which may be defined as a fine slit of nearly zero radius of curvature at the tips. Due to continual development of crack under sustained loading, the stiffness of the structure decreases and when the stiffness becomes so low that the service loads cannot be taken up by the structure any longer, failure occurs by way of fracture. Fracture mechanics as an

engineering discipline refers to the specialized solid mechanics in which the presence of a crack in the structure is assumed and then the analysis is carried out.

Development of fracture mechanics is supposed to be closely related to some well-known catastrophic failures in the past. Fracture mechanics gradually developed from a mere scientific idea to a widespread engineering discipline, primarily because of the fiasco related to the liberty ships during the World War II, where several ships suffered sudden rupture and even broke in two. Poor weld properties with stress concentrations combined with poor choice of brittle materials used in construction lead to the failure. Another tragic accident due to fatigue fracture is the midair disintegration of pressurized cabins of the de Havilland comet jetliner in 1954. Another important catastrophic incident is the fracture due to possible fatigue crack growth of a liquid natural gas storage tank that took place in Cleveland in 1944 killing nearly 130 people.

In 1962, the one year old Kings Bridge in Melbourne, Australia fractured after a span collapsed because of cracks developed in the welded girder. After five years, in 1967 the Point Pleasant Bridge at Point Pleasant, West Virginia in US collapsed without warning, resulting in the loss of 46 lives. Apart from the above characteristic cases, large number of disasters involving failures of pipes, weapons, tanks, ships, railways and aerospace structures have been reported around the globe.

Fracture mechanics studies may be broadly classified into divisions- brittle fracture and ductile fracture. Brittle fracture also known as elastic or cleavage fracture comes with very little or no plastic deformation ahead the crack tip prior to fracture. On the other hand, large plastic deformation is the typical characteristic of ductile fracture also known as fibrous fracture or dimpled rupture. Brittle fracture of engineering components is usually considered more dangerous in the sense that it does not give any prior warning and occurs at stresses much lower than the design stresses. The general characteristics of a brittle fracture as observed from the examination and analysis of structural disasters of the past may be summarized as

- Brittle fracture occurs with very little or no plastic deformation.
- Material which were ductile at ambient temperature also gave way to brittle fracture at stresses much below the yield stress of the material. And these materials were found to have low notch or fracture toughness i.e. the ability to resist loads in the presence of cracks.

- Structural discontinuities like holes, notches, welding defects etc. or preexisting defects such as cracks or flaws generally lead to brittle fracture.

Brittle fracture as observed in most cases usually propagates at very high speeds. The first significant work in the development of fracture mechanics was the work of Inglis [6] which discussed the stress analysis of an elliptical hole in an infinite linear elastic tensile plate and the degeneration of the elliptical hole into a line (sharp crack). Using this work, Griffith [7] in 1920 put forward the use of energy balance approach to study the fracture phenomenon in cracked bodies. This could be considered as the first solution to understand the effect of crack length on the strength of the structure using continuum mechanics based approach. However, the development of fracture mechanics as an engineering discipline was mainly due to contributions of Irwin and his co-workers [8] at the Naval Research Laboratory, Washington DC which began with the study of the Liberty ship failures. Additionally, the linear elastic analysis of cracked bodies in 2D by Westergaard [9] and Williams [10] were two other important milestones in the development of modern fracture mechanics.

The conventional strength based design approach assumes the structure to be free of cracks or flaws and the design criterion only requires the computed maximum stress to be less than the relevant strength of the material suitably reduced by a factor of safety. However, the chances of presence of crack like flaws cannot be precluded in engineering structures. Hence, the need of fracture mechanics based design approach is felt which studies the load bearing capacity of an engineering component assuming the presence of dominant cracks in the structure itself.

In fracture mechanics approach, in addition to the applied stress and structural geometry (which are also used in the strength of materials approach), an additional important structural variable known as the crack length also enters in strength calculations. Combination of these three variables gives the parameter that characterizes the crack or the crack driving force. The critical value of crack driving force known as fracture toughness, which is the ability of the material to resist fracture in presence of cracks and is considered to be a material property. A relationship between applied load, crack size, fracture toughness and structural geometry can be obtained by equating the crack driving force to the fracture toughness which in turn provides the necessary guidelines for structural design. Fracture mechanics based design approach rather than replacing the conventional strength based design approach, in a way supports the conventional approach to prevent catastrophic failures due to brittle fracture.

However, a designer has to strike a balance between both the design approaches as the high strength materials usually have low fracture toughness and low strength materials have high fracture toughness.

Fracture mechanics is not only limited to determining critical size and loading combinations for fracture instability in static conditions, but also aids in predicting life of components that are subjected to time-dependent crack growth mechanisms such as fatigue and stress corrosion cracking. Damage tolerant design and non-destructive testing (NDT) of engineering components form important constitutive elements of this branch of fracture mechanics. Fracture mechanics design philosophy is now extensively used in industries such as aircraft, aerospace, and nuclear, industries, offshore platforms and locomotives, pressure vessels etc. with a view to keep catastrophes at bay.

1.3.1 Concepts of fracture mechanics

Fracture mechanics is the discipline which deals with the study of propagation of cracks in materials. As shown in Fig. 1.6, the three general cases of load application leading to crack propagation are

- Opening mode or mode I- Tensile stress normal to the plane of the crack
- Sliding mode or mode II- Shear stress acts parallel to the plane of the crack and perpendicular to the crack front
- Tearing mode or mode III- Shear stress acts parallel to both the crack plane and crack front

A combination of two or all of the aforementioned modes leads to mixed mode case of loading. Fracture mechanics analyses can be broadly classified into two divisions viz. *linear elastic fracture mechanics* (LEFM) and *elastic plastic fracture mechanics* (EPFM). LEFM is based on the concept of *small scale yielding conditions* (SSY). In small scale yielding conditions, the plastic zone at the crack tip is sufficiently small compared to the crack length and other

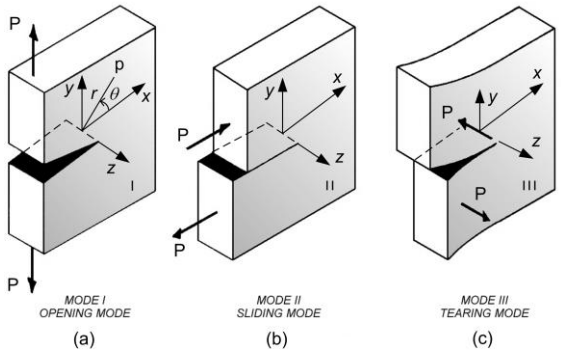

Figure 1.6 Three types of loading

relevant geometric parameters. The stress-strain behavior and load-displacement behavior is linear in LEFM. In LEFM elastic analysis of cracked bodies is usually employed to determine the displacement and stress field in the cracked body. Fracture criteria that are based on the LEFM are applicable for control and prevention of the brittle fracture as it involves very limited amount of plastic deformation ahead of the crack tip. Most of the engineering designs based on fracture mechanics approach are primarily on the brittle fracture. LEFM is well suited for applications which involve high strength materials (which have low fracture toughness) such as aluminum alloys used in aircraft structures. This theory is not valid when significant plastic deformation precedes the failure. This restriction severely limits the application of LEFM to ductile fracture.

In cases where the extent of the plastic zone becomes large compared to the specimen thickness and crack length, the LEFM methodology breaks down and the linear conditions no longer exist due to large scale plasticity. Under such large scale plastic conditions or *large scale yielding conditions* (LSY), elastic-plastic fracture mechanics (EPFM) is employed to characterize the crack tip conditions. This situation generally is observed for highly ductile materials used in nuclear industry. As compared to SSY conditions, fracture under LSY conditions absorb more amount of energy for fracture of components due to more plastic deformation. The severity of the crack in both LEFM and EPFM is characterized by certain fracture mechanics parameters. By comparing with their corresponding critical values of those parameters the severity of the existing crack could be predicted.

1.3.2 Fracture mechanics parameters

The following four fracture mechanics parameters are widely used to measure the potency of an existing crack in an engineering component depending on either LEFM or EPFM conditions as applicable

- Energy release rate (G)
- Stress intensity factor (K)
- J -integral (J)
- Crack tip opening displacement (*CTOD*) or crack opening displacement (COD)

An appropriate parameter is chosen to analyze the given problem depending upon the material and the crack tip conditions. The parameters G and K are used in LEFM analysis, K being more widely employed as compared to G. On the other hand the J -integral and $CTOD$ are useful in EPFM studies.

1.3.2.1 Strain energy release rate

The strain energy release rate G (in honor of Griffith) or simply energy release rate is based on the energy balance which establishes the necessary condition for fracture. The concept of energy release rate is introduced by Irwin [11] in an effort to extend the pioneering work of Griffith [9] to metals. G is a measure of the energy available for the crack growth. An unstable fracture occurs when G attains a critical value, G_c, which is a material property and represents materials resistance to crack growth.

1.3.2.2 Stress intensity factor

Stress intensity factor (SIF), K is the most important fracture mechanics parameter in LEFM (it is a grouped parameter like Reynolds number). SIF is the most widely used to characterize the crack under SSY (brittle or quasi brittle fracture conditions of metals). Unlike G, the SIF is derived from the stress based approach. The magnitude of K depends on the geometry of the cracked structure, crack length and boundary conditions. Unlike the concept of stress concentration factor that determines the magnitude of the stress at a single point, the parameter K provides a complete description of the state of stress, strain and displacement in the vicinity of a crack tip known as the singularity dominated zone (SDZ). Further, the SIF represents the strength of the singularity in linear elastic conditions i.e. the rate at which the stresses approach infinity. Many important phenomena of fracture of metals that fall within the scope of LEFM can be explained with the help of the SIF approach. For example, SIF approach could be used in determination of the safe operating loads for known sizes and locations of existing cracks and for determination of the largest crack size that can exists for given loads without fracture. Further, SIF approach could also be employed for remaining life prediction using the fatigue crack propagation laws such as Paris law and for prediction of crack growth rate for environmentally assisted cracking such as corrosion etc. Due to its practical importance, a collection of SIFs of various cracked configurations are made

available in many handbooks [12, 13]. By comparing the operating K with the critical K_c (or fracture toughness) it is possible to predict whether the existing crack grows or not. Thus it is clear that the knowledge of accurate values of SIFs of a configuration is essential for application of the above fracture criterion. The introduction of the SIF by Irwin and his co-workers did much to establish the basis of modern fracture mechanics.

1.3.2.3 J- integral

Rice [14, 15] introduced the path-independent contour J -integral for applications of fracture mechanics where LEFM is no longer applicable and elastic-plastic deformation due to significant amount of plasticity at the crack tip is to be taken into account. It is one of the widely used parameter in EPFM studies of ductile materials. J -integral is like G based on the energy approach. In fact, there exists a relationship between J, K and G for SSY conditions.

1.3.2.4 Crack opening displacement

The crack opening displacement (*COD*) is an alternative to the J -integral for applications where the plastic deformation is significant as compared to dimensions of the cracked body and is introduced by Wells [16]. It is derived from a displacement based approach. Like J -integral *COD* is also widely employed in EPFM studies.

1.3.3 Stress intensity factors for different modes of loading

The stress intensity factor K is represented according to the mode of loading. Referring to Fig. 1.6, the SIFs corresponding to mode I, mode II and mode III loading cases are designated as K_I, K_{II} and K_{III} respectively.

Referring to the crack-tip local coordinate system in Fig. 1.6 (origin is placed at the center of the crack front), the stress field ahead of a crack tip for linear elastic materials under modes I, Π and ΠI loading conditions can be written as.

$$\lim_{r\to 0}\sigma_{ij}^{(I)} = \frac{K_I}{\sqrt{2\pi r}}\, f_{ij}^{I}(\theta) \tag{1.18}$$

$$\lim_{r\to 0}\sigma_{ij}^{(II)} = \frac{K_{II}}{\sqrt{2\pi r}}\, f_{ij}^{II}(\theta) \tag{1.19}$$

$$\lim_{r\to 0}\sigma_{ij}^{(III)} = \frac{K_{III}}{\sqrt{2\pi r}}\ f_{ij}^{III}(\theta) \tag{1.20}$$

where r and θ are polar coordinates of a point as shown in Fig. 1.6, and f_{ij} are universal functions that only depend on θ and depend upon the loading mode.

It has been observed that majority of cracks are loaded either in the opening mode or under a combined mode. In the mixed mode problems (i.e. when more than one loading mode are present), the individual contributions to a given stress component are additive i.e.

$$\sigma_{ij}^{(total)} = \sigma_{ij}^{(I)} + \sigma_{ij}^{(II)} + \sigma_{ij}^{(III)} \tag{1.21}$$

In such cases, K values of all the participating modes would be required for complete characterization of crack tip conditions. Thus the single parameter description of crack tip conditions using the concept of SIF is quite useful in the sense that from accurate values of K, it is possible to solve for all components of stress, strain and displacement ahead of crack tip as a function of r and θ. The values of K may thus be formally defined as

$$K_{I,II,II} = \sqrt{2\pi r}\lim_{r\to 0}\sigma_{ij}^{(I,II,II)} \tag{1.22}$$

as $r \to 0$ on $\theta = 0^{\circ}$.

1.4 Methods for the determination of stress intensity factors

The SIF plays a vital role in the application of the principles of linear elastic fracture mechanics to practical problems in design and analysis. Determination of SIF for real life components with a crack is therefore very important for prediction of the crack condition. The SIFs can be determined through analytical, numerical and experimental methods.

1.4.1 Analytical methods

The analytical methods are mostly suitable for idealized geometries, loading and boundary conditions. There are number of techniques used in the solution of the SIFs of two-dimensional crack problems. Amongst, very notable methods are conformal mapping, Laurent series expansion, boundary collocation method, integral transform method and weight function method. Theoretical methods are essential for two reasons. First, they provide the correct form of singularities and asymptotic solutions that are useful in analyzing and interpreting the experimental observations and in improving the accuracy of numerical

solutions. Secondly, they provide accurate solutions for relatively simple geometries and for certain idealized material behavior and could be used as benchmark problems for validation of numerical methods and experimental methods.

1.4.2 Numerical methods

Numerical methods for determination of SIF are extremely useful in dealing with the complex configurations usually found in a great many practical problems. Finite element and boundary element methods are widely used for numerical estimations of SIFs. The SIFs can be estimated either by the displacement based methods or energy based methods. The use of numerical methods, particularly finite element methods, has vastly broadened the range of problems that can be solved by computational approaches. A major advantage is that engineers can easily calculate SIFs at their desks, using personal computers and large number of commercially available finite element codes.

1.4.3 Experimental methods

Experimental methods provide new alternatives and opportunities for solving fracture mechanics problems. Many factors make the experimental determination of the SIFs indispensable. Analytical methods for determination of the SIFs are usually based on simplifying assumptions which imply certain detachment from reality and those theories can be verified only by experimentation to convince whether such idealization has not resulted in an undue distortion of the essential features of the problem. The aim of all experimental methods is to extract the SIFs from the measurable data. Several experimental methods have been developed for the measurement of SIFs in the past and some of the widely used experimental methods are caustics, moiré interferometry, photoelasticity and strain gage techniques.

1.4.3.1 The method of caustics

The method of caustics or shadow spot method relies on the deflection of light rays due to stress field gradient. Caustics are three dimensional surfaces in space enclosing a dark region and along which a high intensity of light occurs [17, 18]. When a uniform beam of light is incident on a reflective surface containing geometric nonlinearities, the beam is reflected in

such a way that its intensity varies spatially to form the caustic. This occurs when light is reflected from the region around the crack tip in a polished specimen subjected to load. The caustic can be seen by placing a screen in the reflected light path. A thin ring of high intensity light the caustic, surrounding a dark spot will be observed. The size and shape of the ring, or caustic can be related to the magnitude of SIFs. The SIF is related to diameter of the caustic, specimen thickness, the distance between the reference plane and the specimen and also Young's modulus and Poisson's ratio of the specimen.

The advantage of caustics method is that it can be applied to both transparent and opaque materials. It has also been used with variety of materials such as isotropic, anisotropic and composite material for the determination of SIFs under static and dynamic loading condition. This method is also widely employed for the determination of mixed mode SIFs. However, the data produced were not as reliable as other methods such as moiré interferometry, photoelasticity and strain gage method [19].

1.4.3.2 Moire interferometry

The two basic principles that govern the formation of moiré interferometry fringes are the interference of light and the diffraction of light. It provides contour maps of the in-plane displacement field, from which small strains can be determined [17]. This technique is based on the interference of two regular gratings and widely employed in quasi-static and dynamic loading problems. Out of two gratings, first grating acts as reference which is undeformed. The second grating which is called active grating is affixed to the surface of the specimen and is deformed by the strains experienced in the specimen. Simultaneous viewing of the two gratings produces the fringes due to crossing of these. The order of fringe starts from known zero displacement. Then, SIF is calculated by substitution of the order of fringe and the pitch of the reference grating in appropriate equation. This method is not consistent as compared to other optical method such as photoelasticity and is also more expensive [19].

1.4.3.3 Photoelasticity

Photoelasticity method is by far the most widely used whole-field technique for studying cracked bodies. It is an optical method of experimental stress analysis, which yields a whole field representation of principal stress difference [17]. The difference in the principal stresses is related to the fringe order, material fringe constant and the length of the light path. In this

method the SIF can be determined by measuring the fringe order and position parameters on a fringe loop. This method has also been applied for determination of mixed mode SIFs. Many investigators used this technique to study crack tip stress field for both static and dynamic conditions.

In comparisons of optical analyses of crack tip stress field, the photoelastic results were the most consistent and in a fully equipped laboratory, photoelasticity would be the first choice to provide accurate, repeatable data [19]. Although the idea of using the photoelastic method of stress analysis to the solution of crack problems seems to be attractive, many difficulties are encountered during measurements due to high concentration of the isochromatic fringes near the crack tip which alter the real meaning of the isochromatic pattern of the corresponding problem of the cracked plate.

1.4.3.4 Electrical resistance strain gage

Of all of the techniques of experimental mechanics, by far the most commonly used techniques are those based on electrical resistance strain gage. Moreover, among the experimental techniques for the determination of SIFs strain gage based techniques are relatively simple, easy to use and inexpensive [17]. Electrical resistance strain gages are the most commonly used type of strain sensors and hereafter these gages are named as only strain gages for simple representation. The change in resistance of a conductor with its change in length forms the basis for strain measurement using strain gages.

Strain gages are bonded to the surface of the body and forms a part of it. When the body deforms, the gage also subjected to the same deformation. As a result, resistance of the gage material changes due to changes in its length due to deformation. This resistance change due to deformation is measured in terms of voltage change using a Wheatstone bridge circuit. The output voltage of the Wheatstone bridge circuit can be calibrated to give the axial strain along the strain gage. The measured strain is then related to SIF by employing appropriate analytical equations, and the SIFs can be determined from those equations. Several static as well as dynamic studies of the cracked components have been reported by many investigators using the strain gage techniques. These techniques are also used for experimental determination of mixed mode SIFs. Strain gage methods are as powerful as photoelastic methods and are also cost effective measurements. Due to the minimal investment in

measuring equipment, these techniques are particularly employed in the development of standard methods of measuring the dynamic initiation, propagation and arrest toughness.

1.5 Principle of operation of the electrical resistance strain gage

The electrical resistance strain gage is the most versatile of many devices to measure free surface strains of machine components and structural members. In 1856, Lord Kelvin reported that certain metal wires exhibited a change of electrical resistance with the change in strain. The resistance R of a uniform conductor with a length L, cross-sectional area A and specific resistance ρ is given by

$$R = \rho \frac{L}{A} \tag{1.23}$$

Thus, when a conductor is pulled in the axial direction, a change in electrical resistance occurs due to the change in length of the conductor. This forms the basic principle of working of electrical resistance strain gages. Usually the change in resistance is extremely small quantity. The amount of the resistance change in relation to change in length of the conductor is known as the strain sensitivity of the material of conductor. Since the change in resistance for a change in length of the conductor is so small that special bridge circuits such as Wheatstone bridge and potentiometer bridge circuits are widely employed in practice. The output voltage of bridge circuit is proportional to the change in resistance of strain gages and hence proportional to the axial strain. The most commonly used strain gages are foil gages.

1.5.1 Bonded metallic foil strain gages

Although, it is theoretically possible to measure strain with a single length of wire as the sensing element of the strain gage, in order to sense the strain in a robust way and accurately, modern strain gages are available in a form popularly known as bonded metal foil strain gages. These are most widely used for measurement of surface axial strains. A metallic foil strain gage consists of a very thin rolled foil arranged in a grid pattern. The grid pattern maximizes the amount of metallic wire subject to strain in the parallel direction. Figure 1.7 shows a typical foil strain gage. The dimension between the ends of the grid is the basic measuring length of a strain age, and is called the *gage length*. Henceforth the word strain

gage will be used to denote the bonded metallic foil gages. Most general purpose strain gages produced today are fabricated from the copper-nickel alloy known as Advance or Constantan. The cross sectional area of the grid is minimized to reduce the effect of shear strain and Poisson's effect. The grid is bonded to a thin backing, called the carrier, which is attached directly to the test specimen. Therefore, the strain experienced by the test specimen is transferred directly to the strain gage, which responds with a linear change in electrical resistance.

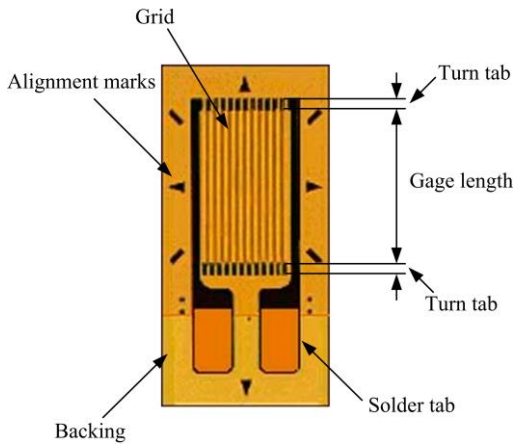

Figure 1.7 Typical foil strain gage (http://www.directindustry.com/prod/vishay-micro-measurements/product-6259-16229.html)

A variety of strain gages such as single element gage, two and three element rosettes, shear gage, strip gage and stress gage, etc., are commercially available for use in various situations. As discussed earlier, the change in resistance is so small that a high sensitive circuits such as Wheatstone bridge circuit is widely employed along with the metallic foil gages to measure the strains. The output voltage of the bridge can be directly related to the surface strains. The overall output of strain sensor depends on gage resistance, lead wire resistance, type of lead wire connection, transverse sensitivity, thermal sensitivity, gage length, gage factor, type of strain gage and excitation voltage of bridge circuit. For accurate measurement of strain the above parameters should be optimized so that error in strain measurement can be reduced. In addition, it is very important to employ the proper adhesive and bonding procedures to achieve precise strain measurements. The most widely used commercially available strain gages are 120Ω, 350Ω and 1000Ω. Using commercially available dedicated strain gage data acquisition systems the accuracy of strain measurement can be further improved and can be made easier. Some of the basic requirements of strain gage are

- Linear strain sensitivity in the elastic range – for accuracy and repeatability.
- High resistivity – for smallest size.
- Low hysteresis – for repeatability and accuracy.

- High strain sensitivity –for maximum electrical output for a given strain.
- Low and controllable temperature coefficient of resistance – for good temperature compensation.
- Wide operating temperature range – for the widest range of applications.
- Good fatigue life – for dynamic measurements.

1.6 Fracture mechanics of orthotropic materials

The presence of cracks are often encountered in orthotropic laminated composites and the study of crack stability of these materials under various loading conditions is crucial. The applicability of the concepts of fracture mechanics put forward by Griffith [7] and Irwin [11] cannot be said to be limited only to isotropic materials. Generally, a simplified case of anisotropy - the orthotropic material is considered to have an understanding of the feasibility of the application of fracture mechanics to anisotropic materials without appreciably narrowing the applicability of the results to practical situations [20, 21].

A material is said to be orthotropic when it possesses three orthogonal planes of elastic symmetry. The assumptions or conditions imposed for the analysis of an orthotropic plate with three planes elastic symmetry containing a through the thickness crack and subjected to arbitrary in-plane loading is as follows [21]

- The material is linearly elastic.
- The plate is thin and of infinite / semi-infinite dimensions.
- The crack is straight and sharp and is parallel to one of the principal planes of elastic symmetry.
- The influence of environment is neglected.

Generally, homogenous composites are believed to behave in an orthotropic linear elastic manner. Therefore, considering near perfect fiber-matrix bonding, the above conditions though simplify the mathematical analysis, in no way limit their applicability to real life cases. The concepts of fracture mechanics pertaining to homogenous isotropic materials have been extended to orthotropic materials after allowing suitable provision to take care of the directional properties of such materials. Comparison of the crack tip stress distribution in an orthotropic plate to that in an isotropic plate shows that the stress singularity at the crack tip

$(\text{as, } r \to 0)$ for both the cases follow the $r^{-1/2}$ order. In addition, though the state of stress in the crack tip vicinity for an orthotropic plate is dependent on the elastic constants of the material $(E_L, E_T, \nu_{LT}, G_{LT})$ unlike that of in isotropic materials, a parameter can be defined to measure the strength of a cracked orthotropic plate similar to isotropic case. Therefore, the stress intensity factors, K_I, K_{II} and K_{III} (section 1.3.3) characterizing the effect of the crack length and the magnitude of the external stresses provides a complete description of the state of stress over some region of the orthotropic body as in case of homogenous isotropic materials.

The crack extension force (G) obtained from energy considerations is generally considered to be a more fundamental parameter related to crack extension. However, in order to obtain G, a knowledge of the direction of the crack growth is necessary. For isotropic materials, the generally accepted hypothesis is that crack growth takes place in the direction perpendicular to the direction of greatest tension and it is experimentally verified. However, for orthotropic materials, the direction of crack growth depends on the strength of the material as well as the state of stress. Therefore, the crack instability of orthotropic plates is generally examined using stress intensity factors as criteria to measure the strength of a cracked orthotropic plate [21]. From the theoretical analysis of the stresses in the vicinity of the crack tip in an orthotropic plate, Wu [21] found that the stress distribution was dependent on the material constants and stress singularity was of the order of $r^{-1/2}$ similar to that of isotropic materials. The theoretical analysis also indicated that the same equations of stress intensity factors as that of isotropic materials could be used to measure the strength of an orthotropic plate containing a crack. Therefore, the estimation of stress intensity factors of orthotropic materials using strain gage based approach would be less cumbersome and also economically viable keeping in mind the clumsy attributes posed by the directional properties of such materials.

1.7 Motivation

The fracture analysis of composite materials is important keeping in view the widespread usage and application of such materials. The accurate determination of fracture parameter, SIF, is crucial in the sense that it aids in taking preventive steps against potential fracture.

Amongst the available experimental methods for estimation of SIF, strain gage methods are comparatively easier to use and cost effective. They can be used on components made of both metallic and non-metallic materials. The strain gage based applications have reached quite a potent stage as far as isotropic materials are concerned.

In view of the importance of fracture mechanics of composites and the importance of SIFs in this area and advantages of strain gage based techniques, the motivation was to undertake studies where strain gage based technique could be applied to determination of fracture parameters in cracked orthotropic composites and study the challenges involved. To understand this an extensive literature review was required which was done and presented in the next chapter.

Chapter 2

Literature review

In this chapter, an exhaustive literature review has been presented in the broad area of strain gage based determination of SIFs with a focus on determination of SIFs in laminated composites in particular. To begin with, the literatures on application of LEFM in laminated composites are discussed in general followed by different techniques including strain gage based applications in particular available in determination of SIFs in laminated composites. Thereafter, various other available strain gage based techniques for determination of SIFs of different types of materials have been discussed. Based on the exhaustive literature review, a summary is presented and specific objectives of the present thesis are laid down.

2.1 LEFM for orthotropic materials

The pioneering work towards the development of fracture mechanics studies of orthotropic materials was started by Irwin [20] in 1962. He proposed counterparts of the Westergaard's equation [9] for orthotropic solids. Wu [21] in 1963 also reported on the feasibility of the linear elastic fracture concept to orthotropic plates by examining the problem of an infinite plate containing a single crack oriented in the direction of one of the planes of elastic symmetry. Through experiments on balsa wood and fiber-glass-reinforced plastic plates, he developed an empirical relation inferring the existence of a general law of fracture for orthotropic materials. Sih et al. [22] developed general equations for crack tip stress fields in rectilinear orthotropic bodies using a complex variable approach in 1965 and observed the presence of an elastic stress singularity of order $r^{-1/2}$ at the crack tip.

In 1978, Dharan [23] proposed that LEFM could be applied to obtain equations relating strain energy release rate to SIF for various modes of crack propagation assuming homogenous, orthotropic relations for a self-similar crack. They obtained good results experimentally for a mode I crack propagation in graphite-epoxy an interlaminar shearing in glass-fiber reinforced epoxy with these restrictive conditions.

Parhizgar et al. [24] also investigated the applications of linear elastic fracture mechanics to orthotropic materials and reportedly verified that fracture toughness of unidirectional composites is a constant independent of material property.

Rossamith et al. [25] analyzed the crack tip stress patterns in a loaded orthotropic, homogenous specimen assuming linear elastic conditions and reported that the degree of orthotropy as well as regular stress fields in the stress functions may have some influence on the overall appearance of maximum shear stress lines around the crack tip in an orthotropic material. Nobile et al. [26] carried out investigations to study the elastostatic fracture response of an infinite orthotropic cracked plate subjected to biaxial uniform loading and pointed out the effects of orthotropy and load biaxiality on the near crack tip fields. They pointed out using both the strain energy density theory and the maximum tensile stress criterion that the value of the crack extension angle depends both on the biaxial load parameter and orthotropic behavior of the material.

2.2 Determination of SIF in cracked composite materials

Due to the limitation of analytical methods in handling general propagations and arbitrary complex geometries and boundary conditions, several numerical and experimental techniques have been developed for solving composite fracture mechanics problems under mode I and mixed mode loading.

2.2.1 Numerical methods

Cruse [27] in 1988 developed boundary element solutions for quasi-static crack propagation in orthotropic media. Boundary element methods (BEM) were also taken up by other researchers in due course. In 1998, Alibadi and Sollero [28] formulated dual boundary element method for crack growth analysis in homogenous orthotropic laminates and demonstrated the application of the method by solving several edge-crack configurations. In 2008, Garcia-Sanchez et al. [29] demonstrated a time-domain BEM for transient dynamic crack analysis in 2D homogenous, anisotropic elastic solids and presented numerical examples to establish the accuracy and robustness of the said method. However, the boundary element method, in spite of its benefits, are ill-suited for non-linear systems and general crack propagation problems.

Alternative available methods include hybrid displacement finite element method by Atluri et al. [30], discrete element method (DEM) by Mohammadi [31], modified crack closure technique (MCCT) and displacement correlation technique (DCT) by Kim and Paulino [32] and various meshless methods. The assumed displacement hybrid finite element model developed by Atluri et al. [30] consists of algebraic system of equations where the nodal displacements and elastic stress intensity factors are the unknowns. The developed model is suitable for analyzing elastic-plastic state in the vicinity of a crack-tip and is demonstrated by numerical results obtained for a tension plate with a central crack, single-edge crack and a quarter-circular crack. In a progressive fracture analysis of composites using DEM, part of the composite model, which is potentially susceptible to damage is represented by discrete elements and the rest of the specimen is modelled with coarser finite elements to reduce analysis time [31]. A specially tailored modified crack closure technique (MCCT) and the displacement correlation technique (DCT) for orthotropic FGMs was presented by Kim and Paulino [32] in 2002 employing the predictor-corrector process. Numerical results established the accuracy of the estimated mixed mode SIFs of the orthotropic FGMs obtained using the developed techniques.

Meshless methods avoid the pre-defined fixed connectivity between the nodal points which are used to define the geometry and set necessary degree of freedoms to discretize the governing equation thereby simplifying the modelling of structures with cracks [33]. The element free Galerkin method (EFG) is one such method which does not require remeshing in crack growth problems and the discrete equations are obtained by Galerkin Method [34]. The conventional EFG was also extended to analysis of discontinuous orthotropic enrichment functions to evaluate SIFs by Ghorasi et al. [35]. The extended finite element method (XFEM) is a combination of finite element and meshless concepts based on the mathematical foundation of Partition of Unity finite element method (PUFEM) [33]. The orthotropic crack-tip enrichment functions for application of XFEM to orthotropic materials was proposed by Asadpoure et al. [36, 37]. A combination of XFEM and isogeometric analysis (IGA) methodologies was developed for general mixed mode crack propagation problems by the introduction of extended isogeometric analysis (XIGA) by Ghorashi et al. [38].

2.2.2 Experimental methods

In experimental analysis of anisotropic materials various techniques have been reported for measurement of fracture parameters. In 1995 Baik et al. [39] used the method of caustics to obtain SIFs in orthotropic materials under mode I and mixed mode static loading conditions. For mode I case, the SIFs obtained were found to be close to that obtained using BEM (boundary element method), and for mixed-mode loading cases, the SIFs obtained show a relative difference of 2.2-2.4% with those obtained using the BEM.

Yao et al. [40] studied the stress singularities of mode I crack tip in orthotropic composites using the reflective caustic technology. A series of caustic experiments of mode I crack tip for glass-fiber woven composites were performed under three-point-bend loading. The experimental results showed good agreement with the numerical results except in the tail part of the caustic pattern due to the effect of the crack tip on crack tip stress field.

Mojtahed and Zachary [41] devised a method for obtaining mode I SIF in orthotropic materials by using photoelastic technique. The set of equations obtained by combining the orthotropic photoelasticity and LEFM laws were used along with half-fringe photoelasticity to determine K_I in a CT specimen made of a transparent unidirectional fiber-glass epoxy material and the results were validated using finite-element based solutions.

Ju and Liu [42] have used the technique of coherent grading sensing (CGS) interferometry to experimentally determine SIF for cracked composite panels (unidirectional graphite-epoxy) under bending (plane-stress deformation). The SIFs measured using the CGS technique when compared with the analytical solution were found to be in good agreement.

Khanna et al. [43] used the technique of transmission photoelasticity to determine the SIFs for cracks in composites. They prepared transparent composites by matching the refractive index of fibers and the quasi-static mode I fracture and the isochromatic fringe patterns obtained were analyzed using orthotropic photoelasticity to obtain mode I SIFs. Opening mode stress field equations in conjunction with an orthotropic stress-optic law were utilized to regenerate the isochromatic fringe patterns obtained and were analyzed using orthotropic photoelasticity to obtain mode I SIFs. Some discrepancies at relatively far distances from the crack tip with otherwise good agreement was observed between the regenerated fringe patterns and the experimentally obtained patterns.

Mogadpalli and Parameswaran [44] investigated on the application of digital image correlation (DIC) to determine SIF for cracks in orthotropic composites. Tests were conducted by loading edge cracked composite panel in remote tension and the SIF was determined from the displacement data using the derived displacement field. There is good agreement (within 2%) between the experimentally determined SIF and that obtained analytically except at very low load (=50N) when the displacement level is too small and at a very high load (=350 N) when the SIF becomes almost twice the K_{IC} of epoxy.

2.2.3 Strain gage based determination of SIF in general and for orthotropic materials in particular

The use of strain gage to determine SIFs near the crack tip was first suggested by Irwin [45] in 1957. However, practically feasible methods based on the strain gages were not realized for long time due to constraints such as measurement of strains at high strain gradients zones in the vicinity of crack tips using finite sized strain gages, local yielding and three-dimensional effects near the crack tip. As reported by Broek [46], a very early attempt to determine the mode I SIFs using strain gages were made by Bhandari and co-workers [47, 48]. They employed strain gage measurements at several points close to the crack tip and extrapolated the measured data to crack tip for determination of SIFs. Despite the above constraints, they reported to obtain accurate values of SIFs. However, no strain gage radial locations were recommended for using the above extrapolation technique [46].

In the meantime, in an effort to establish the range of applicability of two dimensional near tip solutions, Rosakis and Ravi-Chandar [49] experimentally found the extent of three dimensionality of the crack tip stress fields using caustics. Polymethylmethacrylate (PMMA) plates of various thicknesses were considered. They showed that plane stress conditions prevail at distances greater than half the specimen thickness from the crack tip for mode I loading conditions and below this distance the state of stress is three dimensional.

To overcome the constraints in development of strain gage based methods (as mentioned earlier) Dally and Sanford [50] were first to propose a practically viable and theoretically well supported single strain gage technique for determination of the static mode I SIF in two dimensional bodies of isotropic materials. They employed a truncated strain series consisting of three unknown coefficients (multi-parameter strain series) for the

representation of the strains in the experimental specimens. As a consequence, the strain gages could be placed at grater radial distances from the crack tip instead of placing in the vicinity of the crack tip. Further, by use of clever manipulation of the selected multi-parameter strain expressions, they devised a robust technique for experimental determination of the mode I SIF using only one strain gage.

Thus the major advantage of their technique is that a single strain gage located at radial distance sufficiently away from the crack tip is sufficient to determine the mode I SIF of any configuration. For experimental validation of their method three single element strain gages were pasted on an aluminum CT (Compact Tension) specimen. These three gages were located at different radii from the crack tip. They noticed that the error in the measured SIF was more in the first and last strain gages as compared to the intermediate one indicating the importance of radial location of strain gage on determination of accurate values of SIFs. It can be noticed from their technique that the radial location of the single strain gage should be within the realm of applicability of the selected three parameter representation. Consequently, this technique requires prior knowledge regarding the extent of validity of the selected three parameter strain representation (which in turn provides valid or optimal gage locations) which is a function of the geometry of the specimen and applied loading. No suggestions were made by Dally and Sanford [50] on the valid or optimal gage locations. However, based on Rosakis and Ravi-Chandar work [49] they suggested that the strain gages should be placed at distances greater than half the thickness of the specimen from the crack tip in order to avoid three dimensional effects. Clearly this suggestion serves in identifying only the minimum radial distance for the strain gage. The Dally and Sanford [50] single strain gage technique is henceforth will be abbreviated as *DS technique* in the present investigation.

The strain gage techniques were also developed and employed to determine the dynamic SIFs in dynamic fracture problems. A single strain gage technique for measurement of mode I dynamic SIF for propagating crack was developed by Shukla et al. [51], in a similar way to that of DS technique. They considered a two parameter (neglecting the $r^{1/2}$ term) dynamic strain series for the representation of the strain field. A comparison of dynamic SIFs for a propagating crack obtained using their strain gage technique and photoelastic coating method was carried out on a single edge notch plate made of steel and aluminum. In order to determine dynamic SIFs, they mounted four strain gages with equal spacing in a row above the crack tip. It was reported that the dynamic SIFs obtained from strain gage method were

in good agreement with the values obtained from the photoelastic coatings. The distance of strain gages from the crack tip was not reported and no suggestions on valid or optimal locations were also provided.

Another single strain gage technique for measurement of mode I dynamic SIF was also developed by Berger et al. [52], for propagating cracks in a similar way to that of DS technique. They considered a three parameter strain series and included the $r^{1/2}$ term in the selected dynamic strain series which was neglected by Shukla et al. [51], and demonstrated the importance of this term in measuring dynamic SIF. Further, they also developed a crack tip algorithm for precise location of crack tip with respect to the strain gages in a propagating crack. After the precise position of the crack tip was determined, the dynamic SIF was calculated from the strain sensed by the gages. Six strain gages were placed on the line below the crack axis of CT specimen made of alloy steel. No explanation was provided on selected radial locations of strain gages used for measurement of dynamic SIFs. They reported that the measured strains using this technique deviated 5% to 7% from the computed strains.

Because of its simplicity and robust foundations, the DS technique was extensively employed in various studies of experimental fracture mechanics. A review of literature wherein the DS technique was employed for determination of static and dynamic mode I SIFs is presented in the following section.

In an attempt to verify a new technique for the measurement of dynamic initiation toughness (based on detonation of explosives), Dally and Barker [53] employed the DS technique for experimental determination of mode I dynamic SIF of a sharp stationary crack. The dynamic initiation toughness was measured for Homalite 100 using both DS technique and photoelastic method. A dog-bone specimen was used in their experiments. The dynamic loads were induced to the specimen by detonation of explosives. The strain gages were reported to be located within the singularity dominated zone but at a distance greater than half the thickness of the specimen to avoid the three dimensional effects. No further discussion was presented on the selected gage locations. They observed that strain gage method yielded better result as compared to photoelastic method even though it was based on static theory. They reported experimental error on determination of dynamic SIF was about 25 percent.

To study the effect of material composition and thickness of the specimen in determination of static mode I SIF using DS technique, Parnas et al. [54] conducted several experiments. They considered CT specimens made of steel and aluminum of different

thicknesses. Strain gages were pasted at a radial distance from the crack tip greater than half the thickness of the CT specimen and no further discussion was available on radial location of strain gages. However, they suggested from their experimental results that the thickness of the specimen and the region of strain gage location should seriously be considered during the application of DS technique. The SIFs obtained were higher than theoretical and finite element values.

While studying the dimple fracture under shot pulse loading, Rizal and Homma [55] employed the DS technique for measuring the dynamic SIF. The material used in their experiment was aluminum alloy. For measurement of strain, a strain gage was mounted at a distance of 7mm from crack tip according to DS technique. No other discussion was made on the radial locations of the strain gages and the selected radial distance 7 mm was possibly based on their intuition/past experience. They observed that pulse duration was having significant effect on dynamic fracture toughness and reported that the with decrease in pulse duration to a particular limit there would be steep rise in dynamic fracture toughness.

Marur et al. [56] studied the influence of particle size and volume fraction on both the static and dynamic fracture toughness of a composite material. They employed the DS technique for measuring the dynamic SIF. To measure dynamic strain and in turn, the SIF, a single stain gage was pasted at a distance of 0.6 times the thickness of the specimen from the crack tip to avoid the three dimensional effects. No investigation was conducted on whether the selected radial distance was within the realm of strain expressions employed in DS technique or not. Further, no discussion was also made on selection of radial locations for strain gages. It appears that the selected gage location was possibly based on their intuition/past experience. They reported that for a given volume fraction, smaller size particles reduce the dynamic fracture toughness.

Kirugulige and Tippur [57] studied mixed mode dynamic crack growth behavior in functionally graded glass filled epoxy sheets. In order to measure mode I crack initiation toughness of filler, they employed DS technique to obtain dynamic SIF histories. No explanation was made on the selected radial locations of the strain gages on the edge cracked beam specimen. It appears that the selected gage locations were based on their intuition/past experience. Experiments were conducted by alternating load on stiffer side and compliant side.

While studying the viscoelastic effect on the dynamic fracture toughness of a glass fiber reinforced polyester composite, Shirley and Homma [58] employed the DS technique for measurement of dynamic SIF under various loading rates. They pasted a strain gage at a distance of 7mm from the crack tip. No explanation/remarks were provided for the selected radial distance for the strain gage. They observed that the fracture toughness based on stress singularity is significantly affected by the loading rate and while one based on the strain singularity is less affected by the loading rate. They reported that to fully understand loading rate on the dynamic fracture toughness in addition to the fracture behavior for viscoelastic materials, interfacial bonding strength under different loading conditions must be considered.

Wadgaonkar and Parameswaran [59] employed the DS technique for measurement of mode I SIFs on epoxy side and glass bead side of a graded material system. Experiment was conducted on a single edge notch specimen subjected to four point bending. To determine SIFs, two strain gages were installed, one at epoxy rich surface and another at glass bead surface at a radial distance of $3/4^{th}$ of thickness of the plate from the crack tip to avoid three dimensional effects and strain gradients. No further information on radial locations was provided. It seems that the selected radial distance of strain gages may be based on their intuition/past experience. The results showed that the SIFs on the stiffer face of the plate were more than two times those on compliant face.

Owing to the importance of strain gage radial locations, an attempt has been made recently by Sarangi et al. [60-62] in determining valid radial locations for strain gages for the evaluation of mode I SIFs in isotropic materials. Their approach is based on the finite element analysis (FEA) of 2D cracked configurations and the resulting optimal gage locations are appropriate to work with the popular DS technique for the accurate measurement of mode I SIFs. They proposed a methodology to compute the maximum permissible radial location of a strain gage (r_{max}) or the extent of the three parameter zone, which in turn can be used to find the valid or optimal radial locations. Results on valid gage locations obtained using the method [60-62] were shown to be consistent with the theoretical predictions and due to the simplicity and robustness of the method it could be used for any complex experimental specimen. They also showed experimentally [63] that very accurate values of SIF could be obtained when the gages were pasted at optimal locations and highly erroneous SIF resulted when the gages were located at non-optimal locations.

Very limited amount of published work is available on applications of strain gage techniques for determination of mixed mode I/II SIFs for isotropic materials. The very first work in this direction was due to Dally and Berger [64] who extended DS technique to the mixed mode strain field for the determination of static SIFs K_I and K_{II} in isotropic materials. More number of parameters was employed in their method as compared to DS technique so that the strain gages could be placed at greater distances from the crack tip. Due to the use of multiparameter strain field representation, the region of strain field was increased substantially but at the same time more number of strain gages was required to find the unknown coefficients. Two ten element strip gages were pasted on both sides of crack axis in a slant edge cracked plate made of aluminum alloy at equal angle and at equal radius form crack tip to capture corresponding positive and negative strains. No guidelines or procedure was suggested on valid or optimal radial locations for strain gages. It appears that the placement of strip gages, from the crack tip was probably based on their intuition/past experience. It is clear that since they employed strip gages, some of the gages may be at the optimal locations and others may be at unacceptable locations. The SIFs were obtained by graphical extrapolation technique. The SIFs obtained by experimental techniques were compared with both numerical result and published result. An error of about 16.4% in K_I and 29% in K_{II} were reported when they compared their experimental values with the published data. In the present investigation, henceforth, Dally and Berger [64] mixed mode technique is termed as *DB technique* throughout the present investigation.

Kondo et al. [65] proposed a strain gage method for determination of mixed mode SIFs of sharp notched strips. In this technique it was necessary to position the strain gage along more than two different directions for determination of mixed mode SIFs. They employed two strip gages containing five elements for measuring strain along two rays from the bisector angle of the notch. The radial locations of each strain gage were selected based on the theory given by Dally and Sanford [50] for minimizing the averaging errors in gages. No procedure was discussed for valid or optimal radial locations of strain gages. The experimental results of mode I and mode II SIFs were consistently smaller than the theoretical results and within 10% difference for various notch angles and shapes.

Another strain gage technique for determination of mixed mode SIFs was proposed by Dorogoy and Rittel [66] using strain gage rosettes instead of single element gages. The procedure for obtaining the SIFs was presented using numerical studies on a slant edge

cracked plate and no experimental results were reported. They observed from the numerical analysis that the radial location of rosette was an important factor in accurate measurement of SIFs. They recommended that the rosette should be placed as close as possible to the crack tip but outside the plastic zone and three dimensional effects which clearly demands knowledge of unknown SIFs. From the numerical example, they suggested the use of two strain gage rosettes at the same angle and linearly extrapolate their results for obtaining reasonably accurate mixed mode SIFs.

Sarangi et al. [67] proposed a modified version of the Dally and Berger approach [64] for definitive determination of maximum permissible radial location of strain gages ($r_{\max}$) thereby leading to accurate determination of mixed mode SIFs and verified their propositions numerically. They also investigated the effect of crack length to width ratio and state of stress on the $r_{\max}$. They also conducted experiments to study the efficacy of the proposed mixed mode strain gage technique and existence and usefulness of the strain gage locations in accuracy of the estimated SIFs (K_I, K_{II}) [68].

2.2.3.1 Strain gage techniques for determination of SIFs in orthotropic materials

Very few works are available with regard to strain gage application for determination of SIFs in orthotropic laminates. Shukla et al. [69] developed a single strain gage technique for determination of static mode I SIF by employing two-parameter orthotropic strain equations around the crack tip. Their technique was verified by conducting experiments on a glass-epoxy single-edge-notched composite specimen. Although, it was realized that the selected radial locations should be according to the theoretical formulations, the radial location of strain gages for their experimental work were primarily based on minimizing the average errors due to the strain gradients. Based on the averaging error, two strain gages were pasted at distances of 5 mm and 9 mm from the crack tip. The SIF was measured corresponding two locations. The result showed that the strain gage located at 9 mm could produce good agreement with theoretical SIF. But the error in SIF using strain gage located at 5mm was about 18% and they attributed this large error to the three dimensional effects etc. However, there were two major limitations of this technique viz. the two parameter strain series employed by them as opposed to the three parameter strain series proposed by Dally and Sanford [50] truncated the radial distance within which the strain gage can be located for

successful mensuration of strains. Again, no guidelines or recommendations were presented for locating the strain gage.

Khanna and Shukla [70] developed a single strain gage technique for determination of mode I dynamic SIF for a moving crack at a constant speed in the orthotropic composite materials. Theoretical equations of the strain field around a crack moving at a constant velocity in an orthotropic composite material were developed. A procedure was developed to evaluate the optimum size, orientation and location of strain gage for minimizing the average errors for strain gages within the realm of the selected strain expression. A single edge notch (SEN) fracture specimen made from unidirectional glass-epoxy composite laminate was used to determine the SIF for a crack propagating along the direction of fiber reinforcement. The radial location of strain gages on the experimental specimen was decided based on the experimental results on averaging error with the radial locations. No validity or explanation was provided as the selected locations are valid locations to satisfy the realm of the selected strain expression.

Khanna and Shukla [71] also investigated the effect of the position and gage orientation on determination of dynamic SIF using the technique developed by Khanna and Shukla [70]. Based on the maps of singularity dominated zone for certain configurations and experiments on a modified CT specimen made of three different materials they found that their technique [70] determined the dynamic SIFs close to the photoelastic values if the gages were pasted within the singularity dominated zone and oriented at obtuse angles. As stated earlier the strain gradients and three dimensional effects clearly affect the measured strains in such small zones such as singularity dominated zones as is evident in their earlier works [69]. Moreover, a complete map of singularity dominated zone for the experimental specimen is needed apriori for application of their technique.

Cerniglia et al. [72] also employed electrical strain gages to obtain SIFs for composites employing an overdeterministic approach. A SEN specimen of orthotropic Carbon-epoxy laminate was used and SIF values obtained experimentally was found close to the numerical results. They also pointed out the insignificant influence of orthotropy on SIF values. However, the requirement of a large number of strain gages and arbitrary location associated with each strain gage posed as major limitations of their proposed approach.

2.3 Summary of literature review and objectives of the present work

The literature review could be summarized as follows.

- There has been number of works reported on successful implementation of LEFM for orthotropic composites and their successive SIF determination using various methods.
- Among experimental techniques, very few works [69-72] have been reported on strain gage based applications for determination of SIF of orthotropic composites irrespective of the cost effectiveness and ease of use of strain gage techniques.
- The DS technique [50] has been observed to be very popular when isotropic material is concerned and is applied as it is in many investigations of static and dynamic loading conditions. Further it has been extended to other areas for determination of SIFs.
- The DS technique [50] is very widely employed as compared to the other techniques due to the reason that only a single strain gage is sufficient to determine mode I SIF and this gage can be located at a radial distance far from crack tip where the effects of plasticity, three-dimensional state of stress and strain gradients are very minimal.
- Shukla et al. [69] incorporated a partially extended DS technique in their approach by employing a two-parameter strain series equations for the field around the crack tip. They also did not recommend any concrete suggestions for locating the strain gages.
- The DB technique [64] which is an extension of the DS technique is a well-known technique in fracture mechanics for determination of mixed mode SIFs in isotropic materials.
- Locations of strain gages play a vital role in accurate determination of SIFs and Dally and Sanford [50] and Dally and Berger [64] suggested that the strain gage should be placed in the region II in order to avoid strain gradient effect, plasticity effect and three-dimensional effect.
- Sarangi et al. [60-62] proposed optimal radial locations for locating the strain gage in conjunction with the DS technique for accurate evaluation of mode I SIFs in isotropic materials. They also proposed certain altercations in the DB technique and proposed optimal gage locations for single ended mixed mode cracked configuration for

accurate determination of mixed mode SIFs [67]. Through experiments conducted [63, 68], they showed that accurate values of mode I SIF and mixed mode SIFs can be obtained for strain gage located within the proposed optimal gage locations.

- No works are reported till date on strain gage based determination of mixed mode SIFs in orthotropic laminates.

2.3.1 Objectives

Summary of the literature review reveals that strain gage based determination of SIFs is a simple and useful technique. While the DS technique [50] could be successfully implemented for isotropic materials for experimental determination of SIFs, the proper extension of this technique to laminated composites has not seen the light even though there has been very limited efforts. Similarly, strain gage based technique for determination of mixed mode SIFs in laminated composites has not been reported till date in the literatures. Apart from robust theoretical foundation, success of any strain gage technique largely depends on the availability of recommendations for radial locations of strain gages. This forms the motivation for taking up the present study of proposing strain gage based techniques for estimation of mode I and mixed mode SIFs of orthotropic laminates along with quantitative recommendations for valid radial locations of the strain gages. Experimental investigations are also aimed at verification of the proposed technique for determination of SIFs for orthotropic laminates and provide useful recommendations for different types of crack configurations. Based on these observations, the objectives of the present work have been laid as-

1. To develop a theoretical framework for extending the DS technique to homogenous orthotropic materials i.e. development of a single strain gage technique for accurate determination of mode I SIFs of 2D configurations of single and double ended cracked orthotropic laminates.
2. To suggest a procedure for deciding the upper bound on radial gage location (r_{max}) which in turn is useful in estimation of optimal gage location for important single and double ended cracked configurations for accurate determination of mode I SIFs in orthotropic materials.
3. To develop a FE based methodology for determination of r_{max}.

4. To decide the valid or optimal radial location of the strain gage using r_{max} in conjunction with the proposed technique for accurate determination of mode I SIFs in 2D bodies of cracked orthotropic laminates.
5. To study the effect of parameters like crack length to width ratio and the boundary effects on the r_{max} and hence optimal gage locations.
6. To numerically simulate the proposed single strain gage technique for determination of K_I of different single ended and double ended mode I configurations of orthotropic laminates and to study the influence of locating strain gages at optimal and non-optimal radial locations on the accuracy of measured SIFs.
7. To conduct sensitivity analysis numerically to study the effect of discrepancies in strain gage orientations on the accuracy of the estimated SIFs.
8. Experimental determination of mode I SIF for edge cracked $[90_2/0]_{10S}$ Carbon-epoxy laminates using a single strain gage following the proposed technique to establish the
    a. efficacy of the proposed technique in terms of its actual implementation in experimental determination of mode I SIF using a single strain gage.
    b. importance of r_{max} in accurate determination of mode I SIF by determination of mode I SIFs using the readings of strain gage placed within r_{max} (optimal) and outside r_{max} (non-optimal).
    c. repeatability of the experimental results and reproducibility of the complete experiment by repeating the experiments number of times and on different specimens prepared.
9. To develop a theoretical framework for determination of mixed mode SIFs $(K_I$ and $K_{II})$ using minimum number of strain gages for orthotropic materials
10. To develop a FE based methodology for deciding the optimal radial locations of the strain gages (based on the r_{max}) for accurate determination of mixed mode SIFs of orthotropic laminates.
11. To numerically simulate the proposed strain gage technique for determination of mixed mode SIFs $(K_I$ and $K_{II})$ of slant edge cracked panels for different crack

inclination angles and mode mixity and to study the influence of pasting the strain gages at optimal and non-optimal locations on the accuracy of K_I, K_{II}.

12. To study the effect of parameters like crack length to width ratio, the boundary effects and crack inclination angle on the r_{max} of mixed mode configurations.

Chapter 3

Theoretical Formulations

This chapter describes the theoretical formulation for the development of proposed strain gage techniques for determination of mode I and mixed mode (I/II) SIFs of orthotropic laminates. The theoretical development for estimation of valid optimal radial locations for pasting the strain gages for accurate determination of SIFs is also presented here. The finite element formulation along with the details of discretization for analysis of a cracked orthotropic specimen used in the numerical analyses of the present investigation is also discussed briefly.

3.1 The generalized Westergaard approach

In the present investigation, the generalized Westergaard approach has been employed for the theoretical formulations leading to the development of strain gage techniques for determination of SIFs of orthotropic laminates. This section reviews the method of generalized Westergaard approach and applies it to isotropic materials. The application of the approach to the orthotropic laminates are presented in subsequent sections. The generalized Westergaard approach was proposed by Sanford [73] and is a generalization of the familiar Westergaard stress function approach [9] and can be applied to both infinite and finite body problems with arbitrary boundary conditions and containing a single ended crack or a double ended crack (internal crack) with traction free crack faces. For the case of a single ended crack the method is functionally equivalent to the well-known Williams eigen function expansion method [10]. The generalized Westergaard formulation requires an additional analytic function $Y(z)$ in addition to the standard Westergaard stress function $Z(z)$. Accordingly, the modified Airy stress function for mode I (F_I) and mode II (F_{II}) are then given by [73],

$$F_I = \mathrm{Re}\,\overline{\overline{Z_I}}(z) + y\,\mathrm{Im}\,\overline{Z_I}(z) + y\,\mathrm{Im}\,\overline{Y_I}(z) \tag{3.1}$$

$$F_{II} = -y\,\mathrm{Re}\,\overline{Z_{II}}(z) + \mathrm{Im}\,\overline{\overline{Y_{II}}}(z) - y\,\mathrm{Re}\,\overline{Y}_{II}(z) \tag{3.2}$$

where

$$\frac{d\overline{\overline{Z_i}}}{dz}=\overline{Z_i}, \quad \frac{d\overline{Z_i}}{dz}=Z_i, \quad \frac{dZ_i}{dz}=Z_i', \quad \frac{d\overline{Y_i}}{dz}=Y_i \quad \text{where} \quad i=I, II \tag{3.3}$$

The complex analytic functions for opening mode $Z_I(z)$, $Y_I(z)$ and those for shearing mode $Z_{II}(z)$, $Y_{II}(z)$ are defined as

$$Z_I(z)=\sum_{n=0}^{\infty} A_n z^{n-\frac{1}{2}} \quad \text{and} \quad Y_I(z)=\sum_{m=0}^{\infty} B_m z^m \tag{3.4}$$

$$Z_{II}(z)=\sum_{n=0}^{\infty} C_n z^{n-\frac{1}{2}} \quad \text{and} \quad Y_{II}(z)=\sum_{m=0}^{\infty} D_m z^m \tag{3.5}$$

These are series type functions in terms of complex variable $z=x+iy$ (Fig. 3.1) containing infinite number of real coefficients corresponding to opening mode $(A_0, A_1, ..., A_\infty;\ B_0, B_1, ..., B_\infty)$ and shearing mode $(C_0, C_1, ..., C_\infty;\ D_0, D_1, ..., D_\infty)$. These coefficients are functions of boundary conditions and geometry of the cracked configuration. It should be noted that the above approach is argued to be valid for any length of edge cracks (single ended) and only for sufficiently large double ended cracks (internal cracks) [17].

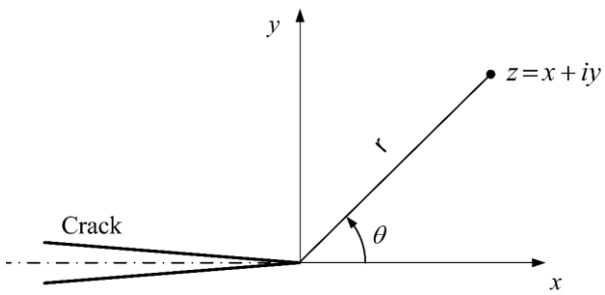

Figure 3.1 The complex plane at the crack tip

For a complex analytic function, such as $Z(z)$ the Cauchy-Riemann equations are given by

$$\begin{aligned} \frac{\partial \operatorname{Re} Z(z)}{\partial x} &= \operatorname{Re} Z' \quad \text{and} \quad \frac{\partial \operatorname{Im} Z(z)}{\partial x} = \operatorname{Im} Z' \\ \frac{\partial \operatorname{Re} Z(z)}{\partial y} &= -\operatorname{Im} Z' \quad \text{and} \quad \frac{\partial \operatorname{Im} Z(z)}{\partial y} = \operatorname{Re} Z' \end{aligned} \tag{3.6}$$

Using Cauchy-Riemann equations and Airy stress function approach, the stress components for mode I in the absence of body forces can be written as

$$\sigma_x = \frac{\partial^2 F_I}{\partial y^2} = \mathrm{Re}\, Z_I - y\,\mathrm{Im}\, Z'_I - y\,\mathrm{Im}\, Y'_I + 2\,\mathrm{Re}\, Y_I$$

$$\sigma_y = \frac{\partial^2 F_I}{\partial x^2} = \mathrm{Re}\, Z_I + y\,\mathrm{Im}\, Z'_I + y\,\mathrm{Im}\, Y'_I \tag{3.7}$$

$$\tau_{xy} = -\frac{\partial^2 F_I}{\partial x \partial y} = y\,\mathrm{Re}\, Z'_I - y\,\mathrm{Re}\, Y'_I - \mathrm{Im}\, Y_I$$

and the stress components for the mode II can be obtained as

$$\sigma_x = \frac{\partial^2 F_{II}}{\partial y^2} = y\,\mathrm{Re}\, Z'_{II} + 2\,\mathrm{Im}\, Z_{II} + y\,\mathrm{Re}\, Y'_{II} + \mathrm{Im}\, Y_{II}$$

$$\sigma_y = \frac{\partial^2 F_{II}}{\partial x^2} = -y\,\mathrm{Re}\, Z'_{II} - y\,\mathrm{Re}\, Y'_{II} + \mathrm{Im}\, Y_{II} \tag{3.8}$$

$$\tau_{xy} = -\frac{\partial^2 F_{II}}{\partial x \partial y} = \mathrm{Re}\, Z_{II} - y\,\mathrm{Im}\, Z'_{II} - y\,\mathrm{Im}\, Y'_{II}$$

Assuming plane stress conditions, the stress-strain relation for linear elastic and isotropic materials are given by

$$\varepsilon_x = \frac{1}{E}\left(\sigma_x - \nu\sigma_y\right)$$

$$\varepsilon_y = \frac{1}{E}\left(\sigma_y - \nu\sigma_x\right) \tag{3.9}$$

$$\gamma_{xy} = \frac{\tau_{xy}}{G}$$

Substituting Eq. (3.7) into Eq. (3.9) equations for strain field corresponding mode I can be obtained as

$$E\,\varepsilon_x = (1-\nu)\,\mathrm{Re}\, Z_I - (1+\nu)\, y\,\mathrm{Im}\, Z'_I - (1+\nu)\, y\,\mathrm{Im}\, Y'_I + 2\,\mathrm{Re}\, Y_I$$

$$E\,\varepsilon_y = (1-\nu)\,\mathrm{Re}\, Z_I + (1+\nu)\, y\,\mathrm{Im}\, Z'_I + (1+\nu)\, y\,\mathrm{Im}\, Y'_I - 2\nu\,\mathrm{Re}\, Y'_I \tag{3.10}$$

$$E\gamma_{xy} = 2(1+\nu)(-y\,\mathrm{Re}\, Y'_I - \mathrm{Im}\, Y_I - y\,\mathrm{Re}\, Z'_I)$$

Similarly substituting Eq. (3.8) into Eq. (3.9) the strain field corresponding to mode II can be obtained as

$$
\begin{aligned}
E\varepsilon_x &= (1+\nu)\, y\, \mathrm{Re}\, Z'_{II} + 2\,\mathrm{Im}\, Z_{II} + (1+\nu)\, y\, \mathrm{Re}\, Y'_{II} + (1-\nu)\,\mathrm{Im}\, Y_{II} \\
E\varepsilon_y &= -(1+\nu)\, y\, \mathrm{Re}\, Z'_{II} - 2\nu\,\mathrm{Im}\, Z_{II} - (1+\nu)\, y\, \mathrm{Re}\, Y'_{II} + (1-\nu)\,\mathrm{Im}\, Y_{II} \\
E\gamma_{xy} &= 2(1+\nu)(-y\,\mathrm{Im}\, Y'_{II} - y\,\mathrm{Im}\, Z'_{II} + \mathrm{Re}\, Z_{II})
\end{aligned}
\tag{3.11}
$$

Substitution of series form of complex functions $Z_I(z)$, $Y_I(z)$, $Z_{II}(z)$ and $Y_{II}(z)$ from Eqs. (3.4) and (3.5) into Eqs. (3.7) and (3.8) and Eqs. (3.10) – (3.11) gives exact representation of stress and strain fields with infinite number of unknown coefficients A_n, B_m, C_n and D_m $(m,n = 0,1,2.....\infty)$. The above discussion illustrates the general procedure of obtaining infinite strain series in mode I and mode II using generalized Westergaard approach. The *first term* or the *leading term* in these series are extremely important in linear elastic fracture mechanics (LEFM) and play vital role in K-based fracture criterion. This term can be obtained by substituting $m,n = 0$ and $z = \cos\theta + i\sin\theta$ in Eqs. (3.7) and (3.8) and Eqs. (3.10) – (3.11). Employing the definition of SIF from

$$
\left.\begin{aligned}
K_I &= \sqrt{2\pi r}\lim_{r\to 0}\sigma_{ij}^{I} \\
K_{II} &= \sqrt{2\pi r}\lim_{r\to 0}\sigma_{ij}^{II}
\end{aligned}\right\} \text{as } r\to 0 \text{ on } \theta = 0^{\circ}
\tag{3.12}
$$

the first terms or the leading terms are found to be related to the respective SIFs as

$$
K_I = \sqrt{2\pi}A_0,\; K_{II} = \sqrt{2\pi}\,C_0 \tag{3.13}
$$

3.2 The Dally and Sanford technique for isotropic materials

Understanding of the Dally and Sanford technique [50] for isotropic materials is extremely useful for extending and developing the theoretical formulations presented in subsequent sections. Therefore, it is briefly presented in this section. The Dally and Sanford single strain gage technique or the DS technique [50] for isotropic materials was the first strain gage based method which could overcome the limitations posed by high strain gradients, plasticity and 3D effects in the neighborhood of the crack tip by examining the state of strain in a region moderately beyond the singularity dominated zone (SDZ) wherein the strains could be described by a low-order truncated (3-paramenter) series expansion and aided in the measurement of K_I of isotropic materials.

The most significant feature of their technique is that only a single strain gage is sufficient to measure the K_I and that strain gage can be placed considerably away from the crack tip in order to avoid strain gradient, plasticity and 3D effects. An important feature of DS technique is the identification of an appropriate zone around the crack tip for strain measurements which may not be influenced by the above effects. SIFs are then determined by equating the measured strains with the theoretical strain series that is valid within the measurement zone. In the DS technique, the region around a crack tip is divided into three zones viz. *zone I, zone II* and *zone III* as shown in Fig. 3.2 in order to identify the suitable zone for strain measurements. Zone I is close to the crack tip and first term of the strain series (singular strain term) in Eq. (3.10) is sufficient to represent the strains within this zone. However, it is not a valid zone for accurate measurement of strains as the stress state in this region could be three dimensional [50] and the measured strains will be severely affected by 3D effect, plasticity and strain gradient effects.

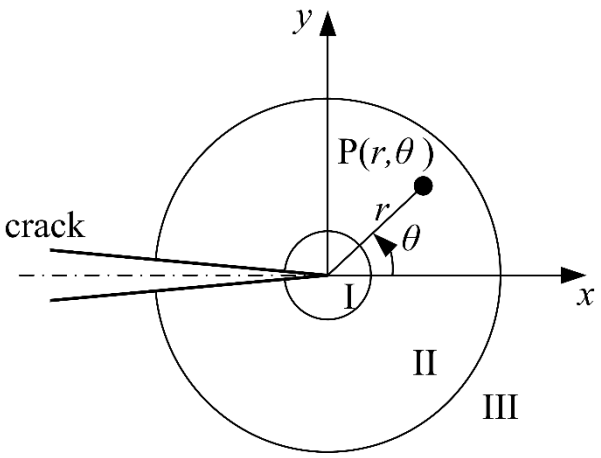

Figure 3.2 Different zones at the crack tip [50]

Zone III is again not suitable for collection of strain data as a very large number of terms in the strain series would be required to yield accurate results. Therefore, the intermediate region or zone II is favored as the optimum zone for accurate measurement of the surface strains. This is defined as a zone in which a singular term plus a small number of higher order terms would accurately describe the strain field. It is assumed that the strain field for the mode I in the zone II can be sufficiently represented by the three parameter series with unknown parameters or coefficients A_0, A_1 and B_0 [50] as opposed to infinite number of coefficients in the strain series. Therefore, the analytical functions in Eq. (3.10) can be written in truncated form using Eq. (3.4) as

$$\begin{aligned}
\mathrm{Re}\,Z_I &= \frac{A_0}{\sqrt{r}}\cos\frac{\theta}{2} + A_1\sqrt{r}\cos\frac{\theta}{2} & \mathrm{Re}\,Y_I &= B_0 \\
\mathrm{Im}\,Z_I &= -\frac{A_0}{\sqrt{r}}\sin\frac{\theta}{2} + A_1\sqrt{r}\sin\frac{\theta}{2} & \mathrm{Im}\,Y_I &= 0 \\
\mathrm{Re}\,Z'_I &= -\frac{A_0}{2}r^{-3/2}\cos\frac{3\theta}{2} + \frac{A_1}{2\sqrt{r}}\cos\frac{\theta}{2} & \mathrm{Re}\,Y'_I &= 0 \\
\mathrm{Im}\,Z'_I &= \frac{A_0}{2}r^{-3/2}\sin\frac{3\theta}{2} - \frac{A_1}{2\sqrt{r}}\sin\frac{\theta}{2} & \mathrm{Im}\,Y'_I &= 0
\end{aligned} \tag{3.14}$$

The three term representation of strain field or the truncated strain series for isotropic materials under plane stress conditions in Zone II can now be written using Eq. (3.14) and relations, $E = 2G(1+\nu)$ and $\kappa = (1-\nu)/(1+\nu)$ as

$$\begin{aligned}
2G\varepsilon_x &= A_0 r^{-1/2}\cos\frac{\theta}{2}\left[\kappa - \sin\frac{\theta}{2}\sin\frac{3\theta}{2}\right] + \frac{2B_0}{(1+\nu)} + A_1 r^{1/2}\cos\frac{\theta}{2}\left[\kappa + \sin^2\frac{\theta}{2}\right] \\
2G\varepsilon_y &= A_0 r^{-1/2}\cos\frac{\theta}{2}\left[\kappa + \sin\frac{\theta}{2}\sin\frac{3\theta}{2}\right] - \frac{2\nu B_0}{(1+\nu)} + A_1 r^{1/2}\cos\frac{\theta}{2}\left[\kappa - \sin^2\frac{\theta}{2}\right] \\
2G\gamma_{xy} &= A_0 r^{-1/2}\left[\sin\theta\cos\frac{3\theta}{2}\right] - A_1 r^{1/2}\left[\sin\theta\cos\frac{\theta}{2}\right]
\end{aligned} \tag{3.15}$$

where A_0, A_1 and B_0 are unknown coefficients which can be determined using geometry of the specimen and loading conditions and are independent of state of stress. Thus by measuring A_0 one can determine K_I from definition (Eq. (3.13)). The normal strain component ε_{aa} defined by an angle ϕ with the crack axis (positive to crack axis) at a point P located by r and θ (Fig. 3.3) can be obtained using strain transformation laws

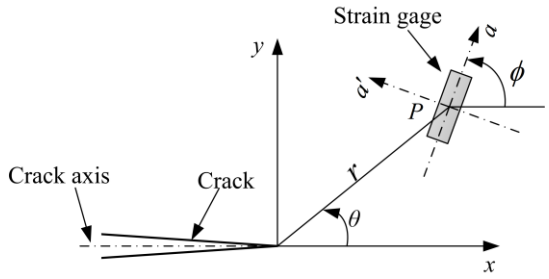

Figure 3.3 Strain gage location and orientation for DS technique

$$\varepsilon_{aa} = \varepsilon_x\cos^2\phi + \varepsilon_y\sin^2\phi + \gamma_{xy}\cos\phi\sin\phi \tag{3.16}$$

as

$$2G\varepsilon_{aa} = A_0 r^{-1/2}\left[\kappa\cos\frac{\theta}{2}-\frac{1}{2}\sin\theta\sin\frac{3\theta}{2}\cos 2\phi+\frac{1}{2}\sin\theta\cos\frac{3\theta}{2}\sin 2\phi\right] + A_1 r^{1/2}\cos\frac{\theta}{2}\left[\kappa+\sin^2\frac{\theta}{2}\cos 2\phi-\frac{1}{2}\sin\theta\sin 2\phi\right]+B_0\left(\kappa+\cos 2\phi\right) \tag{3.17}$$

The coefficient of B_0 term in Eq. (3.14) can be eliminated by selecting the angle ϕ (Fig. 3.3) such that

$$\kappa+\cos 2\phi = 0 \tag{3.18}$$

which gives

$$\cos 2\phi = -\kappa = -\frac{1-\nu}{1+\nu} \tag{3.19}$$

Similarly, using value of ϕ from Eq. (3.19), coefficient of A_1 can also be made zero if the angle θ (Fig. 3.3) is selected as

$$\kappa+\sin^2\frac{\theta}{2}\cos 2\phi-\frac{1}{2}\sin\theta\sin 2\phi = 0 \tag{3.20}$$

which gives

$$\tan\frac{\theta}{2} = -\cot 2\phi \tag{3.21}$$

Thus by placing a single strain gage (Fig. 3.4) on the radial line OM defined by θ (Eq. (3.21)) at an appropriate radial distance r from the crack tip and orienting the gage at an angle ϕ (according Eq. (3.19)), the strain ε_{aa} can be measured, which in turn is related to K_I by

$$2G\varepsilon_{aa} = \frac{K_I}{\sqrt{2\pi r}}\left[\kappa\cos\frac{\theta}{2}-\frac{1}{2}\sin\theta\sin\frac{3\theta}{2}\cos 2\phi+\frac{1}{2}\sin\theta\cos\frac{3\theta}{2}\sin 2\phi\right] \tag{3.22}$$

Thus, from the selected values of Poisson's ratio ν and radial distance r, K_I can be determined from the measured strain ε_{aa}. It may be noted from Eqs. (3.19) and (3.21) that K_I can also be determined by placing a strain gage on the line ON which makes an angle of $-\theta$ with respect to the crack axis. In such case the orientation angle of the gage should be $-\phi$ as shown in Fig. 3.4. As shown Fig. 3.4, the lines OM and ON defined by $+\theta$ and $-\theta$ (Eq. (3.19)) respectively are termed as the *positive gage line* and *negative gage line* respectively.

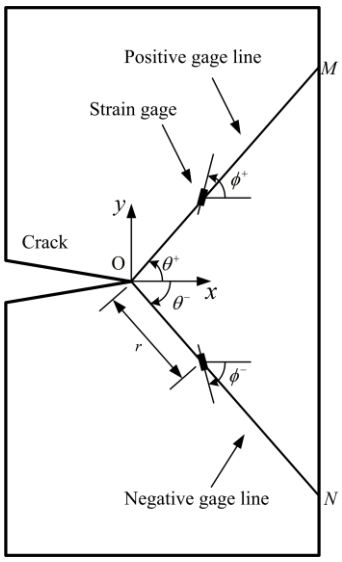

Figure 3.4 Gage lines and strain gage location for DS technique

3.3 The generalized Westergaard approach for orthotropic materials

The first step towards developing a strain gage technique is the selection of appropriate stress functions that satisfy all the boundary conditions. The stresses in an orthotropic laminate containing a through crack was studied by Irwin [20] and Wu [21]. They modified the Westergaard's stress function [9] for isotropic materials to deal with the directional properties of such materials. However, Liu [74] pointed out that Irwin [20] and Wu's [21] solution cannot reduce to Westergaard's solution when the orthotropic properties are reduced to isotropic ones. They proposed new stress functions to this effect which provide equations for stress and displacement fields such that not only the orthotropic materials are taken care of but these equations also boil down to isotropic equations under conditions of material isotropy. Therefore, two types of stress functions are available viz. the one proposed by Irwin [20] and the other proposed by Liu [74] and one of the stress functions is needed for the development of generalized Westergaard approach for orthotropic materials. In the present investigation a study has been carried out to compare the available stress functions. This study is based on comparison of SIFs obtained using displacements derived from each of the two stress functions. The detailed study is presented separately in Chapter 7. The results of the

study clearly indicate that stress functions proposed by Irwin [20] are found to be more accurate than that proposed by Liu [74] as far as estimated SIFs are concerned and hence Irwin's stress functions are considered in the present investigation.

The stress-strain relations for a two dimensional specially orthotropic body under plane stress conditions $\left(\sigma_z = \tau_{yz} = \tau_{zx} = 0\right)$ may be written as

$$\begin{aligned} \varepsilon_x &= a_{11}\sigma_x + a_{12}\sigma_y \\ \varepsilon_y &= a_{12}\sigma_x + a_{22}\sigma_y \\ \gamma_{xy} &= a_{66}\tau_{xy} \end{aligned} \tag{3.23}$$

where $a_{11} = 1/E_L$, $a_{12} = -\nu_{LT}/E_L = -\nu_{TL}/E_T$, $a_{22} = 1/E_T$ and $a_{66} = 1/G_{LT}$ and E_L, E_T, G_{LT} are the effective longitudinal and in-plane transverse and shear modulus respectively and ν_{LT}, ν_{TL} denote in-plane Poisson's ratio (Eq. (1.15)). The equations for stress equilibrium and strain compatibility are not affected by non-isotropy. Therefore, the equations for compatibility conditions can be satisfied by an Airy's stress function, F when the body forces are neglected such that

$$\sigma_x = \partial^2 F/\partial y^2 \qquad \sigma_y = \partial^2 F/\partial x^2 \quad \text{and} \quad \tau_{xy} = -\partial^2 F/\partial x \partial y \tag{3.24}$$

The strain compatibility equation for plane deformation is given by

$$\frac{\partial^2 \varepsilon_x}{\partial y^2} + \frac{\partial^2 \varepsilon_y}{\partial x^2} = \frac{\partial^2 \gamma_{xy}}{\partial x \partial y} \tag{3.25}$$

Substituting Eqs. (3.23) and (3.24) into the Eq. (3.25) gives forth order partial differential equation with constant coefficients as

$$a_{11}\frac{\partial^4 F}{\partial y^4} + \left(a_{66} + 2a_{12}\right)\frac{\partial^4 F}{\partial y^2 \partial x^2} + a_{22}\frac{\partial^4 F}{\partial x^4} = 0 \tag{3.26}$$

Solution of any elasticity problem would require Eq. (3.26) to be solved subjected to appropriate boundary conditions. Westergaard [9] observed that the stress around a mathematical crack on the axis $y = 0$ can be solved by a single stress function in isotropic materials. Considering the problem of a two dimensional orthotropic body containing a

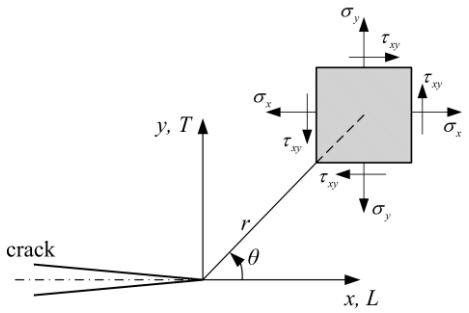

Figure 3.5 Arbitrary crack in the complex domain in orthotropic body

crack (Fig. 3.5), Irwin [20] later proposed counterparts of the Westergaard type of stress functions to specially orthotropic materials for mode I and mode II conditions as

$$F_I = \frac{1}{2}\left[\mathrm{Re}\,\overline{\overline{Z}}_I(z_1)+\mathrm{Re}\,\overline{\overline{Z}}_I(z_2)\right]-\frac{\beta}{2\alpha}\left[\mathrm{Re}\,\overline{\overline{Z}}_I(z_1)-\mathrm{Re}\,\overline{\overline{Z}}_I(z_2)\right]$$
$$F_{II} = -\frac{1}{2\alpha}\left[\mathrm{Im}\,\overline{\overline{Z}}_{II}(z_1)-\mathrm{Im}\,\overline{\overline{Z}}_{II}(z_2)\right] \tag{3.27}$$

where $\overline{Z}_{I,II}(z_i)$ and $\overline{\overline{Z}}_{I,II}(z_i)$ are the first and second integrals with respect to $z_i\,(i=1,2)$ of the complex function $Z_{I,II}(z_i)$, analogous to those for isotropic materials (Eqs. (3.4 – 3.5)) and is given by

$$Z_I(z_i)_{i=1,2}=\sum_{n=0}^{\infty}A_n\left(z_i^{\,n-1/2}\right)_{i=1,2} \quad \text{and} \quad Z_{II}(z_i)_{i=1,2}=\sum_{n=0}^{\infty}C_n\left(z_i^{\,n-1/2}\right)_{i=1,2} \tag{3.28}$$

and $z_i\,(i=1,2)$ are given by

$$z_1 = x+iy_1 = x+i(\beta+\alpha)y = r_1e^{i\theta_1}$$
$$z_2 = x+iy_2 = x+i(\beta-\alpha)y = r_2e^{i\theta_2} \tag{3.29}$$

Also,

$$\tan\theta_1=(\beta+\alpha)\tan\theta \qquad \tan\theta_2=(\beta-\alpha)\tan\theta$$
$$r_1^2=r^2\left(\cos^2\theta+(\beta+\alpha)^2\sin^2\theta\right) \qquad r_2^2=r^2\left(\cos^2\theta+(\beta-\alpha)^2\sin^2\theta\right) \tag{3.30}$$

Subscripts I and II represent the Mode I (opening mode) and Mode II (forward shear) conditions respectively. Additionally,

$$2\beta^2=\frac{a_{66}+2a_{12}}{2a_{11}}+\sqrt{\frac{a_{22}}{a_{11}}};\; 2\alpha^2=\frac{a_{66}+2a_{12}}{2a_{11}}-\sqrt{\frac{a_{22}}{a_{11}}} \tag{3.31}$$

The generalized Westergaard's approach [73] allows a much larger class of finite boundary fracture problems to be addressed. The modified version of mode I stress function for orthotropic materials proposed by Irwin (Eq. 3.27) in line with the generalized Westergaard approach [73] was proposed by Shukla et al. [69] and is given by

$$F_I = \frac{1}{2}\left[\mathrm{Re}\,\overline{\overline{Z}}_I(z_1)+\mathrm{Re}\,\overline{\overline{Z}}_I(z_2)\right]-\frac{\beta}{2\alpha}\left[\mathrm{Re}\,\overline{\overline{Z}}_I(z_1)-\mathrm{Re}\,\overline{\overline{Z}}_I(z_2)\right]$$
$$-\frac{\beta}{2\alpha}\left[\mathrm{Re}\,\overline{\overline{Y}}_I(z_1)-\mathrm{Re}\,\overline{\overline{Y}}_I(z_2)\right] \tag{3.32}$$

where $\overline{Y}_I(z_i)$ and $\overline{\overline{Y}}_I(z_i)$ are the first and second integrals with respect to $z_i\,(i=1,2)$ of the complex analytical function, $Y_I(z_i)$ for opening mode analogous to that for isotropic

materials (Eq. (3.4)). The complex analytical functions $Y_I\left(z_{1,2}\right)$ for orthotropic materials may be written as

$$Y_I(z_i)_{i=1,2}=\sum_{m=0}^{\infty}B_m\left(z_i^{\,m}\right)_{i=1,2} \tag{3.33}$$

In absence of body forces, the stress field equations for mode I loading of an orthotropic laminate can be obtained from the modified stress function, F_I using the Cauchy-Riemann equations (Eq. (3.6)) as

$$\begin{aligned}
\sigma_x &= \partial^2 F_I / \partial y^2 \\
&= \frac{\left(\beta^2-\alpha^2\right)}{2\alpha}\left\{(\alpha+\beta)\,\mathrm{Re}\,Z_I\left(z_1\right)+(\alpha-\beta)\,\mathrm{Re}\,Z_I\left(z_2\right)\right\} \\
&\qquad +\frac{\beta}{2\alpha}\left\{(\alpha+\beta)^2\,\mathrm{Re}\,Y_I\left(z_1\right)-(\beta-\alpha)^2\,\mathrm{Re}\,Y_I\left(z_2\right)\right\} \\
\sigma_y &= \partial^2 F_I / \partial x^2 \\
&= \frac{(\alpha-\beta)}{2\alpha}\mathrm{Re}\,Z_I\left(z_1\right)+\frac{(\alpha+\beta)}{2\alpha}\mathrm{Re}\,Z_I\left(z_2\right)-\frac{\beta}{2\alpha}\mathrm{Re}\,Y_I\left(z_1\right)+\frac{\beta}{2\alpha}\mathrm{Re}\,Y_I\left(z_2\right) \\
\tau_{xy} &= -\partial^2 F_I / \partial x\partial y \\
&= \frac{\left(\alpha^2-\beta^2\right)}{2\alpha}\left\{\mathrm{Im}\,Z_I\left(z_1\right)-\mathrm{Im}\,Z_I\left(z_2\right)\right\} \\
&\qquad -\frac{\beta}{2\alpha}\left\{(\beta+\alpha)\,\mathrm{Im}\,Y_I\left(z_1\right)-(\beta-\alpha)\,\mathrm{Im}\,Y_I\left(z_2\right)\right\}
\end{aligned} \tag{3.34}$$

The strain field equations corresponding to mode I conditions obtained by assuming plane stress conditions by substituting Eq. (3.34) into Eq. (3.23) is given as

$$\varepsilon_x = a_{11}\sigma_x + a_{12}\sigma_y$$
$$= \frac{(\alpha-\beta)}{2\alpha}\left\{a_{12} - a_{11}(\alpha+\beta)^2\right\}\mathrm{Re}\,Z_I(z_1) + \frac{(\alpha+\beta)}{2\alpha}\left\{a_{12} - a_{11}(\beta-\alpha)^2\right\}\mathrm{Re}\,Z_I(z_2)$$
$$+ \frac{\beta}{2\alpha}\left\{a_{11}(\alpha+\beta)^2 - a_{12}\right\}\mathrm{Re}\,Y_I(z_1) + \frac{\beta}{2\alpha}\left\{a_{12} - a_{11}(\beta-\alpha)^2\right\}\mathrm{Re}\,Y_I(z_2)$$

$$\varepsilon_y = a_{12}\sigma_x + a_{22}\sigma_y \tag{3.35}$$
$$= \frac{(\alpha-\beta)}{2\alpha}\left\{a_{22} - a_{12}(\alpha+\beta)^2\right\}\mathrm{Re}\,Z_I(z_1) + \frac{(\alpha+\beta)}{2\alpha}\left\{a_{22} - a_{11}(\beta-\alpha)^2\right\}\mathrm{Re}\,Z_I(z_2)$$
$$+ \frac{\beta}{2\alpha}\left\{a_{12}(\alpha+\beta)^2 - a_{22}\right\}\mathrm{Re}\,Y_I(z_1) + \frac{\beta}{2\alpha}\left\{a_{22} - a_{12}(\beta-\alpha)^2\right\}\mathrm{Re}\,Y_I(z_2)$$

$$\gamma_{xy} = a_{66}\tau_{xy}$$
$$= \frac{a_{66}}{2\alpha}\left(\alpha^2-\beta^2\right)\left\{\mathrm{Im}\,Z_I(z_1) - \mathrm{Im}\,Z_I(z_2)\right\} - \frac{a_{66}\beta}{2\alpha}\left\{(\beta+\alpha)\,\mathrm{Im}\,Y_I(z_1) - (\beta-\alpha)\,\mathrm{Im}\,Y_I(z_2)\right\}$$

For mode II class of problems for orthotropic materials, the modified version of stress function as per generalized Westergaard approach [73] can be proposed as

$$F_{II} = \frac{1}{2}\left[\mathrm{Re}\,\overline{\overline{Y_{II}}}(z_1) - \mathrm{Re}\,\overline{\overline{Y_{II}}}(z_2)\right] - \frac{1}{2\alpha}\left[\mathrm{Im}\,\overline{\overline{Z_{II}}}(z_1) - \mathrm{Im}\,\overline{\overline{Z_{II}}}(z_2)\right]$$
$$- \frac{1}{2\alpha}\left[\mathrm{Re}\,\overline{\overline{Y_{II}}}(z_1) - \mathrm{Re}\,\overline{\overline{Y_{II}}}(z_2)\right] \tag{3.36}$$

where $\overline{Y_{II}}(z_i)$ and $\overline{\overline{Y_{II}}}(z_i)$ are the first and second integrals with respect to $z_i\,(i=1,2)$. In order to ensure that the deformation conforms to the in-plane shear mode of deformation, the analytical functions $Z_{II}(z_i)$ and $Y_{II}(z_i)$ are selected such as to satisfy the stress boundary conditions, $\tau_{xy}=0$ on the crack faces and $\sigma_y=0$ on $y=0$ for all x (Fig. 3.5). The complex analytical function $Z_{II}(z_i)$ is same as in Eq. (3.28) and the function $Y_{II}(z_i)$ for shearing mode type loading of orthotropic materials is selected analogous to that for isotropic materials (Eq. (3.5)) and are given by

$$Y_{II}(z_i)_{i=1,2} = \sum_{m=0}^{\infty} D_m\left(z_i^{\,m}\right)_{i=1,2} \tag{3.37}$$

which satisfy all the aforementioned boundary conditions. Akin to mode I case, the stress components for mode II loading can be obtained using Cauchy-Riemann equations (Eq. (3.6)) as

$$\sigma_x = \partial^2 F_{II} / \partial y^2$$
$$= \frac{(1-\alpha)}{2\alpha}\left\{(\beta+\alpha)^2 \operatorname{Re} Y_{II}(z_1) - (\beta-\alpha)^2 \operatorname{Re} Y_{II}(z_2)\right\}$$
$$+ \frac{1}{2\alpha}\left\{(\beta+\alpha)^2 \operatorname{Im} Z_{II}(z_1) - (\beta-\alpha)^2 \operatorname{Im} Z_{II}(z_2)\right\}$$
$$\sigma_y = \partial^2 F_{II} / \partial x^2$$
$$= \frac{(1-\alpha)}{2\alpha}\left\{\operatorname{Re} Y_{II}(z_2) - \operatorname{Re} Y_{II}(z_1)\right\}$$
$$- \frac{1}{2\alpha}\left\{\operatorname{Im} Z_{II}(z_1) - \operatorname{Im} Z_{II}(z_2)\right\} \qquad (3.38)$$
$$\tau_{xy} = -\partial^2 F_{II} / \partial x \partial y$$
$$= \frac{(1-\alpha)}{2\alpha}\left\{(\beta-\alpha) \operatorname{Im} Y_{II}(z_2) - (\beta+\alpha) \operatorname{Im} Y_{II}(z_1)\right\}$$
$$+ \frac{1}{2\alpha}\left\{(\beta+\alpha) \operatorname{Re} Z_{II}(z_1) - (\beta-\alpha) \operatorname{Re} Z_{II}(z_2)\right\}$$

Similarly, the strain components for mode II obtained by substituting Eq. (3.38) into Eq. (3.23) are given by

$$\varepsilon_x = a_{11}\sigma_x + a_{12}\sigma_y$$
$$= \frac{(1-\alpha)}{2\alpha}\left\{a_{11}(\alpha+\beta)^2 - a_{12}\right\} \operatorname{Re} Y_{II}(z_1) - \frac{(1-\alpha)}{2\alpha}\left\{a_{11}(\beta-\alpha)^2 - a_{12}\right\} \operatorname{Re} Y_{II}(z_2)$$
$$+ \frac{1}{2\alpha}\left\{a_{11}(\alpha+\beta)^2 - a_{12}\right\} \operatorname{Im} Z_{II}(z_1) - \frac{1}{2\alpha}\left\{a_{11}(\beta-\alpha)^2 - a_{12}\right\} \operatorname{Im} Z_{II}(z_2)$$

$$\varepsilon_y = a_{12}\sigma_x + a_{22}\sigma_y$$
$$= \frac{(1-\alpha)}{2\alpha}\left\{a_{12}(\alpha+\beta)^2 - a_{22}\right\} \operatorname{Re} Y_{II}(z_1) - \frac{(1-\alpha)}{2\alpha}\left\{a_{12}(\beta-\alpha)^2 - a_{22}\right\} \operatorname{Re} Y_{II}(z_2) \qquad (3.39)$$
$$+ \frac{1}{2\alpha}\left\{a_{12}(\alpha+\beta)^2 - a_{22}\right\} \operatorname{Im} Z_{II}(z_1) - \frac{1}{2\alpha}\left\{a_{12}(\beta-\alpha)^2 - a_{22}\right\} \operatorname{Im} Z_{II}(z_2)$$

$$\gamma_{xy} = a_{66}\tau_{xy}$$
$$= \frac{(1-\alpha)}{2\alpha} a_{66}\left\{(\beta-\alpha) \operatorname{Im} Y_{II}(z_2) - (\beta+\alpha) \operatorname{Im} Y_{II}(z_1)\right\}$$
$$+ \frac{a_{66}}{2\alpha}\left\{(\beta+\alpha) \operatorname{Re} Z_{II}(z_1) - (\beta-\alpha) \operatorname{Re} Z_{II}(z_2)\right\}.$$

The displacement components for mode I can be obtained by integrating the strain components in Eq. (3.35) as

$$
\begin{aligned}
u_I &= \int (\varepsilon_x)_I \, dx \\
&= \frac{(\alpha-\beta)}{2\alpha}\left\{a_{12} - a_{11}(\alpha+\beta)^2\right\} \mathrm{Re}\,\overline{Z_I}(z_1) + \frac{(\alpha+\beta)}{2\alpha}\left\{a_{12} - a_{11}(\beta-\alpha)^2\right\} \mathrm{Re}\,\overline{Z_I}(z_2) + \\
&\quad \frac{\beta}{2\alpha}\left\{a_{11}(\alpha+\beta)^2 - a_{12}\right\} \mathrm{Re}\,\overline{Y_I}(z_1) + \frac{\beta}{2\alpha}\left\{a_{12} - a_{11}(\beta-\alpha)^2\right\} \mathrm{Re}\,\overline{Y_I}(z_2)
\end{aligned} \tag{3.40}
$$

$$
\begin{aligned}
v_I &= \int (\varepsilon_y)_I \, dx \\
&= \frac{(\alpha-\beta)}{2\alpha}\left\{a_{22} - a_{12}(\alpha+\beta)^2\right\} \frac{\mathrm{Im}\,\overline{Z_I}(z_1)}{(\beta+\alpha)} + \frac{(\alpha+\beta)}{2\alpha}\left\{a_{22} - a_{11}(\beta-\alpha)^2\right\} \frac{\mathrm{Im}\,\overline{Z_I}(z_2)}{(\beta-\alpha)} + \\
&\quad \frac{\beta}{2\alpha}\left\{a_{12}(\alpha+\beta)^2 - a_{22}\right\} \frac{\mathrm{Im}\,\overline{Y_I}(z_1)}{(\beta+\alpha)} + \frac{\beta}{2\alpha}\left\{a_{22} - a_{12}(\beta-\alpha)^2\right\} \frac{\mathrm{Im}\,\overline{Y_I}(z_2)}{(\beta-\alpha)}
\end{aligned}
$$

Similarly, integrating Eq. (3.39) , the displacement components for mode II are obtained as

$$
\begin{aligned}
u_{II} &= \int (\varepsilon_x)_{II} \, dx \\
&= \frac{1}{2\alpha}\left\{a_{11}(\alpha+\beta)^2 - a_{12}\right\} \mathrm{Im}\,\overline{Z_{II}}(z_1) - \frac{1}{2\alpha}\left\{a_{11}(\beta-\alpha)^2 - a_{12}\right\} \mathrm{Im}\,\overline{Z_{II}}(z_2) \\
&\quad + \frac{1-\alpha}{2\alpha}\left\{a_{11}(\alpha+\beta)^2 - a_{12}\right\} \mathrm{Re}\,\overline{Y_{II}}(z_1) - \frac{1-\alpha}{2\alpha}\left\{a_{11}(\beta-\alpha)^2 - a_{12}\right\} \mathrm{Re}\,\overline{Y_{II}}(z_2)
\end{aligned} \tag{3.41}
$$

$$
\begin{aligned}
v_{II} &= \int (\varepsilon_y)_{II} \, dx \\
&= -\frac{1}{2\alpha}\left\{a_{12}(\alpha+\beta)^2 - a_{22}\right\} \frac{\mathrm{Re}\,\overline{Z_{II}}(z_1)}{(\beta+\alpha)} + \frac{1}{2\alpha}\left\{a_{12}(\beta-\alpha)^2 - a_{22}\right\} \frac{\mathrm{Re}\,\overline{Z_{II}}(z_2)}{(\beta-\alpha)} \\
&\quad - \frac{1-\alpha}{2\alpha}\left\{a_{12}(\alpha+\beta)^2 - a_{22}\right\} \frac{\mathrm{Re}\,\overline{Y_{II}}(z_1)}{(\beta+\alpha)} + \frac{1-\alpha}{2\alpha}\left\{a_{12}(\beta-\alpha)^2 - a_{22}\right\} \frac{\mathrm{Re}\,\overline{Y_{II}}(z_2)}{(\beta-\alpha)}
\end{aligned}
$$

In Eqs. (3.40) and (3.41) the rigid body motions are neglected and therefore the constants of integration may be set to zero without losing any generality. Eqs. (3.34) – (3.35) and Eqs. (3.38) – (3.41) can accurately represent the stress, strain and displacement fields respectively in a cracked orthotropic laminate for mode I or mode II loading conditions with infinite number of unknown coefficients A_n, B_m, C_n and D_m after substitution of series form of complex functions $Z_{I,II}(z_{1,2})$ and $Y_{I,II}(z_{1,2})$. The first term in these series which aids in SIF determination as per Eq. (3.13) can be obtained by substituting $m=0, n=0$ and $r_1 = \cos\theta_1 + i\sin\theta_1, r_2 = \cos\theta_2 + i\sin\theta_2$ in Eqs. (3.34) – (3.35) and Eqs. (3.38) – (3.41).

3.3.1 Leading terms for mode I loading

The expressions for leading term for stress and strain components corresponding to mode I loading for an orthotropic material from Eqs. (3.34) and (3.35) are given by

$$\begin{aligned}
\sigma_x &= \frac{\left(\beta^2-\alpha^2\right)}{2\alpha}A_0\left\{(\alpha+\beta)r_1^{-1/2}\cos\frac{\theta_1}{2}+(\alpha-\beta)r_2^{-1/2}\cos\frac{\theta_2}{2}\right\}\\
\sigma_y &= \frac{A_0}{2\alpha}\left\{(\alpha-\beta)r_1^{-1/2}\cos\frac{\theta_1}{2}+(\alpha+\beta)r_2^{-1/2}\cos\frac{\theta_2}{2}\right\}\\
\tau_{xy} &= \frac{\left(\beta^2-\alpha^2\right)}{2\alpha}A_0\left\{r_1^{-1/2}\sin\frac{\theta_1}{2}-r_2^{-1/2}\sin\frac{\theta_2}{2}\right\}
\end{aligned} \tag{3.42}$$

and

$$\begin{aligned}
\varepsilon_x &= A_0\left\{\frac{(\alpha-\beta)}{2\alpha}r_1^{-1/2}\cos\frac{\theta_1}{2}\left[a_{12}-a_{11}(\alpha+\beta)^2\right]+\frac{(\alpha+\beta)}{2\alpha}r_2^{-1/2}\cos\frac{\theta_2}{2}\left[a_{12}-a_{11}(\beta-\alpha)^2\right]\right\}\\
\varepsilon_y &= A_0\left\{\frac{(\alpha-\beta)}{2\alpha}r_1^{-1/2}\cos\frac{\theta_1}{2}\left[a_{22}-a_{12}(\alpha+\beta)^2\right]+\frac{(\alpha+\beta)}{2\alpha}r_2^{-1/2}\cos\frac{\theta_2}{2}\left[a_{22}-a_{12}(\beta-\alpha)^2\right]\right\}\\
\gamma_{xy} &= A_0\frac{a_{66}}{2\alpha}\left(\beta^2-\alpha^2\right)\left\{r_1^{-1/2}\sin\frac{\theta_1}{2}-r_2^{-1/2}\cos\frac{\theta_2}{2}\right\}
\end{aligned} \tag{3.43}$$

The displacement field near the crack tip under plane stress conditions can be obtained from Eq. (3.40) as

$$\begin{aligned}
u_I &= A_0\left\{\frac{(\alpha-\beta)}{\alpha}\left[a_{12}-a_{11}(\alpha+\beta)^2\right]r_1^{1/2}\cos\frac{\theta_1}{2}+\frac{(\alpha+\beta)}{\alpha}\left[a_{12}-a_{11}(\beta-\alpha)^2\right]r_2^{1/2}\cos\frac{\theta_2}{2}\right\}\\
v_I &= A_0\left\{\frac{(\alpha-\beta)}{\alpha(\beta+\alpha)}\left[a_{22}-a_{12}(\alpha+\beta)^2\right]r_1^{1/2}\sin\frac{\theta_1}{2}+\frac{(\alpha+\beta)}{\alpha(\beta-\alpha)}\left[a_{22}-a_{12}(\beta-\alpha)^2\right]r_2^{1/2}\sin\frac{\theta_2}{2}\right\}
\end{aligned} \tag{3.44}$$

It is clear from Eqs. (3.42) and (3.43) that each stress and strain component is inversely proportional to the square-root of the radial distance r of a point from the crack tip and they tend to infinity as r approaches zero. Such solutions are also called as *singular solutions*. Unlike the stress and strain components, the displacement equations (Eq. (3.44)) do not contain singularity and are finite near the crack tip. This is a typical characteristic of LEFM.

3.3.2 Leading terms for mode II loading

The expressions for leading term for the stress, strain and displacement components near the crack tip for plane stress conditions corresponding to mode II loading for an orthotropic material using Eqs. (3.38), (3.39) and (3.41) are given by

$$\begin{aligned}
\sigma_x &= -\frac{C_0}{2\alpha}\left\{(\beta+\alpha)^2\, r_1^{-1/2}\,\sin\frac{\theta_1}{2} - (\beta-\alpha)^2\, r_2^{-1/2}\,\sin\frac{\theta_2}{2}\right\} \\
\sigma_y &= \frac{C_0}{2\alpha}\left\{r_1^{-1/2}\,\sin\frac{\theta_1}{2} - r_2^{-1/2}\,\sin\frac{\theta_2}{2}\right\} \\
\tau_{xy} &= \frac{C_0}{2\alpha}\left\{(\beta+\alpha) r_1^{-1/2}\,\cos\frac{\theta_1}{2} - (\beta-\alpha) r_2^{-1/2}\,\cos\frac{\theta_2}{2}\right\}
\end{aligned} \tag{3.45}$$

$$\begin{aligned}
\varepsilon_x &= -\frac{C_0}{2\alpha}\left\{\left[a_{11}(\alpha+\beta)^2 - a_{12}\right] r_1^{-1/2}\sin\frac{\theta_1}{2} - \left[a_{11}(\beta-\alpha)^2 - a_{12}\right] r_2^{-1/2}\sin\frac{\theta_2}{2}\right\} \\
\varepsilon_y &= -\frac{C_0}{2\alpha}\left\{\left[a_{12}(\alpha+\beta)^2 - a_{22}\right] r_1^{-1/2}\sin\frac{\theta_1}{2} - \left[a_{12}(\beta-\alpha)^2 - a_{22}\right] r_2^{-1/2}\sin\frac{\theta_2}{2}\right\} \\
\gamma_{xy} &= \frac{a_{66}}{2\alpha} C_0\left\{(\beta+\alpha) r_1^{-1/2}\sin\frac{\theta_1}{2} - (\beta-\alpha) r_2^{-1/2}\sin\frac{\theta_2}{2}\right\}
\end{aligned} \tag{3.46}$$

and

$$\begin{aligned}
u_{II} &= \frac{C_0}{\alpha}\left\{\left[a_{11}(\alpha+\beta)^2 - a_{12}\right] r_1^{1/2}\sin\frac{\theta_1}{2} + \left[a_{11}(\beta-\alpha)^2 - a_{12}\right] r_2^{1/2}\sin\frac{\theta_2}{2}\right\} \\
v_{II} &= \frac{C_0}{\alpha}\left\{\frac{1}{(\beta+\alpha)}\left[a_{12}(\alpha+\beta)^2 - a_{22}\right] r_1^{1/2}\cos\frac{\theta_1}{2} + \frac{1}{(\beta-\alpha)}\left[a_{11}(\beta-\alpha)^2 - a_{12}\right] r_2^{1/2}\cos\frac{\theta_2}{2}\right\}
\end{aligned} \tag{3.47}$$

Once again the singular behavior in stress and strain components can also be noticed in mode II loading from Eqs. (3.45) and (3.46).

3.4 Proposed single strain gage technique for the determination of mode I SIF (K_I) of orthotropic materials

A single strain gage technique developed for the determination of K_I of orthotropic composites in the lines of the DS technique [50] is presented here. Similar to the DS technique, a three term or a truncated series is considered for strain representation in the intermediate zone (Zone II, Fig. 3.2) for orthotropic laminates. The analytical functions in the strain components in Eq. (3.35) can be written in truncated form using Eqs. (3.28) and (3.33) as

$$\begin{aligned}
&\mathrm{Re}\, Z_I(z_i)_{i=1,2} = \frac{A_0}{\sqrt{r_{i=1,2}}}\cos\frac{\theta_{i=1,2}}{2} + A_1\sqrt{r_{i=1,2}}\cos\frac{\theta_{i=1,2}}{2} \\
&\mathrm{Im}\, Z_I(z_i)_{i=1,2} = -\frac{A_0}{\sqrt{r_{i=1,2}}}\sin\frac{\theta_{i=1,2}}{2} + A_1\sqrt{r_{i=1,2}}\sin\frac{\theta_{i=1,2}}{2} \\
&\mathrm{Re}\, Y_I(z_i)_{i=1,2} = B_0 \\
&\mathrm{Im}\, Y_I(z_i)_{i=1,2} = 0
\end{aligned} \tag{3.48}$$

The three term representation of strain field for orthotropic laminates under plane stress conditions in Zone II can now be written by substituting Eq. (3.48) into Eq. (3.35) as

$$\begin{aligned}
\varepsilon_x = {} & A_0\left\{\left[r_1^{-1/2}\cos\frac{\theta_1}{2}\times\left(\frac{\alpha-\beta}{2\alpha}\left(a_{12}-a_{11}(\alpha+\beta)^2\right)\right)\right]+\left[r_2^{-1/2}\cos\frac{\theta_2}{2}\times\left(\frac{\alpha+\beta}{2\alpha}\left(a_{12}-a_{11}(\beta-\alpha)^2\right)\right)\right]\right\} \\
& + A_1\left\{\left[r_1^{1/2}\cos\frac{\theta_1}{2}\times\left(\frac{\alpha-\beta}{2\alpha}\left(a_{12}-a_{11}(\alpha+\beta)^2\right)\right)\right]+\left[r_2^{1/2}\cos\frac{\theta_2}{2}\times\left(\frac{\alpha+\beta}{2\alpha}\left(a_{12}-a_{11}(\beta-\alpha)^2\right)\right)\right]\right\} \\
& + B_0\left\{a_{11}\frac{\beta}{2\alpha}\left[(\alpha+\beta)^2-(\beta-\alpha)^2\right]\right\}
\end{aligned} \tag{3.49}$$

$$\begin{aligned}
\varepsilon_y = {} & A_0\left\{\left[r_1^{-1/2}\cos\frac{\theta_1}{2}\times\left(\frac{\alpha-\beta}{2\alpha}\left(a_{22}-a_{12}(\alpha+\beta)^2\right)\right)\right]+\left[r_2^{-1/2}\cos\frac{\theta_2}{2}\times\left(\frac{\alpha+\beta}{2\alpha}\left(a_{22}-a_{12}(\beta-\alpha)^2\right)\right)\right]\right\} \\
& + A_1\left\{\left[r_1^{1/2}\cos\frac{\theta_1}{2}\times\left(\frac{\alpha-\beta}{2\alpha}\left(a_{22}-a_{12}(\alpha+\beta)^2\right)\right)\right]+\left[r_2^{1/2}\cos\frac{\theta_2}{2}\times\left(\frac{\alpha+\beta}{2\alpha}\left(a_{22}-a_{12}(\beta-\alpha)^2\right)\right)\right]\right\} \\
& + B_0\left\{a_{12}\frac{\beta}{2\alpha}\left[(\alpha+\beta)^2-(\beta-\alpha)^2\right]\right\}
\end{aligned} \tag{3.50}$$

and

$$\gamma_{xy} = A_0\left\{\frac{a_{66}}{2\alpha}\left(\alpha^2-\beta^2\right)\left(r_2^{-1/2}\sin\frac{\theta_2}{2}-r_1^{-1/2}\sin\frac{\theta_1}{2}\right)\right\} + A_1\left\{\frac{a_{66}}{2\alpha}\left(\alpha^2-\beta^2\right)\left(r_1^{1/2}\sin\frac{\theta_1}{2}-r_2^{1/2}\sin\frac{\theta_2}{2}\right)\right\} \tag{3.51}$$

The normal strain component ε_{aa} at an angle ϕ with the crack axis (CCW direction with crack axis is positive) for orthotropic materials at a point P located by r and θ (Fig. 3.3) can be obtained using strain transformation laws

$$\varepsilon_{aa} = \varepsilon_x\cos^2\phi+\varepsilon_y\sin^2\phi+\gamma_{xy}\cos\phi\sin\phi \tag{3.52}$$

as

$$\begin{aligned}\varepsilon_{aa} = {} & A_0\left\{\left[\frac{1}{\sqrt{r_1}}\left(\left(\cos\frac{\theta_1}{2}\frac{\alpha-\beta}{2\alpha}\left(\begin{array}{l}\cos^2\phi\left(-a_{11}(\alpha+\beta)^2+a_{12}\right)\\ +\sin^2\phi\left(-a_{12}(\alpha+\beta)^2+a_{22}\right)\end{array}\right)\right)\right.\right.\right.\\ & \left.\left.\left.-\left(\sin\frac{\theta_1}{2}a_{66}\sin\phi\cos\phi\left(\alpha^2-\beta^2/2\alpha\right)\right)\right)\right]\\ & +\left[\frac{1}{\sqrt{r_2}}\left(\left(\cos\frac{\theta_2}{2}\frac{\alpha+\beta}{2\alpha}\left(\begin{array}{l}\cos^2\phi\left(-a_{11}(\alpha-\beta)^2+a_{12}\right)\\ +\sin^2\phi\left(-a_{12}(\alpha-\beta)^2+a_{22}\right)\end{array}\right)\right)\right.\right.\\ & \left.\left.+\left(\sin\frac{\theta_2}{2}a_{66}\sin\phi\cos\phi\left(\alpha^2-\beta^2/2\alpha\right)\right)\right)\right]\Bigg\}\\ & +A_1\left\{\left[\sqrt{r_1}\left(\left(\cos\frac{\theta_1}{2}(\alpha-\beta/2\alpha)\left(\begin{array}{l}\cos^2\phi\left(-a_{11}(\alpha+\beta)^2+a_{12}\right)\\ +\sin^2\phi\left(-a_{12}(\alpha+\beta)^2+a_{22}\right)\end{array}\right)\right)\right.\right.\right.\\ & \left.\left.\left.+\left(\sin\frac{\theta_1}{2}a_{66}\sin\phi\cos\phi\left(\alpha^2-\beta^2/2\alpha\right)\right)\right)\right]\\ & +\left[\sqrt{r_2}\left(\left(\cos\frac{\theta_2}{2}(\alpha+\beta/2\alpha)\left(\begin{array}{l}\cos^2\phi\left(-a_{11}(\alpha-\beta)^2+a_{12}\right)\\ +\sin^2\phi\left(-a_{12}(\alpha-\beta)^2+a_{22}\right)\end{array}\right)\right)\right.\right.\\ & \left.\left.-\left(\sin\frac{\theta_2}{2}a_{66}\sin\phi\cos\phi\left(\alpha^2-\beta^2/2\alpha\right)\right)\right)\right]\Bigg\}\\ & +B_0\left\{\frac{\beta}{2\alpha}\left[(\alpha+\beta)^2-(\beta-\alpha)^2\right]\left(a_{11}\cos^2\phi+a_{12}\sin^2\phi\right)\right\}\end{aligned} \tag{3.53}$$

Inspection of Eq. (3.53) suggests that the contribution of B_0 term can be made zero by setting the coefficient of B_0 term equal to zero which leads to selecting angle ϕ such that

$$\frac{\beta}{2\alpha}\left[(\alpha+\beta)^2-(\beta-\alpha)^2\right]\left(a_{11}\cos^2\phi+a_{12}\sin^2\phi\right)=0 \tag{3.54}$$

which leads to

$$\tan^2\phi=-a_{11}/a_{12}=1/\nu_{LT} \tag{3.55}$$

Similarly, the contribution of A_1 term in Eq. (3.53) can also be made zero if coefficient of A_1 term is set to zero such that

$$\begin{aligned}&\sqrt{r_1}\left\{\left(\cos\frac{\theta_1}{2}\frac{\alpha-\beta}{2\alpha}\begin{pmatrix}\cos^2\phi\left(-a_{11}(\alpha+\beta)^2+a_{12}\right)\\+\sin^2\phi\left(-a_{12}(\alpha+\beta)^2+a_{22}\right)\end{pmatrix}\right)+\left(\sin\frac{\theta_1}{2}a_{66}\sin\phi\cos\phi\left(\frac{\alpha^2-\beta^2}{2\alpha}\right)\right)\right\}\\&+\sqrt{r_2}\left\{\left(\cos\frac{\theta_2}{2}\frac{\alpha+\beta}{2\alpha}\begin{pmatrix}\cos^2\phi\left(-a_{11}(\alpha-\beta)^2+a_{12}\right)\\+\sin^2\phi\left(-a_{12}(\alpha-\beta)^2+a_{22}\right)\end{pmatrix}\right)-\left(\sin\frac{\theta_2}{2}a_{66}\sin\phi\cos\phi\left(\frac{\alpha^2-\beta^2}{2\alpha}\right)\right)\right\}=0\end{aligned} \tag{3.56}$$

Substituting r_1, r_2, θ_1 and θ_2 in terms of r and θ from Eq. (3.30) and ϕ from Eq. (3.55) in Eq. (3.56) gives

$$\begin{aligned}&\sqrt[4]{\left(\cos^2\theta+(\beta+\alpha)^2\sin^2\theta\right)}\left\{\begin{bmatrix}\frac{1}{E_T}\left(\frac{1-\nu_{LT}\nu_{TL}}{1+\nu_{LT}}\right)\frac{\alpha-\beta}{2\alpha}\cos\left(\frac{1}{2}\left(\tan^{-1}\left((\beta+\alpha)\tan\theta\right)\right)\right)\end{bmatrix}\right.\\&\left.\begin{bmatrix}-\left[\frac{1}{G_{LT}}\left(\frac{\nu_{LT}}{(1+\nu_{LT})\sqrt{\nu_{TL}}}\right)\frac{1}{2\alpha}\sin\left(\frac{1}{2}\left(\tan^{-1}\left((\beta+\alpha)\tan\theta\right)\right)\right)\right]\end{bmatrix}\right\}+\\&\sqrt[4]{\left(\cos^2\theta+(\beta-\alpha)^2\sin^2\theta\right)}\left\{\begin{bmatrix}\left[\frac{1}{E_T}\left(\frac{1-\nu_{LT}\nu_{TL}}{1+\nu_{LT}}\right)\frac{\alpha+\beta}{2\alpha}\cos\left(\frac{1}{2}\left(\tan^{-1}\left((\beta-\alpha)\tan\theta\right)\right)\right)\right]\end{bmatrix}\right.\\&\left.\begin{bmatrix}+\left[\frac{1}{G_{LT}}\left(\frac{\nu_{LT}}{(1+\nu_{LT})\sqrt{\nu_{TL}}}\right)\frac{1}{2\alpha}\sin\left(\frac{1}{2}\left(\tan^{-1}\left((\beta-\alpha)\tan\theta\right)\right)\right)\right]\end{bmatrix}\right\}=0\end{aligned} \tag{3.57}$$

Eq. (3.57) gives the value of θ at which the contribution of the A_1 term becomes zero in Eq. (3.53). Eq. (3.57) can be solved graphically to obtain the value of θ for which the A_1 term becomes zero. Thus, with the θ and ϕ as given by Eq. (3.57) and Eq. (3.55) respectively, the strain ε_{aa} in Eq. (3.53) can be written in terms of r, θ and unknown coefficient A_0 as

$$\varepsilon_{aa}=\frac{1}{\sqrt{r}}\times A_0\left\{\begin{array}{l}\dfrac{1}{E_T}\left(\dfrac{1-\nu_{LT}\nu_{TL}}{1+\nu_{LT}}\right)\dfrac{1}{2\alpha}\left[\begin{array}{l}\dfrac{\cos\left(\frac{1}{2}\tan^{-1}\left((\beta+\alpha)\tan\theta\right)\right)}{\sqrt[4]{\left(\cos^2\theta+(\beta+\alpha)^2\sin^2\theta\right)}}(\alpha-\beta)\\ \qquad+\dfrac{\cos\left(\frac{1}{2}\tan^{-1}\left((\beta-\alpha)\tan\theta\right)\right)}{\sqrt[4]{\left(\cos^2\theta+(\beta-\alpha)^2\sin^2\theta\right)}}(\alpha+\beta)\end{array}\right]\\ +\dfrac{1}{G_{LT}}\left(\dfrac{\nu_{LT}}{(1+\nu_{LT})\sqrt{\nu_{TL}}}\right)\dfrac{1}{2\alpha}\left[\begin{array}{l}\dfrac{\sin\left(\frac{1}{2}\tan^{-1}\left((\beta+\alpha)\tan\theta\right)\right)}{\sqrt[4]{\left(\cos^2\theta+(\beta+\alpha)^2\sin^2\theta\right)}}\\ \qquad-\dfrac{\sin\left(\frac{1}{2}\tan^{-1}\left((\beta-\alpha)\tan\theta\right)\right)}{\sqrt[4]{\left(\cos^2\theta+(\beta-\alpha)^2\sin^2\theta\right)}}\end{array}\right]\end{array}\right\} \tag{3.58}$$

Thus, by placing a single strain gage as shown in Fig. 3.6 at a radial distance, r from the crack tip along the line at angle of θ (Eq. (3.57)) and oriented at an angle of ϕ (Eq. (3.55)), the measured strain ε_{aa} can be equated to Eq. (3.58) to obtain the value of unknown coefficient A_0. The mode I SIF can then be determined using Eq. (3.13). The proposed approach remains valid also for negative values of angle θ and ϕ as in the DS technique for isotropic materials (section 3.2). The gage line starts at the crack tip and terminates at the outer boundaries of the cracked plate. However, while equating the reading from strain gage to the strain expression given by Eq. (3.58), it is important to ensure that the strain gage is placed at such a radial distance where the expression given by Eq. (3.58) obtained using the three parameter strain series is valid. The coefficient, A_0 and hence K_I can be determined accurately subjected to this condition only. Therefore, it is important to know the upper limit on the radial location up to which the three parameter strain series could be correctly represented by the strain gage readings. The following section describes the method for deciding upon the radial location, r for the strain gage, which is also an important parameter for successful experimentation.

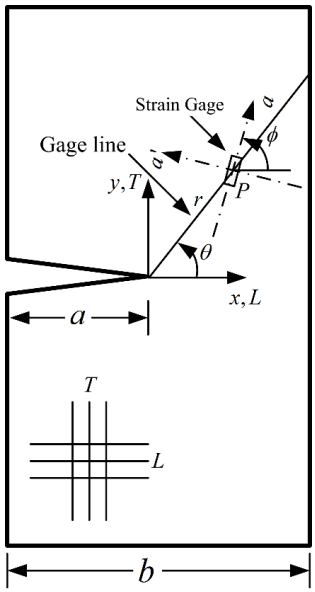

Figure 3.6 Strain gage location for a plane orthotropic mode I specimen

3.5 Proposed approach for the determination of optimal radial locations of the strain gage for measurement of K_I of orthotropic materials

As discussed in Chapter 1 and 2, it is evident that the radial distance, r of a strain gage is an important parameter for determination of accurate values of K_I. Therefore, if the gages are located very close to the crack tip, then the strain measurements may be affected by strain gradients and 3D effects. On the other hand if the gages are located significantly far away from the crack tip then the Eq. (3.58) may not be applicable for strain measurements although the aforesaid effects can be avoided at such locations. This is because the measured strain at such a large distance may also have contribution due to the coefficients other than A_0, A_1 and B_0. Therefore prior knowledge of valid radial location or distance for strain gage is essential for the accurate determination of K_I of orthotropic laminates.

It was observed that 3D effects and other factors which rendered the plane stress solutions invalid prevailed up to a radial distance equal to the thickness of the plate from the crack tip for orthotropic composites [69]. Therefore, the minimum radial distance $r_{\min}$ for strain measurements on the free surface (which are under plane stress conditions) should be greater than the thickness of the plate [69]. As a consequence, the optimal or valid radial location r for strain gage can now be given as

$$r_{\min}\left(=thickness\,of\ \ plate\right) \le r \le r_{\max} \tag{3.59}$$

where $r_{\max}$ is defined as the maximum radial distance from the crack tip or the upper bound for the valid radial location for the strain gage. As described above, Eq. (3.58) is valid only up to a certain radial distance from the crack tip and beyond that radial distance more number of coefficients or parameters other than A_0, A_1 and B_0 would be needed to represent the strain field. The $r_{\max}$ may be defined as the extent of validity of Eq. (3.58) or the extent of three parameter representations along the radial line defined by θ (Eq. 3.57). Further, $r_{\max}$ may also be interpreted as the extent of zone II. Thus it is evident that in order to assess the optimal gage locations it is necessary to know the value of $r_{\max}$ of a given cracked configuration. Sarangi et al. [60-62] were the first to propose optimal gage locations to be used in

collaboration with the DS technique. The theoretical foundation for determination of $r_{\max}$ of any single ended cracked configuration for orthotropic materials is presented in the following paragraphs. For a given cracked configuration, applied load and material properties, the terms within bracket {} become constant along with A_0 and therefore Eq. (3.58) can be written as

$$\varepsilon_{aa} = \frac{C}{\sqrt{r}} \tag{3.60}$$

where *C* is a constant. Taking logarithm on both sides of Eq. (3.60) results as

$$\ln(\varepsilon_{aa}) = -\frac{1}{2}\ln(r) + \ln(C) \tag{3.61}$$

Eq. (3.61) is valid along the line given by Eq. (3.57) for $r \le r_{\max}$. Thus a plot of Eq. (3.61) on log-log axes depicts a straight line of slope equal to – 0.5, with an intercept of $\ln(C)$ (Fig. 3.7). Theoretically, the straight line property will break beyond $r > r_{\max}$ as more than three parameters are required in Eq. (3.58) to estimate ε_{aa}. Further, the plot of Eq. (3.61) for $r > r_{\max}$ will no longer be a straight line but a nonlinear one (in logarithmic scale) due to the domination of more parameters other than A_0, A_1 and B_0.

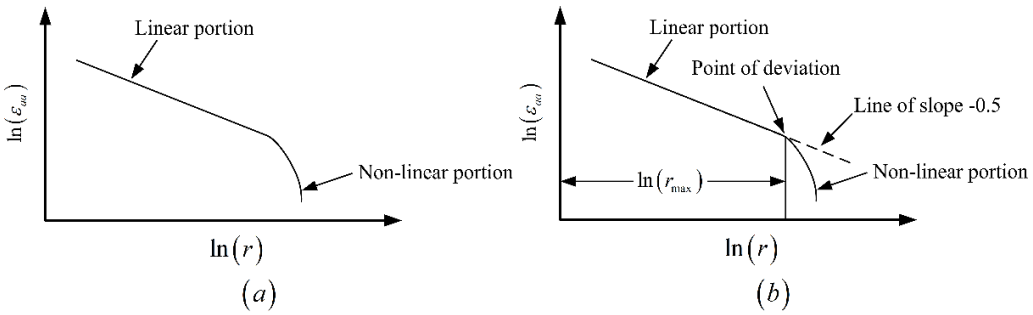

Figure 3.7 (a) Plot of $\ln(\varepsilon_{aa})$ versus $\ln(r)$ (b) linear and non-linear variation of $\ln(\varepsilon_{aa})$ and $\ln(r)$ along the gage line

Using the straight line property exhibited by Eq. (3.61), the value of $r_{\max}$ can be accurately estimated from the log-log plots of ε_{aa} and r. It is evident that the extent of the three parameter zone or the maximum permissible radial distance of strain gage, $r_{\max}$ is the terminal point of the straight line portion or the beginning point of the nonlinear portion of the above plot. The extent of the straight line portion is clearly a function of A_0, A_1 and B_0. Therefore, the $r_{\max}$ is in turn a function of geometry of the given cracked body and boundary conditions.

Once the r_{max} value of a cracked configuration is determined, then the valid or optimal strain gage location that will ensure correct measurement of strains according to Eq. (3.58) can be easily obtained using Eq. (3.59).

A reliable procedure is needed for accurate identification of r_{max} or the end point of the straight line in Eq. (3.61) which gives maximum permissible radial location of a strain gage for K_I determination of orthotropic laminates. A method for determination of r_{max} using finite element analysis is presented in the present investigation. In this approach, the strain ε_{aa} at a large number of points either along the gage line (Fig. 3.6) is computed using appropriate numerical analysis (finite element analysis (FEA)) of the cracked domain. If the proposed theoretical basis presented in this section are correct then a graph similar to that shown in Fig. 3.7(a) can be obtained on the log-log scale with a distinct linear and non-linear portions. Because of logarithmic plot a reliable procedure is needed for accurate identification of end point of the straight line portion. For this purpose the following procedure is devised in the present investigation.

(a) First a line of slope – 0.5 is superposed on to the plots of $\ln(\varepsilon_{aa})$ versus $\ln(r)$ as shown in Fig. 3.7(b).

(b) Considering this line as the exact solution, absolute percent relative error in computed values of $\ln(\varepsilon_{aa})$ is then determined at all values of radius in the plot.

(c) Finally, the r_{max} or the point of deviation on the log-log plot from the superposed line is evaluated as the value of the radius at which the error reaches a value $\leq$ 1% (as one observes from right to left in Fig. 3.7 (b)).

Thus if r_{max} is estimated for a given specimen prior to experimentation, the correct locations of strain gage can be assessed using Eq. (3.59).

3.6 Proposed strain gage technique for the determination mixed mode SIFs (K_I and K_{II}) of orthotropic materials

Strain gage based determination of mixed mode SIFs of orthotropic composites is not available till date to the best of author's knowledge. Therefore, in this section an attempt has been made to develop a strain gage technique for the determination of K_I and K_{II} of

orthotropic materials. The proposed technique for mixed mode cases is essentially an extension of the proposed mode I technique by incorporating mode II strain components into the formulation in addition to mode I strain components. Since a three parameter strain expression worked well for mode I case both in case of isotropic and orthotropic materials, a three parameter series representation (mode I coefficients A_0, A_1, B_0 and mode II coefficients C_0, C_1, D_0) has been considered to represent the strain field around the crack tip for Zone II (Fig. 3.2) for determination of mixed mode SIFs of orthotropic materials to reduce mathematical complications in the present investigation. The mixed mode strain field in the Zone II (Fig. 3.2) can be obtained by superposing the mode I and mode II strain field equations in Eqs. (3.35) and (3.39) respectively as follows

$$\begin{aligned}
\varepsilon_x &= (\varepsilon_x)_I + (\varepsilon_x)_{II} \\
&= \frac{(\alpha-\beta)}{2\alpha}\left\{a_{12} - a_{11}(\alpha+\beta)^2\right\}\mathrm{Re}\,Z_I(z_1) + \frac{(\alpha+\beta)}{2\alpha}\left\{a_{12} - a_{11}(\beta-\alpha)^2\right\}\mathrm{Re}\,Z_I(z_2) \\
&\quad + \frac{\beta}{2\alpha}\left\{a_{11}(\alpha+\beta)^2 - a_{12}\right\}\mathrm{Re}\,Y_I(z_1) + \frac{\beta}{2\alpha}\left\{a_{12} - a_{11}(\beta-\alpha)^2\right\}\mathrm{Re}\,Y_I(z_2) \\
&\quad + \frac{(1-\alpha)}{2\alpha}\left\{a_{11}(\alpha+\beta)^2 - a_{12}\right\}\mathrm{Re}\,Y_{II}(z_1) - \frac{(1-\alpha)}{2\alpha}\left\{a_{11}(\beta-\alpha)^2 - a_{12}\right\}\mathrm{Re}\,Y_{II}(z_2) \\
&\quad + \frac{1}{2\alpha}\left\{a_{11}(\alpha+\beta)^2 - a_{12}\right\}\mathrm{Im}\,Z_{II}(z_1) - \frac{1}{2\alpha}\left\{a_{11}(\beta-\alpha)^2 - a_{12}\right\}\mathrm{Im}\,Z_{II}(z_2)
\end{aligned} \tag{3.62}$$

$$\begin{aligned}
\varepsilon_y &= (\varepsilon_y)_I + (\varepsilon_y)_{II} \\
&= \frac{(\alpha-\beta)}{2\alpha}\left\{a_{22} - a_{12}(\alpha+\beta)^2\right\}\mathrm{Re}\,Z_I(z_1) + \frac{(\alpha+\beta)}{2\alpha}\left\{a_{22} - a_{11}(\beta-\alpha)^2\right\}\mathrm{Re}\,Z_I(z_2) \\
&\quad + \frac{\beta}{2\alpha}\left\{a_{12}(\alpha+\beta)^2 - a_{22}\right\}\mathrm{Re}\,Y_I(z_1) + \frac{\beta}{2\alpha}\left\{a_{22} - a_{12}(\beta-\alpha)^2\right\}\mathrm{Re}\,Y_I(z_2) \\
&\quad + \frac{(1-\alpha)}{2\alpha}\left\{a_{12}(\alpha+\beta)^2 - a_{22}\right\}\mathrm{Re}\,Y_{II}(z_1) - \frac{(1-\alpha)}{2\alpha}\left\{a_{12}(\beta-\alpha)^2 - a_{22}\right\}\mathrm{Re}\,Y_{II}(z_2) \\
&\quad + \frac{1}{2\alpha}\left\{a_{12}(\alpha+\beta)^2 - a_{22}\right\}\mathrm{Im}\,Z_{II}(z_1) - \frac{1}{2\alpha}\left\{a_{12}(\beta-\alpha)^2 - a_{22}\right\}\mathrm{Im}\,Z_{II}(z_2)
\end{aligned} \tag{3.63}$$

and

$$\begin{aligned}
\gamma_{xy} &= (\gamma_{xy})_I + (\gamma_{xy})_{II} \\
&= \frac{a_{66}}{2\alpha}\left(\alpha^2-\beta^2\right)\left\{\mathrm{Im}\,Z_I(z_1) - \mathrm{Im}\,Z_I(z_2)\right\} - \frac{a_{66}\beta}{2\alpha}\left\{(\beta+\alpha)\,\mathrm{Im}\,Y_I(z_1) - (\beta-\alpha)\,\mathrm{Im}\,Y_I(z_2)\right\} \\
&\quad + \frac{(1-\alpha)}{2\alpha}a_{66}\left\{(\beta-\alpha)\,\mathrm{Im}\,Y_{II}(z_2) - (\beta+\alpha)\,\mathrm{Im}\,Y_{II}(z_1)\right\} \\
&\quad + \frac{a_{66}}{2\alpha}\left\{(\beta+\alpha)\,\mathrm{Re}\,Z_{II}(z_1) - (\beta-\alpha)\,\mathrm{Re}\,Z_{II}(z_2)\right\}
\end{aligned} \tag{3.64}$$

The analytical functions in Eqs. (3.62 – 3.64) corresponding to the mode I components can be written using a three parameter series representation using Eq. (3.48). Using a similar approach, the analytical functions in Eqs. (3.62 – 3.64) corresponding to the mode II components can be written using a three parameter series representation as

$$\begin{aligned}
&\mathrm{Re}\, Z_{II}\left(z_i\right)_{i=1,2} = \frac{C_0}{\sqrt{r_{i=1,2}}}\cos\frac{\theta_{i=1,2}}{2} + C_1\sqrt{r_{i=1,2}}\cos\frac{\theta_{i=1,2}}{2} \\
&\mathrm{Im}\, Z_{II}\left(z_i\right)_{i=1,2} = -\frac{C_0}{\sqrt{r_{i=1,2}}}\sin\frac{\theta_{i=1,2}}{2} + C_1\sqrt{r_{i=1,2}}\sin\frac{\theta_{i=1,2}}{2} \\
&\mathrm{Re}\, Y_{II}\left(z_i\right)_{i=1,2} = D_0 \\
&\mathrm{Im}\, Y_{II}\left(z_i\right)_{i=1,2} = 0
\end{aligned} \tag{3.65}$$

Therefore, the rectangular strain components ε_{xx}, ε_{yy} and γ_{xy} (in terms of both mode I and mode II coefficients) at any point within the zone II for plane stress conditions of orthotropic materials can be obtained by substituting Eqs. (3.48) and (3.65) into Eqs. (3.62 – 3.64) as

$$\begin{aligned}
\varepsilon_x = {} & A_0\left\{\begin{array}{l}\left[r_1^{-1/2}\cos\frac{\theta_1}{2}\times\left(\frac{\alpha-\beta}{2\alpha}\left(a_{12}-a_{11}(\alpha+\beta)^2\right)\right)\right] \\ \quad +\left[r_2^{-1/2}\cos\frac{\theta_2}{2}\times\left(\frac{\alpha+\beta}{2\alpha}\left(a_{12}-a_{11}(\beta-\alpha)^2\right)\right)\right]\end{array}\right\} \\
& + A_1\left\{\begin{array}{l}\left[r_1^{1/2}\cos\frac{\theta_1}{2}\times\left(\frac{\alpha-\beta}{2\alpha}\left(a_{12}-a_{11}(\alpha+\beta)^2\right)\right)\right] \\ \quad +\left[r_2^{1/2}\cos\frac{\theta_2}{2}\times\left(\frac{\alpha+\beta}{2\alpha}\left(a_{12}-a_{11}(\beta-\alpha)^2\right)\right)\right]\end{array}\right\} + B_0\left\{a_{11}\frac{\beta}{2\alpha}\left[(\alpha+\beta)^2-(\beta-\alpha)^2\right]\right\} \\
& - C_0\left\{\begin{array}{l}\left[r_1^{-1/2}\sin\frac{\theta_1}{2}\times\frac{1}{2\alpha}\left(a_{11}(\alpha+\beta)^2-a_{12}\right)\right] \\ \quad -\left[r_2^{-1/2}\sin\frac{\theta_2}{2}\times\frac{1}{2\alpha}\left(a_{11}(\beta-\alpha)^2-a_{12}\right)\right]\end{array}\right\} \\
& + C_1\left\{\begin{array}{l}\left[r_1^{1/2}\sin\frac{\theta_1}{2}\times\frac{1}{2\alpha}\left(a_{11}(\alpha+\beta)^2-a_{12}\right)\right] \\ \quad -\left[r_2^{1/2}\cos\frac{\theta_2}{2}\times\frac{1}{2\alpha}\left(a_{11}(\beta-\alpha)^2-a_{12}\right)\right]\end{array}\right\} + D_0\left\{a_{11}\frac{1-\alpha}{2\alpha}\left[(\alpha+\beta)^2-(\beta-\alpha)^2\right]\right\}
\end{aligned} \tag{3.66}$$

$$\varepsilon_y = A_0\left\{\begin{array}{l}\left[r_1^{-1/2}\cos\frac{\theta_1}{2}\times\left(\frac{\alpha-\beta}{2\alpha}\left(a_{22}-a_{12}(\alpha+\beta)^2\right)\right)\right]\\ \quad+\left[r_2^{-1/2}\cos\frac{\theta_2}{2}\times\left(\frac{\alpha+\beta}{2\alpha}\left(a_{22}-a_{12}(\beta-\alpha)^2\right)\right)\right]\end{array}\right\}$$
$$+A_1\left\{\begin{array}{l}\left[r_1^{1/2}\cos\frac{\theta_1}{2}\times\left(\frac{\alpha-\beta}{2\alpha}\left(a_{22}-a_{12}(\alpha+\beta)^2\right)\right)\right]\\ \quad+\left[r_2^{1/2}\cos\frac{\theta_2}{2}\times\left(\frac{\alpha+\beta}{2\alpha}\left(a_{22}-a_{12}(\beta-\alpha)^2\right)\right)\right]\end{array}\right\}+B_0\left\{a_{12}\frac{\beta}{2\alpha}\left[(\alpha+\beta)^2-(\beta-\alpha)^2\right]\right\} \quad (3.67)$$
$$-C_0\left\{\begin{array}{l}\left[r_1^{-1/2}\sin\frac{\theta_1}{2}\times\frac{1}{2\alpha}\left(a_{12}(\alpha+\beta)^2-a_{22}\right)\right]\\ \quad-\left[r_2^{-1/2}\sin\frac{\theta_2}{2}\times\frac{1}{2\alpha}\left(a_{12}(\beta-\alpha)^2-a_{22}\right)\right]\end{array}\right\}$$
$$+C_1\left\{\begin{array}{l}\left[r_1^{1/2}\sin\frac{\theta_1}{2}\times\frac{1}{2\alpha}\left(a_{12}(\alpha+\beta)^2-a_{22}\right)\right]\\ \quad+\left[r_2^{1/2}\cos\frac{\theta_2}{2}\times\frac{1}{2\alpha}\left(a_{12}(\beta-\alpha)^2-a_{22}\right)\right]\end{array}\right\}+D_0\left\{a_{12}\frac{1-\alpha}{2\alpha}\left[(\alpha+\beta)^2-(\beta-\alpha)^2\right]\right\}$$

and

$$\begin{aligned}\gamma_{xy} &= A_0\left\{\frac{a_{66}}{2\alpha}\left(\alpha^2-\beta^2\right)\left(r_2^{-1/2}\sin\frac{\theta_2}{2}-r_1^{-1/2}\sin\frac{\theta_1}{2}\right)\right\}\\ &+A_1\left\{\frac{a_{66}}{2\alpha}\left(\alpha^2-\beta^2\right)\left(r_1^{1/2}\sin\frac{\theta_1}{2}-r_2^{1/2}\sin\frac{\theta_2}{2}\right)\right\}\\ &+C_0\left\{\frac{a_{66}}{2\alpha}\left((\beta+\alpha)r_1^{-1/2}\cos\frac{\theta_1}{2}-(\beta-\alpha)r_2^{-1/2}\sin\frac{\theta_2}{2}\right)\right\}\\ &+C_1\left\{\frac{a_{66}}{2\alpha}\left((\beta+\alpha)r_1^{1/2}\cos\frac{\theta_1}{2}-(\beta-\alpha)r_2^{1/2}\sin\frac{\theta_2}{2}\right)\right\}\end{aligned} \quad (3.68)$$

Now, referring to Fig. 3.8, the strain at a particular location (r,θ) in the Zone II in the direction $a-a$ defined by an arbitrary angle ϕ with the crack axis may be written as using strain transformation equation as

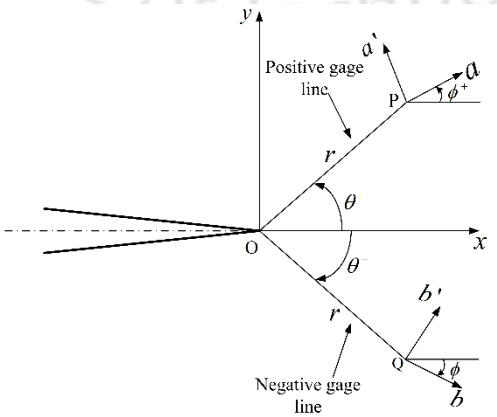

Figure 3.8 Strain gage location and orientation for mixed mode

$$A_0\left\{\left[\frac{1}{\sqrt{r_1}}\left(\begin{array}{l}\left(\cos\frac{\theta_1}{2}\frac{\alpha-\beta}{2\alpha}\left(\begin{array}{l}\left(a_{12}\cos^2\phi+a_{22}\sin^2\phi\right)\\-\left(\beta+\alpha\right)^2\left(a_{11}\cos^2\phi+a_{12}\sin^2\phi\right)\end{array}\right)\right)\\-\left(\sin\frac{\theta_1}{2}a_{66}\sin\phi\cos\phi\left(\frac{\alpha^2-\beta^2}{2\alpha}\right)\right)\end{array}\right)\right]+\left[\frac{1}{\sqrt{r_2}}\left(\begin{array}{l}\left(\cos\frac{\theta_2}{2}\frac{\alpha+\beta}{2\alpha}\left(\begin{array}{l}\left(a_{12}\cos^2\phi+a_{22}\sin^2\phi\right)\\-\left(\beta-\alpha\right)^2\left(a_{11}\cos^2\phi+a_{12}\sin^2\phi\right)\end{array}\right)\right)\\+\left(\sin\frac{\theta_2}{2}a_{66}\sin\phi\cos\phi\left(\frac{\alpha^2-\beta^2}{2\alpha}\right)\right)\end{array}\right)\right]\right\}$$

$$+A_1\left\{\left[\sqrt{r_1}\left(\begin{array}{l}\left(\cos\frac{\theta_1}{2}\frac{\alpha-\beta}{2\alpha}\left(\begin{array}{l}\left(a_{12}\cos^2\phi+a_{22}\sin^2\phi\right)\\-\left(\beta+\alpha\right)^2\left(a_{11}\cos^2\phi+a_{12}\sin^2\phi\right)\end{array}\right)\right)\\+\left(\sin\frac{\theta_1}{2}a_{66}\sin\phi\cos\phi\left(\frac{\alpha^2-\beta^2}{2\alpha}\right)\right)\end{array}\right)\right]+\left[\sqrt{r_2}\left(\begin{array}{l}\left(\cos\frac{\theta_2}{2}\frac{\alpha+\beta}{2\alpha}\left(\begin{array}{l}\left(a_{12}\cos^2\phi+a_{22}\sin^2\phi\right)\\-\left(\beta-\alpha\right)^2\left(a_{11}\cos^2\phi+a_{12}\sin^2\phi\right)\end{array}\right)\right)\\-\left(\sin\frac{\theta_2}{2}a_{66}\sin\phi\cos\phi\left(\frac{\alpha^2-\beta^2}{2\alpha}\right)\right)\end{array}\right)\right]\right\}$$

$$\varepsilon_{aa}=+B_0\left\{\frac{\beta}{2\alpha}\left[\left(\alpha+\beta\right)^2-\left(\beta-\alpha\right)^2\right]\left(a_{11}\cos^2\phi+a_{12}\sin^2\phi\right)\right\} \tag{3.69}$$

$$+C_0\left\{\left[\frac{1}{\sqrt{r_1}}\left(\begin{array}{l}\left(\sin\frac{\theta_1}{2}\frac{1}{2\alpha}\left(\begin{array}{l}\left(\beta+\alpha\right)^2\left(a_{11}\cos^2\phi+a_{12}\sin^2\phi\right)\\-\left(a_{12}\cos^2\phi+a_{22}\sin^2\phi\right)\end{array}\right)\right)\\+\left(\cos\frac{\theta_1}{2}a_{66}\sin\phi\cos\phi\left(\frac{\beta+\alpha}{2\alpha}\right)\right)\end{array}\right)\right]-\left[\frac{1}{\sqrt{r_2}}\left(\begin{array}{l}\left(\sin\frac{\theta_2}{2}\frac{1}{2\alpha}\left(\begin{array}{l}\left(\beta-\alpha\right)^2\left(a_{11}\cos^2\phi+a_{12}\sin^2\phi\right)\\-\left(a_{12}\cos^2\phi+a_{22}\sin^2\phi\right)\end{array}\right)\right)\\-\left(\cos\frac{\theta_2}{2}a_{66}\sin\phi\cos\phi\left(\frac{\beta-\alpha}{2\alpha}\right)\right)\end{array}\right)\right]\right\}$$

$$+C_1\left\{\left[\sqrt{r_1}\left(\begin{array}{l}\left(\sin\frac{\theta_1}{2}\frac{1}{2\alpha}\left(\begin{array}{l}\left(\beta+\alpha\right)^2\left(a_{11}\cos^2\phi+a_{12}\sin^2\phi\right)\\-\left(a_{12}\cos^2\phi+a_{22}\sin^2\phi\right)\end{array}\right)\right)\\+\left(\cos\frac{\theta_1}{2}a_{66}\sin\phi\cos\phi\left(\frac{\beta+\alpha}{2\alpha}\right)\right)\end{array}\right)\right]+\left[\sqrt{r_2}\left(\begin{array}{l}\left(\sin\frac{\theta_2}{2}\frac{1}{2\alpha}\left(\begin{array}{l}\left(\beta-\alpha\right)^2\left(a_{11}\cos^2\phi+a_{12}\sin^2\phi\right)\\-\left(a_{12}\cos^2\phi+a_{22}\sin^2\phi\right)\end{array}\right)\right)\\-\left(\cos\frac{\theta_2}{2}a_{66}\sin\phi\cos\phi\left(\frac{\beta-\alpha}{2\alpha}\right)\right)\end{array}\right)\right]\right\}$$

$$+D_0\left\{\frac{1-\alpha}{2\alpha}\left[\left(\alpha+\beta\right)^2-\left(\beta-\alpha\right)^2\right]\left(a_{11}\cos^2\phi+a_{12}\sin^2\phi\right)\right\}$$

Inspection of Eq. (3.69) indicates that the coefficients of the terms containing B_0, D_0 become zero similar to that of mode I case (Eq. 3.55) by selection of angle ϕ such that

$$\tan^2\phi=-\frac{a_{11}}{a_{12}}=1/\nu_{LT} \tag{3.70}$$

Similarly, the coefficient of A_1 term in Eq. (3.69) (which is a mode I component) can be made zero to give the value of θ similar to mode I case as

$$\sqrt[4]{\left(\cos^2\theta+(\beta+\alpha)^2\sin^2\theta\right)}\left\{\begin{array}{l}\left[\frac{1}{E_T}\left(\frac{1-\nu_{LT}\nu_{TL}}{1+\nu_{LT}}\right)\frac{\alpha-\beta}{2\alpha}\cos\left(\frac{1}{2}\left(\tan^{-1}\left((\beta+\alpha)\tan\theta\right)\right)\right)\right]\\ -\left[\frac{1}{G_{LT}}\left(\frac{\nu_{LT}}{(1+\nu_{LT})\sqrt{\nu_{TL}}}\right)\frac{1}{2\alpha}\sin\left(\frac{1}{2}\left(\tan^{-1}\left((\beta+\alpha)\tan\theta\right)\right)\right)\right]\end{array}\right\}+$$

$$\sqrt[4]{\left(\cos^2\theta+(\beta-\alpha)^2\sin^2\theta\right)}\left\{\begin{array}{l}\left[\frac{1}{E_T}\left(\frac{1-\nu_{LT}\nu_{TL}}{1+\nu_{LT}}\right)\frac{\alpha+\beta}{2\alpha}\cos\left(\frac{1}{2}\left(\tan^{-1}\left((\beta-\alpha)\tan\theta\right)\right)\right)\right]\\ +\left[\frac{1}{G_{LT}}\left(\frac{\nu_{LT}}{(1+\nu_{LT})\sqrt{\nu_{TL}}}\right)\frac{1}{2\alpha}\sin\left(\frac{1}{2}\left(\tan^{-1}\left((\beta-\alpha)\tan\theta\right)\right)\right)\right]\end{array}\right\}=0 \qquad (3.71)$$

Thus, the angles ϕ and θ which allows these simplifications are exactly the same as in the case of determination of K_I of orthotropic laminates (section 3.4). After the terms containing B_0, D_0 and A_1 are made zero, the strain expression ε_{aa} contain only the terms with coefficients A_0, C_0 and C_1. For positive values of angular orientations, θ and ϕ along the positive gage line, the strain ε_{aa} along the positive gage line (Fig. 3.8) is

$$\begin{aligned}\varepsilon_{aa} = {} & A_0\left\{\begin{array}{l}\left(a_{12}\cos^2\phi+a_{22}\sin^2\phi\right)\left(\frac{\alpha-\beta}{2\alpha}\frac{1}{\sqrt{r_1}}\cos\frac{\theta_1}{2}+\frac{\alpha+\beta}{2\alpha}\frac{1}{\sqrt{r_2}}\cos\frac{\theta_2}{2}\right)\\ +\left(a_{66}\sin\phi\cos\phi\left(\frac{\alpha^2-\beta^2}{2\alpha}\right)\right)\left(\frac{1}{\sqrt{r_2}}\sin\frac{\theta_2}{2}-\frac{1}{\sqrt{r_1}}\sin\frac{\theta_1}{2}\right)\end{array}\right\}\\ & +C_0\left\{\begin{array}{l}\frac{1}{2\alpha}\left(a_{12}\cos^2\phi+a_{22}\sin^2\phi\right)\left(\frac{1}{\sqrt{r_1}}\sin\frac{\theta_1}{2}-\frac{1}{\sqrt{r_2}}\sin\frac{\theta_2}{2}\right)\\ +\left(\frac{a_{66}\sin\phi\cos\phi}{2\alpha}\right)\left(\frac{(\beta+\alpha)}{\sqrt{r_1}}\cos\frac{\theta_1}{2}-\frac{(\beta-\alpha)}{\sqrt{r_2}}\cos\frac{\theta_2}{2}\right)\end{array}\right\}\\ & +C_1\left\{\begin{array}{l}\frac{1}{2\alpha}\left(a_{12}\cos^2\phi+a_{22}\sin^2\phi\right)\left(\sqrt{r_2}\sin\frac{\theta_2}{2}-\sqrt{r_1}\sin\frac{\theta_1}{2}\right)\\ +\left(\frac{a_{66}\sin\phi\cos\phi}{2\alpha}\right)\left((\beta+\alpha)\sqrt{r_1}\cos\frac{\theta_1}{2}-(\beta-\alpha)\sqrt{r_2}\cos\frac{\theta_2}{2}\right)\end{array}\right\}\end{aligned} \qquad (3.72)$$

Similarly, for negative values of both ϕ and θ (since for negative value of ϕ, the angle θ is also negative), the strain ε_{bb} along the negative gage line (Fig. 3.8) can be obtained as

$$A_0\left\{\begin{array}{l}\left(a_{12}\cos^2\phi+a_{22}\sin^2\phi\right)\left(\dfrac{\alpha-\beta}{2\alpha}\dfrac{1}{\sqrt{r_1}}\cos\dfrac{\theta_1}{2}+\dfrac{\alpha+\beta}{2\alpha}\dfrac{1}{\sqrt{r_2}}\cos\dfrac{\theta_2}{2}\right)\\ +\left(a_{66}\sin\phi\cos\phi\left(\dfrac{\alpha^2-\beta^2}{2\alpha}\right)\right)\left(\dfrac{1}{\sqrt{r_2}}\sin\dfrac{\theta_2}{2}-\dfrac{1}{\sqrt{r_1}}\sin\dfrac{\theta_1}{2}\right)\end{array}\right\}$$

$$\varepsilon_{bb}=\ -C_0\left\{\begin{array}{l}\dfrac{1}{2\alpha}\left(a_{12}\cos^2\phi+a_{22}\sin^2\phi\right)\left(\dfrac{1}{\sqrt{r_1}}\sin\dfrac{\theta_1}{2}-\dfrac{1}{\sqrt{r_2}}\sin\dfrac{\theta_2}{2}\right)\\ +\left(\dfrac{a_{66}\sin\phi\cos\phi}{2\alpha}\right)\left(\dfrac{(\beta+\alpha)}{\sqrt{r_1}}\cos\dfrac{\theta_1}{2}-\dfrac{(\beta-\alpha)}{\sqrt{r_2}}\cos\dfrac{\theta_2}{2}\right)\end{array}\right\} \qquad (3.73)$$

$$-C_1\left\{\begin{array}{l}\dfrac{1}{2\alpha}\left(a_{12}\cos^2\phi+a_{22}\sin^2\phi\right)\left(\sqrt{r_2}\sin\dfrac{\theta_2}{2}-\sqrt{r_1}\sin\dfrac{\theta_1}{2}\right)\\ +\left(\dfrac{a_{66}\sin\phi\cos\phi}{2\alpha}\right)\left((\beta+\alpha)\sqrt{r_1}\cos\dfrac{\theta_1}{2}-(\beta-\alpha)\sqrt{r_2}\cos\dfrac{\theta_2}{2}\right)\end{array}\right\}$$

Thus, a strain gage placed at a radial distance r from the crack tip on a line making an angle of $\theta(-\theta)$ and gage orientation $\phi(-\phi)$ on the positive (negative) gage line with the crack axis measures strains containing only the terms A_0, C_0 and C_1 as per Eq. (3.72) and Eq. (3.73) respectively provided the gages are located within the extent of applicability of these equations. Following the approach suggested by Dally and Berger [64] (DB technique), adding Eqs. (3.72) and (3.73) after substituting the r_1, r_2, θ_1 and θ_2 values from Eq. (3.30) and then multiplying with $\sqrt{r}$ gives

$$\begin{aligned}\left(\varepsilon_{aa}+\varepsilon_{bb}\right)\sqrt{r}&=2A_0\left\{\begin{array}{l}\left(a_{12}\cos^2\phi+a_{22}\sin^2\phi\right)\left(\dfrac{\alpha-\beta}{2\alpha}\dfrac{1}{\sqrt[4]{\left(\cos^2\theta+(\beta+\alpha)^2\sin^2\theta\right)}}\cos\dfrac{\theta_1}{2}\right.\\ \left.+\dfrac{\alpha+\beta}{2\alpha}\dfrac{1}{\sqrt[4]{\left(\cos^2\theta+(\beta-\alpha)^2\sin^2\theta\right)}}\cos\dfrac{\theta_2}{2}\right)\\ +\left(a_{66}\sin\phi\cos\phi\left(\dfrac{\alpha^2-\beta^2}{2\alpha}\right)\right)\left(\dfrac{1}{\sqrt[4]{\left(\cos^2\theta+(\beta-\alpha)^2\sin^2\theta\right)}}\sin\dfrac{\theta_2}{2}\right.\\ \left.-\dfrac{1}{\sqrt[4]{\left(\cos^2\theta+(\beta+\alpha)^2\sin^2\theta\right)}}\sin\dfrac{\theta_1}{2}\right)\end{array}\right\} \qquad (3.74)\\ &=A_0I_1\end{aligned}$$

which contains only coefficients pertaining to mode I loading and I_1 is a material property dependent constant given by

$$I_1 = 2\left\{\begin{array}{l}\left(a_{12}\cos^2\phi + a_{22}\sin^2\phi\right)\left(\begin{array}{l}\dfrac{\alpha-\beta}{2\alpha}\dfrac{1}{\sqrt[4]{\left(\cos^2\theta+(\beta+\alpha)^2\sin^2\theta\right)}}\cos\dfrac{\theta_1}{2} \\ +\dfrac{\alpha+\beta}{2\alpha}\dfrac{1}{\sqrt[4]{\left(\cos^2\theta+(\beta-\alpha)^2\sin^2\theta\right)}}\cos\dfrac{\theta_2}{2}\end{array}\right) \\ +\left(a_{66}\sin\phi\cos\phi\left(\dfrac{\alpha^2-\beta^2}{2\alpha}\right)\right)\left(\begin{array}{l}\dfrac{1}{\sqrt[4]{\left(\cos^2\theta+(\beta-\alpha)^2\sin^2\theta\right)}}\sin\dfrac{\theta_2}{2} \\ -\dfrac{1}{\sqrt[4]{\left(\cos^2\theta+(\beta+\alpha)^2\sin^2\theta\right)}}\sin\dfrac{\theta_1}{2}\end{array}\right)\end{array}\right\} \tag{3.75}$$

Similarly, subtraction of Eq. (3.73) from Eq. (3.72) after substituting the r_1, r_2, θ_1 and θ_2 values from Eq. (3.30) and then multiplying with $\sqrt{r}$ gives

$$\begin{aligned}(\varepsilon_{aa}-\varepsilon_{bb})\sqrt{r} = 2C_0 &\left\{\begin{array}{l}\dfrac{1}{2\alpha}\left(a_{12}\cos^2\phi + a_{22}\sin^2\phi\right)\left(\begin{array}{l}\dfrac{1}{\sqrt[4]{\left(\cos^2\theta+(\beta+\alpha)^2\sin^2\theta\right)}}\sin\dfrac{\theta_1}{2} \\ -\dfrac{1}{\sqrt[4]{\left(\cos^2\theta+(\beta-\alpha)^2\sin^2\theta\right)}}\sin\dfrac{\theta_2}{2}\end{array}\right) \\ +\left(\dfrac{a_{66}}{2\alpha}\sin\phi\cos\phi\right)\left(\begin{array}{l}\dfrac{(\beta+\alpha)}{\sqrt[4]{\left(\cos^2\theta+(\beta+\alpha)^2\sin^2\theta\right)}}\cos\dfrac{\theta_2}{2} \\ -\dfrac{(\beta-\alpha)}{\sqrt[4]{\left(\cos^2\theta+(\beta-\alpha)^2\sin^2\theta\right)}}\cos\dfrac{\theta_1}{2}\end{array}\right)\end{array}\right\} \\ &+2C_1 r\left\{\begin{array}{l}\dfrac{1}{2\alpha}\left(a_{12}\cos^2\phi + a_{22}\sin^2\phi\right)\left(\begin{array}{l}\sqrt[4]{\left(\cos^2\theta+(\beta-\alpha)^2\sin^2\theta\right)}\sin\dfrac{\theta_2}{2} \\ -\sqrt[4]{\left(\cos^2\theta+(\beta+\alpha)^2\sin^2\theta\right)}\sin\dfrac{\theta_1}{2}\end{array}\right) \\ +\left(\dfrac{a_{66}}{2\alpha}\sin\phi\cos\phi\right)\left(\begin{array}{l}(\beta+\alpha)\sqrt[4]{\left(\cos^2\theta+(\beta+\alpha)^2\sin^2\theta\right)}\cos\dfrac{\theta_1}{2} \\ -(\beta-\alpha)\sqrt[4]{\left(\cos^2\theta+(\beta-\alpha)^2\sin^2\theta\right)}\cos\dfrac{\theta_2}{2}\end{array}\right)\end{array}\right\} \\ &= C_0 I_2 + C_1 r I_3\end{aligned} \tag{3.76}$$

which now contains coefficients relating to mode II loading only and I_2 and I_3 are constants dependent on the material property given by

$$I_2 = 2\left\{\begin{array}{l}\dfrac{1}{2\alpha}\left(a_{12}\cos^2\phi + a_{22}\sin^2\phi\right)\left(\begin{array}{r}\dfrac{1}{\sqrt[4]{\left(\cos^2\theta+(\beta+\alpha)^2\sin^2\theta\right)}}\sin\dfrac{\theta_1}{2} \\ -\dfrac{1}{\sqrt[4]{\left(\cos^2\theta+(\beta-\alpha)^2\sin^2\theta\right)}}\sin\dfrac{\theta_2}{2}\end{array}\right) \\ +\left(\dfrac{a_{66}}{2\alpha}\sin\phi\cos\phi\right)\left(\begin{array}{r}\dfrac{(\beta+\alpha)}{\sqrt[4]{\left(\cos^2\theta+(\beta+\alpha)^2\sin^2\theta\right)}}\cos\dfrac{\theta_2}{2} \\ -\dfrac{(\beta-\alpha)}{\sqrt[4]{\left(\cos^2\theta+(\beta-\alpha)^2\sin^2\theta\right)}}\cos\dfrac{\theta_1}{2}\end{array}\right)\end{array}\right\}$$

$$I_3 = 2\left\{\begin{array}{l}\dfrac{1}{2\alpha}\left(a_{12}\cos^2\phi + a_{22}\sin^2\phi\right)\left(\begin{array}{r}\sqrt[4]{\left(\cos^2\theta+(\beta-\alpha)^2\sin^2\theta\right)}\sin\dfrac{\theta_2}{2} \\ -\sqrt[4]{\left(\cos^2\theta+(\beta+\alpha)^2\sin^2\theta\right)}\sin\dfrac{\theta_1}{2}\end{array}\right) \\ +\left(\dfrac{a_{66}}{2\alpha}\sin\phi\cos\phi\right)\left(\begin{array}{r}(\beta+\alpha)\sqrt[4]{\left(\cos^2\theta+(\beta+\alpha)^2\sin^2\theta\right)}\cos\dfrac{\theta_1}{2} \\ -(\beta-\alpha)\sqrt[4]{\left(\cos^2\theta+(\beta-\alpha)^2\sin^2\theta\right)}\cos\dfrac{\theta_2}{2}\end{array}\right)\end{array}\right\} \tag{3.77}$$

Thus, the quantities on the LHS of Eqs. (3.74) and (3.76) yields A_0 and C_0 respectively as $r \to 0$. It is evident from Eqs. (3.74) and (3.76) that a minimum of two strain gages located at different radii on both the positive and negative gage lines each at an angle of ϕ with the crack axis will be required for the determination of K_I and K_{II} of orthotropic laminates as shown in Fig. 3.9. Further, the corresponding gages on each gage line should be placed at the same radial distance from the crack tip as shown in Fig. 3.9. Eqs. (3.72 – 3.74) and Eq. (3.76) can be rewritten in a simplified form as

$$\varepsilon_{aa} = A_0\frac{I_1}{2\sqrt{r}} + C_0\frac{I_2}{2\sqrt{r}} + C_1 I_3\sqrt{r} \tag{3.78}$$

$$\varepsilon_{bb} = A_0\frac{I_1}{2\sqrt{r}} - C_0\frac{I_2}{2\sqrt{r}} - C_1 I_3\sqrt{r} \tag{3.79}$$

$$\frac{(\varepsilon_{aa}+\varepsilon_{bb})\sqrt{r}}{I_1} = A_0 \tag{3.80}$$

$$\frac{(\varepsilon_{aa}-\varepsilon_{bb})\sqrt{r}}{I_2} = C_0 + \frac{C_1 r}{I_2} I_3 \tag{3.81}$$

In the present investigation, the coefficients A_0, C_0 and C_1 are determined from the best fit plots of the experimentally measured quantities on the L.H.S of Eqs. (3.80) and (3.81) to the straight lines of the form on the R.H.S of Eqs. (3.80) and (3.81) respectively. Using the values of the coefficients A_0 and C_0 from the best-fit regression, the mixed mode SIFs, K_I and K_{II} can be respectively determined employing Eq. (3.13). As can be observed, the proposed technique for determination of mixed mode SIFs of orthotropic materials provides well defined angles, gage orientation (ϕ) and orientation of the gage line (θ), but not the appropriate radial locations of placing the gages. In the case of one or all of the strain gages being located very close to the crack tip, the strain measurements will be affected by strain gradients and 3D effects. These effects may be averted by pasting the gages quite far away from the crack tip, in such case Eqs. (3.78) and (3.79) may not be applicable for strain measurements at such large distances since more than three parameters may be required to represent the strain at such larger distances.. It is clear that the strain gages should be within the zone of domination of the parameters A_0, A_1, B_0, C_0, C_1 and D_0 and at the same time should not be very close to the crack tip. Therefore, a prior knowledge of the valid radial locations for pasting the gages in imperative for successful implementation of the proposed technique for accurate determination of K_I and K_{II}.

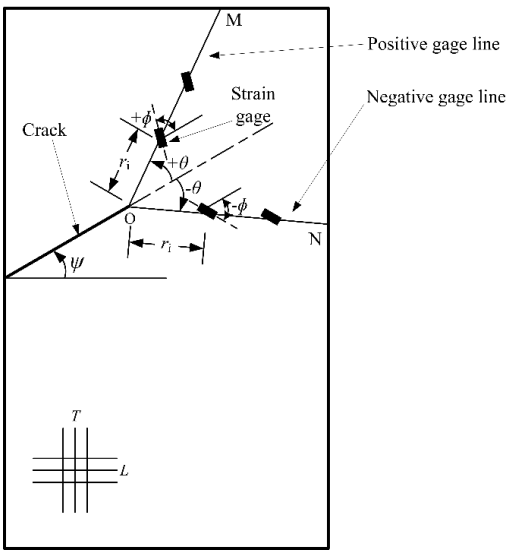

Figure 3.9 Strain gage locations for a plane slant edge-cracked orthotropic specimen

3.7 Proposed approach for determination of optimal radial locations of the strain gages for measurement of K_I and K_{II} of orthotropic materials

The radial location of the strain gages play a crucial role in the accuracy of the SIFs determined using strain gage techniques. Similar to the mode I case, the minimum radial

distance r_{min} for strain measurements is governed by the presence of 3D state of stress near the crack tip. Accordingly, r_{min} is given by

$$r_{min} = \text{thickness of the specimen} \quad [69] \tag{3.82}$$

The maximum radial distance, r_{max} of the gages from the crack tip is the extent of validity of the three parameter strain series represented by Eqs. (3.78) and (3.79) on the positive and negative gage lines respectively. Conversely, Eqs. (3.78) and (3.79) can represent the strain field accurately along the positive and negative gage line upto a radial distance of r_{max}. However, the extent of the validity of Eq. (3.78) along the positive gage line (Fig. 3.9), say r_{max}^{+}, may not be equal to the extent of validity of Eq. (3.79) along the negative gage line (Fig. 3.9), say r_{max}^{-}. In order to take into account the extent of validity along both the positive and negative gage line, the maximum permissible radial location or upper bound of placing the strain gages, for a given specimen is given by

$$r_{max} = \text{minimum}\left[r_{max}^{+}, r_{max}^{-} \right] \tag{3.83}$$

Consequently, the optimal or valid radial locations r_i $(i = 1, 2)$ for all strain gages along both the gage lines can now be given by

$$r_{min} \le r_i \le r_{max} \tag{3.84}$$

A straight forward extension of the procedure for the determination of r_{max} for mode I problems is not possible for mixed mode (I/II) loading cases due to the presence of more number of unknown coefficients in Eqs. (3.78) and (3.79) as compared to mode I problems and the resultant requirement of more than one strain gage in the proposed technique. Therefore, application of curve fitting based on linear regression models is proposed in the investigation and is described as follows

A finite element based approach has been proposed for the accurate determination of r_{max} value for a given mixed mode cracked configuration in the present investigation. The parameters ε_{aa} and ε_{bb} are computed at large number of points along the positive and negative gage lines (OM and ON) using FEA of a given mixed mode cracked configuration (Fig. 3.9). The quantities on LHS of Eqs. (3.80) and (3.81) are then computed at those points using finite element solutions. It is of utmost importance that the radial distances from the crack tip to the corresponding points along the positive and negative gage lines should be

same for the computation of the LHS quantities of Eqs. (3.80) and (3.81) and hence the finite element meshes should be designed accordingly.

Using regression, straight line with a zero slope and a constant intercept of A_0 is fitted to the computed values of $\left\{\left(\varepsilon_{aa}+\varepsilon_{bb}\right)\sqrt{r}\right\}/I_1$ as a function of radial location, r. These computed values at larger values of r are then gradually erased from the data set until the best fit curve is obtained. The value of the coefficient A_0 for the best-fit regression is noted. Similarly, straight line of form $C_0+\left(C_1 r I_3/I_2\right)$ is fitted to the computed values of $\left\{\left(\varepsilon_{aa}-\varepsilon_{bb}\right)\sqrt{r}\right\}/I_2$ and the values of the coefficients C_0 and C_1 are obtained from the best fit regression model.

Consistency and accuracy in the computed unknown coefficients $\left(A_0, C_0 \text{ and } C_1\right)$ can be ensured by:

- The corresponding plots of LHS and RHS quantities should be congruent to each other to the maximum possible radial distance from the crack tip.
- The % relative error between the LHS and RHS quantities should be $\leq 1\%$ within the maximum possible radial distance.
- The quality of the fit defined by the coefficient of determination R^2 should be very close to 1.

Using the best fit regression values of A_0, C_0 and C_1, the RHS quantities of Eqs. (3.78) and (3.79) can be compared with the LHS quantities (i.e. ε_{aa} and ε_{bb}) when plotted against the radial distance from the crack tip for all points on the positive and negative gage line. Apparently, the RHS quantities of Eqs. (3.78) and (3.79) can accurately represent the finite element values of ε_{aa} and ε_{bb} along both the gage lines upto a certain radial distance only since only a three parameter representation of the strain field around the crack tip has been considered. The point of deviation of the RHS of Eq. (3.78) from FE values of ε_{aa} gives $r_{\max}^{+}$ and the RHS of Eq. (3.79) from the FE values of ε_{bb} gives $r_{\max}^{-}$ for a given configuration. A reliable error criterion of 1% between the two quantities has been employed to obtain the quantities $r_{\max}^{+}$ and $r_{\max}^{-}$

Thus, the maximum permissible radial location for pasting the strain gages for a given configuration with a given set of material properties is the minimum of $r_{\max}^{+}$ and $r_{\max}^{-}$ (Eq. (3.83)) which satisfies all the equations Eq. (3.78) – (3.81). Thus, two strain gages are to be pasted on each gage line for the determination of K_I and K_{II} using the proposed technique such that the radial distance of each gage from the crack tip is greater than the distance equal to thickness of the plate (to avoid 3D effects) but less than the $r_{\max}$ value of a given configuration (Eq. (3.82)). It is advisable to paste the gages as far as possible from the crack tip to avoid errors due to complications such as strain gradient and 3D effects.

It may be noteworthy that the consistency and the accuracy of evaluation of $r_{\max}$ (and hence unknown coefficients A_0, C_0 and C_1) depend not only on the mesh gradation but also on how the best-fit process is carried out and the field variables employed therein. It has been noticed from extensive numerical investigation that highly erroneous and inconsistent coefficients and hence $r_{\max}$ are obtained if Eq. (3.78) and (3.79) are used directly for the best fit process instead of using Eq. (3.80) and (3.81) as suggested in the present investigation. The said observation is found to be true even in the case of highly refined FE meshes. Eqs. (3.80) and (3.81) spare us the complications of handling too many coefficients as in Eq. (3.78) and (3.79). Also, Eqs. (3.80) and (3.81) need only a linear best fit which eases out the numerical complexities and can be carried out with substantial efficiency.

3.8 Displacement extrapolation technique (DET) for the determination of SIFs of orthotropic materials using FEA

The present investigation necessitated development of a new orthotropic SIF extraction method from the finite element solution of field variables. The SIFs of experimental specimens have been estimated using the present technique and are employed for the purpose of comparison in Chapter 6. Although commercial software ANSYS® is employed in all analyses of the present investigation, its in-built technique (KCALC) for estimation of SIFs are suitable only for isotropic materials. The proposed technique depends on displacement extrapolation of nodal displacements around the crack tip. Hence, for analysis of cracks in orthotropic media, a methodology similar to that behind the KCALC command has been developed. The proposed method calls for displacement values of the crack tip elements along

the crack faces which are then employed to extract the mixed mode SIFs. These post-processing analyses has been carried out using MATLAB.

To obtain a good representation of the crack-tip, quarter-point elements as suggested by Barsoum [75] and Henshell and Shaw [76] are used. The square root linear elastic singularity for stresses and strains in obtained by shifting a quarter to the crack-tip, the mid side nodes for all surrounding elements. Ayhan et al. [77] proposed a method for performing fracture analyses of orthotropic materials using ANSYS®. They used the crack tip displacement fields of such materials and incorporated them into an ANSYS® macro. Figure 3.10 shows the crack tip element distribution modelled using collapsed quarter point elements. The nodes belonging to the first row crack tip elements on the crack face are numbered. It has been assumed that the $y-$displacement with respect to the crack tip local co-ordinate system is given by [77]

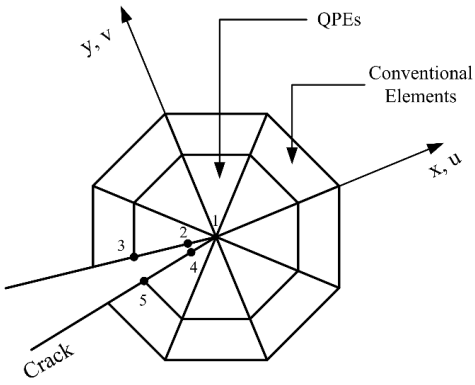

Figure 3.10 Conventional and quarter point elements around the crack tip and along the crack faces

$$\frac{\nabla v}{\sqrt{r}} = A + Br \tag{3.85}$$

where A and B are unknown constants and r is the distance from the crack tip. The differences between the displacement values of corresponding nodes across from each other are given by

$$\nabla v_{24} = v_2 - v_4, \nabla v_{35} = v_3 - v_5 \tag{3.86}$$

Again, using Eq. (3.85), it may be shown that

$$\frac{\nabla v_{24}}{\sqrt{r_2}} = A + Br_2, \frac{\nabla v_{35}}{\sqrt{r_3}} = A + Br_3 \tag{3.87}$$

Solving the equations in Eq. (3.81) for A and B and using the relation $r_3 = 4r_2$ for quarter point elements, we obtain

$$A=\frac{8\nabla v_{24}-\nabla v_{35}}{3\sqrt{r_3}},\ B=\frac{4\nabla v_{35}-8\nabla v_{24}}{3r_3^{\frac{3}{2}}} \tag{3.88}$$

Similarly, for displacements parallel to the crack face i.e. u displacements it may be written that

$$\frac{\nabla u}{\sqrt{r}}=C+Dr \tag{3.89}$$

and C and D are given by

$$C=\frac{8\nabla u_{24}-\nabla u_{35}}{3\sqrt{r_3}},\ D=\frac{4\nabla u_{35}-8\nabla u_{24}}{3r_3^{\frac{3}{2}}} \tag{3.90}$$

When the displacements (u,v) are evaluated along the crack faces $(\theta=\pm\pi;\theta_1=\theta_2=\pm\pi;r_1=r_2=r$ in Eq. (3.30)) for the crack tip element of orthotropic materials, assuming only the singular term representation to be suffice, the displacements under mode I condition using Eq. (3.44) are given by

$$u_I^+=u_I^-=0 \tag{3.91}$$

and

$$\begin{aligned} v_I^+ &= A_0\left\{\begin{array}{l} 2r^{\frac{1}{2}}\left[\frac{(\alpha-\beta)}{2\alpha(\beta+\alpha)}\left(a_{22}-a_{12}(\alpha+\beta)^2\right)\right] \\ +2r^{\frac{1}{2}}\left[\frac{(\alpha+\beta)}{2\alpha(\beta-\alpha)}\left(a_{22}-a_{11}(\beta-\alpha)^2\right)\right] \end{array}\right\} \\ &= 4A_0r^{\frac{1}{2}}\frac{\beta a_{22}}{\beta^2-\alpha^2} \end{aligned} \tag{3.92}$$

$$v_I^-=-4A_0r^{\frac{1}{2}}\frac{\beta a_{22}}{\beta^2-\alpha^2} \tag{3.93}$$

where, u_I^+,v_I^+ are the displacement components for $\theta=+\pi$ and u_I^-,v_I^- are the displacement components for $\theta=-\pi$. Therefore, the net displacement along the crack faces for mode I case is given as

$$\nabla u_I = u_I^+ - u_I^- = 0 \tag{3.94}$$

$$\nabla v_I = v_I^+ - v_I^- = 8A_0 r^{\frac{1}{2}} \frac{\beta a_{22}}{\beta^2 - \alpha^2} \tag{3.95}$$

Similarly, under mode II loading conditions the expressions for displacements using Eq. (3.47) are given by

$$\begin{aligned} u_{II}^+ &= C_0 \left\{ r^{\frac{1}{2}} a_{11} (\beta + \alpha)^2 - r^{\frac{1}{2}} a_{11} (\beta - \alpha)^2 \right\} \\ &= 4C_0 r^{\frac{1}{2}} a_{11} \beta \end{aligned} \tag{3.96}$$

$$u_{II}^- = -4C_0 r^{\frac{1}{2}} a_{11} \beta \tag{3.97}$$

and

$$v_{II}^+ = v_{II}^- = 0 \tag{3.98}$$

where, u_{II}^+, v_{II}^+ are the displacement components for $\theta = +\pi$ and u_{II}^-, v_{II}^- are the displacement components for $\theta = -\pi$. Therefore, net displacement along crack face for mode II case is given by

$$\nabla u_{II} = u_{II}^+ - u_{II}^- = 8C_0 \left\{ r^{\frac{1}{2}} a_{11} \beta \right\} \tag{3.99}$$

$$\nabla v_{II} = v_{II}^+ - v_{II}^- = 0 \tag{3.100}$$

The displacement components for mixed mode conditions are obtained by superposing the mode I (Eqs. (3.94) and (3.95)) and mode II components (Eqs. (3.99) and (3.100)) and can be written as

$$\begin{aligned} \nabla u_{I+II} &= \nabla u_I + \nabla u_{II} = 8C_0 \left\{ r^{\frac{1}{2}} a_{11} \beta \right\} \\ \nabla v_{I+II} &= \nabla v_I + \nabla v_{II} = 8A_0 r^{\frac{1}{2}} \frac{\beta a_{22}}{\beta^2 - \alpha^2} \end{aligned} \tag{3.101}$$

As r approaches the crack tip, only the first term in Eqs. (3.85) and (3.89) become predominant. Therefore, taking limit, Eq. (3.85) can be expressed using Eq. (3.95) as

$$\lim_{r\to 0}\frac{\nabla v}{\sqrt{r}} = A = 8A_0\frac{\beta a_{22}}{\beta^2-\alpha^2} \tag{3.102}$$

which gives

$$A_0 = \frac{A\left(\beta^2-\alpha^2\right)}{8\beta a_{22}} \tag{3.103}$$

and Eq. (3.89) can be expressed using Eq. (3.99) as

$$\lim_{r\to 0}\frac{\nabla u}{\sqrt{r}} = C = 8C_0 a_{11}\beta \tag{3.104}$$

which gives

$$C_0 = \frac{C}{8a_{11}\beta} \tag{3.105}$$

A and C are given by Eqs. (3.88) and (3.90) respectively. The coefficients A_0 and C_0 are related to the stress intensity factors according to the Eq. (3.13). Numerical results showing the performance of the proposed displacement extrapolation method is presented in Chapter 7.

3.9 Finite element formulation

The application of Finite Element Method for the evaluation of SIFs in 2D bodies is widely used for non-standard crack configurations. In the present investigation, linear elastic finite element analysis of various cracked configurations has been carried out using displacement based FE method. For this purpose commercial software ANSYS® has been utilized for numerical analysis. In the present work, PLANE183 element embodied in ANSYS® is used for discretization of the cracked domains. PLANE183 is a higher order 2D, eight noded isoparametric quadrilateral element (Q8). These elements are well suited for both plane stress and plane strain conditions. At the crack tip, the elements have been modeled using quarter

point elements (QPEs) obtained by using PLANE 183 to incorporate square root singularity which arises in LEFM [75]. Dhondt [78] also made use of quarter point elements (QPES) to study the fracture behavior of a 3D crack under mixed mode conditions in an anisotropic material. The details of these elements including the FE formulation have been presented in the following sections.

3.9.1 Eight noded quadrilateral element

The eight noded isoparametric quadrilateral element (Q8) which permits modeling of complicated shapes is generally used to solve fracture mechanics problems. The Q8 is shown in Fig. 3.11.

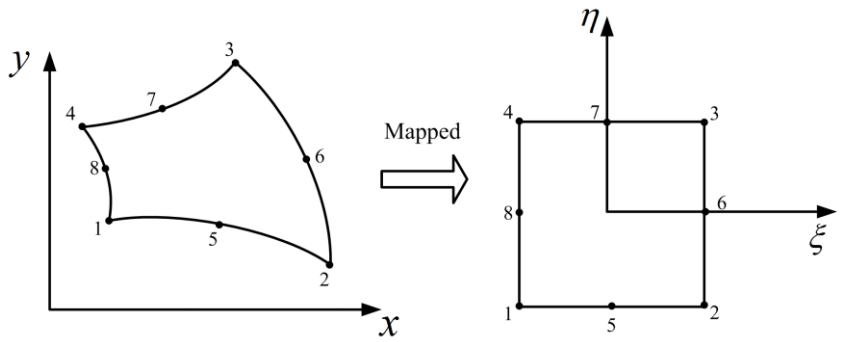

Figure 3.11 Eight noded quadrilateral isoparametric element represented in natural coordinates

Being isoparametric element, the geometric variables are expressed in a similar way as field variable. Thus, in Q8

$$x = \sum_{i=1}^{8} N_i x_i \tag{3.106}$$

$$y = \sum_{i=1}^{8} N_i y_i \tag{3.107}$$

Similarly, the field variables are also represented as

$$u = \sum_{i=1}^{8} N_i u_i \tag{3.108}$$

$$v = \sum_{i=1}^{8} N_i v_i \tag{3.109}$$

where the $N_i (i = 1, 2..., 8)$ are shape functions, (x_i, y_i) are nodal coordinates and (u_i, v_i) are nodal displacements. Shape function must be expressed in a natural co-ordinate system for numerical integration. Natural coordinate (ξ, η) systems are dimensionless and have a maximum absolute magnitude of one. They are defined with reference to the element rather than with reference to the global co-ordinate system in which the element resides (Fig. 3.11). The shape functions for a Q8 element are expressed in natural coordinates as

$$\begin{aligned} N_1 &= \frac{1}{4}(1+\xi)(1-\eta) - \frac{1}{2}(N_8 + N_5) & N_5 &= \frac{1}{2}(1-\xi^2)(1-\eta) \\ N_2 &= \frac{1}{4}(1-\xi)(1+\eta) - \frac{1}{2}(N_5 + N_6) & N_6 &= \frac{1}{2}(1+\xi)(1-\eta^2) \\ N_3 &= \frac{1}{4}(1-\xi)(1-\eta) - \frac{1}{2}(N_6 + N_7) & N_7 &= \frac{1}{2}(1-\xi^2)(1-\eta) \\ N_4 &= \frac{1}{4}(1+\xi)(1-\eta) - \frac{1}{2}(N_7 + N_8) & N_8 &= \frac{1}{2}(1+\xi)(1-\eta^2) \end{aligned} \tag{3.110}$$

The displacements within the element in terms of nodal displacements can be expressed as

$$\{U\} = \begin{Bmatrix} u \\ v \end{Bmatrix} = [N]\{X\}_e \tag{3.111}$$

where $\{U\}$ is the displacement vector of an element, with the shape function matrix

$$[N] = \begin{bmatrix} N_1 & 0 & N_2 & 0 & N_3 & 0 & N_4 & 0 & N_5 & 0 & N_6 & 0 & N_7 & 0 & N_8 & 0 \\ 0 & N_1 & 0 & N_2 & 0 & N_3 & 0 & N_4 & 0 & N_5 & 0 & N_6 & 0 & N_7 & 0 & N_8 \end{bmatrix} \tag{3.112}$$

and nodal displacement

$$\{X\}_e^T = \{u_1 \quad v_1 \quad u_2 \quad v_2 \quad u_3 \quad v_3 \quad u_4 \quad v_4 \quad u_5 \quad v_5 \quad u_6 \quad v_6 \quad u_7 \quad v_7 \quad u_8 \quad v_8\} \tag{3.113}$$

The governing equations of equilibrium for the plane elastostatic problems are given by

$$\frac{\partial \sigma_{xx}}{\partial x} + \frac{\partial \tau_{xy}}{\partial y} + f_x = 0 \tag{3.114}$$

$$\frac{\partial \tau_{xy}}{\partial x} + \frac{\partial \sigma_{yy}}{\partial y} + f_y = 0 \tag{3.115}$$

where f_x and f_y denote the body force per unit volume along the x and y direction; σ_{xx} and σ_{yy} are the normal stresses and τ_{xy} is the in-plane shear stress. The strain matrix

associated with the plane stress and plane strain problems in terms of nodal displacement vector is then given by

$$\{\varepsilon\} = \begin{Bmatrix} \varepsilon_{xx} \\ \varepsilon_{yy} \\ \gamma_{xy} \end{Bmatrix} = \begin{Bmatrix} \dfrac{\partial u}{\partial x} \\ \dfrac{\partial v}{\partial y} \\ \dfrac{\partial u}{\partial y} + \dfrac{\partial v}{\partial x} \end{Bmatrix} = \begin{bmatrix} \dfrac{\partial}{\partial x} & 0 \\ 0 & \dfrac{\partial}{\partial y} \\ \dfrac{\partial}{\partial y} & \dfrac{\partial}{\partial x} \end{bmatrix} \begin{Bmatrix} u \\ v \end{Bmatrix} = \begin{bmatrix} \dfrac{\partial}{\partial x} & 0 \\ 0 & \dfrac{\partial}{\partial y} \\ \dfrac{\partial}{\partial y} & \dfrac{\partial}{\partial x} \end{bmatrix} [N]\{X\}_e \tag{3.116}$$

According to the standard notation the strain matrix is

$$\{\varepsilon\} = [B]\{X\}_e \tag{3.117}$$

The matrix $[B]$ is also called strain displacement matrix and can be represented as

$$[B] = \begin{bmatrix} \dfrac{\partial}{\partial x} & 0 \\ 0 & \dfrac{\partial}{\partial y} \\ \dfrac{\partial}{\partial y} & \dfrac{\partial}{\partial x} \end{bmatrix} [N] \tag{3.118}$$

Then the stress-strain relationship for an element is given by

$$\{\sigma\} = \begin{Bmatrix} \sigma_{xx} \\ \sigma_{yy} \\ \tau_{xy} \end{Bmatrix} = [D]\{\varepsilon\} = [D][B]\{X\}_e \tag{3.119}$$

where $[D]$ is the elasticity matrix and is given for plane stress for orthotropic materials as

$$[D]_{Plane-Stress} = \begin{bmatrix} \dfrac{E_L}{1-\nu_{LT}\nu_{TL}} & \dfrac{\nu_{TL}E_L}{1-\nu_{LT}\nu_{TL}} & 0 \\ \dfrac{\nu_{LT}E_T}{1-\nu_{LT}\nu_{TL}} & \dfrac{E_T}{1-\nu_{LT}\nu_{TL}} & 0 \\ 0 & 0 & G_{LT} \end{bmatrix} \tag{3.120}$$

Here, E, ν and G are Young's modulus, Poisson's ratio and Shear modulus respectively. The displacements, derivatives of displacements, strains and stresses at any point within the

element can be easily computed once $\{X\}_e$ of an element is known. The element stiffness matrix which relates the unknown nodal displacements to the applied forces on an element can be given as

$$[K]_e = t\int_A [B]^T [D][B]\,dxdy \tag{3.121}$$

where $[D]$ is the elasticity matrix consisting of element material constants. The matrix $[B]$ which relates strains and displacements, is a function of (x, y) and t is thickness of the element (assumed constant). The differential area $dxdy$ can be replaced by

$$dxdy = |J|\; d\xi\, d\eta \tag{3.122}$$

where $|J|$ is the determinant of the Jacobian matrix and is given by

$$|J| = \frac{\partial x}{\partial \xi}\frac{\partial y}{\partial \eta} - \frac{\partial x}{\partial \eta}\frac{\partial y}{\partial \xi} \tag{3.123}$$

Then Eq. (3.121) becomes

$$[K]_e = t\int_{-1}^{1}\int_{-1}^{1} [B(\xi,\eta)]^T [D][B(\xi,\eta)]|J|\,d\xi d\eta \tag{3.124}$$

where, $[B(\xi,\eta)] = \begin{pmatrix} \frac{\delta\xi}{\delta x} & \frac{\delta\eta}{\delta x} & 0 & 0 \\ 0 & 0 & \frac{\delta\xi}{\delta y} & \frac{\delta\eta}{\delta y} \\ \frac{\delta\xi}{\delta x} & \frac{\delta\eta}{\delta y} & \frac{\delta\xi}{\delta x} & \frac{\delta\eta}{\delta x} \end{pmatrix} \begin{pmatrix} \frac{\delta}{\delta\xi} & 0 \\ \frac{\delta}{\delta\eta} & 0 \\ 0 & \frac{\delta}{\delta\xi} \\ 0 & \frac{\delta}{\delta\eta} \end{pmatrix} [N]$ The above equation is now entirely a function of local co-ordinates (ξ,η). Numerical integration is required to be employed over the area for the evaluation of element stiffness matrix $[K]_e$.

3.9.2 Quarter point elements (QPEs)

Quarter point elements are extensively used in LEFM for modeling the inverse square root singularity at the crack tip. A large number of conventional elements are required to model

the same singularity at the crack tip. Barsoum [75] and Henshell and Shaw [76] were first to discover the quarter point elements which can be easily generated from any conventional elements containing mid-side nodes. The singularity in the QPE is achieved by shifting the mid-side nodes on edges that are connected to the crack tip by an amount of quarter of length of the edge towards the crack tip. Such a simple and bodily movement of nodes ensures accurate estimation of the SIFs and modeling of $1/\sqrt{r}$ singularity with less number of elements around the crack tip. In the present investigation the mid-side nodes of selected Q8 element are shifted to quarter points, to generate QPEs around the crack tip. The conventional Q8 elements are first collapsed to six noded triangular elements and arranged in a standard *spider-web pattern* around the crack tip. Finally, the mid-side nodes are shifted to build the QPEs. All these steps are carried out by ANSYS® automatically using its in built command KSCON. The proof for ability to represent $1/\sqrt{r}$ singularity by the Q8 element used in the present investigation is presented in the following section.

3.9.3 Collapsed six-noded triangular quarter point elements

Figure 3.12 shows a collapsed Q8 crack-tip element, in which nodes 1, 4 and 8 are collapsed at the crack tip. This triangle is generated by collapsing the side 1-4 of the quadrilateral in Fig. 3.11.

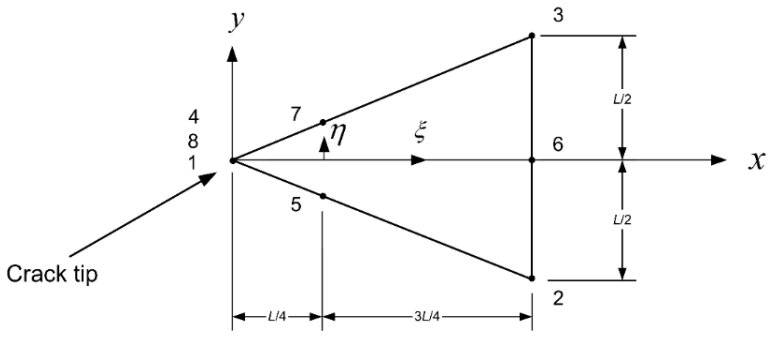

Figure 3.12 Six noded quadrilateral isoparametric element with mid-side nodes at the quarter point [76]

In this case the singularity is investigated along the $x-$axis (i.e., $\eta = 0$) using

$$x = N_1 x_1 + N_2 x_2 + N_3 x_3 + N_4 x_4 + N_5 x_5 + N_6 x_6 + N_7 x_7 + N_8 x_8 \qquad (3.125)$$

the x - coordinate along the $x-$axis is given by

$$x=-\frac{1}{4}(1+\xi)(1-\xi)l_1-\frac{1}{4}(1+\xi)(1-\xi)l_1+\frac{1}{2}(1-\xi^2)\frac{l_1}{4}+\frac{1}{2}(1+\xi)l_1+\frac{1}{2}(1-\xi^2)\frac{l_1}{4} \tag{3.126}$$

which simplifies to

$$x=(\xi^2+2\xi+1)\frac{l_1}{4} \tag{3.127}$$

Therefore, ξ in terms of x can be given as

$$\xi=\left[-1+2\sqrt{\frac{x}{l_1}}\right] \tag{3.128}$$

The displacement u along $x-$axis is given by

$$u=N_1u_1+N_2u_2+N_3u_3+N_4u_4+N_5u_5+N_6u_6+N_7u_7+N_8u_8 \tag{3.129}$$

Substituting shape functions and Eq. (3.128) into Eq. (3.129) and differentiating w.r.t x, the strain in the x-direction is then given by

$$\varepsilon_{xx}=\frac{\partial u}{\partial x}=-\frac{1}{2}\left[\frac{1}{\sqrt{(xL)}}-\frac{2}{L}\right]u_2+\frac{1}{2}\left[-\frac{1}{\sqrt{(xL)}}+\frac{2}{L}\right]u_3+\left(\frac{1}{\sqrt{(xL)}}-\frac{2}{L}\right)u_7+\frac{1}{2}\left[\frac{1}{\sqrt{(xL)}}\right]u_6+\left[\frac{1}{\sqrt{(xL)}}-\frac{2}{L}\right]u_5 \tag{3.130}$$

Thus, Eq. (3.130) shows that the strain singularity along the $x-$axis is $\frac{1}{\sqrt{x}}$ as $x\to 0$.

3.10 Summary

In this chapter, detailed formulation of the development of proposed strain gage techniques for the determination of mode I and mixed mode SIFs of orthotropic materials along with propositions for valid strain gage locations is presented. Proceeding with the Irwin proposed stress functions [20] and employing the Generalized Westergaard approach [73] coupled with the DS technique, theoretical basis of a single strain gage method for the determination of mode I SIF of orthotropic laminates is presented and a FE based approach has been proposed for the determination of optimal radial location of the strain gage for accurate determination of K_I. Similarly, extending the proposed mode I technique to mixed mode (I/II) case, a

detailed formulation of the methodology is also developed for the first time for the determination of K_I and K_{II} of orthotropic composites using multi strain gages. A FE based approach for estimation of optimal gage locations of the strain gages for accurate determination of mixed mode SIFs is also presented. The displacement extrapolation technique for extraction of orthotropic SIFs from FE solutions has also been proposed and explained in detail.

Chapter 4

Determination of r_{max} and numerical simulation of mode I experiments in orthotropic materials

This chapter presents the numerical simulation of determination of mode I SIF of orthotropic laminates using the proposed single strain gage technique discussed in section 3.4. First the determination of r_{max} and optimal strain gage locations using the proposed finite element based approach (explained in section 3.5) for the cracked orthotropic specimen is implemented in this chapter. Different types of cracked configuration such as edge cracked plate, center cracked plate , double edge cracked plate and eccentric center cracked plate have been considered to substantiate the efficacy of the proposed technique in accurate determination of mode I SIF and to demonstrate the importance of r_{max} . In addition, the effect of crack geometry and boundary on the r_{max} has also been presented in this chapter. Sensitivity study has also been carried out to analyze the effect of deviation in predetermined gage orientations on the estimated SIFs before going into real time experimentations. Finite element analyses in all the examples of the present investigation are carried out using ANSYS® employing eight noded isoparametric quadrilateral elements (Q8) and the square root singularity at the crack tips is modelled using collapsed quarter point elements (Q8 QPEs) (section 3.9).

4.1 Edge cracked orthotropic laminate

An edge cracked $[0_2/90]_{2S}$ glass-epoxy laminate has been considered for numerical simulation of the single strain technique on single ended cracked configurations, the effective properties of which are listed in Table 4.1. Corresponding to these properties, the values of α and β are estimated as 0.9684 and 1.4496 respectively using Eq. (3.31). Corresponding to $\alpha =$ 0.9684 and $\beta =$ 1.4496 solution of Eq. (3.57) and Eq. (3.55) gives $\theta =$ 54.27° (Fig. 4.1) and $\phi =$ 68.01° which are used in finite element analysis. Different dimensions of the

edge-cracked specimen considered for different analyses and the applied stress are listed in Table 4.2.

Table 4.1 Effective laminate properties

Longitudinal modulus	E_L	33.3 GPa
Transverse modulus	E_T	24.6 GPa
Poison's ratio	ν_{LT}	0.163
Shear modulus	G_{LT}	5.2 GPa

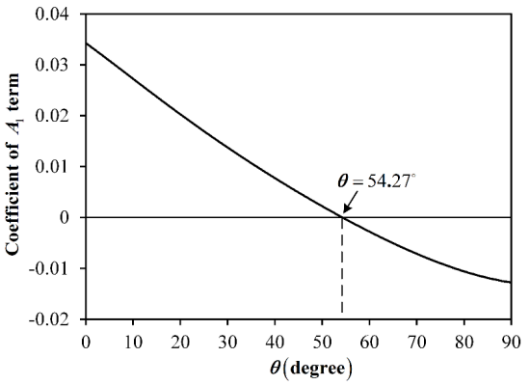

Figure 4.1 Plot of Eq. (3.57) for θ ranging from 0° to 90°

Table 4.2 Geometric and loading parameters of edge cracked orthotropic laminates

Section	b (mm)	a/b	h/b	t (mm)	σ (MPa)
4.1.1		0.4			
4.1.2	50	0.1-0.8	1.5	1	100
4.1.3		0.4			

4.1.1 Determination of r_{max} for edge cracked orthotropic laminate

This example elaborates the general procedure for the determination of r_{max} for any single ended cracked orthotropic plate subjected to mode I loading using finite element method. The $[0_2/90]_{2S}$ glass-epoxy laminate with an edge cracked configuration and subjected to uniform tensile stress (Fig. 4.2(a)) is considered to illustrate the procedure. The same problem has also been studied by Shukla et al. [69].

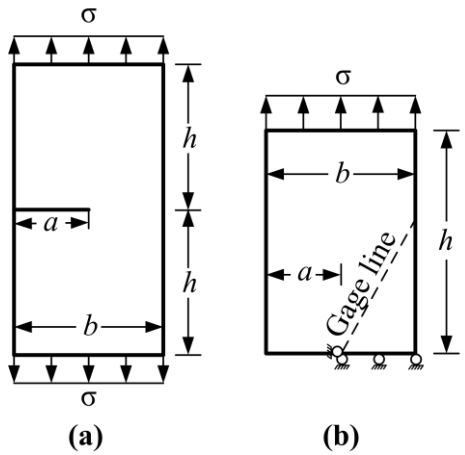

Figure 4.2(a) An orthotropic edge-cracked plate; (b) corresponding solution domain

Figure 4.2(b) shows analysis domain for the finite element studies along with the symmetric boundary conditions. The loading and geometric parameters of the edge cracked plate are presented in Table 4.2.

In order to study the influence of the mesh refinement on the convergence of r_{max} values, an edge cracked plate with $a/b=0.4$ and three meshes for this configuration with increasing mesh density is considered (Fig. 4.3). Other parameters pertaining to this example have been presented in Table 4.2. The number of elements (NE) and number of nodes (NN) are also mentioned in Fig. 4.3.

The meshes in Fig. 4.3 are designed such that the nodes of several elements are made to lie along a radial line (Fig. 4.2(b)) which makes an angle of θ(=54.27°) with the axis of the crack (Eq. (3.57), Fig. 4.1). This line begins at the crack-tip and terminates at one of the outer boundaries of the cracked plate. According to the present technique, a single strain gage is required to be placed at an appropriate location on this line and oriented in the direction of ϕ(=68.01°) (Eq. (3.55)) in order to measure the linear strain ε_{aa} (Eq. 3.58, Fig. 3.6). This line is termed as the *gage-line*.The strains of each of the nodes are computed along the gage line and being in the global coordinates these are transformed to linear strain ε_{aa} in the direction defined by the angle ϕ. The radial distances (r) of each of the nodes along the gage line are then computed.

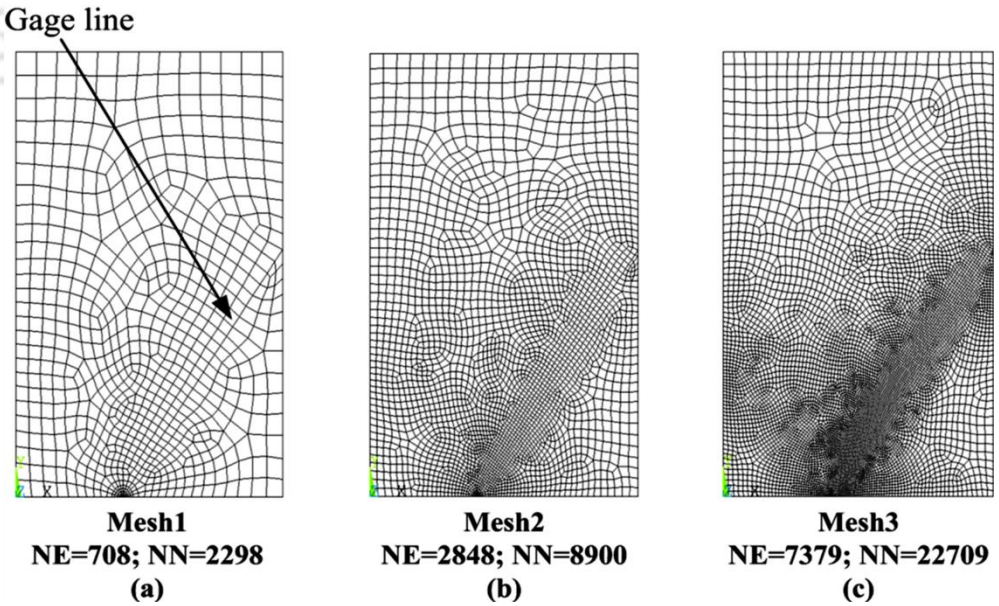

Figure 4.3 Different finite element meshes used for the convergence study of r_{max} of the edge cracked orthotropic laminate with $a/b=0.4$

Following Eq. (3.61), plots of computed values of $\ln(\varepsilon_{aa})$ versus $\ln(r)$ obtained from each of the three meshes of Fig. 4.3 are shown in Fig. 4.4. Crack tip point is not plotted as the radius of this point is zero. It may be observed from the plots in Fig. 4.4 that each plot consists of well demarcated zones defining the linear and non-linear portions (in logarithmic scale) as predicted by the theory in section 3.5. It can also be noticed that the linear trend extends up to a certain radial distance and thereafter gradually turns to the non-linear portion. The extent of the straight line portion of the plots is observed to have gradually increased as the meshes are refined and can be seen more prominently in fine meshes than in coarse meshes due to less number of elements. As discussed earlier, the initial linear part is due to the dominance of the three parameters (Eq. (3.53)) and the nonlinear part is due to the presence of more than three parameters in the expression for ε_{aa}. The results presented in Fig. 4.4 also strongly confirm that the selection of coefficients (A_0, B_0, A_1) that are retained in the three parameter strain series (Eq. (3.53)) appears to be valid. The first point in all these plots in Fig. 4.4 is the strain value at the corner node of the quarter point element. The deviation of this point from the straight line portion may be due to the effect of the constant strain term of the quarter point elements [79]. It is evident that the radius at end point of the linear portion of the plots in Fig. 4.4 is simply the $r_{\max}$ or the extent of the three parameter strain series (Eq. (3.53)) along the gage line or the maximum permissible radial distance $(r_{\max})$ of strain gage in accordance with the present single strain gage technique (section 3.5).

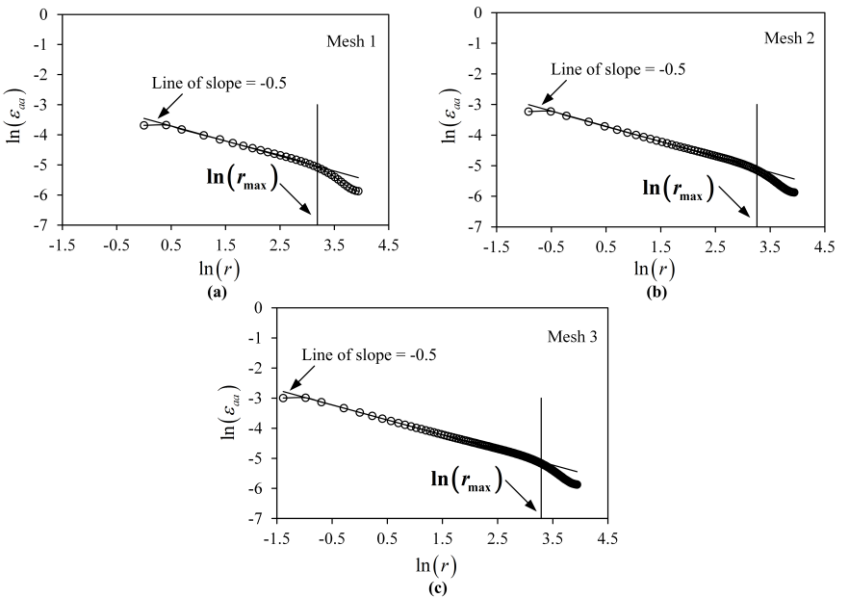

Figure 4.4 Variation of $\ln(\varepsilon_{aa})$ with $\ln(r)$ along the gage line for the sequence of meshes in Fig. 4.3

In the present example, the procedure described in section 3.5 has been employed to determine precisely the terminal point of the linear portion of the plot i.e., the value of $r_{\max}$. Accordingly, a line of slope – 0.5 is first superposed on to the plots on $\ln(\varepsilon_{aa})$ versus $\ln(r)$. Considering this line as the exact solution, absolute percent relative error in computed values of $\ln(\varepsilon_{aa})$ is then determined at all values of radius in the plot. Finally, the $r_{\max}$ or the point of deviation of the log-log plot from the superposed line is estimated as the radius at which the percent error reaches 1% (as one observes from right to left).

Following the above procedure, straight lines having slope of – 0.5 are superposed on to all the plots of $\ln(\varepsilon_{aa})$ versus $\ln(r)$ in Fig. 4.4. It can be observed from Fig. 4.4 that the initial straight line portions of the plots and the superposed line are congruent to each other up to a certain radial distance and the numerical results deviate thereafter. The congruence to a greater extent can be noticed in the plots of the results obtained from the very fine mesh (Mesh 3, Fig. 4.4(c)) due to better accuracy in the computed results. Therefore, it can be concluded from Fig. 4.4(c) that deviation of the finite element results from the superposed line is due to the presumable dominance of higher order coefficients other than A_0, B_0 and A_1 in Eq. (3.53).

Figure 4.5 shows the percent relative error between the superposed line and that of the finite element results of $\ln(\varepsilon_{aa})$ at different radii along the entire gage line. It can be observed from Fig. 4.5 that the error decreases monotonically from the right towards left. The estimated values of $r_{\max}$ are marked in Fig. 4.4 for different meshes. The corresponding numerical values of the $r_{\max}$ are presented in Table 4.3. It can be noticed from the results of Table 4.3 that as the meshes are refined $r_{\max}$ values converges. No improvement is noticed as the meshes are further refined. Finally, it is also interesting to note that similar trends and

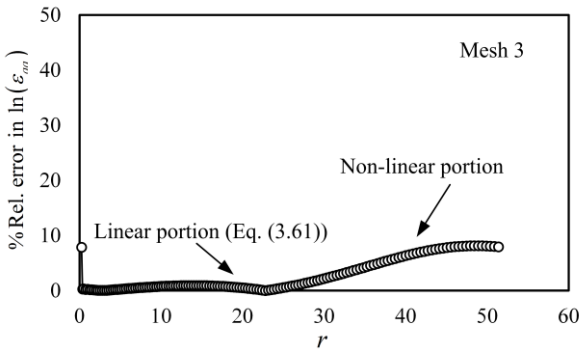

Figure 4.5 Percentage relative error in computed values of $\ln(\varepsilon_{aa})$ obtained using results of plot in Fig. 4.4(c)

observations have also been reported for the cracked panels made of isotropic materials [56-58]. No further convergence in the value of r_{max} is noticeable upon subsequent mesh refinement than that present in Mesh 3. Therefore, the r_{max} value of the edge-cracked plate considered in the example can be taken up as 26.85 mm.

Table 4.3 Convergence of the r_{max} with mesh refinement for $a/b = 0.4$

Mesh	r_{max} (mm)
Mesh 1	24.22
Mesh 2	25.99
Mesh 3	26.85

4.1.2 Effect of a/b ratio on r_{max}

In order to understand the effect of a/b on r_{max} of single-ended cracked configurations, edge cracked composite plate with a/b ranging from 0.1 to 0.8 in steps of 0.1 are considered in this section. The other details of these configurations are presented in Table 4.2. Very fine finite element meshes for all a/b values employed in the present study are shown in Fig. 4.6.

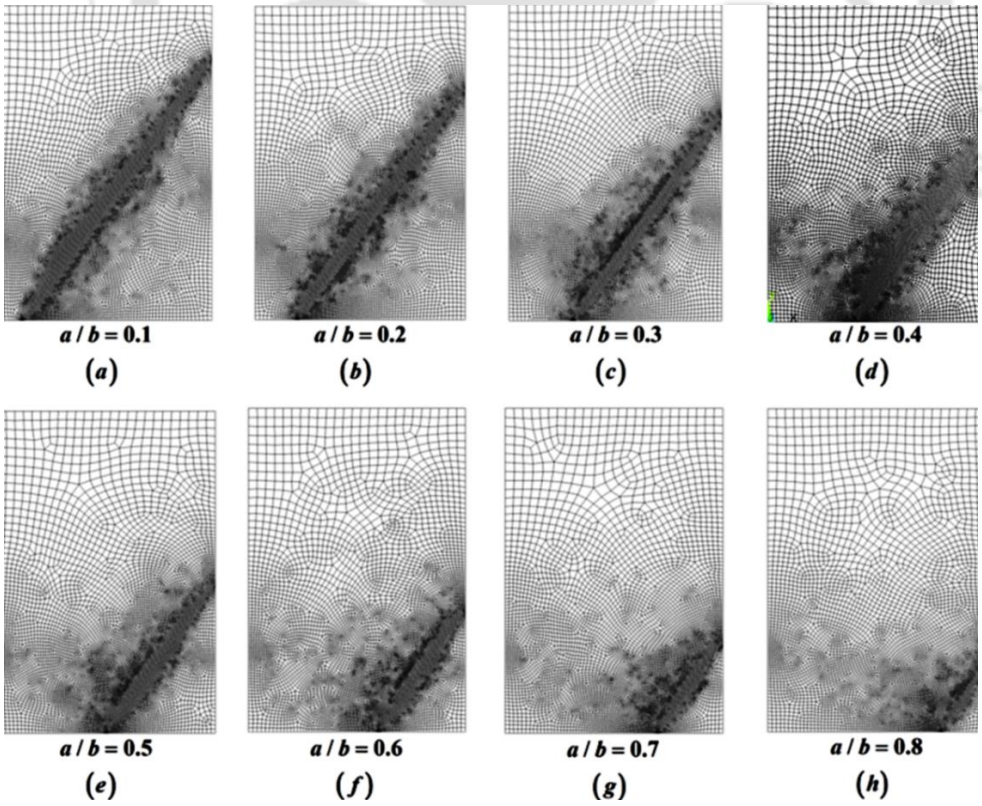

Figure 4.6 Finite element meshes for the edge-cracked orthotropic laminates employed to study the effect of a/b on r_{max}

Here also, large number of elements are made to fall on the gage lines for accurate prediction of strain value, ε_{aa}. The plots of $\ln(\varepsilon_{aa})$ versus $\ln(r)$ corresponding to $a/b = 0.1$ to 0.8 are shown in Fig. 4.7. Following the procedure described in the previous example, the estimated value of r_{max} corresponding to each configuration is presented in Table 4.4.

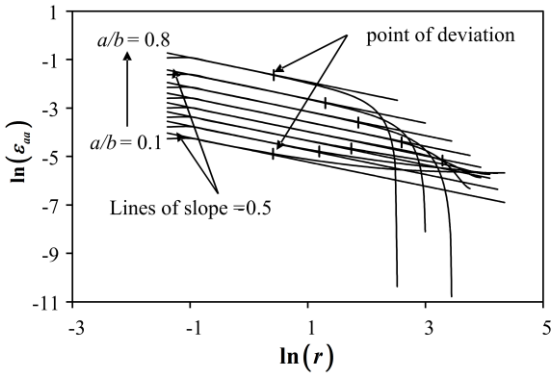

Figure 4.7 Variation of $\ln(\varepsilon_{aa})$ with $\ln(r)$ for the edge cracked orthotropic laminates with different values of a/b

Table 4.4 Variation of the r_{max}/b with a/b of the edge cracked configuration

a/b	r_{max} (mm)	r_{max}/b
0.1	1.51	0.0302
0.2	3.05	0.061
0.3	5.69	0.1138
0.4	26.85	0.5372
0.5	13.39	0.2678
0.6	6.42	0.1284
0.7	3.66	0.0732
0.8	1.52	0.0304

Variation of the r_{max} as a function of a/b is presented in Fig. 4.8 to observe the effect of a/b on r_{max}. It can be seen from Fig. 4.8 that as a/b increases the r_{max} value increases initially and then decreases. It may be pointed out that similar results have also been obtained by Sarangi et al. [61] for edge cracked panels made of isotropic materials. Moreover, Chona et al. [80] also found similar results while investigating the extent of the singularity dominated zone (SDZ) of various cracked configurations and reported the decrease in size of the SDZ with the increase in a/b. A probable explanation to the observed trend of variation of r_{max} with a/b could be provided based on the experimental results of Chona et al. [80]. They showed using photoelastic studies that, magnitude of all the coefficients (singular and

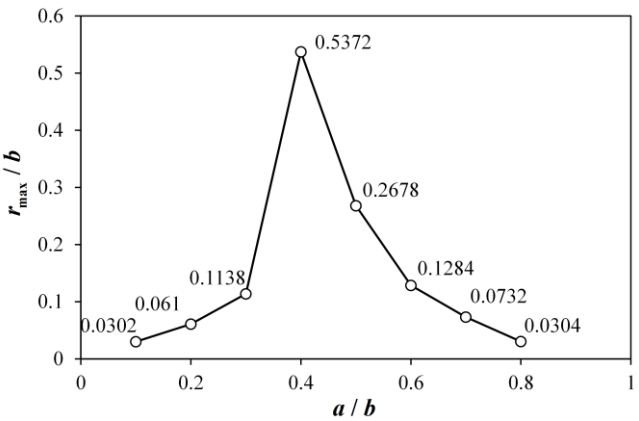

Figure 4.8 Variation of r_{max}/b with a/b for the edge cracked orthotropic laminate

nonsingular) increased gradually with the increase in a/b and after a certain value of a/b, the magnitude of nonsingular terms sharply increased with increase in a/b values. Referring to Eq. (3.61), for a given set of orthotropic material properties, the extent of the linear portion and hence the r_{max} value is a function of magnitude of the nonsingular terms, relative to the singular term A_0. Referring to Fig. 4.8, as a/b is increased, the magnitude of the singular term A_0 dominates over the magnitude of nonsingular terms initially. As a result, the r_{max} value increases (due to the increase in the linear portion as compared to nonlinear portion, Fig. 4.7) with the increase in a/b ratio. With further increase in a/b, the magnitude of nonsingular terms have dominated over the singular term, due to which the nonlinear portions increases and hence r_{max} decreases. Thus, relative increase in magnitude of the A_0 leads to increase in the r_{max} value, while increase in magnitude of the nonsingular terms results in decrease in the r_{max} value.

4.1.3 Numerical simulation of the proposed single strain gage technique for single ended cracked orthotropic laminates

The purpose of this example is to simulate the proposed single strain gage technique for determination of mode I SIF in orthotropic composite laminates and to demonstrate the importance of optimal locations of strain gage (r_{max}). The numerical results of this section are intended to verify the efficacy of the present formulations presented in sections 3.4 and 3.5. For this purpose, an edge cracked panel made of $[0_2/90]_{2S}$ glass epoxy (Fig. 4.2(a)) with $a/b=0.4$ and subjected to mode I loading is again considered here. Material properties and geometric, loading details of this problem domain are presented in Tables 4.1 and 4.2 respectively. The analytical expression for mode I SIF of this configuration is given by [13]

$$K_I = Y_I(a/b)\sigma\sqrt{a} \tag{4.1}$$

where σ is the applied stress, a is the crack length and Y_I is the specimen geometric factor given by

$$Y_I = 1.99 - 0.41(a/b) + 18.7(a/b)^2 - 38.48(a/b)^3 + 53.85(a/b)^4 \tag{4.2}$$

Finite element analysis of the above configuration is carried out using a mesh that is similar to the mesh shown in Fig. 4.3(c). As stated earlier for determination of SIF using a single

strain gage, the strain gage needs to located along $\theta = 54.27°$ and oriented at $\phi = 68.01°$ (Fig. 3.6). The computed strains ε_{aa} at all the nodes on the gage line are considered as the measured strains using a single strain gage oriented at angle of $\phi = 68.01°$ with the crack axis at the corresponding radial distances. Following the procedure explained in the previous examples, the $r_{\max}$ value of this configuration is found to be 26.85 mm. Therefore, according to the present approach (section 3.5, Eq. (3.59)), any radial distance of the strain gage from the crack tip that satisfies

$$1\text{mm} < r < 26.85\text{mm} \tag{4.3}$$

is an optimal or valid gage location for accurate determination of mode I SIF for the problem considered. The gage locations for which $r \geq r_{\max}$ are invalid or non-optimal locations. Accordingly, the strain ε_{aa} is sampled at two optimal gage locations (for which, $1\text{mm} < r < 26.85\text{mm}$) and two non-optimal gage locations (for which, $r > 26.85\text{mm}$) as shown in Table 4.5. For this configuration at $\sigma = 100\,\text{MPa}$ the reference value of mode I SIF determined using Eq. (4.1) is K_I =52.80 MPa$\sqrt{\text{m}}$. The measured mode I SIF using a single strain gage located at those optimal and non-optimal radii are determined using the simulated finite element strain values ε_{aa} at those radii using Eqs. (3.58) and (3.13) (Table 4.5).The percent relative error in measured K_I is computed as

$$\%\,\text{Rel.error} = \frac{K_{\text{Referencesolution}} - K_{\text{measured or simulated}}}{K_{\text{Referencesolution}}} \times 100 \tag{4.4}$$

The percent relative error in measured or simulated K_I at optimal and non-optimal radii are also shown in Table 4.5.

Table 4.5 Simulated mode I SIFs at the optimal and non-optimal strain gage locations for the edge cracked orthotropic laminate ($r_{\max} = 26.85\,\text{mm}$)

$r\,(\text{mm})$	ε_{aa}	$K_I\left(\text{MPa}\sqrt{\text{m}}\right)$	% Relative Error
22.07	6.68E-03	53.01	0.39
23.15	6.45E-03	52.43	0.71
29.56	5.17E-03	47.48	10.08
31.95	4.73E-03	45.17	14.46

It may be observed from results of Table 4.5 that very small error of the order of 1% can be expected in the measured K_I values using the proposed technique if the strain gage is placed at an optimal location. Moreover, the results of Table 4.5 also clearly demonstrate that highly inaccurate or unacceptable errors (as high as 14%) in measured K_I can be expected if the gages are pasted beyond the r_{max} value. The results in the above table clearly show that using the proposed single gage technique very accurate values of mode I SIF, K_I can be obtained for a single ended cracked orthotropic composite specimens using a single strain gage. The results in Table 4.5 however also demonstrates that very accurate SIFs can be determined only if the gages are placed at optimal locations which in turn can be decided using the proposed parameter r_{max}. The above results also corroborate the finite element based approach for accurate determination of the r_{max} value of cracked orthotropic laminates.

4.2 Double ended cracked orthotropic laminates

The single strain gage technique developed for orthotropic laminates using single ended crack theories are tested on orthotropic laminates having double ended cracks for which orthotropic laminates having different configurations such as center cracked configuration, double edge cracked configuration and eccentric center cracked configuration are considered.

4.2.1 Center cracked orthotropic laminate

A center cracked $[0_2/90]_{2S}$ glass-epoxy laminate (Fig. 4.9(a)) has been considered for the numerical simulations, the effective properties of which are listed in Table 4.1. Corresponding to these properties, the same values of values of α, β, θ and ϕ are obtained as that for the edge cracked specimen (section 4.1) as 0.9684, 1.4496 , 54.27° and 68.01° respectively which are used in finite element analysis. Figure 4.9(b) shows the solution domain used for the FEA

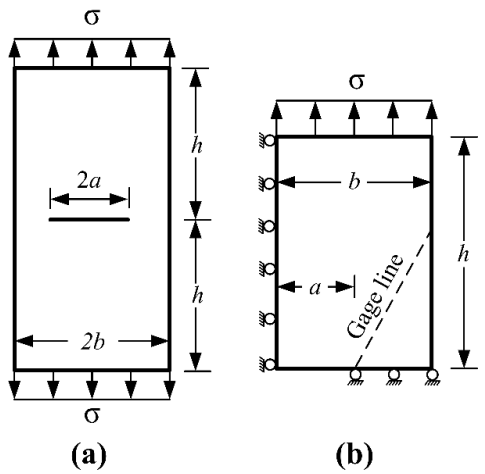

Figure 4.9 (a) A center-cracked orthotropic plate (b) corresponding solution domain

describing the symmetric boundary conditions employed. Different dimensions of the specimen and crack considered for different analyses are listed in Table 4.6.

Table 4.6 Geometric and loading parameters of center cracked orthotropic laminates

Section	b (mm)	a/b	h/b	t (mm)	σ (MPa)
4.2.1.1	50	0.4	1.5	1	100
4.2.1.2		0.1-0.8			
4.2.4		0.4			
4.2.5		0.4			

4.2.1.1 Determination of r_{max} for the center cracked orthotropic laminate

This example is intended to demonstrate the procedure for computation of r_{max} of any given double-ended cracked component and that the parameter r_{max} converges with the mesh refinement. Further, different values of the crack length to width ratio (a/b) ranging from 0.1 to 0.8 in steps of 0.1 have been considered to show the dependence of r_{max} on a/b ratio. To analyse the effect of mesh refinement on the convergence of r_{max} values, three levels of meshes with increasing mesh density (Fig. 4.10) have been considered for a centre cracked plate (Fig. 4.9(a), a/b =0.4).

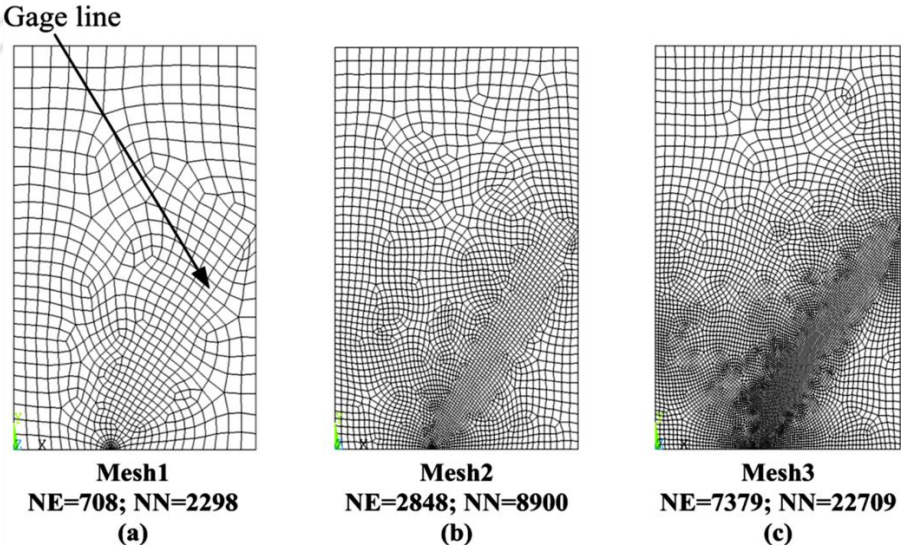

Figure 4.10 Different finite element meshes used for the convergence study of r_{max} of the center cracked orthotropic laminate with $a/b = 0.4$

In keeping with the proposed technique, a single strain gage placed at a location, r on the gage line having an inclination of θ (Eq. (3.57); Fig. 4.1) and oriented along ϕ (Eq. (3.55)) could measure the linear strain ε_{aa} (Fig. 3.6 and Eq. (3.58)). The radial distance (r) of each of these nodes on the gage line from the crack tip are then computed and the values of ε_{aa} at these nodes are recorded. In the present work, the value of $r_{\max}$ has been determined utilizing the procedure given in section 3.5. The plots of $\ln(\varepsilon_{aa})$ versus $\ln(r)$ for the sequence of meshes shown in Fig. 4.10 are obtained as shown in Fig. 4.11. The value of $\ln(r)$ would be undefined at the crack tip point since at this point $r = 0$ and hence is not plotted. A line with a slope – 0.5 is then superimposed on to the plots on $\ln(\varepsilon_{aa})$ versus $\ln(r)$. Considering this line to be the exact solution, absolute percent relative error between the computed values of $\ln(\varepsilon_{aa})$ and the exact solution is then evaluated at all the radial points along the gage line. Finally, the $r_{\max}$ or the point of divergence of the plots on $\ln(\varepsilon_{aa})$ versus $\ln(r)$ from the superposed line is considered to be the value of $\ln(r)$ till which the percent error is ≤ 1% while moving from right to left in Fig. 4.11. It is noteworthy from the plots in Fig. 4.11 that in each graph the linear and non-linear portions can be demarcated very well as predicted by the theory in section 3.5. As proposed, the linear portion truly represents the three parameters (Eq. (3.53)) and nonlinear portion exhibits the requirement of more parameters for representation of ε_{aa}. The results presented in Fig. 4.11 also substantiate the selection of coefficients (A_0, B_0, A_1)

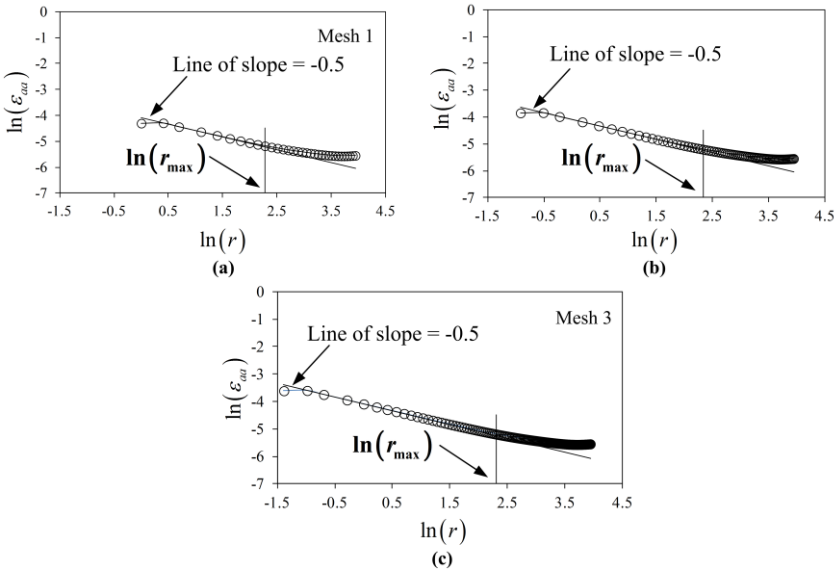

Figure 4.11 Variation of $\ln(\varepsilon_{aa})$ with $\ln(r)$ along the gage line for the sequence of meshes in Fig. 4.10

retained in the three parameter strain series (Eq. (3.53)). The first point in all these plots in Fig. 4.11 is corresponding to the strain value at the corner node of the quarter point element which deviates from the straight line portion due to the effect of the constant strain term of the quarter point elements [79]. The values of r_{max} determined following the method described in this section are marked in Fig. 4.11 and the corresponding numerical values are presented in Table 4.7. It may be observed that as the meshes are refined the r_{max} value converges. Therefore, recommended value of the r_{max} is taken up as that value after which no changes with further refinement is observed. Thus, for the centre cracked panel with a/b as 0.4 r_{max} is set as 10.03 mm.

Table 4.7 Convergence of the r_{max} with mesh refinement for $a/b = 0.4$

Mesh	r_{max} (mm)
Mesh 1	11.57
Mesh 2	10.32
Mesh 3	10.03

4.2.1.2 Effect of crack length on the r_{max}

This section helps in understanding the effect of a/b on the r_{max} for centre cracked composite plates. For this purpose, centre cracked plates with a/b ranging from 0.1 to 0.8 in steps of 0.1 are considered. Table 4.6 enlists the other details for these configurations. For estimation of r_{max}, a typical mesh selected after proper convergence study is shown in Fig. 4.10 (c). Plots of $\ln(\varepsilon_{aa})$ versus $\ln(r)$ for all values of a/b is shown in Fig. 4.12 and the r_{max} values corresponding to each configuration is presented in Table 4.8. It should be noted from Fig. 4.12 that the linear nature continues till a certain value of radial distance is reached and then progresses to the

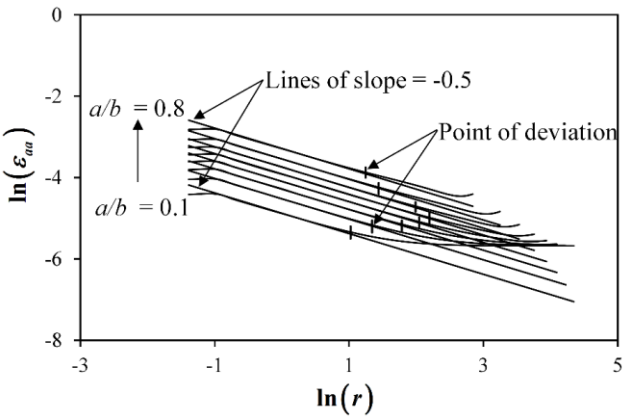

Figure 4.12 Variation of $\ln(\varepsilon_{aa})$ with $\ln(r)$ for the centre cracked orthotropic laminates with different values of a/b

non-linear trend for all values of a/b as expected from the present theoretical formulation (section 3.4).

Table 4.8 Variation of the r_{max}/b with a/b of the center-cracked orthotropic laminates

a/b	r_{max} (mm)	r_{max}/b
0.1	2.78	0.0556
0.2	5.16	0.1032
0.3	7.62	0.1524
0.4	10.03	0.2006
0.5	12.11	0.2422
0.6	9.14	0.1828
0.7	5.99	0.1198
0.8	3.47	0.0694

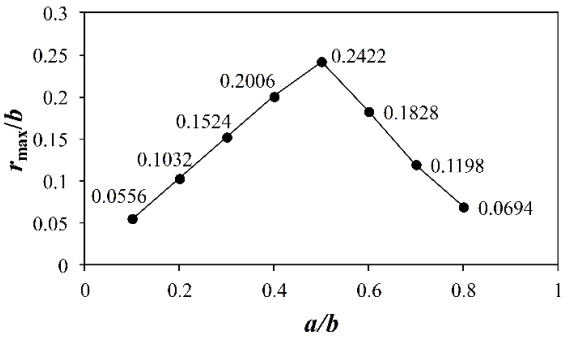

Figure 4.13 Variation of r_{max}/b with a/b for the center cracked orthotropic laminate

A plot of the variation of r_{max}/b with a/b is presented in Fig. 4.13 to observe the effect of a/b on r_{max}. It can be observed from Fig. 4.13 that as a/b increases, the r_{max} value increases initially, reaches a maximum and then decreases. It may be noteworthy that similar results were also reported by Sarangi et al. [61] and Chona et al. [80] for cracked configurations made of isotropic materials. Based on the previous works of other researchers [61, 80] it may be seen that at low values of a/b, the r_{max} value increases with the increase in a/b as the crack length is the controlling parameter due to absence of boundary effect on the r_{max} This is the case for a/b upto 0.5. As a/b is further increased, r_{max} decreases with the increase in a/b which implies that the net ligament length $(b-a)$ is the controlling parameter for changes in r_{max}. This explains the bell-shaped curve in Fig. 4.13. Initially, at low values of a/b when there is insignificant boundary effects, the changes in r_{max} is controlled by changes in a/b. However, as the crack tip proceeds further towards the outer boundaries, the net ligament length decreases and a point is reached when the controlling parameter is shifted from the crack length to the net ligament, $b-a$.

4.2.2 Double edge cracked orthotropic laminate

The second example considered in this section is a double edge cracked panel (DECP) made of $[0_2/90]_{2S}$ glass-epoxy, subjected to uniform tensile stress (Fig. 4.14(a)). The geometric parameters of the double edge cracked panels considered in this section along with the loads applied are provided in Table 4.9. The same values of α, β, θ and ϕ are obtained for the DECP plates as that for the centre cracked plates as 0.9684, 1.4496 , 54.27° and 68.01° respectively for the same effective laminate properties in Table 4.1. In this example, the r_{max} values for different values of a/b ranging from 0.1 to 0.7 in steps of 0.1 under plane stress conditions have been estimated using the approach described in the previous example. A typical mesh that has been employed in the present example is shown in Fig. 4.14(b).

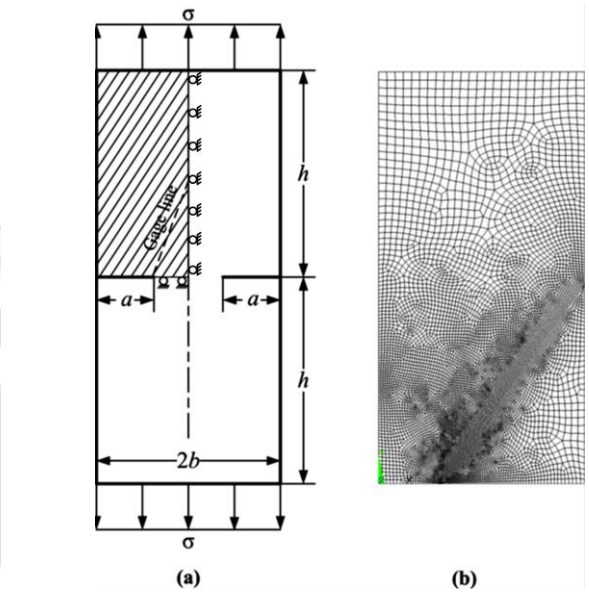

Figure 4.14 (a) An orthotropic DECP with FEA domain (shaded) (b) a typical finite element mesh for the DECP

Table 4.9 Geometric and loading parameters orthotropic laminates with other mode I configurations

Section	Description	b (mm)	a/b	h/b	t (mm)	σ (MPa)
4.2.2	DECP	50	0.1-0.7	2	1	100
4.2.3	ECCP		0.4			

Following the procedure described in section 3.5, plots of variation of $\ln(\varepsilon_{aa})$ versus $\ln(r)$ for different a/b ratios have been presented in Fig. 4.15. It could be seen from Fig. 4.15 that in each case, there is a definite linear portion followed by non-linear portion as predicted by the theory. The r_{max} values are extracted from Fig. 4.15 and tabulated in Table 4.10. It could be pointed out that each crack on either side can be increased to a maximum length of b.

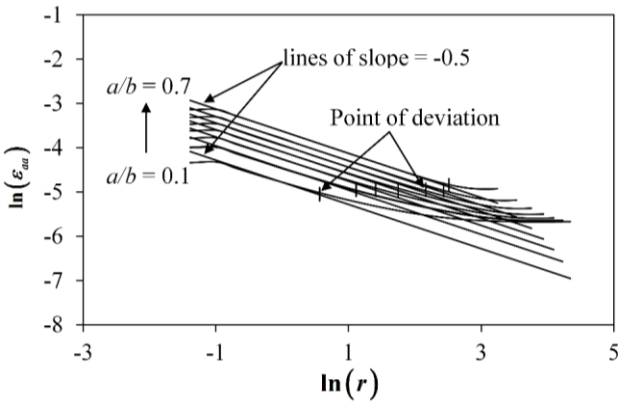

Figure 4.15 Variation of $\ln(\varepsilon_{aa})$ with $\ln(r)$ for different values of a/b for the orthotropic DECP

Table 4.10 Variation of the r_{max}/b with a/b for the orthotropic DECP

a/b	r_{max} (mm)	r_{max}/b
0.1	1.76	0.0351
0.2	3.05	0.0609
0.3	4.09	0.0818
0.4	5.74	0.1148
0.5	8.71	0.1742
0.6	11.38	0.2277
0.7	12.34	0.2468

Variation of r_{max}/b as a function of a/b is presented in Fig. 4.16. It is observed from Fig. 4.16 that the value of r_{max} increases with the increase in a/b for the DECP. It may be due to the fact that with the increase in a/b, the crack tips in a double edge cracked configuration move away from their respective boundaries (Fig. 4.14(a)) and hence crack length is the only controlling parameter for variations in r_{max} values. Therefore, it may be pointed out that in a double edge cracked plate the domain boundries exercise no control over the r_{max} values.

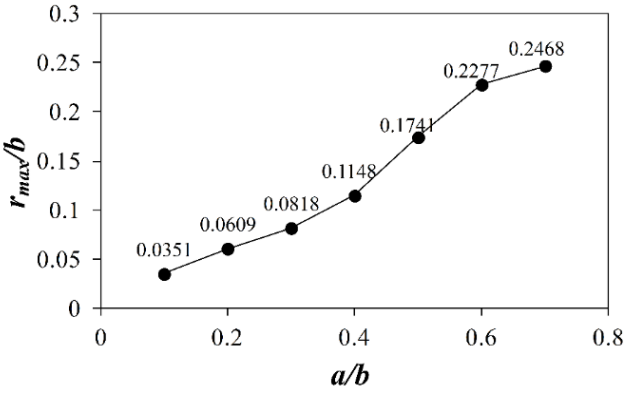

Figure 4.16 Variation of r_{max}/b with a/b for the orthotropic DECP

4.2.3 Eccentric center cracked orthotropic laminate

The purpose of this example is to establish that the proposed technique for estimation of r_{max} can be used to determine r_{max} of complicated configurations like the eccentric centre cracked (ECCP) $[0_2/90]_{2S}$ glass-epoxy plate subjected to uniform tensile stress (Fig. 4.17(a)). Here the eccentricity ratio (e/b) is only varied from 2.5% to 15%, keeping constant crack length and width of the plate. The geometric parameters and loads applied considered in this example are provided in Table 4.9. The parameters $\alpha = 0.9684$, $\beta = 1.4496$, $\theta = 54.27°$ (Fig. 4.1) and $\phi = 68.01°$ determined from the material properties in Table 4.1 are same as for the other mode I configurations and are employed in the finite element analysis. Figure 4.17(b) shows a typical mesh of eccentric cracked plate which is employed in finite element analysis.

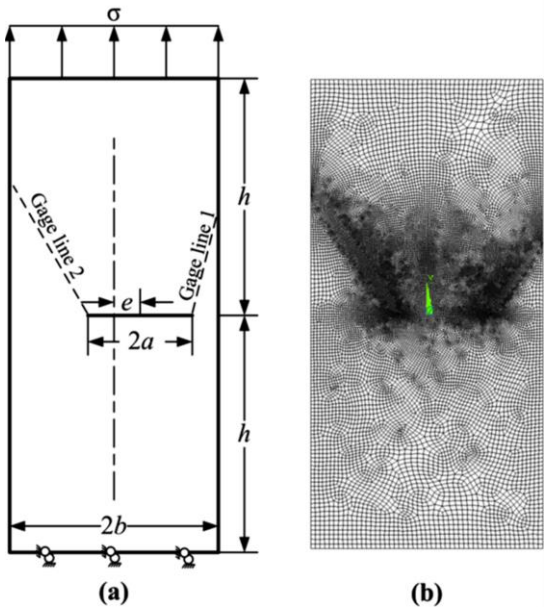

Figure 4.17 (a) An orthotropic ECCP with FEA domain (b) a typical finite element mesh for the ECCP

Figures 4.18 and 4.19 show plots of $\ln(\varepsilon_{aa})$ versus $\ln(r)$ obtained using the values at the right crack tip and left crack tip for an eccentricity ratio of 15%. Similar trend has been obtained for the other values of eccentricity ratio as well. The r_{max} values obtained at both the tips are different and are presented in Table 4.11 for different e/b. Variation of r_{max}/b as a function of e/b is presented in Fig. 4.20. It can be observed that the r_{max} values show a decreasing trend along the right gage line and an increasing one along the left gage line with the variation of e/b. This trend is as

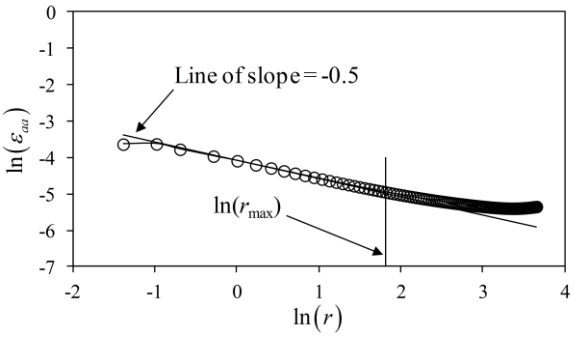

Figure 4.18 Variation of $\ln(\varepsilon_{aa})$ with $\ln(r)$ along the right gage line for 15% eccentricity ratio.

expected and is according to the explanation provided in previous examples. It may be pointed out that the increase in eccentricity ratio leads to the shifting of the right crack tip closer to the boundary and the shifting of left crack tip away from the boundary. Hence, it may be surmised that due to boundary effects the r_{max} value decreases along the right gage line whereas due to minimal boundary effects r_{max} increases along the left gage line.

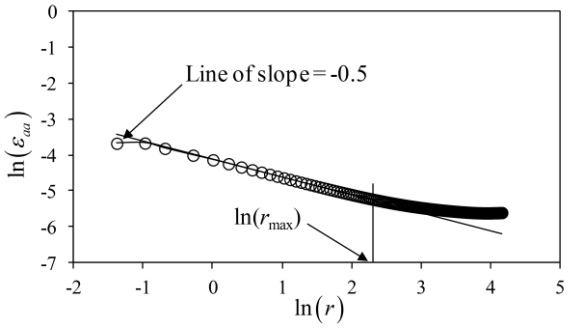

Figure 4.19 Variation of $\ln(\varepsilon_{aa})$ with $\ln(r)$ along the left gage line for 15% eccentricity ratio.

Table 4.11 Variation of the r_{max}/b with % eccentricity for the orthotropic ECCP

Eccentricity (%)	Right gage line (Gage line 1)		Left gage line (Gage line 2)	
	r_{max} (mm)	r_{max}/b	r_{max} (mm)	r_{max}/b
2.5	7.72	0.1544	8.25	0.165
5.0	7.46	0.1492	8.51	0.1702
7.5	7.20	0.144	9.00	0.18
10.0	6.94	0.1388	9.03	0.1806
12.5	6.68	0.1336	9.29	0.1858
15	6.13	0.1226	10.12	0.2024

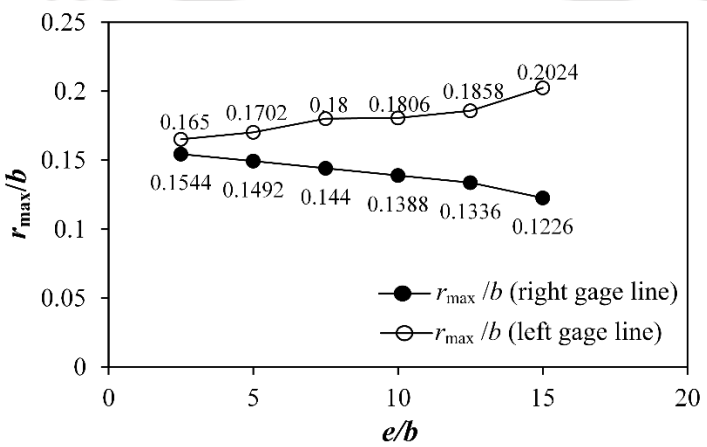

Figure 4.20 Variation of r_{max}/b with e/b along the right and the left gage line for the ECCP.

4.2.4 Numerical simulation of the proposed single strain gage technique for double ended cracked orthotropic laminates

Simulation of the proposed single strain gage technique for the determination of K_I in double ended cracked orthotropic laminates has been presented in this example. Pure mode I loading in a $[0_2/90]_{2S}$ glass epoxy laminate with center crack (Fig. 4.9(a)) having $a/b=0.4$ is considered. The effective properties of the laminate are same as listed in Table 4.1 and the geometric and loading details of this problem domain are presented in Table 4.6. For this configuration, the analytical expression for K_I is [13]

$$K_I = Y_I\left(a/b\right)\sigma\sqrt{a} \tag{4.5}$$

where σ is the applied stress, a is the crack length and Y_I is the specimen geometric factor given by

$$Y_I = 1.77 + 0.227\left(a/b\right) - 0.510\left(a/b\right)^2 - 2.699\left(a/b\right)^3 \tag{4.6}$$

which forms the reference solution. For this configuration, at $\sigma = 100\,\text{MPa}$ the reference value of K_I using Eq. (4.5) is found to be $K_I = 27.6\ \text{MPa}\sqrt{\text{m}}$. For the determination of SIF using the proposed method, the gage must to be located along $\theta = 54.27^\circ$ and oriented at $\phi = 68.01^\circ$ for this particular configuration. The recommended value of $r_{\max}$ for this configuration is found to be 10.03 mm (Table 4.7). Considering the plate thickness as 1 mm, the optimal radial location for a strain gage is any location that satisfies the equation

$$1\,\text{mm} < r < 10.03\,\text{mm} \tag{4.7}$$

Any gage location beyond $r_{\max}$ is a non-optimal location and can lead to highly erroneous measurement of SIF. Strain values are sampled at four points, two within the $r_{\max}$ and two outside the $r_{\max}$ and the simulated SIF at those locations obtained using Eqs. (3.58) and (3.13) are presented in Table 4.12. The percentage relative error in K_I measured at those locations is computed using Eq. (4.4).

Table 4.12 Simulated mode I SIFs at the optimal and non-optimal strain gage locations for the center cracked orthotropic laminate $\left(r_{\max}=10.03\,\text{mm}\right)$

$r\,(\text{mm})$	ε_{aa}	$K_I\left(\text{MPa}\sqrt{\text{m}}\right)$	% Relative Error
2.01	1.18E-02	28.11	1.8
6.01	6.92E-03	28.2	2.1
12.76	5.06E-03	31.3	13.4
20.6	4.34E-03	33.3	20.65

It can be observed from results of Table 4.12 that accurate values of mode I SIFs (order of error 2 %) can be measured at optimal locations that are well within the $r_{\max}$ value. Moreover, the results of Table 4.12 also clearly demonstrate that the error in measured K_I is as high as 20.65% when the gage locations are outside the $r_{\max}$ value. These results substantiate that the present technique of determination of K_I using a single strain gage can be used for accurate determination of K_I even for double ended cracked orthotropic composite specimens if the gages are placed within the optimal locations.

4.2.5 Sensitivity analysis

Since the singe strain gage technique for determination of K_I holds good for a particular angular location (θ) and orientation (ϕ) of the strain gage, it is important to understand the sensitivity of measured K_I to the angular orientation. While the angular location (or gage line) could be drawn most accurately, there may be possibility of little deviation in ϕ as pasting of strain gage is done manually. Therefore, the objective of this example is to assess (via sensitivity analysis) the effect of the deviation in strain gage orientation angle (ϕ) that may arise while pasting the strain gages on the measured SIF. For this purpose, a $\left[0_2/90\right]_{2S}$ centre cracked laminate with $a/b=0.4$ and geometric and loading details mentioned in Table 4.6 is considered (Fig. 4.9 (a)). Corresponding to the stiffness properties in Table 4.1, the values of values of α,β,θ and ϕ are obtained as 0.9684, 1.4496 , 54.27° and 68.01° respectively . For this configuration, the value of $r_{\max}$ is found to be 10.03 mm (Table 4.7). To carry out the sensitivity analysis, the angle ϕ has been varied by $\pm 0.5^{\circ}$ at an optimal gage

location of $r = 6.01\text{mm}$ (Table 4.12). For no variation of the angular position ϕ the percentage relative error in computed K_I is found to be 2.1% (Table 4.12). The detailed analysis of changes in K_I for 0.5° variation in ϕ has been shown in Table 4.13.

Table 4.13 Sensitivity analysis for a variation of 0.5° in the gage orientation ϕ

Sl. No.	$r(\text{mm})$	ϕ	Deviation	$K_I\left(\text{MPa}\sqrt{\text{m}}\right)$	% Relative error
1	6.01	67.51°	-0.5°	28.43	3.01
2	6.01	68.51°	$+0.5^\circ$	29.01	4.91

It is interesting to note from the results of Tables 4.13 that though the percentage relative error in K_I for deviation in gage orientation is higher than the K_I estimated (Table 4.12) without gage orientation deviation, the difference between the two is not abruptly high. In general, strain gage manufactures also provide a greater angular deviation than considered here as a tolerance for obtaining accurate strain measurements. Precluding the chances of such available tolerance, it may be concluded that though a deviation of 0.5° in the angle may be viable, it would be judicious not to allow for such deviations since during experiments various factors other than strain gage pasting may have direct or indirect impact on the output.

4.3 Summary

The proposed single strain gage technique for determination of mode I SIF of orthotropic laminates have been simulated in this chapter for different mode I configurations (edge-cracked plate, center cracked plate, double edge cracked plate and eccentric center cracked plate) employing the proposed optimal gage locations for each configuration. The $r_{\max}$ values which help is ascertaining the optimal gage location $\left(r_{\min}(=\text{plate thickness}) < r < r_{\max}\right)$ of each mode I configurations have been obtained employing the methodology proposed in section 3.5. The dependence of the $r_{\max}$ values on the a/b ratio has also been studied. The following observations were made as a follow-up of the numerical analyses.

- The finite element strain variations for the mode I configurations follow the trend as predicted by theory.

- Results obtained show that the r_{max} value increases initially with increase in a/b ratio, reaches a maximum and then decreases. At low values of a/b ratio, due to negligible boundary effect, crack length, (a) is the controlling parameter for r_{max}. But with increase in a/b ratio, the net ligament length decreases and at a particular point due to boundary effects, the controlling parameter shifts from the crack length to the net ligament length, $(b-a)$.
- Numerical simulations of the proposed single strain gage technique for estimation of K_I of orthotropic materials have been presented for both single and double ended cracked orthotropic laminate configurations. The results obtained clearly ensure that using the proposed technique very accurate values of K_I can be obtained for single ended and double ended cracked orthotropic composite specimens using a single strain gage provided the gages are placed within the optimal locations according to Eq. (3.59).

Chapter 5

Determination of r_{max} and numerical simulation of mixed mode experiments in orthotropic materials

This chapter presents the numerical simulation of determination of mixed mode SIFs (K_I / K_{II}) of orthotropic laminates using the proposed strain gage technique detailed in section 3.6. Based on formulations presented in section 3.7, determination of r_{max} or optimal gage locations using the finite element based method of a slant edge cracked orthotropic laminate for accurate measurement of $K_{I,II}$ is also presented here. Additionally, the effect of crack length to width ratio on the r_{max} has been investigated and presented in this chapter. Two types of orthotropic laminate specimens viz. $[0_2/90]_{2S}$ glass-epoxy and $[90_2/0]_{10S}$ carbon-epoxy have been considered to simulate the determination of mixed mode (I/II) SIFs of the slant edge cracked plate. Finite element analyses in all the examples are carried out in ANSYS® using eight noded isoparametric quadrilateral elements (Q8) and the square root singularity at the crack tips is modelled using collapsed quarter point elements (Q8 QPEs) (section 3.9).

5.1 $[0_2/90]_{2S}$ Glass-epoxy laminate with slant edge cracked configuration

A $[0_2/90]_{2S}$ glass-epoxy slant edge-cracked plate (SECP) subjected to uniform tensile stress as shown in Fig. 5.1(a) with effective laminate properties, geometric and loading details as shown in Table 5.1 has been considered here to numerically simulate the proposed approach for the determination of mixed mode SIFs of orthotropic laminates using strain gages (section 3.6). Corresponding to these properties, the values of values of α, β, θ and ϕ obtained as 0.9684, 1.4496 , 54.27° and 68.01° respectively which are used in the finite element analysis.

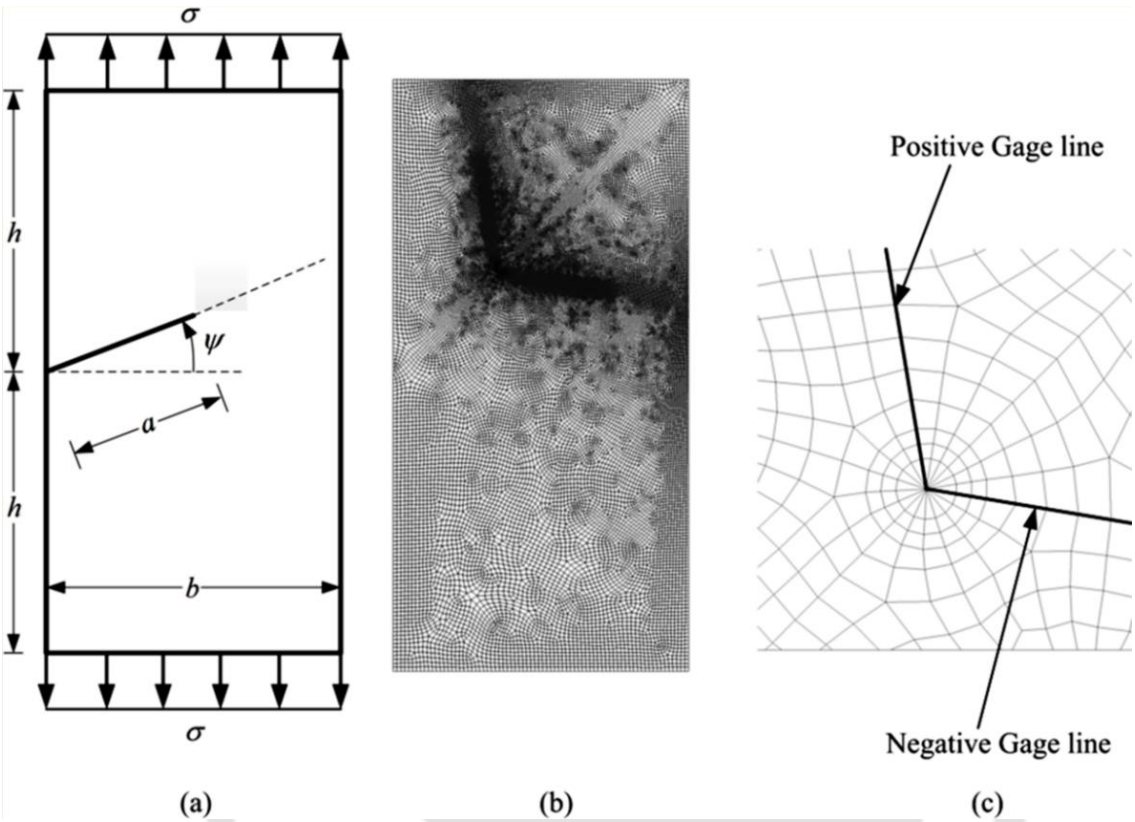

Figure 5.1 (a) Geometry of the $[0_2/90]_{2S}$ glass-epoxy SECP under uniform tension (b) typical FE mesh used (c) enlarged view of the crack tip region

Table 5.1 Geometric, loading and material parameters for the $[0_2/90]_{2S}$ glass-epoxy SECP specimens

Section	b (mm)	a/b	h/b	ν_{LT}	E_L (GPa)	E_T (GPa)	G_{LT} (GPa)	σ (GPa)	t (mm)
5.1.1	150	0.5	1	0.163	33.3	24.6	5.2	1	1
5.1.2		0.2-0.7							
5.1.3		0.5							
5.1.4		0.5							

5.1.1 Determination of r_{max} for the $[0_2/90]_{2S}$ Glass-epoxy SECP

The proposed procedure for determination of r_{max} as discussed in section 3.7 has been employed for the analysis. For this purpose, a SECP specimen as shown in Fig. 5.1(a) with $\psi = 45^{\circ}$ and $a/b = 0.5$ has been considered. Figures 5.1(b) and 5.1(c) show a typical finite element mesh with an enlarged view of the mesh around the crack tip respectively employed in the present investigation.

The meshes are so designed such that the consecutive nodes of several elements enforced along the positive and negative gage lines (Fig. 3.9) are at equal distances from the crack tip. This is essential because the proposed approach calls for strain gages to be pasted at equal distances measured from the crack tip along the positive and negative gage line respectively. For FEA, the bottom edge of the plate is completely constrained and a uniform tensile stress is applied on the top edge of the plate. Following the procedure described in section 3.7, the strain values ε_{aa} and ε_{bb} of the nodes along the positive and negative gage lines are noted from the FE results. Figures 5.2(a) and 5.2(b) show the plots of $\{(\varepsilon_{aa}+\varepsilon_{bb})\sqrt{r}\}/I_1$ and $\{(\varepsilon_{aa}-\varepsilon_{bb})\sqrt{r}\}/I_2$ versus radial distance (r) with their respective straight line fits for the $[0_2/90]_{2S}$ glass-epoxy SECP with $a/b = 0.5$.

The values of the coefficients A_0, C_0 and C_1 for the best fit plots along with the correlation coefficient (R^2) are also shown in Figs. 5.2(a) and 5.2(b) respectively. It may be observed that the parameters $\{(\varepsilon_{aa}+\varepsilon_{bb})\sqrt{r}\}/I_1$ and $\{(\varepsilon_{aa}-\varepsilon_{bb})\sqrt{r}\}/I_2$ start to deviate from their respective best fit plots from certain radial points as seen in Figs. 5.2(a) and (b). This indicates that accurate representation of $\{(\varepsilon_{aa}+\varepsilon_{bb})\sqrt{r}\}/I_1$ and $\{(\varepsilon_{aa}-\varepsilon_{bb})\sqrt{r}\}/I_2$ beyond those points require more number of coefficients other than A_0, C_0 and C_1 in the respective expressions (Eq. (3.80) and Eq.(3.81)). Conversely, these points of deviation (Figs. 5.2(a) and (b)) also indicate that these are the maximum radial distances from the crack tip upto which the best-fit can be obtained by satisfying all the conditions as mentioned in section 3.6.

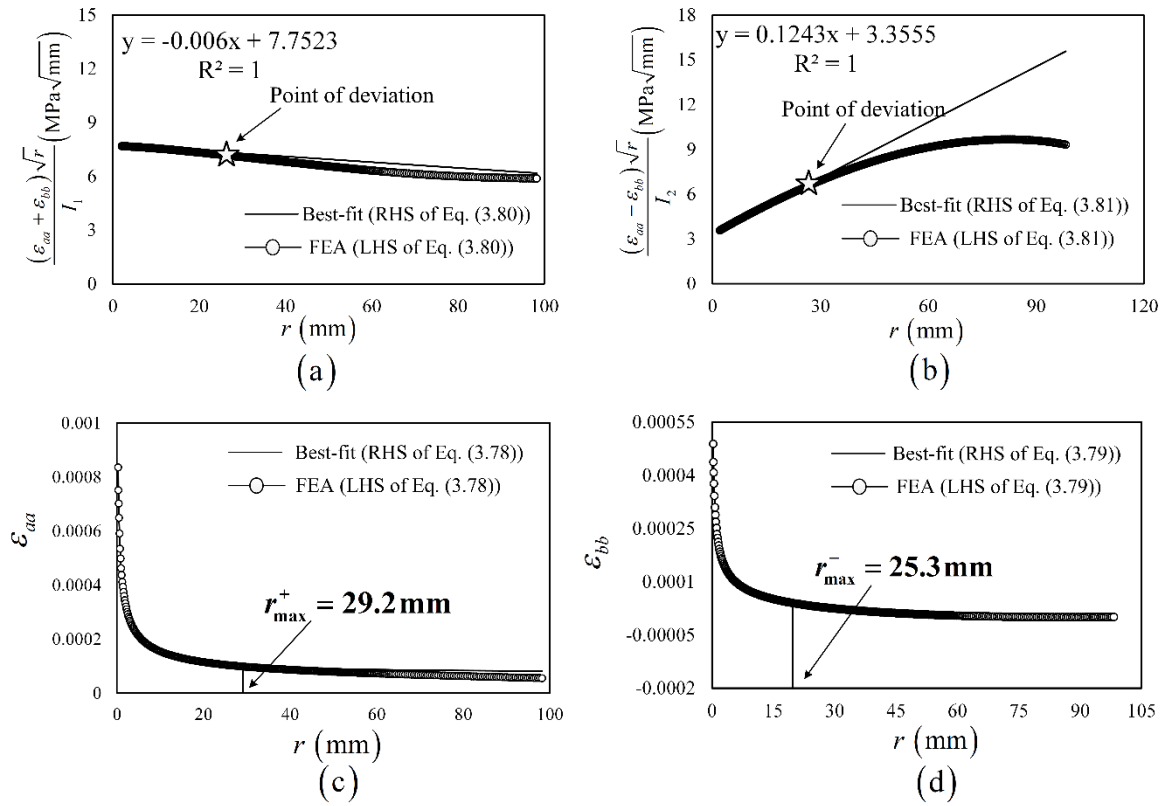

Figure 5.2 Plots for $[0_2/90]_{2S}$ glass-epoxy SECP with $a/b=0.5$ (a) Determination of A_0, (b) Determination of C_0 and C_1, (c) Determination of r^{+}_{max} and (d) Determination of r^{-}_{max}

Using the values of the best-fit coefficients A_0, C_0 and C_1, the strains ε_{aa} and ε_{bb} can be calculated at any point along the positive and negative gage line by employing Eq. (3.78) and Eq. (3.79) respectively. At the same time ε_{aa} and ε_{bb} can be obtained directly from the FE solutions. Figures 5.2(c) and 5.2(d) show the plot of the comparison of the strain values ε_{aa} and ε_{bb} along the positive and negative gage lines obtained from the FEA and those obtained using Eqs. (3.78) and (3.79) for $[0_2/90]_{2S}$ glass-epoxy SECP with $a/b=0.5$.

As discussed in section 3.7, the RHS of Eqs. (3.78) and (3.79) cannot represent the strain field accurately for the entire gage length of the positive and negative gage lines respectively as they contain only a fewer number of coefficients. As a consequence, the strain values deviate from their corresponding FE solutions of the LHS of Eqs. (3.78) and (3.79) from certain radial points which gives the value of r^{+}_{max} i.e. the maximum permissible radial distance for strain gages along the positive gage line and r^{-}_{max} i.e. the maximum permissible

radial distance for strain gages along the negative gage line. The radii corresponding to the points of deviation along the positive gage line $\left(r_{\max}^{+}=29.2\,\text{mm}\right)$ and along the negative gage line $\left(r_{\max}^{-}=25.3\,\text{mm}\right)$ for the $\left[0_2/90\right]_{2S}$ glass-epoxy laminate as shown in Figs. 5.2(c) and (d) respectively clearly represent the extent of the three parameter strain series along the positive and negative gage lines and is different along both the gage lines as expected.

As stated in section 3.7, the point of deviations in Fig. 5.2 (c) and (d) i.e. $r_{\max}^{+}$ and $r_{\max}^{-}$ are the radial distances at which the percent relative error between the LHS and RHS quantities of Eqs. (3.78) and (3.79) is less than or equal to 1%. Since the values of $r_{\max}^{+}$ and $r_{\max}^{-}$ i.e. the extent of the three parameter zone are different along the positive and negative gage lines, it is clear that the maximum permissible radial distance satisfying all the conditions on both the gage lines is the minimum of $r_{\max}^{+}$ and $r_{\max}^{-}$ i.e. 25.3 mm within which the strain gages should be pasted along both the gage lines for accurate estimation of mixed mode SIFs since all the equations (Eqs. (3.78 – 3.81)) are valid in this region. Thus, the $r_{\max}$ for the $\left[0_2/90\right]_{2s}$ glass-epoxy SECP configuration with $a/b=0.5$ is $r_{\max}=\min\left[r_{\max}^{+},r_{\max}^{-}\right]=25.3\,\text{mm}$.

Convergence study for $r_{\max}$ considering meshes with three gradations of refinement (coarse mesh with 2359 elements, medium mesh with 8294 elements and refined mesh with 32163 elements) is shown in Fig. 5.3 for the $\left[0_2/90\right]_{2S}$ glass-epoxy SECP with $a/b=0.5$. Plots showing determination of $r_{\max}$ of the coarser and medium meshes are shown in Figs. 5.4 and 5.5 respectively. The finer mesh results are already presented in Fig. 5.2. The corresponding numerical values of $r_{\max}$ are presented in Table 5.2. It may be observed from Table 5.2 that as the meshes are refined, $r_{\max}$ value converges. No changes in $r_{\max}$ noticed with further refinement of the meshes.

Table 5.2 Convergence of the $r_{\max}$ with mesh refinement for the $\left[0_2/90\right]_{2S}$ glass-epoxy SECP with $a/b=0.5$

Mesh	$r_{\max}\,(\text{mm})$
Coarse	30.3
Medium	26.2
Fine	25.3

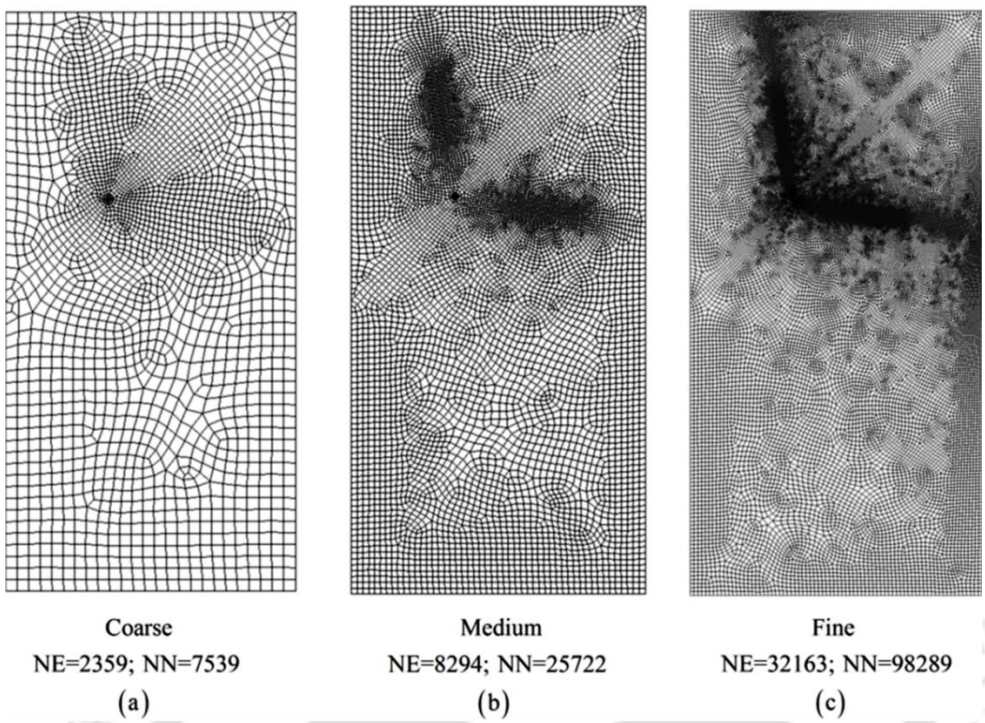

Figure 5.3 Different finite element meshes used for the convergence study of r_{max} of the glass-epoxy SECP specimen with $a/b = 0.5$

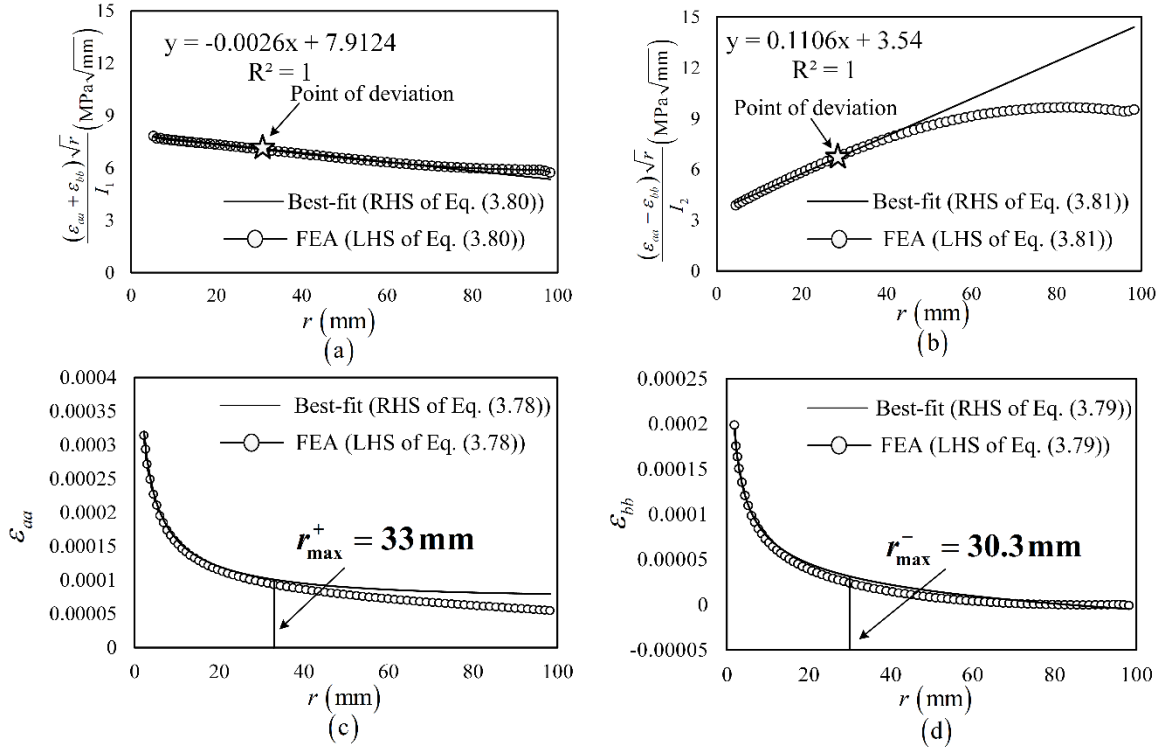

Figure 5.4 Plots for $[0_2/90]_{2S}$ glass-epoxy SECP with $a/b = 0.5$ (coarse mesh) (a) Determination of A_0, (b) Determination of C_0 and C_1, (c) Determination of r^+_{max} and (d) Determination of r^-_{max}

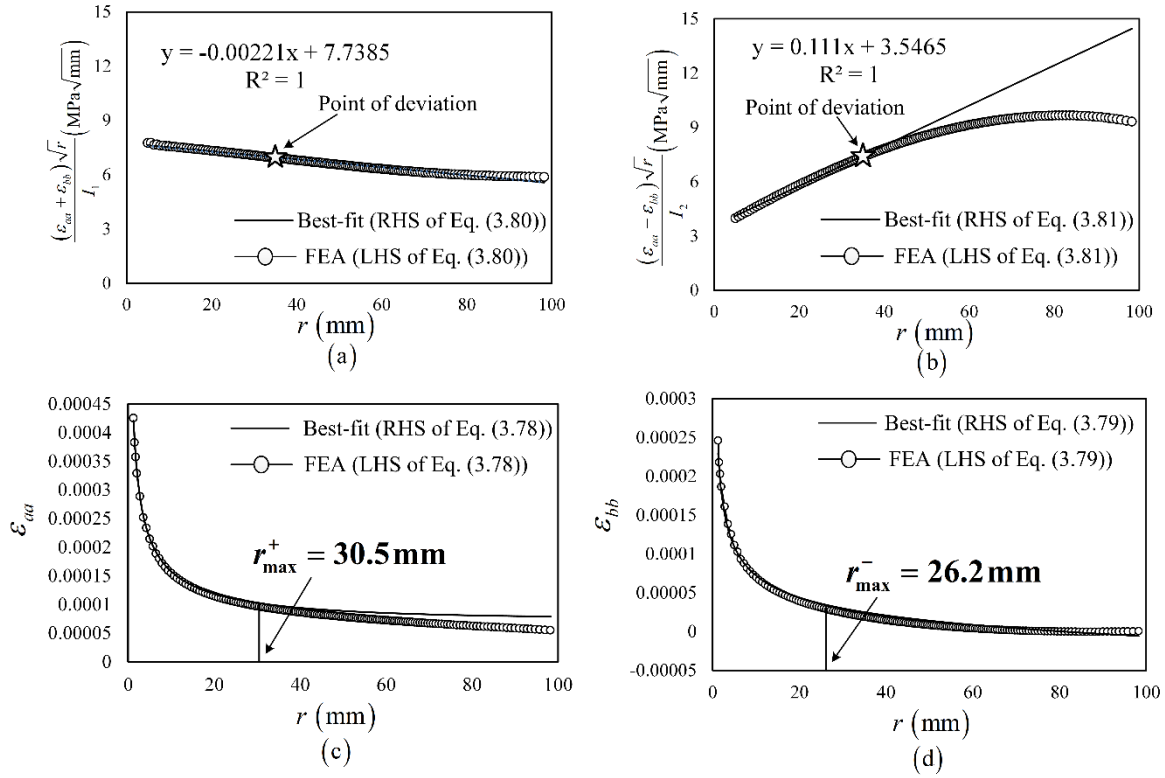

Figure 5.5 Plots for $[0_2/90]_{2S}$ glass-epoxy SECP with $a/b=0.5$ (medium mesh) (a) Determination of A_0, (b) Determination of C_0 and C_1, (c) Determination of r_{max}^{+} and (d) Determination of r_{max}^{-}

5.1.2 Influence of a/b ratio and crack inclination angle (ψ) on r_{max}

The effect of a/b ratio on the r_{max} values has been studied in this section for the $[0_2/90]_{2S}$ glass epoxy SECP with properties mentioned in Table 5.1 for different values of crack inclination angle, ψ. A SECP with crack inclination angles of $\psi = 15°$, 30°, 45°, 60° and 75° (Fig. 5.1(a)) and a/b ratio ranging from 0.2 to 0.7 in steps of 0.1 is considered for the study. Other parameters of the cracked plate are shown in Table 5.1. Following the procedure described in section 3.7 and 5.1.1, the values of r_{max} for all values of a/b is determined. Figures 5.6 – 5.10 show all the plots pertaining to r_{max} determination for the SECP with $\psi = 45^{\circ}$ made of $[0_2/90]_{2S}$ glass epoxy laminate with a/b ratio of 0.2, 0.3, 0.4, 0.6 and 0.7 respectively. The results of $a/b=0.5$ have already been presented in section 5.1.1.

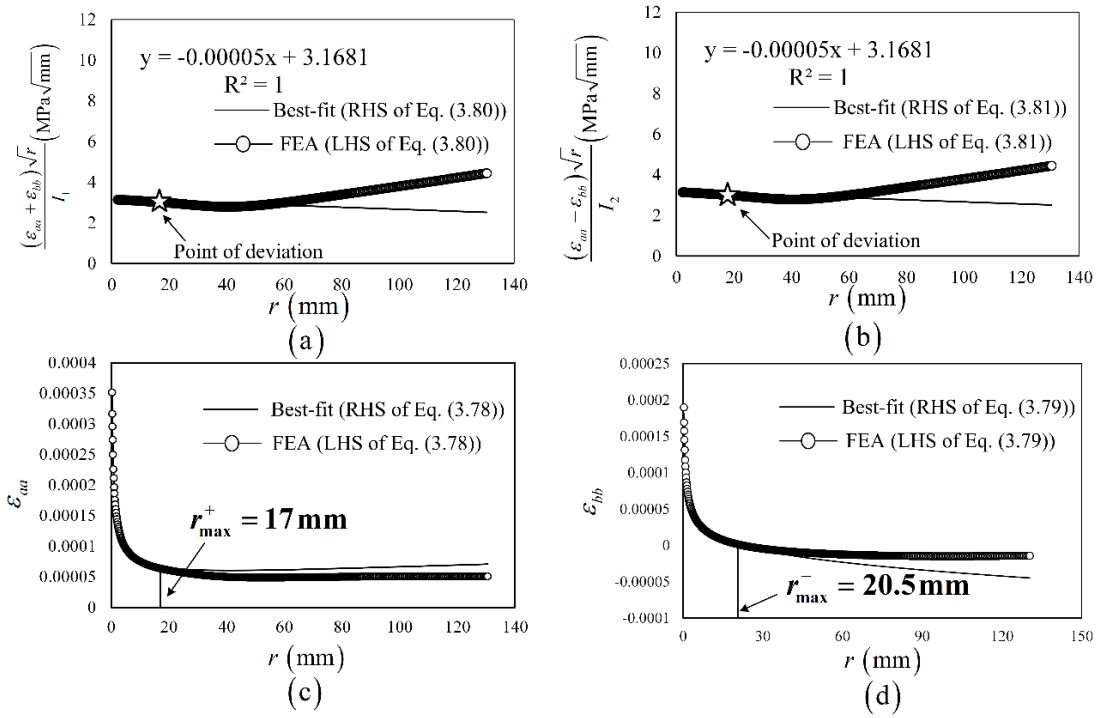

Figure 5.6 Plots for $[0_2/90]_{2S}$ glass-epoxy SECP with $a/b = 0.2$ (a) Determination of A_0, (b) Determination of C_0 and C_1, (c) Determination of r^+_{max} and (d) Determination of r^-_{max}

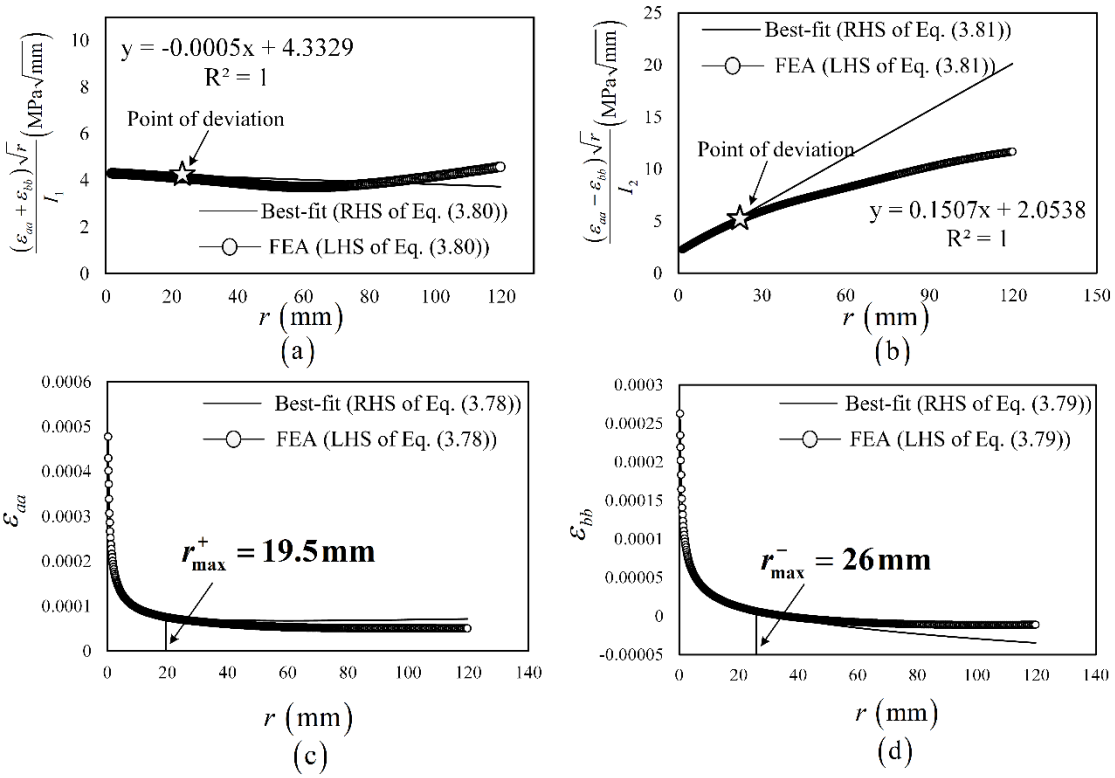

Figure 5.7 Plots for $[0_2/90]_{2S}$ glass-epoxy SECP with $a/b = 0.3$ (a) Determination of A_0, (b) Determination of C_0 and C_1, (c) Determination of r^+_{max} and (d) Determination of r^-_{max}

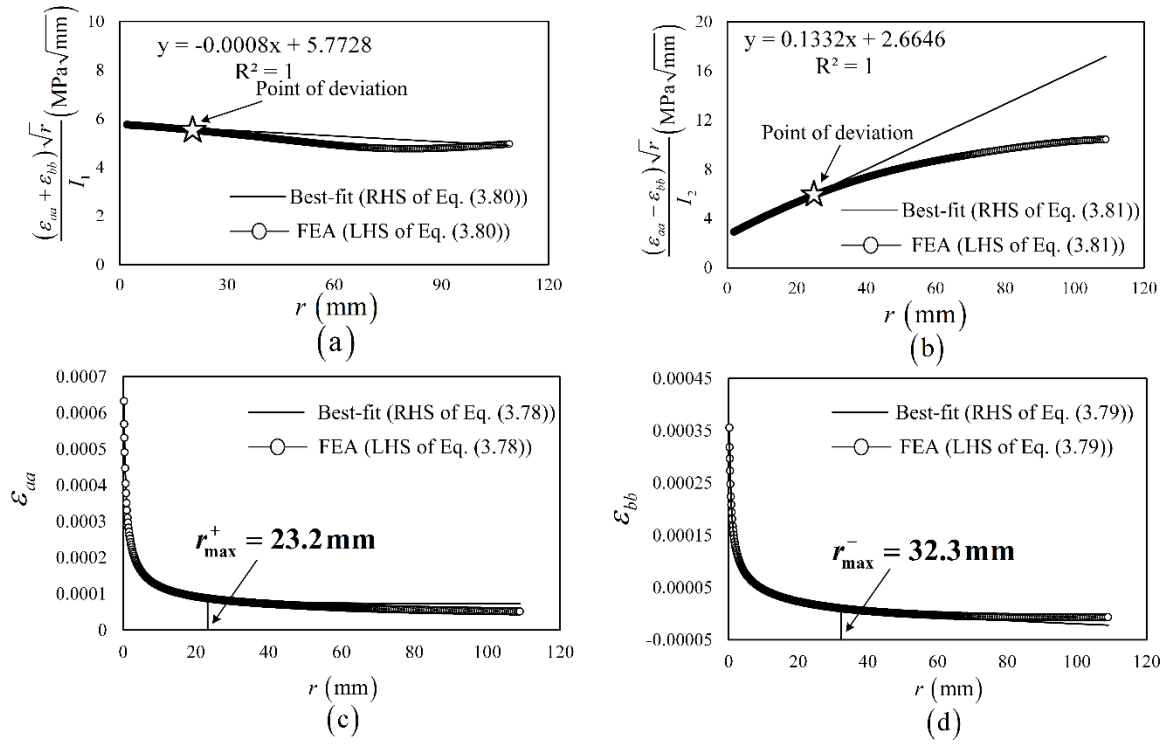

Figure 5.8 Plots for $[0_2/90]_{2S}$ glass-epoxy SECP with $a/b = 0.4$ (a) Determination of A_0, (b) Determination of C_0 and C_1, (c) Determination of r_{max}^{+} and (d) Determination of r_{max}^{-}

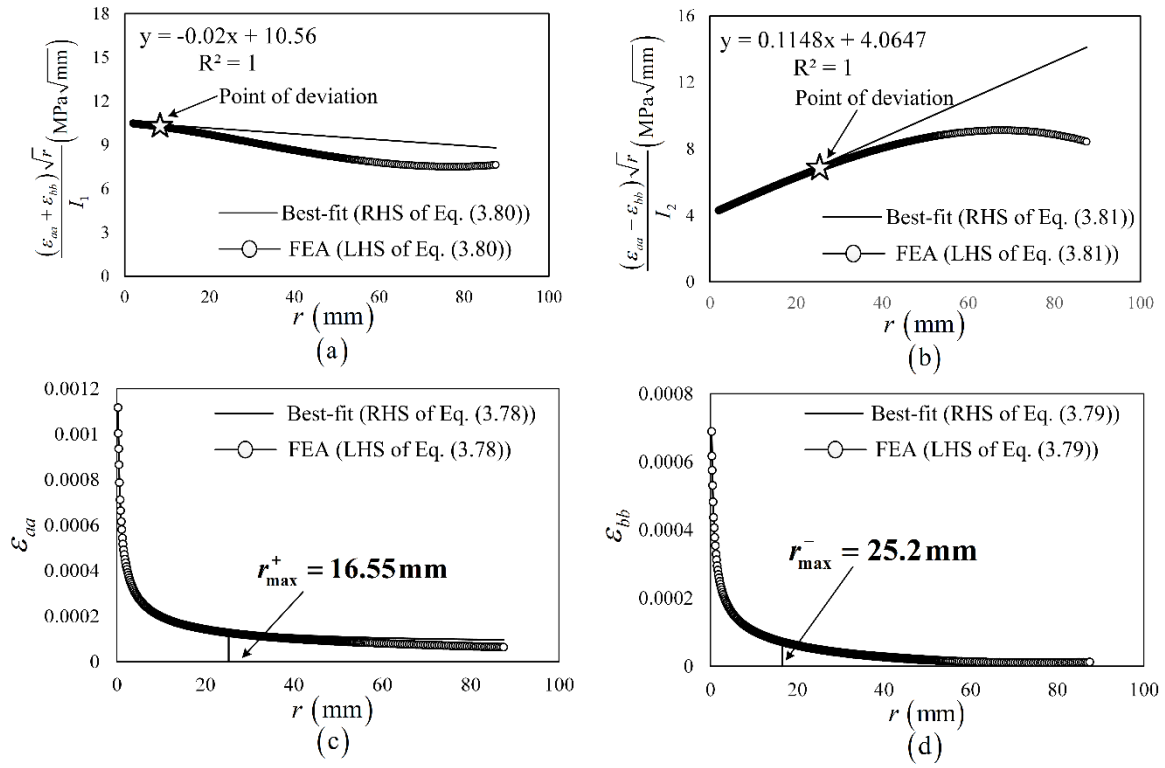

Figure 5.9 Plots for $[0_2/90]_{2S}$ glass-epoxy SECP with $a/b = 0.6$ (a) Determination of A_0, (b) Determination of C_0 and C_1, (c) Determination of r_{max}^{+} and (d) Determination of r_{max}^{-}

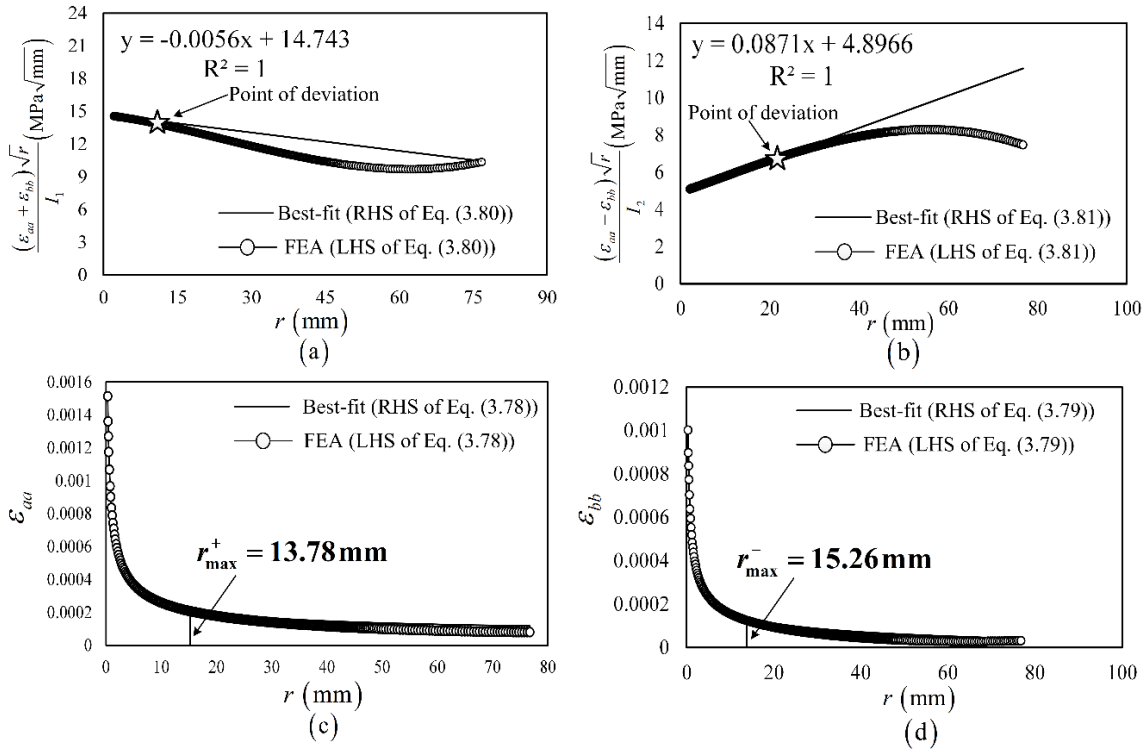

Figure 5.10 Plots for $[0_2/90]_{2S}$ glass-epoxy SECP with $a/b = 0.7$ (a) Determination of A_0, (b) Determination of C_0 and C_1, (c) Determination of r_{max}^{+} and (d) Determination of r_{max}^{-}

Table 5.3 shows the r_{max} values for the SECP with different a/b ratios for the $[0_2/90]_{2S}$ glass epoxy SECP for a crack inclination angle of $\psi = 45^{\circ}$. The variation of non-dimensional r_{max}/b is potted as a function of a/b ratio for each ψ in Fig. 5.11 (a). Interestingly, the variation of r_{max}/b with a/b follows the trend similar to that observed for mode I configurations (Chapter 4). For each value of ψ, the r_{max} increases with increasing a/b, reaches a maximum and decreases as the crack tip approaches boundary i.e. at higher values of a/b. This may be attributed to the fact that parameters controlling the variation of r_{max} like the number of terms in the strain series representation or the boundary effects exercise the same influence be it a mode I or a mixed mode configuration. At low values of a/b when

Table 5.3 Variation of the r_{max}/b with a/b of the $[0_2/90]_{2S}$ glass epoxy SECP for $\psi = 45^{\circ}$

a/b	r_{max} (mm)	r_{max}/b
0.2	17	0.113
0.3	19.5	0.13
0.4	23.2	0.155
0.5	25.3	0.195
0.6	16.6	0.168
0.7	13.8	0.092

there is negligible or minimal boundary influence, the crack length is the only parameter that influences the r_{max} along the gage lines and therefore r_{max} increases with increase in crack length. However, as the crack length increases, a point is reached where the boundary effects starts increasing which in turn have an impact on the r_{max} along the gage lines and the r_{max} starts decreasing with further increase in crack length.

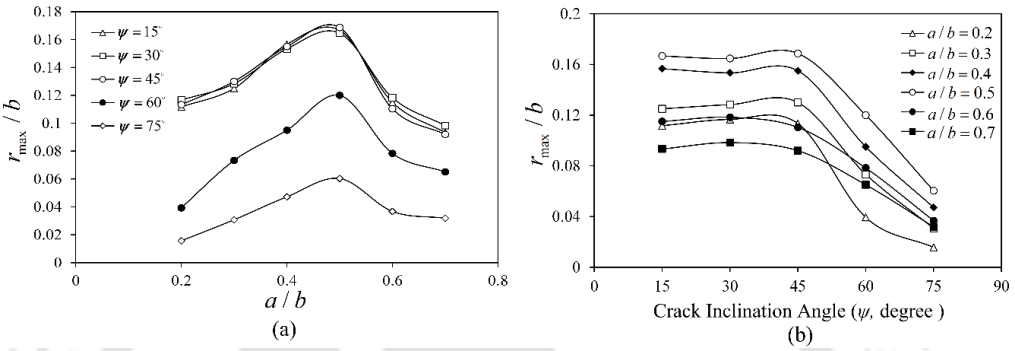

Figure 5.11 (a) Variation of r_{max}/b as a function of a/b for ψ = 15°, 30°, 45°, 60° and 75° (b) Variation of r_{max}/b as a function of ψ for different a/b for the $[0_2/90]_{2S}$ glass-epoxy SECP

Figure 5.11 (b) shows the variation in non-dimensional r_{max}/b as a function of crack inclination angle (ψ) for each a/b ratio for the $[0_2/90]_{2S}$ glass epoxy SECP. It may be observed that for a particular a/b ratio, though initially r_{max} is almost independent of ψ, it shows a gradual decline with further increase in ψ beyond 45°. For a slant edge cracked configuration, as crack inclination angle increases, the positive gage line moves towards the boundary edges. However, for a crack inclination angle variation of up to 45°, the boundary effects being negligible, there is minimal or no variation in the r_{max}. But beyond 45°, the positive gage line inches very close to the boundary and therefore, there is a decline in the r_{max} value with increase in the crack inclination angle due to probable boundary effects.

5.1.3 Numerical simulation of the proposed strain gage technique for determination of K_I, K_{II} of the $[0_2/90]_{2S}$ Glass-epoxy SECP

This section presents the numerical simulation of the proposed method for the determination of mixed mode SIFs (K_I, K_{II}) for the $[0_2/90]_{2S}$ glass-epoxy SECP with $a/b = 0.5$,

$\psi = 45^{\circ}$ and effective properties mentioned in Table 5.1. In order to numerically simulate the strain gage based determination of K_I and K_{II} following the proposed method in section 3.6 using four strain gages (two along positive and two along negative), the strain values at nodes along the gage line are considered to be strain gage readings (ε_{aa} and ε_{bb}). Using these strain values, SIFs have been calculated using Eqs. (3.80), (3.81) and (3.13). Further to understand the importance of optimal gage locations based on $r_{\max}$ on the accuracy of determination of SIFs, these strain readings (representing strain gage readings) are obtained for different combinations of strain gage placements from case 1, where the strain gages are placed at optimal locations till case 5, where all the strain gages are placed beyond the $r_{\max}$ (non-optimal locations) and different combinations in between. The optimal strain gage locations are given by the equation, $r_{\min} < r < r_{\max}$ as explained in section 3.7. All these combinations of strain gage locations from case 1 to case 5 are shown in Table 5.4. Using these strain values sampled at different combinations, mixed mode SIFs have been determined (using the procedure in section 3.6) to access the importance of proposed optimal gage locations.

Table 5.4 Simulated K_I and K_{II} at optimal and non-optimal locations for the $[0_2/90]_{2S}$ glass-epoxy SECP with $a/b = 0.5$ $(r_{\max} = 25.3\text{mm})$

Case	r_1 and r_2 (mm)	ε_{aa}	ε_{bb}	K_I $\left(\text{MPa}\sqrt{\text{mm}}\right)$	% Rel. Err.	K_{II} $\left(\text{MPa}\sqrt{\text{mm}}\right)$	% Rel. Err.
1	$r_1 = 7.03$	1.81E-04	8.82E-04	19.07	0.52	8.34	0.91
	$r_2 = 10.23$	1.53E-04	6.86E-04				
2	$r_1 = 10.23$	1.53E-04	6.86E-04	19.00	0.91	8.39	1.51
	$r_2 = 12.28$	1.41E-04	5.99E-04				
3	$r_1 = 12.28$	1.41E-04	5.99E-04	18.92	1.31	8.47	2.42
	$r_2 = 17.15$	1.22E-04	4.53E-04				
4	$r_1 = 17.15$	1.22E-04	4.53E-04	17.72	7.58	9.07	9.69
	$r_2 = 30$	9.72E-05	2.40E-05				
5	$r_1 = 30$	9.72E-05	2.40E-05	17.32	9.67	10.10	22.12
	$r_2 = 36$	9.01E-05	1.79E-05				

The values of K_I and K_{II} determined by employing the displacement extrapolation technique using nodal displacement values of the crack tip elements are found to be 19.17 $\text{MPa}\sqrt{\text{mm}}$ and 8.27 $\text{MPa}\sqrt{\text{mm}}$ for the $[0_2/90]_{2S}$ glass-epoxy SECP with $a/b=0.5$ respectively (section 3.8). These values are used as reference solutions to test the accuracy of the simulated values of K_I and K_{II} determined employing the proposed strain gage technique. Table 5.4 shows the % relative error of the numerically simulated K_I and K_{II} values with the reference solution obtained using ANSYS®. It may be seen that for gage locations at optimal gage locations, the % relative error in K_I and K_{II} is low whereas strain readings outside r_{max} (non-optimal locations) leads to fairly high error percentage in SIFs. It was also observed that even when one of the strain gages is placed outside r_{max}, keeping the other within r_{max} (along both the gage lines) the error jumps from a mere value of 2.4% to 9.7%.

5.1.4 Simulation of the proposed mixed mode strain gage technique for varying crack inclination angles

In the present section, the proposed approach for determination of $K_{I,II}$ of orthotropic laminates has been tested for variations in crack inclination angle (ψ = 15°, 30°, 45°, 60° and 75° in Fig. 5.1(a)) for the $[0_2/90]_{2S}$ glass epoxy SECP with $a/b=0.5$ and effective laminate properties mentioned in Table 5.1. Following the procedure illustrated in the previous section, K_I and K_{II} have been estimated for all values of ψ at optimal locations given by case 1 in table 5.3. The results of the analysis are presented in Table 5.5. Table 5.5 compares the numerically simulated K_I and K_{II} values with their reference values obtained using the DET

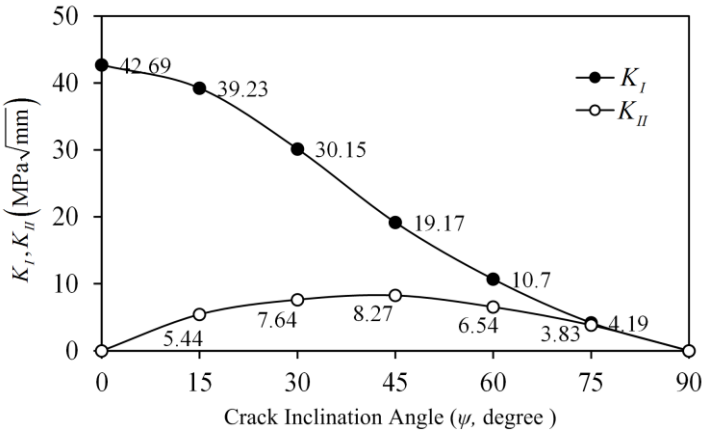

Figure 5.12 Variations of K_I and K_{II} with ψ for the $[0_2/90]_{2S}$ glass epoxy SECP with $a/b=0.5$

(as detailed in sections 3.8). It is evident from the results presented in Table 5.4 that the proposed approach promises to determine accurate values of mixed mode SIFs irrespective of crack inclination angle, provided the gages are located at optimal locations. Figure 5.12 show the variations of the mixed mode SIFs with respect to different crack angles, $\psi = 0°$–90° for the $[0_2/90]_{2S}$ glass epoxy SECP with $a/b = 0.5$ obtained using the present method. For all cases, K_I decreases steadily with increase in the crack angle, whereas K_{II} increases and reaches a maximum at $\psi = 45^{\circ}$, and then decreases. Similar observations for variations in $K_{I,II}$ with respect to crack angle were made by other researchers [41, 43 and 44].

Table 5.5 Comparison of numerically simulated K_I and K_{II} with reference values for different crack inclination angles for the $[0_2/90]_{2S}$ glass epoxy SECP with $a/b = 0.5$

Crack inclination angle, ψ	$K_I\left(\text{MPa}\sqrt{\text{mm}}\right)$			$K_{II}\left(\text{MPa}\sqrt{\text{mm}}\right)$		
	Proposed method (Section 3.6)	Ref. value	% Rel. err.	Proposed method (Section 3.6)	Ref. value	% Rel. err.
15°	39.22	39.15	0.19	5.44	5.31	2.25
30°	30.15	29.93	0.58	7.64	7.55	1.19
45°	19.17	19.25	0.39	8.27	8.14	1.59
60°	10.78	10.57	1.89	6.54	6.62	1.21
75°	4.19	4.06	2.99	3.83	3.74	2.41

5.2 $[90_2/0]_{10S}$ Carbon-epoxy laminate with slant edge cracked configuration

Here, $[90_2/0]_{10S}$ Carbon-epoxy slant edge-cracked plate (SECP) subjected to uniform tensile stress as shown in Fig. 5.13(a) with effective laminate properties, geometric and loading details as shown in Table 5.6 has been considered to numerically simulate the proposed approach for the determination of mixed mode SIFs of orthotropic laminates using strain

gages (section 3.6) similar to the $[0_2/90]_{2S}$ glass-epoxy laminate. Corresponding to these properties, the values of values of α, β, θ and ϕ are obtained as 2.063, 1.889, 61° and 84° respectively and are employed in the current finite element analysis.

Table 5.6 Geometric, loading and material parameters for the $[90_2/0]_{10S}$ carbon-epoxy specimens

Section	b (mm)	a/b	h/b	ν_{LT}	E_L (GPa)	E_T (GPa)	G_{LT} (GPa)	σ (GPa)	t (mm)
5.1.1	150	0.5	1	0.01	67.43	142.7	4.304	1	1
5.1.2		0.2-0.7							
5.1.3		0.5							
5.1.4		0.5							

5.2.1 Determination of r_{max} for the $[90_2/0]_{10S}$ Carbon-epoxy SECP

Figure 5.13(b) shows a typical finite element mesh considered after proper convergence study and employed for determination of r_{max} of the $[90_2/0]_{10S}$ Carbon-epoxy SECP with $a/b = 0.5$ and $\psi = 45°$. In keeping with the proposed technique (section 3.6), two strain gages pasted at equal distances measured from the crack tip within optimal locations $(r_{min} < r < r_{max})$ along the positive and negative gage line are required to estimate the mixed mode SIFs. Here, the r_{max} of a configuration has been estimated utilizing the procedure described in Section 3.7 and illustrated in Section 5.1.1. Following similar steps, the strain values ε_{aa} and ε_{bb} of the nodes along the positive and negative gage lines are noted from the FE results. Figures 5.14 (a) and (b) show the plots

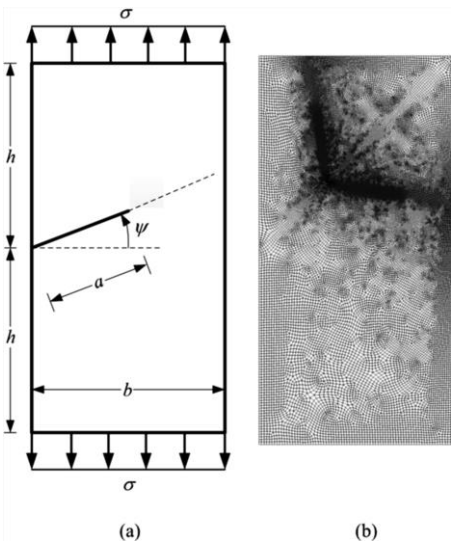

Figure 5.13 (a) Geometry of the $[90_2/0]_{10S}$ carbon-epoxy SECP under uniform tension, (b) typical FE mesh used

of $\left\{\left(\varepsilon_{aa}+\varepsilon_{bb}\right)\sqrt{r}\right\}/I_1$ and $\left\{\left(\varepsilon_{aa}-\varepsilon_{bb}\right)\sqrt{r}\right\}/I_2$ versus radial distance (r) respectively with their individual straight line fits along with the values of the coefficients A_0, C_0 and C_1 for the best fit plots for the $\left[90_2/0\right]_{10S}$ Carbon-epoxy SECP with $a/b=0.5$.

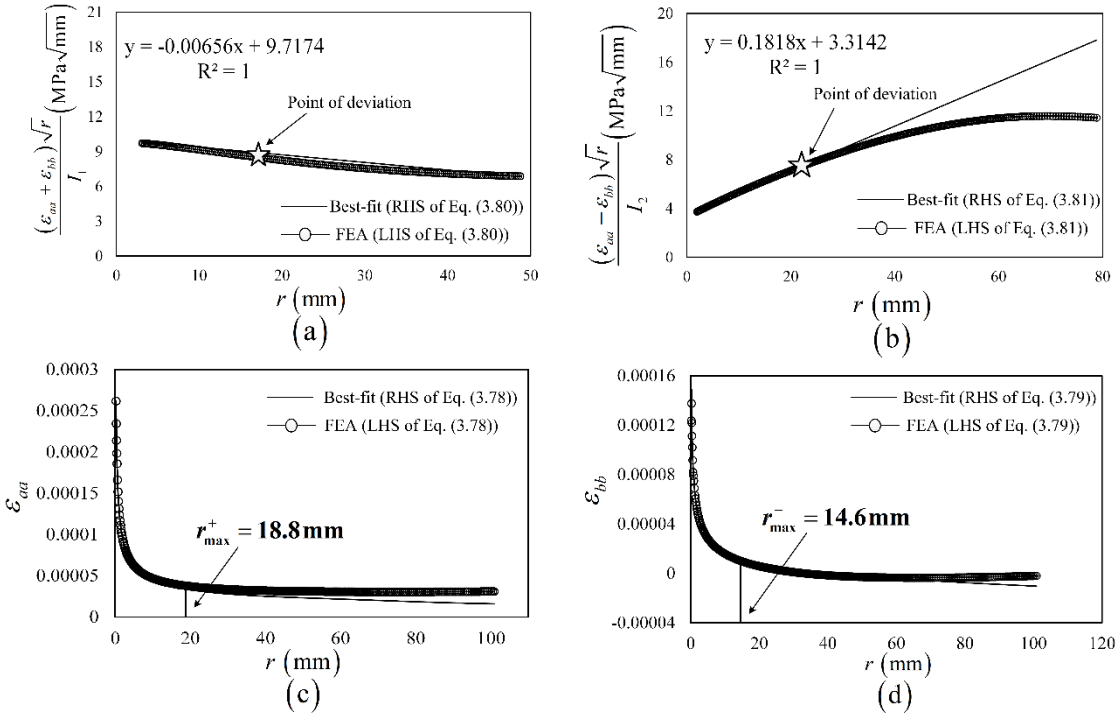

Figure 5.14 Plots for $\left[90_2/0\right]_{10S}$ glass-epoxy SECP with $a/b=0.5$ (a) Determination of A_0, (b) Determination of C_0 and C_1, (c) Determination of r_{max}^{+} and (d) Determination of r_{max}^{-}

The parameters $\left\{\left(\varepsilon_{aa}+\varepsilon_{bb}\right)\sqrt{r}\right\}/I_1$ and $\left\{\left(\varepsilon_{aa}-\varepsilon_{bb}\right)\sqrt{r}\right\}/I_2$ start to deviate from their respective best fit plots from certain radial points as seen in Figs. 5.14 (a) and (b). Using the values of the best-fit coefficients A_0, C_0 and C_1, the strains ε_{aa} and ε_{bb} along the positive and negative gage line calculated by employing Eq. (3.78) and Eq. (3.79) are compared with the ε_{aa} and ε_{bb} obtained directly from the FE solutions as seen in the Figs. 5.14 (c) and 5.14 (d) respectively. As discussed in section 3.7 and 5.1.1, the strain values calculated using Eq. (3.78) and Eq. (3.79) deviate from their corresponding FE solutions from certain radial points which gives the value of r_{max}^{+} i.e. maximum permissible radial distance for strain gages along the positive gage line as 18.8 mm and r_{max}^{-} i.e. maximum permissible radial distance for strain gages along the negative gage line as 14.6 mm for the $\left[90_2/0\right]_{10S}$ Carbon-epoxy SECP. These

values have been estimated using a 1% relative error criterion between the LHS and RHS quantities as explained in section 5.1.1. The extent of the three parameter strain series along the positive and negative gage lines or maximum permissible radial distance for the strain gages being different along both the gage lines, the minimum of r_{max}^{+} and r_{max}^{-} i.e. 14.6 mm is the r_{max} since all the equations (Eqs. (3.78 – 3.81)) are valid in this region.

5.2.2 Influence of a/b ratio and crack inclination angle (ψ) on r_{max}

The effect of a/b ratio on the r_{max} values has been studied in this section for the $[90_2/0]_{10S}$ Carbon-epoxy SECP with effective properties, geometric parameters and loading details mentioned in Table 5.6 for different values of crack inclination angle, ψ (=15°, 30°, 45°, 60° and 75°). The values of r_{max} for all values of a/b ranging from 0.2 to 0.7 in steps of 0.1 are determined using the procedure described in Section 3.7. Figures 5.15 – 5.19 show all the plots pertaining to r_{max} determination for the $[90_2/0]_{10S}$ Carbon-epoxy SECP with $\psi = 45^{\circ}$ with a/b ratio of 0.2, 0.3, 0.4, 0.6 and 0.7 respectively. The results of $a/b = 0.5$ have already been presented in section 5.2.1.

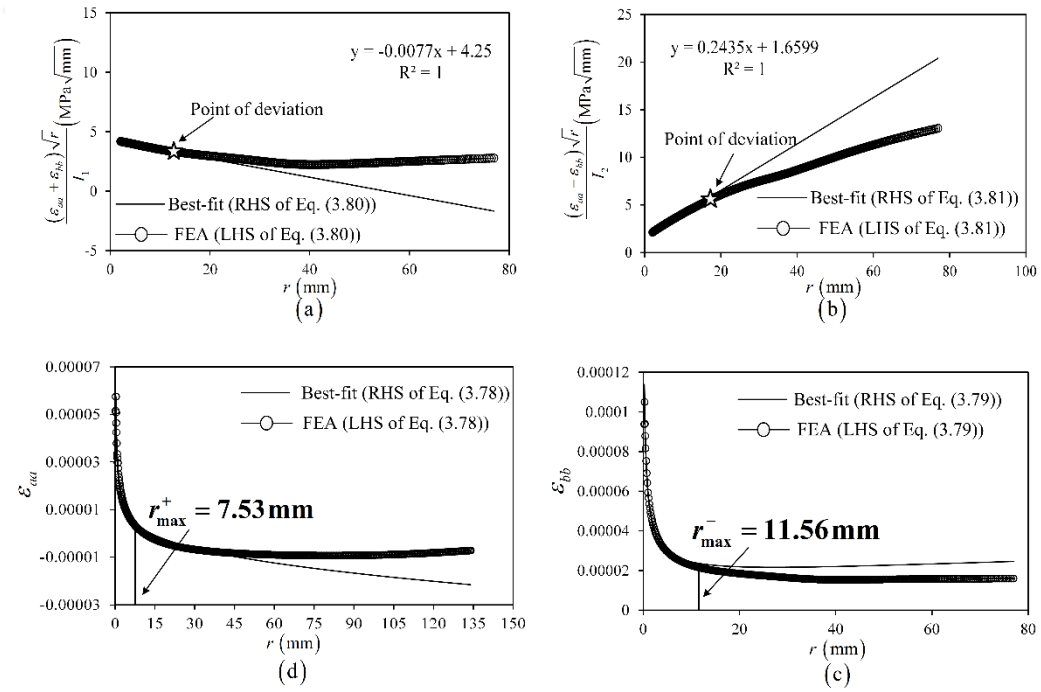

Figure 5.15 Plots for $[90_2/0]_{10S}$ glass-epoxy SECP with $a/b = 0.2$ (a) Determination of A_0, (b) Determination of C_0 and C_1, (c) Determination of r_{max}^{+} and (d) Determination of r_{max}^{-}

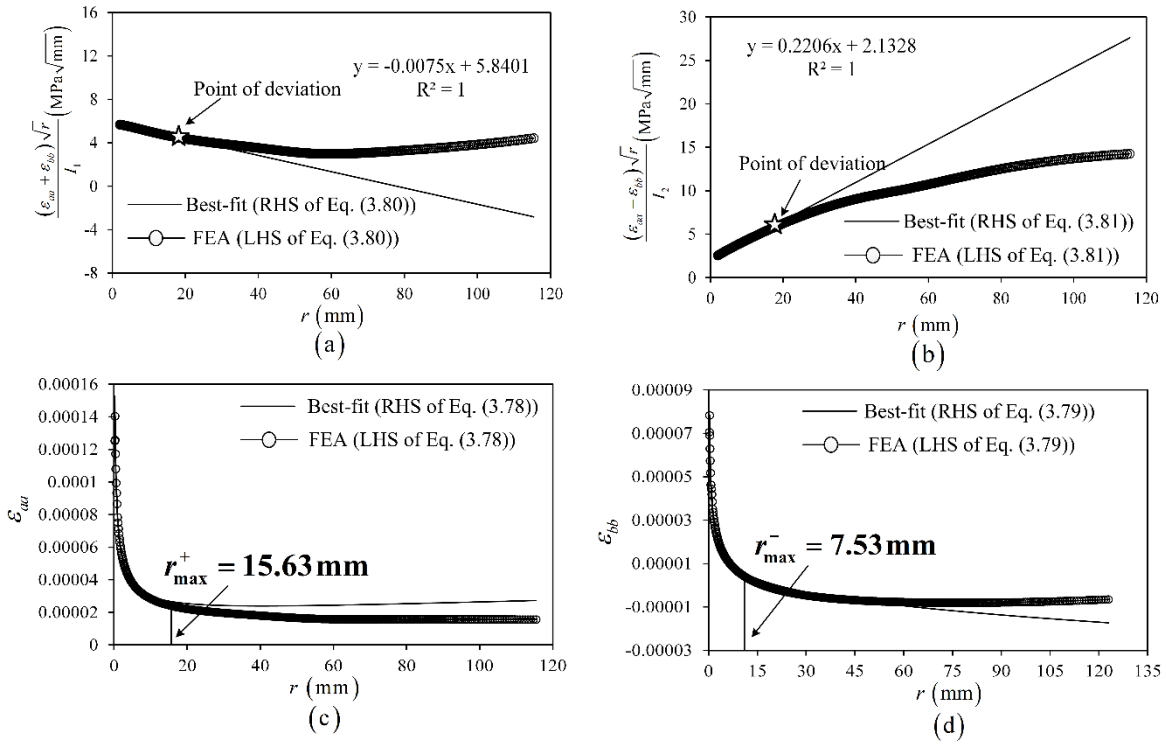

Figure 5.16 Plots for $\left[90_2/0\right]_{10S}$ glass-epoxy SECP with $a/b=0.3$ (a) Determination of A_0, (b) Determination of C_0 and C_1, (c) Determination of r_{max}^{+} line and (d) Determination of r_{max}^{-}

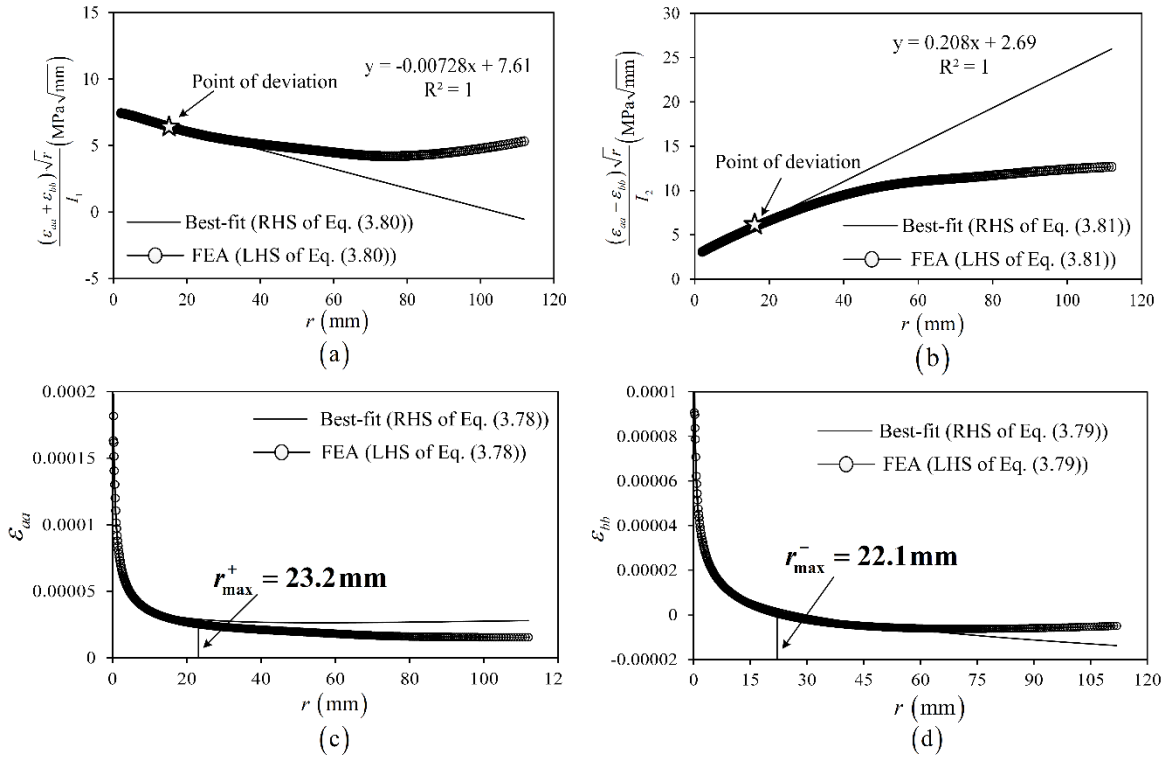

Figure 5.17 Plots for $\left[90_2/0\right]_{10S}$ glass-epoxy SECP with $a/b=0.4$ (a) Determination of A_0, (b) Determination of C_0 and C_1, (c) Determination of r_{max}^{+} and (d) Determination of r_{max}^{-}

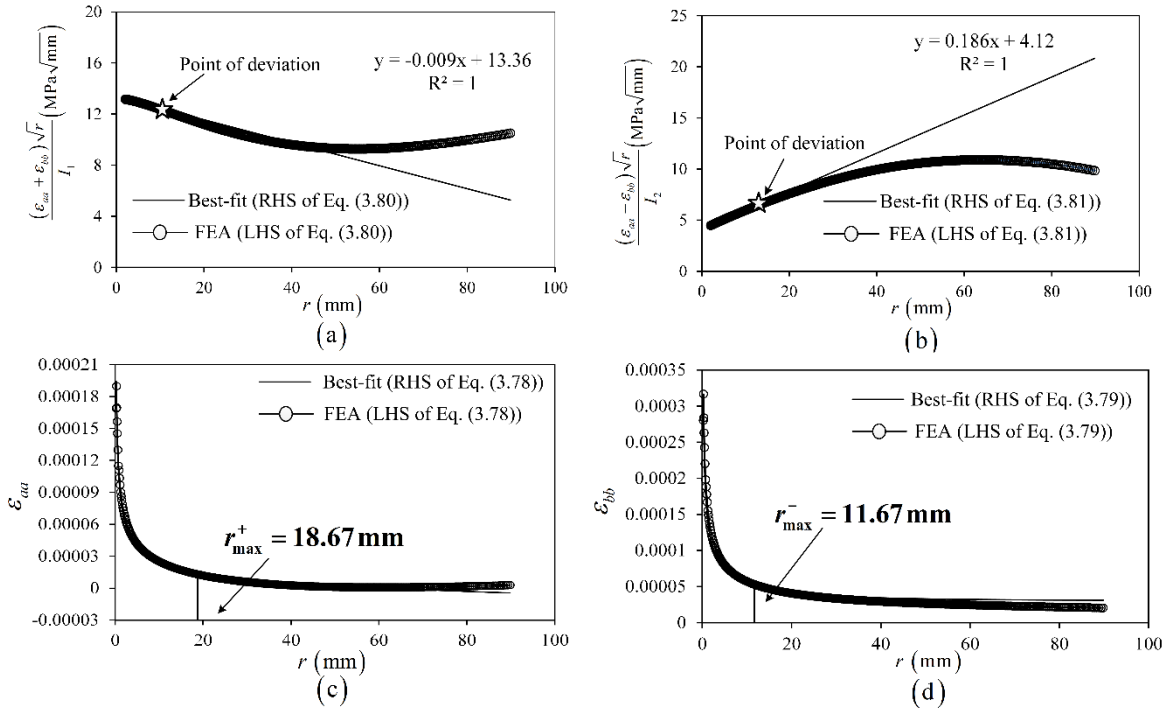

Figure 5.18 Plots for $[90_2/0]_{10S}$ glass-epoxy SECP with $a/b = 0.6$ (a) Determination of A_0, (b) Determination of C_0 and C_1, (c) Determination of r_{max}^{+} and (d) Determination of r_{max}^{-}

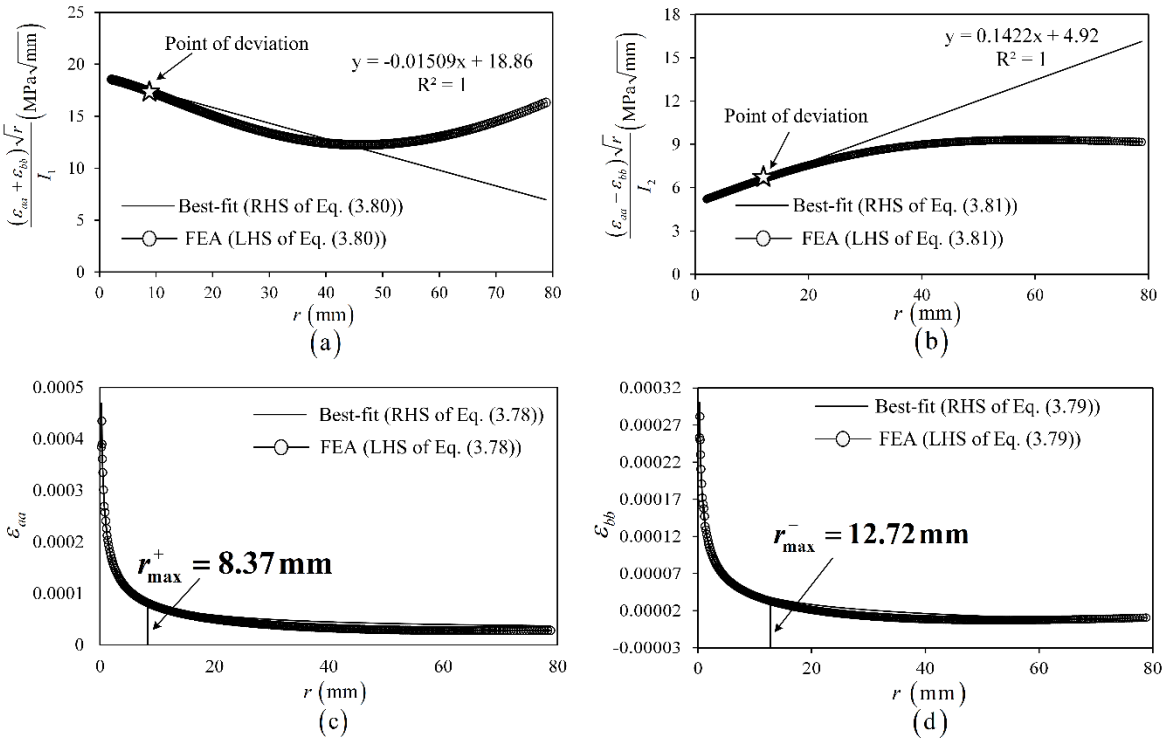

Figure 5.19 Plots for $[90_2/0]_{10S}$ glass-epoxy SECP with $a/b = 0.7$ (a) Determination of A_0, (b) Determination of C_0 and C_1, (c) Determination of r_{max}^{+} and (d) Determination of r_{max}^{-}

Table 5.7 shows the r_{max} values for the SECP with different a/b ratios for the $[90_2/0]_{10S}$ Carbon-epoxy SECP for a crack inclination angle of $\psi = 45^{\circ}$. In a similar way, the r_{max} values of SECP configurations for all other ψ values have been computed and presented in Fig 5.20 (a) as function of a/b. The r_{max} value increases with increasing a/b, reaches a maximum and decreases as the crack tip approaches boundary like in mode I case (Chapter 4) and in the previous $[0_2/90]_{2S}$ glass epoxy SECP example section 5.1.2. Figure 5.20 (b) shows the variation in non-dimensional r_{max}/b as a function of crack inclination angle (ψ) for each a/b ratio. The variation of r_{max} with ψ for the $[90_2/0]_{10S}$ Carbon-epoxy SECP follows a trend similar to that of the $[0_2/90]_{2S}$ glass epoxy SECP. It shows little or no variation up to 45° with a gradual decline at higher values of ψ beyond 45°.

Table 5.7 Variation of the r_{max}/b with a/b of the $[90_2/0]_{10S}$ carbon epoxy SECP for $\psi = 45^{\circ}$

a/b	r_{max} (mm)	r_{max}/b
0.2	7.53	0.0502
0.3	10.98	0.0732
0.4	22.1	0.1473
0.5	14.6	0.0973
0.6	11.67	0.0778
0.7	8.37	0.0558

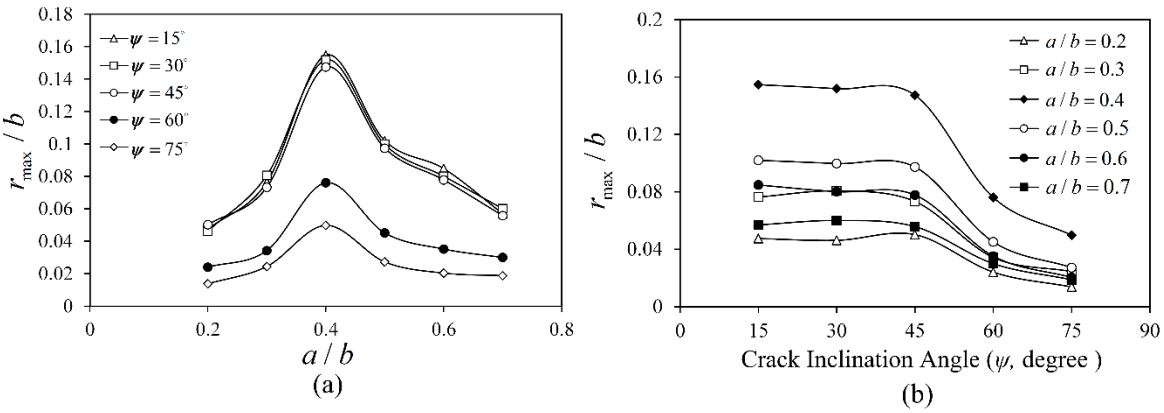

Figure 5.20 (a) Variation of r_{max}/b as a function of a/b for ψ = 15°, 30°, 45°, 60° and 75° (b) Variation of r_{max}/b as a function of ψ for different a/b for the $[0_2/90]_{2S}$ glass-epoxy SECP

5.2.3 Numerical simulation of the proposed strain gage technique for determination of K_I, K_{II} of the $\left[90_2/0\right]_{10S}$ Carbon-epoxy SECP

This section presents the numerical simulation of the proposed mixed mode strain gage technique for the accurate determination of mixed mode SIFs (K_I, K_{II}) for the $\left[90_2/0\right]_{10S}$ Carbon-epoxy SECP with $a/b = 0.5$ and $\psi = 45^\circ$. The properties of the configuration are listed in Table 5.6.

Table 5.8 Simulated K_I and K_{II} at optimal and non-optimal locations for the $\left[90_2/0\right]_{10S}$ carbon-epoxy SECP with $a/b = 0.5$ $(r_{max} = 14.6\,\text{mm})$

Case	r_1 and r_2 (mm)	ε_{aa}	ε_{bb}	K_I $\left(\text{MPa}\sqrt{\text{mm}}\right)$	% Rel. Err.	K_{II} $\left(\text{MPa}\sqrt{\text{mm}}\right)$	% Rel. Err.
1	$r_1 = 5.08$	6.11E-05	2.81E-05	24.01	1.34	8.27	1.22
	$r_2 = 9.16$	4.65E-05	1.74E-05				
2	$r_1 = 9.16$	4.65E-05	1.74E-05	23.71	2.57	8.57	4.9
	$r_2 = 13.12$	3.95E-05	1.17E-05				
3	$r_1 = 13.12$	3.95E-05	1.17E-05	21.91	9.9	9.15	11.96
	$r_1 = 20.05$	3.28E-05	5.79E-06				
4	$r_1 = 20.05$	3.28E-05	5.79E-06	20.35	16.37	9.90	21.16
	$r_2 = 26$	2.94E-05	2.60E-06				

Strain values at considered at nodal positions along both the gage lines for different cases of strain gage placements. In case 1 and case 2, both the nodal positions are within the optimal location, in case 3 one gage position is within r_{max} and another outside r_{max} and in case 4 where both the gage positions are outside r_{max} .The reference values of K_I and K_{II} are determined employing the displacement extrapolation technique (section 3.8) as 24.33 $\text{MPa}\sqrt{\text{mm}}$ and 8.17 $\text{MPa}\sqrt{\text{mm}}$ respectively for the $\left[90_2/0\right]_{10S}$ Carbon-epoxy SECP with $a/b = 0.5$ and $\psi = 45^\circ$ (section 3.8).

Tables 5.8 shows the comparison of the numerically simulated K_I and K_{II} with the reference values. It may be observed that for gage locations within $r_{max}\,(=14.6\text{ mm})$ % relative error in K_I and K_{II} is low whereas strain readings outside r_{max} give comparatively high error percentage. The % relative error in K_I and K_{II} is quite high also for the case when one gage location is within r_{max} and another outside r_{max}. It may be pointed out that the % relative error in the numerically estimated K_I and K_{II} at different radial positions follow similar trend as in previous example where K_I and K_{II} has been estimated for $[0_2/90]_{2S}$ glass-epoxy SECP.

5.2.4 Simulation of the proposed mixed mode technique with varying crack inclination angles

Here, the K_I and K_{II} have been estimated through numerical simulation for the $[90_2/0]_{10S}$ Carbon-epoxy SECP with $a/b=0.5$ and effective laminate properties mentioned in Table 5.6 for different values of crack inclination angle $\psi =$ 15°, 30°, 45°, 60° and 75°. Here the K_I and K_{II} values have been estimated at the optimal gage locations. Figure 5.21 shows the variations of the estimated mixed mode SIFs with respect to different crack inclination angles, $\psi =$ 0°– 90°. The variation in K_I and K_{II} follow the same trend as has been observed by other researchers in the past [41, 43, 44] and also in the previous example for the $[0_2/90]_{2S}$ glass-epoxy SECP (section 5.1.4). K_I decreases steadily with the increase in ψ whereas K_{II} increases with increase ψ, reaches a maximum at $\psi=45^\circ$ and then decreases.

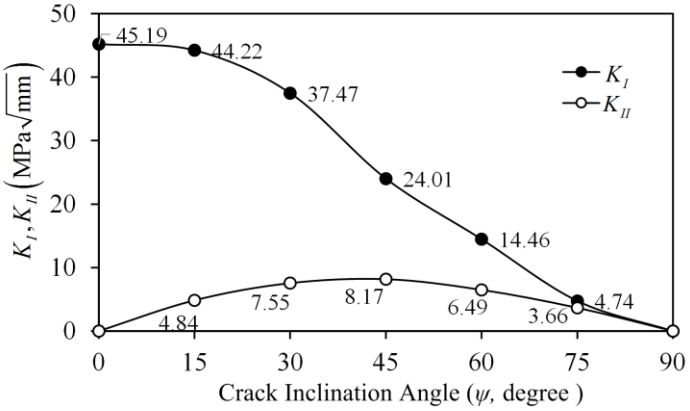

Figure 5.21 Variations of K_I and K_{II} with ψ for the $[90_2/0]_{10S}$ carbon epoxy SECP with $a/b=0.5$

Tables 5.9 compares the numerically simulated K_I and K_{II} values obtained employing the proposed methodology with reference values obtained using the DET (section 3.8). It may very well be observed that the proposed strain gage technique for determination of K_I, K_{II} of orthotropic laminates (section 3.6) provides very accurate SIFs for a wide range of crack inclination angles when the gages are located at optimal gage locations.

Table 5.9 Comparison of numerically simulated K_I and K_{II} with reference values for different crack inclination angles for the $[90_2/0]_{10S}$ carbon- epoxy SECP with $a/b=0.5$

Crack inclination angle, ψ	$K_I\left(\text{MPa}\sqrt{\text{mm}}\right)$			$K_{II}\left(\text{MPa}\sqrt{\text{mm}}\right)$		
	Proposed method (Section 3.6)	Ref. value	% Rel. err.	Proposed method (Section 3.6)	Ref. value	% Rel. err.
15°	44.22	43.57	1.5	4.84	4.71	2.76
30°	37.47	37.77	0.79	7.55	7.68	1.69
45°	24.01	24.33	1.34	8.17	8.27	1.22
60°	14.46	14.18	1.97	6.49	6.35	2.20
75°	4.74	4.66	2.99	3.66	3.57	2.52

Tables 5.9 compares the numerically simulated K_I and K_{II} values obtained employing the proposed methodology with reference values obtained using the DET (sections 3.8). It may very well be observed that the proposed strain gage technique for determination of K_I, K_{II} of orthotropic laminates (section 3.6) provides very accurate SIFs for a wide range of crack inclination angles when the gages are located at optimal gage locations.

5.3 Summary

The proposed method for determination of mixed mode SIFs of orthotropic laminates using strain gages has been numerically simulated for both $[0_2/90]_{2S}$ glass-epoxy and $[90_2/0]_{10S}$ carbon-epoxy SECPs employing the proposed optimal gage location criterion for each

configuration. The r_{max} value (minimum of r_{max}^{+} and r_{max}^{-}) which decides the optimal gage location (r_{min} (= plate thickness)$< r < r_{max}$) has been determined for different mixed mode SECP specimens based on the formulations presented in section 3.7. The dependence of the r_{max} values on the a/b ratio and crack inclination angle has also been studied. The following observations are made as part of the numerical analyses.

- The finite element strain variations for both the laminate configurations follow the trend predicted by the theoretical formulations.
- The variation of r_{max} with a/b ratio for a given crack inclination angle, ψ shows that similar to mode I cases, for mixed mode configurations also r_{max} value increases with increasing a/b, reaches a maximum and decreases as the crack tip approaches boundary.
- The r_{max} value shows little or no variation for a particular a/b for variations in crack inclination angle upto 45°. However, due to increase in boundary effects with the crack moving closer towards the boundary edges beyond 45°, r_{max} decreases.
- Numerical simulation of the strain gage technique for estimation of mixed mode SIFs of orthotropic laminates shows that for gage locations within the optimal locations, very accurate values of SIFs are obtained whereas at non-optimal locations outside r_{max}, the % relative error increases significantly.
- The proposed strain gage approach for determination mixed mode SIFs of orthotropic laminates determines very accurate SIFs for different crack inclination angles as can be seen from the numerical investigation.

Chapter 6

Experimental determination of mode I SIF of orthotropic laminates

This chapter presents the experimental determination of mode I SIF of orthotropic laminates using the proposed single strain gage technique (section 3.4) with suggested optimal gage locations as described in section 3.5. For this purpose edge cracked configurations made of $[90_2/0]_{10S}$ carbon-epoxy laminates have been prepared with different crack length to width ratios (a/b) and experiments have been conducted. The importance of optimal strain gage locations and the effect of placing the strain gage within or outside the optimal locations on the accuracy of measured K_I have been substantiated by experimental results.

6.1 Details of the test specimen

The test specimen considered is an edge cracked configuration subjected to tensile loading as shown in Fig. 6.1. In the present investigation, specially designed Carbon-Epoxy laminates with $[90_2/0]_{10S}$ stacking sequence have been used to prepare all the test pieces. The test pieces with the desired configuration and stacking sequence have been supplied by VSSC (Vikram Sarabhai Space Centre, Indian Space Research Organization, Government of India) for the present research work. The specimens have been fabricated from UMS45Y13/M18 prepreg using standard autoclave molding methods of laminate manufacturing. The prepregs were cut into the required shape and orientation using CNC prepreg cutting machine and the lay-up has been done manually as per the required sequence on surface plate. The specimens have been vacuum bagged and cured in autoclave at 4.0 bar pressure and 0.8 bar vacuum at 175^0C for 2 hrs, maintaining the heating and cooling rate at 3^0C/minute. The specimen are cut to the required configuration using diamond cutter saw machine. The laminate shows a fiber volume fraction of 66%. The elastic properties of the laminate as provided by ISRO are specified in Table 6.1.

Table 6.1 Properties of carbon-epoxy lamina and $[90_2/0]_{10S}$ carbon-epoxy laminate

UD carbon-epoxy lamina		$[90_2/0]_{10S}$ carbon-epoxy laminate	
Property	Value	Property	Value
E_1	211 GPa	Longitudinal modulus (E_L)	67.44 GPa
E_2	6.056 GPa	Transverse modulus (E_T)	142.7 GPa
ν_{12}	0.246	Poisson's ratio (ν_{LT})	0.01
G_{12}	4.452 GPa	Shear modulus (G_{LT})	4.304 GPa

The details of geometry and the notch are also shown in Fig. 6.1. It may be observed that the crack is located at a distance of 155 mm from the top edge and 145 mm from the bottom edge and not exactly at the center. However, this slight offset has negligible effect on the mode of loading that the specimen undergoes and hence its SIF value [12].

The width (b) and the thickness (t) of the test specimens are 150 mm and 7.8 mm respectively. The holes near the top and the bottom edges aid in transferring the tensile load to the specimen (Fig. 6.1) through clevis grips and pins. A sharp crack of length 1 mm and root radius 0.24 mm has been introduced along the existing rectangular notch of width 2 mm using jewelry saw of thickness 0.22 mm. The length of the sharp crack was not extended beyond 1mm, since beyond 1mm maintaining the alignment of the axis of the sharp crack with the notch is difficult. In addition, the carbon-epoxy laminates being an opaque surface, maintaining uniformity of the

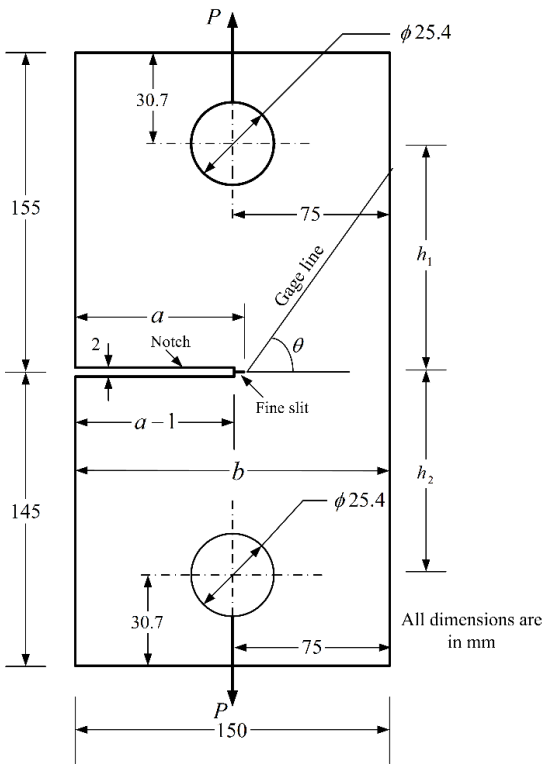

Figure 6.1 A typical edge cracked mode I specimen

crack front throughout the laminate thickness becomes difficult. Extreme care has been taken to maintain crack of length 1 mm on both sides of the plate. The total crack length after induction of the sharp crack has been used to compute the a/b ratios for the test specimens. The final dimensions of all the test specimens are summarized in Table 6.2. Dimensions of the specimens and loading conditions are chosen such that the plane stress conditions prevail.

Table 6.2 Details of edge-cracked mode I specimens

a/b	$a(\text{mm})$	$b(\text{mm})$	$t(\text{mm})$	$h(\text{mm})$
0.39	59	150	7.8	$300\begin{Bmatrix}h_1=155\\h_2=145\end{Bmatrix}$
0.51	76			
0.61	92			
0.71	106			

6.2 Verification of material properties of the $[90_2/0]_{10S}$ Carbon-Epoxy laminates

In order to experimentally determine the mode I SIFs of the edge-cracked Carbon-epoxy laminates using the proposed single strain gage technique and verify the optimal strain gage locations for the selected specimens, accurate values of equivalent laminate properties are required. Referring to Eqs. (3.55) and (3.57), it requires accurate values of equivalent properties as input in the FEA to obtain the maximum permissible radial location of the strain gage $(r_{\max})$. Further in conducting the experiments for determination of SIFs using strain gages, accurate values of the equivalent properties are required. Theoretical equivalent laminate properties of the specimens were provided by ISRO and are substantiated using experiments in this section. For a stacking sequence of $[90_2/0]_{10S}$, the effective stiffness properties determined using classical laminate theory (section 1.2.2) are enlisted in Table 6.2 Experimental verification of E_L, E_T, G_{LT} and ν_{LT} for the $[90_2/0]_{10S}$ carbon-epoxy laminate has been conducted by carrying out a total of three tests on each specimen shown in Figs. 6.2 and 6.3 respectively. Tests in the present section have been conducted according to ASTM

D3039/3039M-08. All the specimens have been fabricated from the same $[90_2/0]_{10S}$ carbon-epoxy laminate panel which was used to prepare the various cracked configurations of the present investigation.

Figure 6.2 Rectangular specimen for determination of E_T pasted with strain gages (ASTM D3039/D3039M-08 Specimen)

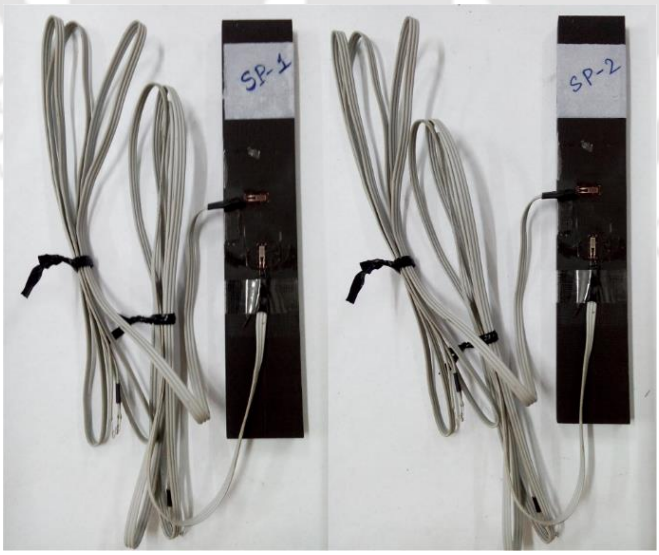

Figure 6.3 Rectangular specimen for determination of E_L pasted with strain gages (ASTM D3039/D3039M-08 Specimen)

In case of the tensile tests, the specimens have been monotonically loaded in closed loop servo hydraulic INSTRON 8801 machine (100 kN capacity) under displacement control with a strain rate of 0.1mm/min. Strain gage readings on one face have been obtained using electrical resistance strain gages of type BFLA–2–8, Make: TML Japan, for the axial as well the transverse strain. Details of the strain gage specifications are given in Table 6.3 and the image of a typical strain gage is shown in Fig. 6.4. Utmost care has been taken while pasting the strain gages to ensure defect free bonding following the standard procedures of strain gage pasting. In all these cases, the measured strains (longitudinal as well as transverse) have been stored, digitized and processed with the help of cDAQ-9178 data acquisition system of National Instruments (NI) along with LabVIEW^{TM} software.

Table 6.3 Details of strain gage

Parameters	Specifications
Type	BFLA-2-8
Gage length	2 mm
Gage factor	2.10 ± 1%
Gage resistance	120 ± 0.3 Ω
Transverse sensitivity	0.3%
Test condition	23°C 50% RH

Figure 6.4 A typical 2 mm gage length, pre-wired strain gage

Figure 6.5 shows the raw data corresponding to one of the two rectangular specimens when loaded along longitudinal direction (Fig. 6.2) obtained from the tensile tests and the corresponding best-fit lines. Figure 6.5 (a) shows the engineering stress strain diagram for determination of Young's modulus (E_T). The slope of the best-fit line in Fig. 6.5 (a) is the Young's modulus (E_T) Figure 6.5 (b) shows the load versus axial strain as well as load versus transverse strain for the measurement of Poisson's ratio (ν_{TL}). According to ASTM E132-04, Poisson's ratio is defined as the negative ratio of the slope of line of transverse strain to the slope of line of axial strain in Fig. 6.5 (b).

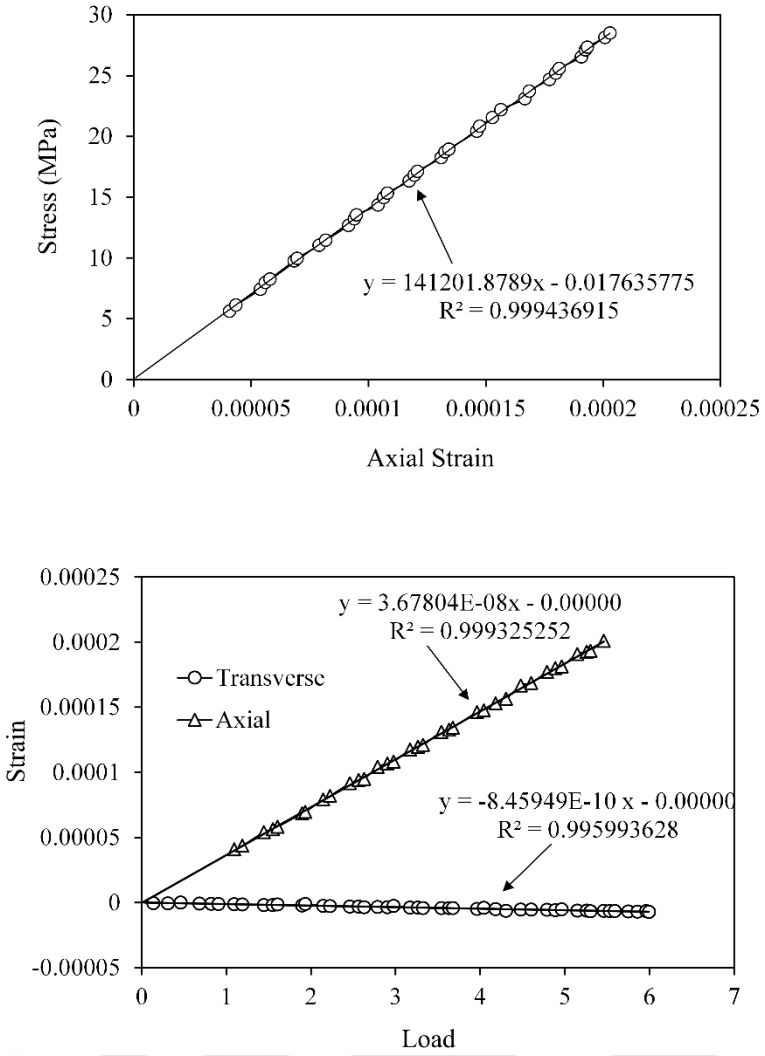

Figure 6.5 Tensile test data for rectangular specimen loaded along longitudinal direction (Fig. 6.2)

Figure 6.6 shows the raw data from a typical test corresponding to one of the two rectangular specimens loaded along transverse direction (Fig. 6.3) obtained from the tensile tests and the corresponding best-fit lines. Analogous to the previous case, here also Young's modulus (E_L) and minor Poisson's ratio (ν_{LT}) have been measured from the slopes of these best-fit lines. Table 6.4 shows the mean values (of three repeated test) of Young's moduli (E_L, E_T) and Poisson's ratio (ν_{LT}, ν_{TL}) for all the specimens. The mean values of $E_L = 68.95\,\text{GPa}$, $E_T = 141.15\,\text{GPa}$, ν_{LT} =0.0106 and ν_{TL} =0.0212 as shown in Table 6.4 are found to be in good accordance with the properties provided by ISRO (Table 6.1) i.e. they follow the relationship $E_L / E_T = \nu_{LT} / \nu_{TL}$.

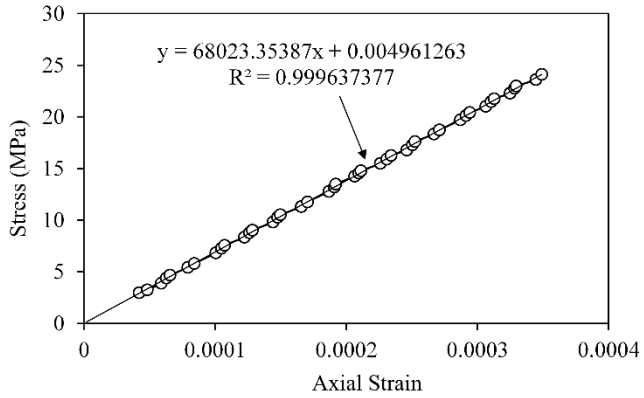

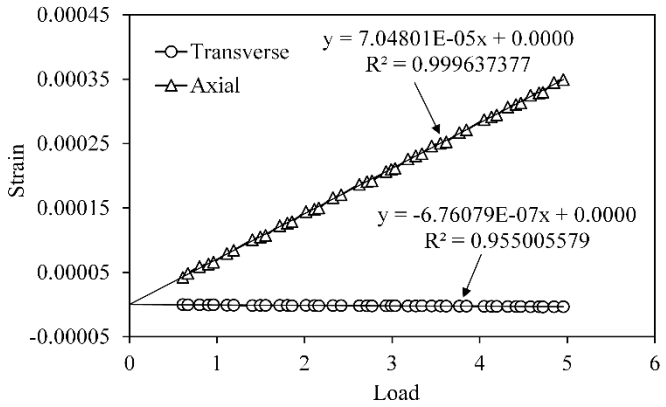

Figure 6.6 Tensile test data for rectangular specimen loaded along lateral direction (Fig 6.3)

Table 6.4 Experimentally determined material properties

Case	Specimen	E (GPa)	Mean	ν	Mean
Longitudinal direction (Fig. 6.2)	SP-1	E_T = 140.8	E_T =141.15	ν_{TL} = 0.0209	ν_{TL} =0.0212
	SP-2	E_T = 141.5		ν_{TL} = 0.0215	
Transverse direction (Fig. 6.3)	SP-1	E_L = 68.5	E_L = 68.95	ν_{LT} = 0.0107	ν_{LT} =0.0106
	SP-2	E_L = 69.4		ν_{LT} = 0.01055	

Due to the requirement of either rosette or a shear testing machine for the calculation of G_{LT} the experimental verification of the shear modulus has not been carried out. However, noting the conformity between the experimentally determined stiffness properties and the

analytically estimated properties, it can very well be presumed that the value of the shear modulus G_{LT} will also be in accordance with the properties given by ISRO (Table 6.1). Thereby, using the values of the compliances (Table 6.1) as determined theoretically and verified experimentally, further experimentations on the verification of the single strain gage technique and the optimal gage location for orthotropic materials is carried out.

6.3 Determination of r_{max} of the experimental specimens

The material properties of the $[90_2/0]_{10S}$ Carbon-Epoxy laminates have been used to compute the r_{max} values numerically for the select configurations. Based on the r_{max} value of these configurations, optimum strain gage locations have been identified (based on Eq. (3.59)) and strain gages have been pasted at those selected locations in order to substantiate the importance of optimal locations of strain gages in accurate determination of SIFs. The dimensions of the mode I test specimens are given in Table 6.2.

The procedure detailed in section 3.5 has been used to obtain the r_{max} values of the mode I experimental specimens. Plane stress conditions are assumed for the test cases and the full plate has been modelled for the FEA. For the FEA, point load has been applied on the top point of the upper hole, while the arc length in contact with the clevis pin on the bottom hole has been restricted for both u and v displacements (Fig. 6.7). The finite element discretization has been done using the eight noded isoparametric elements and collapsed quarter point elements have been used to model the region around the crack tip [71, 72]. Figures 6.8 (a), (b), (c) and (d) show the finite element meshes (along with NN: number of nodes and NE: number of elements) for all the four configurations with $a/b = 0.39$, 0.51, 0.61 and 0.71 respectively obtained after convergence study. It should be noted that the gage line (the line along which

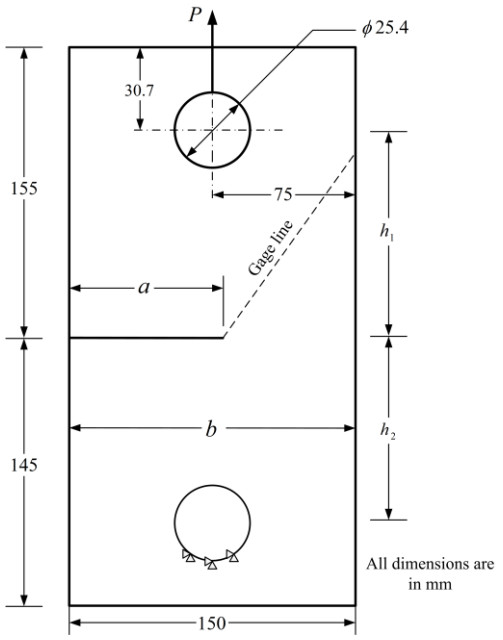

Figure 6.7 FEA model for the edge-cracked mode I specimens

ε_{aa} is to be measured as shown in Figs. 6.1 and 6.7) is also sufficiently refined in all the meshes in Fig. 6.8 for plotting Eq. (3.61).

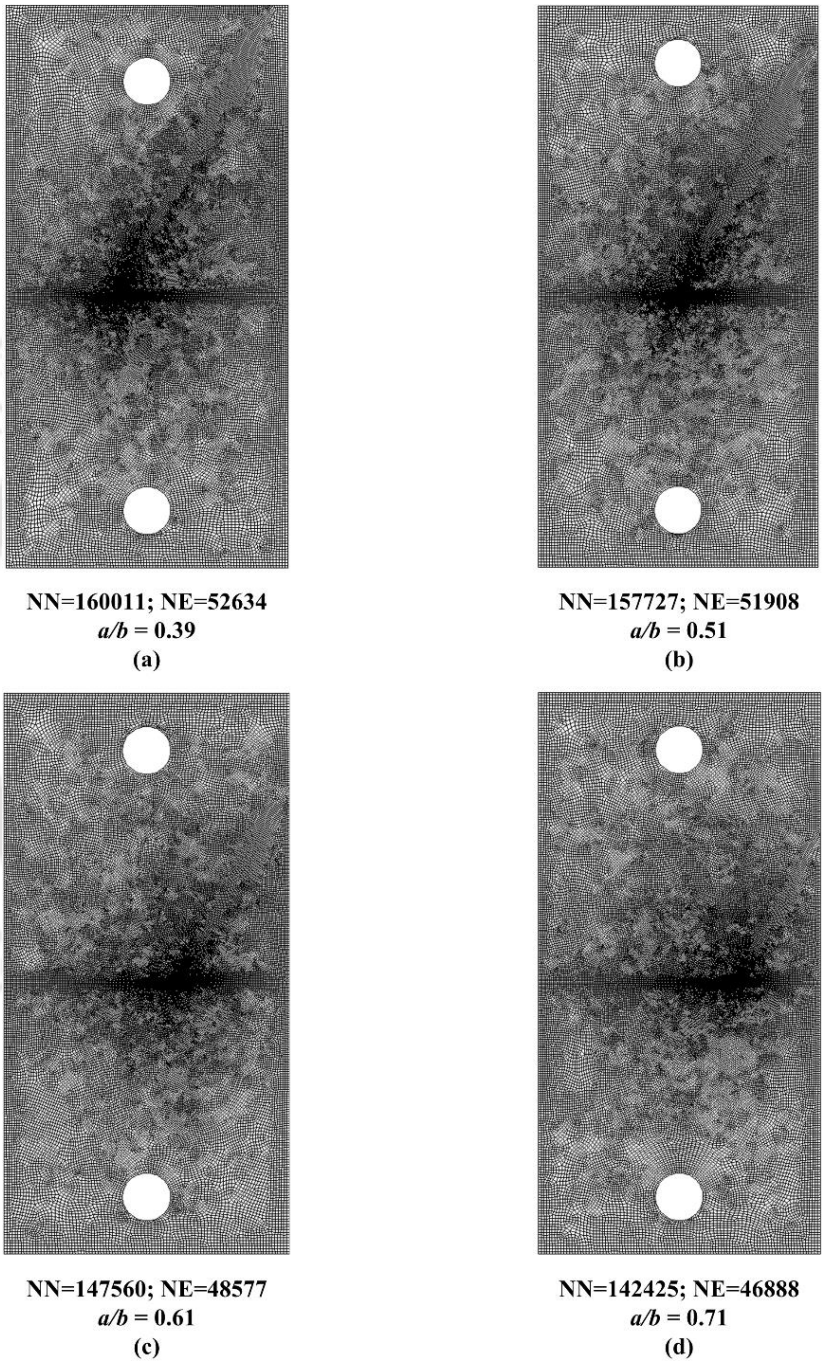

Figure 6.8 Finite element meshes for the mode I specimens with different a/b

Figures 6.9(a), (b), (c) and (d) show the plots of $\ln(\varepsilon_{aa})$ versus $\ln(r)$ of the nodal values along the gage line for $a/b = 0.39$, 0.51, 0.61 and 0.71 respectively. It is observed that each

plot consists of a distinguishable linear portion followed by a non-linear portion as predicted in theory (section 3.5). The linear trend exists up to a certain radial distance and thereafter turns to the non-linear portion. Following the procedure described in section 3.5, a relative error of 1% has been used to compute the r_{max} value or the extent of the linearity of the plots in Fig. 6.9.

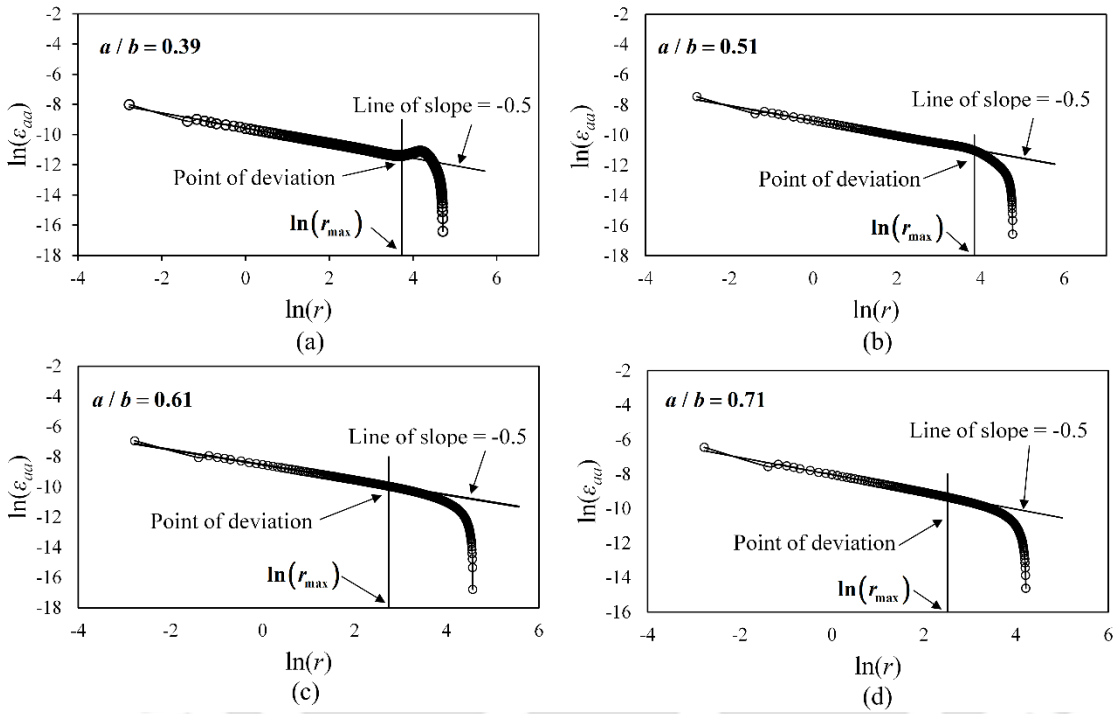

Figure 6.9 Plot of $\ln(\varepsilon_{aa})$ versus $\ln(r)$ for different mode I specimens (a) $a/b = 0.39$, (b) $a/b = 0.51$, (c) $a/b = 0.61$, (d) $a/b = 0.71$

The r_{max} values for the four selected configurations are shown in Table 6.5. As expected, with increasing a/b, the r_{max} values shows an increasing trend followed by a decreasing one as can be seen from Fig. 6.10.

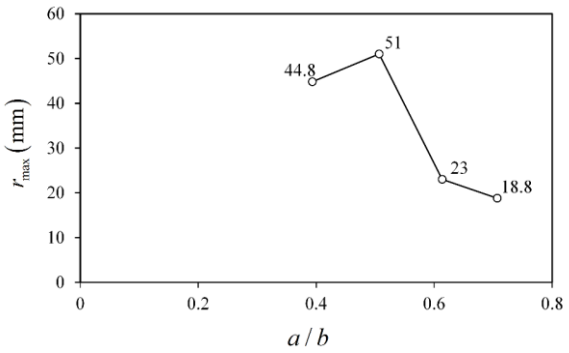

Figure 6.10 Variation of r_{max} as a function of a/b

Table 6.5 r_{max} values of different mode I specimens

a/b	r_{max} (mm)
0.39	44.8
0.51	51
0.61	23
0.71	18.8

6.4 Determination of mode I SIF using FEA

From the FE meshes shown in Figs. 6.9 (a), (b), (c) and (d), displacement values of the nodes of the elements along the crack face are extracted and mode I SIF, K_I has been computed for all four experimental specimens using the DET explained in section 3.8. The performance of the proposed DET technique for estimation of K_I and K_{II} of cracked orthotropic laminates is presented separately in Chapter 7. The normalized SIF, f_I is calculated as

$$f_I = \frac{K_I}{\sigma\sqrt{\pi a}} \tag{6.1}$$

where a is the crack length and $\sigma = P/(b \times t)$. The computed normalized SIF values, f_I for the selected experimental specimens are presented in Table 6.6. These values have been used as reference for the verification of the experimentally determined values of mode I SIF of the selected specimens and to study the effect of optimal locations in the subsequent sections. Using the $r_{\max}$ values computed in section 6.3, experiments have been conducted by pasting strain gages at optimal locations (Eq. 3.59) and outside the optimal zone $(r > r_{\max})$ to study the effects of radial positioning of the strain gage on the degree of accuracy of the SIF value that can be determined using the present single strain gage. Based on the readings from the strain gages placed at different radial locations, K_I is calculated following Eq. (3.58) and Eq. (3.13), and the normalized SIF is calculated using Eq. (6.1). The percentage relative error in f_I is calculated as

Table 6.6 Computed f_I of the different mode I specimens

a/b	f_I
0.39	2.062
0.51	2.768
0.61	4.657
0.71	7.582

$$\%\,\text{Relative error} = \left(\frac{f_I^{\,reference\ solution} - f_I^{\,experimental}}{f_I^{\,reference\ solution}} \right) \times 100 \tag{6.2}$$

where $f_I^{\,reference\ solution}$ is obtained from Table 6.6 and $f_I^{\,experimental}$ is estimated the from experimental results.

6.5 Details of experiment and experimental set-up

This section details various equipment employed in the present experimental study. A closed loop servo hydraulic INSTRON 8801 machine with 100 kN capacity has been used to load the selected edge cracked specimens under displacement control mode with an actuator speed of 0.1 mm/min. Clevis grips coupled with rod-end bearing have been used to transfer the tensile load from the machine to the specimen.

Electrical resistance strain gages for composite materials of type BFLA-2-8 (gage length of 2 mm) and make: TML Japan have been employed to measure the strains on the loaded specimens (Fig. 6.4 and Table 6.3). To ascertain precise and flawless bonding, the strain gages have been pasted on the specimens with extreme care and control. Utmost care has also been taken to maintain radial position and orientation (θ, ϕ) associated with each strain gage.

NI data acquisition system consisting of cDAQ-9178 chassis has been used to measure, digitize and process the strains. The required number of half-bridge analog input modules (NI 9237 having 4 channels 24 Bit) along with the LabVIEW^{TM} software has been used for the strain measurements. The successive load values from the INSTRON machine during the entire experiment have been obtained using the universal analog input module (NI 9219 having 4 channels 24 Bit,) for synchronized measurement of loads with strains at each time step in terms of voltage signals. A BNC cable connected between the load cell of the INSTRON and the NI 9219 enables this.

Experiments on each of the test specimens ($a/b = 0.39$, 0.51, 0.61 and 0.71) have been conducted three times to check the consistency and repeatability of the results and to show the importance of optimal gage locations. Experiments have also been conducted on three identical specimens with $a/b = 0.51$ to further ensure the reproducibility of the results obtained.

Quarter bridge Wheatstone bridge circuit has been employed for measurement of strains in all the experiments. Quarter bridge completion accessories (NI 9944) have been added to the NI 9237 strain gage module to achieve this. The sampling rate for data in all these modules has been set to 2000 Hz. LabVIEW^{TM} has been used to interface the DAQ system with the digital computer and this software is also used for processing and storing of experimental data. In all the experiments, offset nulling and shunt calibration of strain gages

have been done before actual data acquisition during loading the specimen. An excitation voltage of 2.5V is set in all the experiments.

Figure 6.11 shows the snap shot of a typical virtual instrumentation using DAQ assistant used in one of the experiments. The specimen with strain gages pasted on it is put into the clevis grips of INSTRON machine once the instrumentation part prior to data acquisition is ready. Both spacer blocks and rod-end bearings are employed to eliminate bending while imparting axial load i.e. ensuring pure mode I loading to the cracked specimens as shown in Fig.6.12.The dimensions of the spacer blocks are machined to perfection so as to meet the perfect alignment criterion.

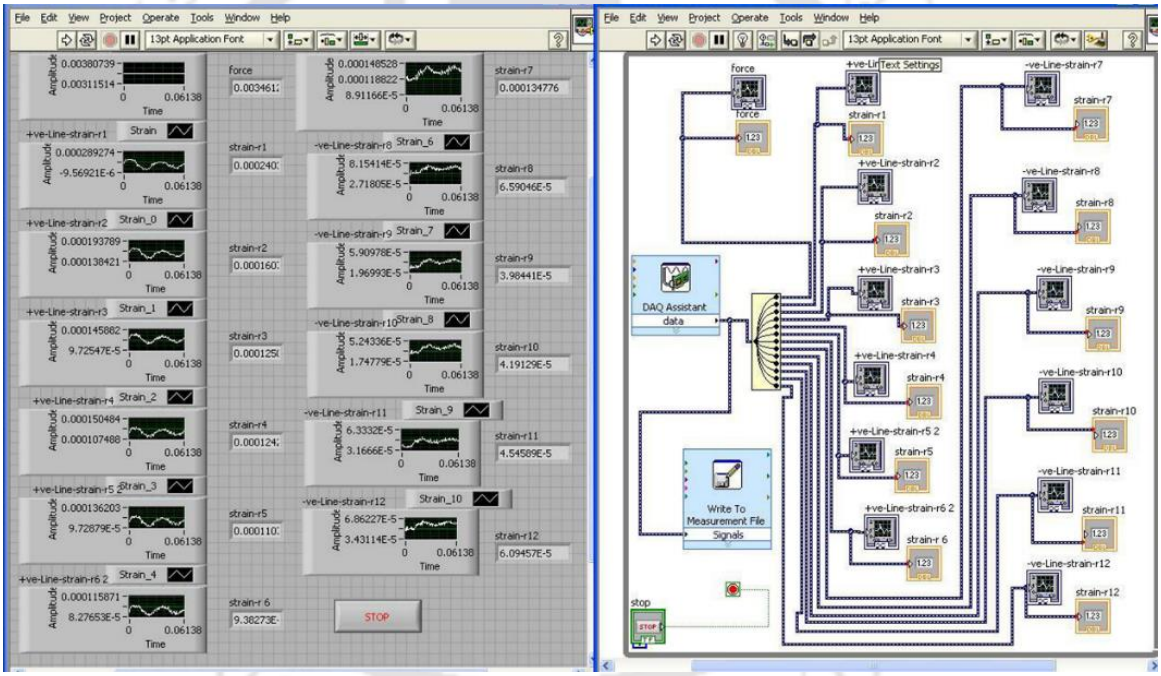

Figure 6.11 DAQ assistant of LabVIEW™ programming for a typical experiment

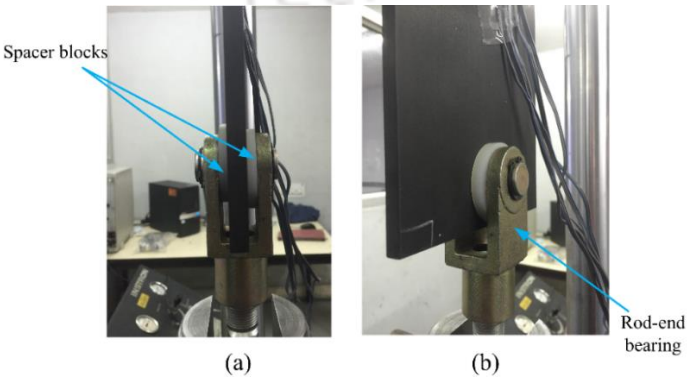

Figure 6.12 Specimen with the spacer blocks in the clevis

Figure 6.13 Using a plumb to check the alignment

The alignment of the specimen is also checked using a plumb before loading (Fig. 6.13). During loading, both force and strain data are stored simultaneously for further post-processing. Figure 6.14 shows the photograph of the complete experimental setup emphasizing all the important components described in this section.

Figure 6.14 Photograph of complete experimental set-up

Typically, placing strain gages away from crack tip helps in obtaining unadulterated strain values without the influence of strain gradient and 3D effects. In the present investigation, the gage locations are selected beyond a distance equal to thickness (t) of the plate to avoid 3D effects [69]. The measurement errors due to the strain gradients is taken care of by selecting strain gages with small gage length and width [81-83]. Very small gages of 2 mm gage length have been employed for strain measurements in the present experiments. Additionally, Dally and Sanford [50] also showed that placing strain gages at a distance where the ratio of radial distance of center of the strain gage to the length of the gage is more than four reduces strain gradient error significantly. The gage locations in all the experimental specimens of the present study have been selected as per the aforementioned norms to minimize the factors that directly or indirectly adversely affect the strain readings.

6.6 Experimental determination of K_I of the edge-cracked $\left[90_2 / 0\right]_{10S}$ carbon-epoxy laminates using the proposed single strain gage technique

Here experimental values of mode I SIFs of the orthotropic laminates have been determined using the strain gage readings and using the procedure described in sections 3.4 and 3.5. The existence and usefulness of the optimal gage locations are also verified in terms of the degree of accuracy of the experimentally obtained K_I. Figures 6.15(a), (b), (c) and (d) shows the photograph of the edge cracked orthotropic Carbon-Epoxy panels with $a/b = 0.39$, 0.51, 0.61 and 0.71 pasted with strain gages used in the present experiments. Corresponding to the materials properties in Table 6.1, the gage orientation, ϕ (Eq. 3.55) is found to be 84° and the gage line orientation, θ (Eq. 3.57) is found to be 61°. All the pasted strain gages in Fig. 6.15 conform to the angular orientations θ and ϕ.

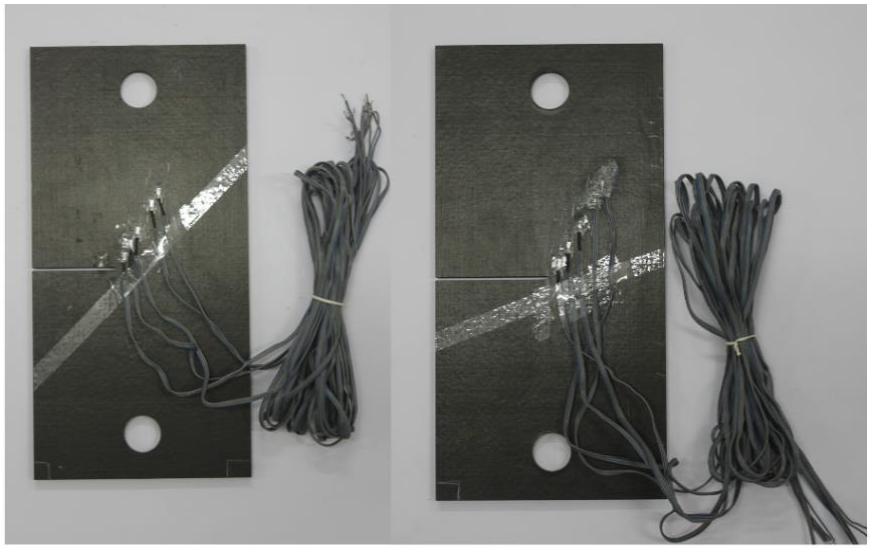

(a) (b)

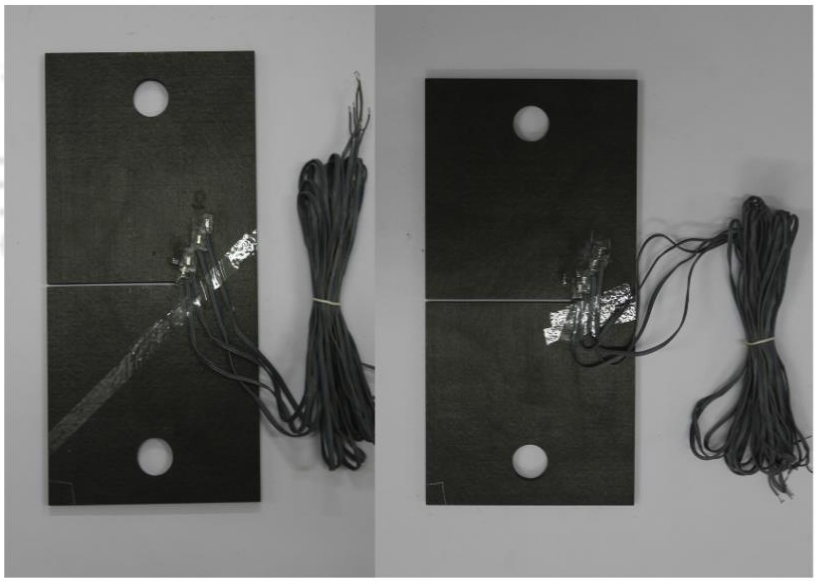

(c) (d)

Figure 6.15 Mode I orthotropic laminates with strain gages pasted (a) $a/b = 0.39$, (b) $a/b = 0.51$, (c) $a/b = 0.61$, (d) $a/b = 0.71$

According to the proposed theory, the optimal locations for the strain gages should be in the range $r_{min} \le r \le r_{max}$ to achieve high accuracy in the measured SIFs. The r_{min} for the specimens considered in the present investigation is 7.8 mm (Eq. 3.59), which is the thickness of the laminate (Table 6.2). Strain gages pasted beyond the r_{max} would result in inaccurate SIF values and thus are non-optimal locations as per the proposed approach in section 3.5. Strain

gage locations for all the three specimens used in the present study are shown in Table 6.7 and have been decided based on aforementioned observations and the concept of optimal gage locations.

Table 6.7 Selected strain gage locations for the mode I experiments with different a/b

a/b	r_{max} (mm)	r_1 (mm)	r_2 (mm)	r_3 (mm)	r_4 (mm)	r_5 (mm)
		Optimal locations			Non-Optimal locations	
0.39	44.8	10	22	32	50	60
0.51	51	10	19	35	60	70
		Optimal locations			Non-Optimal locations	
0.61	23	10	18	30	40	-----
0.71	18.8	9	17	35	45	-----

For a/b = 0.39, the value of r_{max} obtained from the proposed approach is 44.8 mm. Therefore, three strain gages pasted at r_1 = 10 mm, r_2 = 22 mm and r_3 = 32 mm are optimal locations and two other strain gages are pasted beyond r_{max} at r_4 = 50 mm and r_5 = 60 mm and hence are non-optimal locations. Similarly, for each of the three specimens with a/b = 0.51, the r_{max} = 51 mm has been obtained from the numerical method. Here also three strain gages at r_1 = 10 mm, r_2 = 19 mm and r_3 = 38 mm have been pasted at optimal locations while two other strain gages have been pasted at r_4 = 60 mm and r_5 = 70 mm i.e. beyond r_{max} (non-optimal locations). For a/b = 0.61, the r_{max} value has been obtained from the FEA as 23 mm. Based on this r_{max} value, two strain gages have been pasted at r_1 = 10 mm and r_2 = 18 mm to measure strains at optimal locations, and two other strain gages are pasted outside r_{max} at r_3 = 30 mm and r_4 = 40 mm. Similarly, for a/b = 0.71, the estimated value of r_{max} is 18.8 mm and two strain gages are located at optimal locations i.e., one at r_1 = 9 mm and other at r_2 = 17 mm . Two more gages are positioned at non-optimal locations (i.e. $r > r_{max}$) at r_3 = 35 mm and r_4 = 45.

Locations of strain gages in all the test specimens are intentionally chosen some within and outside the optimal zone to verify the importance of optimal strain gage location in terms of experimentally evaluated value of K_I. Experiments have been repeated three times in all the specimens to ensure the repeatability of the results. Foot corrections have been done in all the experimental data by subtracting the strain value corresponding to zero load from all the measured strain gage readings.

6.6.1 Experimental results for $a/b = 0.39$

The experimental specimen with a/b = 0.39 is shown in Fig. 6.15 (a). Figure 6.16 shows the raw data of measured strain ε_{aa} by the strain gage (circled data points) at r_1 = 10 mm versus the applied load for a/b = 0.39 for all the three repeated tests. The best-fit straight lines (solid lines) to the raw data with the corresponding slopes and the correlation coefficients R^2 are also shown in Fig. 6.16. As expected, in all the repeated tests, the measured strains are linearly proportional to the applied load as implied by the good values of R^2. Further, the slopes of best-fit straight lines in all plots of Fig. 6.16 are nearly same thereby reinforcing the excellent calibration of the entire experimental setup.

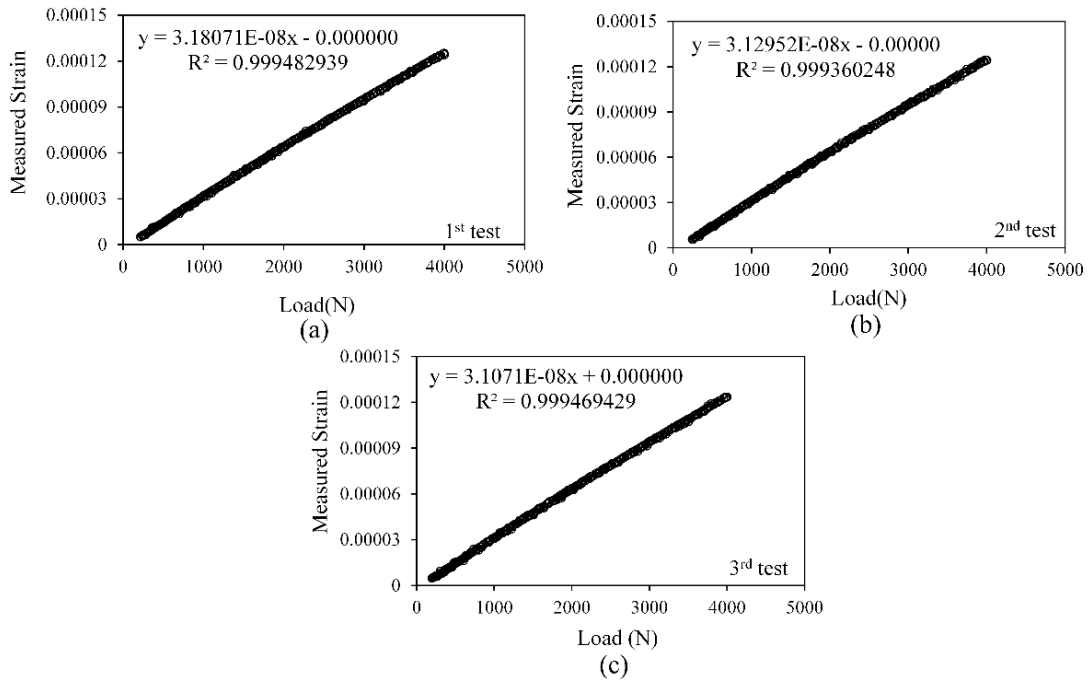

Figure 6.16 Measured strain (ε_{aa}) at $r_1 = 10$ mm for $a/b = 0.39$ for three repeated tests

Similarly, Figs. 6.17 – 6.20 show the raw data of measured strains ε_{aa} (circled data points) versus applied load corresponding to the strain gage readings at r_2 = 22 mm, r_3 = 32 mm, r_4 = 50 mm and r_5 = 60 mm in all the three repeated tests.

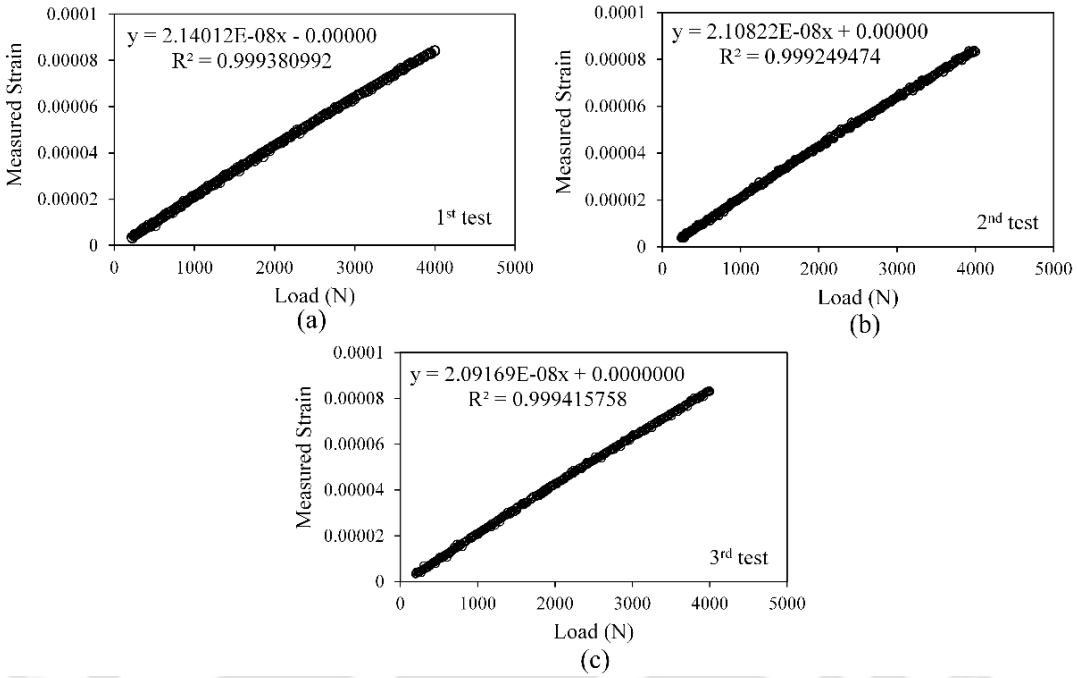

Figure 6.17 Measured strain (ε_{aa}) at $r_2 = 22\,\text{mm}$ for $a/b = 0.39$ for three repeated tests

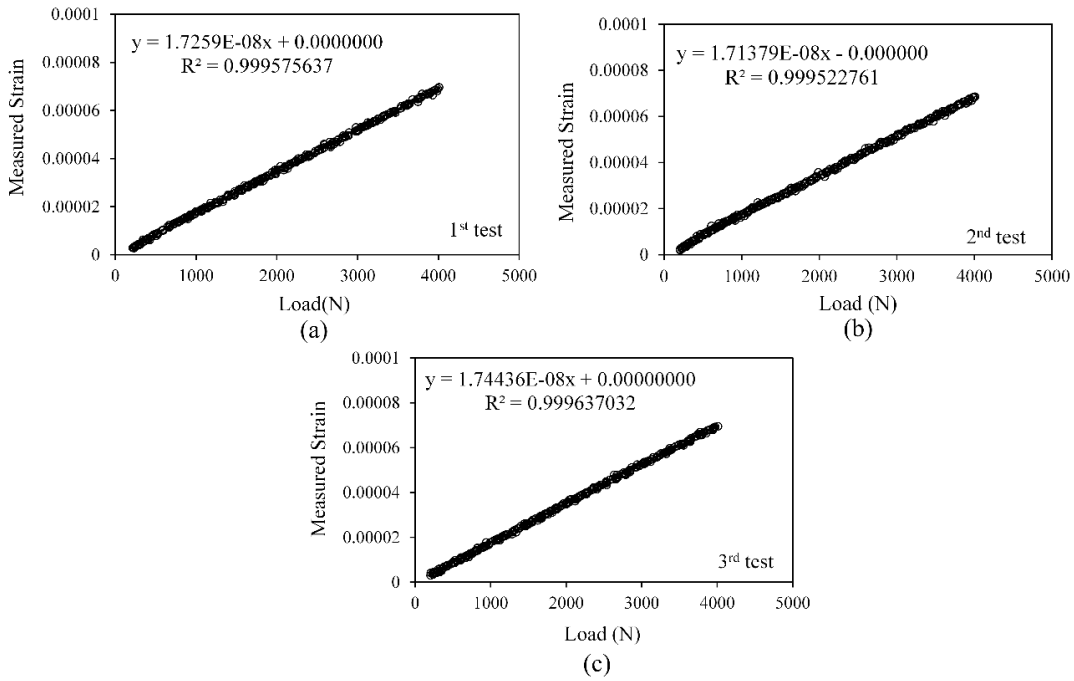

Figure 6.18 Measured strain (ε_{aa}) at $r_3 = 32\,\text{mm}$ for $a/b = 0.39$ for three repeated tests

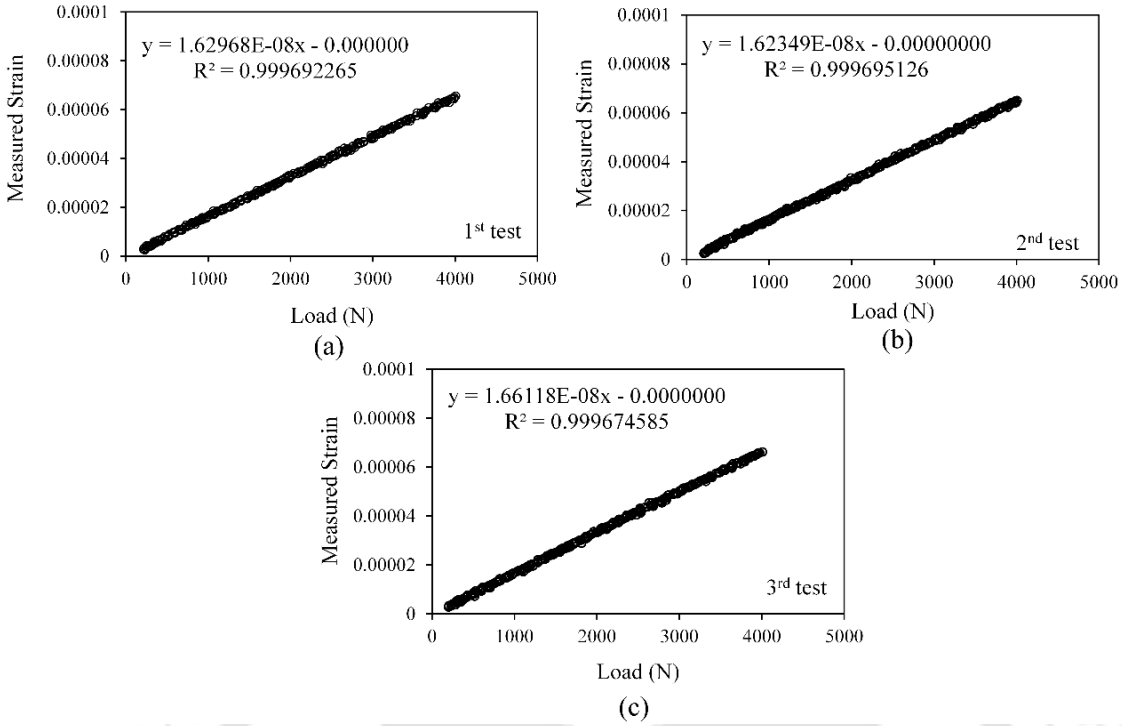

Figure 6.19 Measured strain (ε_{aa}) at $r_4 = 50\,\text{mm}$ for $a/b = 0.39$ for three repeated tests

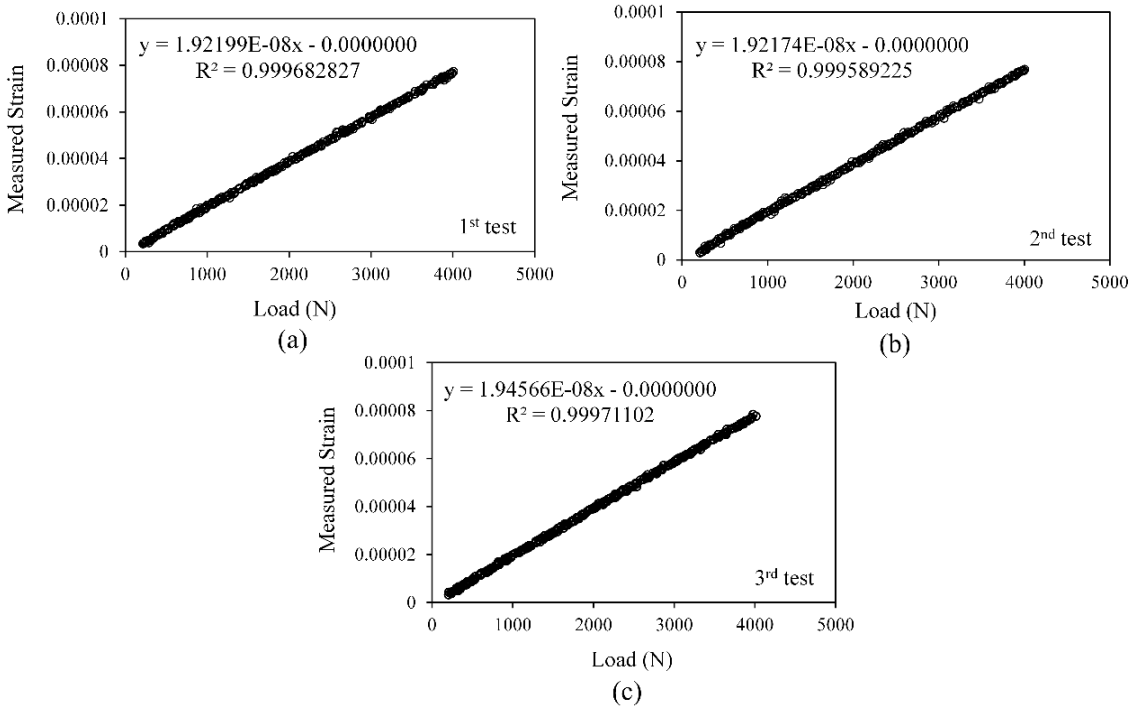

Figure 6.20 Measured strain (ε_{aa}) at $r_5 = 60\,\text{mm}$ for $a/b = 0.39$ for three repeated tests

The best-fit lines (solid lines) to the raw data along with the corresponding slopes and correlation coefficient R^2 are also shown in Figs. 6.17 – 6.20. A perfectly linear trend between the measured strains and the applied load and nearly same values of slopes of best-fit lines have been observed for each of the plot corresponding to a particular strain gage location. Table 6.8 shows the measured strains ε_{aa} for the strain gage located at $r_1 = 10\,\text{mm}$ obtained from the best-fit equations of a typical test (1st test in Fig. 6.16) for different values of applied loads. Using these strains, the singular coefficient, A_0 and hence K_I is then evaluated employing Eqs. (3.58) and (3.13) and material properties presented in Table 6.1. f_I is calculated using Eq. (6.1).

Table 6.8 Variation of K_I and f_I at $r_1 = 10\,\text{mm}$ with applied load in the 1st test $a/b = 0.39$

Load (N)	Measured strain, ε_{aa}	$K_I\left(\text{MPa}\sqrt{\text{mm}}\right)$	f_I
50	1.59036E-06	1.208	2.066
100	3.18071E-06	2.416	2.066
150	4.77107E-06	3.624	2.066
200	6.36142E-06	4.833	2.066
250	7.95178E-06	6.041	2.066
300	9.54213E-06	7.249	2.066

The experimentally measured values of K_I and f_I at different loads obtained using strain gage readings at $r_1 = 10\,\text{mm}$ are also shown in Table 6.8. It could be observed from the Table 6.8 that as expected while K_I is increasing with the increase in applied load, f_I remains constant irrespective of the applied load. Similar trends have also been obtained with the strain data of the other repeated tests as the slopes of the straight lines in each plot in Fig. 6.16 are almost equal.

Similarly, Tables 6.9 – 6.12 show the measured strains ε_{aa} for the strain gages located at $r_2 = 22$ mm, $r_3 = 32$ mm, $r_4 = 50$ mm and $r_5 = 60$ mm respectively obtained from the best fit equations of Figs. 6.17(a) – 6.20(a) respectively for different values of applied load. Using

these strain values and equivalent laminate properties (E_L, E_T, G_{LT} and ν_{LT} in Table 6.2) in Eq. (3.58) and Eq. (3.13), K_I has been computed for each load value and listed in the Tables 6.9 – 6.12. Using these experimental values of K_I, the f_I values are determined by employing Eq. (6.1) and are listed in Tables 6.9 – 6.12.

Table 6.9 Variation of K_I and f_I at $r_2 = 22\,\text{mm}$ with applied load in the 1st test $a/b = 0.39$

Load (N)	Measured strain, ε_{aa}	$K_I\left(\text{MPa}\sqrt{\text{mm}}\right)$	f_I
50	1.05682E-06	1.191	2.036
100	2.11364E-06	2.382	2.036
150	3.17046E-06	3.572	2.036
200	4.22728E-06	4.763	2.036
250	5.2841E-06	5.954	2.036
300	6.34092E-06	7.145	2.036

Table 6.10 Variation of K_I and f_I at $r_3 = 32\,\text{mm}$ with applied load in the 1st test $a/b = 0.39$

Load (N)	Measured strain, ε_{aa}	$K_I\left(\text{MPa}\sqrt{\text{mm}}\right)$	f_I
50	8.6295E-07	1.173	2.005
100	1.7259E-06	2.345	2.005
150	2.58885E-06	3.518	2.005
200	3.4518E-06	4.691	2.005
250	4.31475E-06	5.864	2.005
300	5.1777E-06	7.036	2.005

Table 6.11 Variation of K_I and f_I at $r_4 = 50\,\text{mm}$ with applied load in the 1st test $a/b = 0.39$

Load (N)	Measured strain, ε_{aa}	$K_I\left(\text{MPa}\sqrt{\text{mm}}\right)$	f_I
50	8.11195E-07	1.378	2.356
100	1.62239E-06	2.756	2.356
150	2.43359E-06	4.134	2.356
200	3.24478E-06	5.512	2.356
250	4.05598E-06	6.890	2.356
300	4.86717E-06	8.268	2.356

Table 6.12 Variation of K_I and f_I at $r_5 = 60\,\text{mm}$ with applied load in the 1st test $a/b = 0.39$

Load (N)	Measured strain, ε_{aa}	$K_I\left(\text{MPa}\sqrt{\text{mm}}\right)$	f_I
50	9.59565E-07	1.785	3.053
100	1.91913E-06	3.571	3.053
150	2.8787E-06	5.357	3.053
200	3.83826E-06	7.142	3.053
250	4.79783E-06	8.928	3.053
300	5.75739E-06	10.714	3.053

It could be noted from Tables 6.9 – 6.12 that here also K_I is increasing with increasing load while f_I remains constant with the load as expected. It should be noted that similar trends have been obtained with the strain data of other repeated tests as the slopes of the best-fit straight lines for all the tests corresponding to a particular strain gage location in Figs. 6.17 – 6.20 are almost equal. Table 6.13 shows the experimental values of f_I obtained at r_1, r_2, r_3, r_4 and r_5 for each of the three repeated experiments for a/b = 0.39 and their average values.

It could be observed that in all the three tests at a given location (r_1, r_2, r_3, r_4 or r_5) f_I values are very close to each other showing the repeatability of the results.

Table 6.13 Experimental values of f_I for three repeated tests for $a/b = 0.39$

Test	f_I				
	$r_1 = 10$ mm	$r_2 = 22$ mm	$r_3 = 32$ mm	$r_4 = 50$ mm	$r_5 = 60$ mm
1	2.066	2.036	2.000	2.367	3.053
2	2.033	2.031	1.991	2.358	3.058
3	2.018	2.015	2.005	2.413	3.096
Average	2.039	2.027	1.999	2.379	3.070

Table 6.14 shows the comparison of average non-dimensional SIF obtained from all the strain gages located at r_1, r_2, r_3, r_4 and r_5 with the reference solution obtained using DET (Table 6.6) in terms of the % relative error.

Table 6.14 Experimental values of f_I for $a/b = 0.39$ at different gage locations

Location	f_I		% Relative Error
	Reference Solution (Table 6.6)	Experimental Value	
Optimal $(r_1 = 10\,\text{mm} < r_{\max})$	2.062	2.039	1.11
Optimal $(r_2 = 22\,\text{mm} < r_{\max})$		2.027	1.68
Optimal $(r_3 = 32\,\text{mm} < r_{\max})$		1.999	3.04
Non- optimal $(r_4 = 50\,\text{mm} > r_{\max})$		2.379	15.38
Non- optimal $(r_5 = 60\,\text{mm} > r_{\max})$		3.070	48.92

It is observed from the results in Table 6.14 that the % relative error in f_I which is determined from the strain gage readings at the optimal location r_1, r_2, r_3 $(< r_{\max})$ is very less while those determined from the strain gage readings at the non-optimal location r_4, r_5 $(> r_{\max})$ is as high

as 49%. The above results clearly indicate that very accurate values of mode I SIFs can be determined using the proposed single strain gage technique when the gage is located at the proposed optimal locations. These experimental observations clearly substantiates the theoretical basis of the proposed numerical approach for determination of r_{max} and its existence and importance in deciding the optimal strain gage location for accurate determination of mode I SIF of orthotropic composites.

6.6.2 Experimental results for $a/b = 0.51$

Figure 6.15 (b) shows the specimen with $a/b = 0.51$ pasted with strain gages as per the radial locations mentioned in Table 6.7. As the same laminate is used to prepare all the test specimens, the angular coordinates of the gages are same as for $a/b = 0.39$. Like in previous section for $a/b = 0.39$ three repeated tests have been conducted on the specimen with $a/b = 0.51$.

Figure 6.21 shows the raw data of measured strains ε_{aa} (circled data points) for the strain gage located at r_1 = 10 mm versus the applied load for the specimen with a/b = 0.51 for all the three repeated tests.

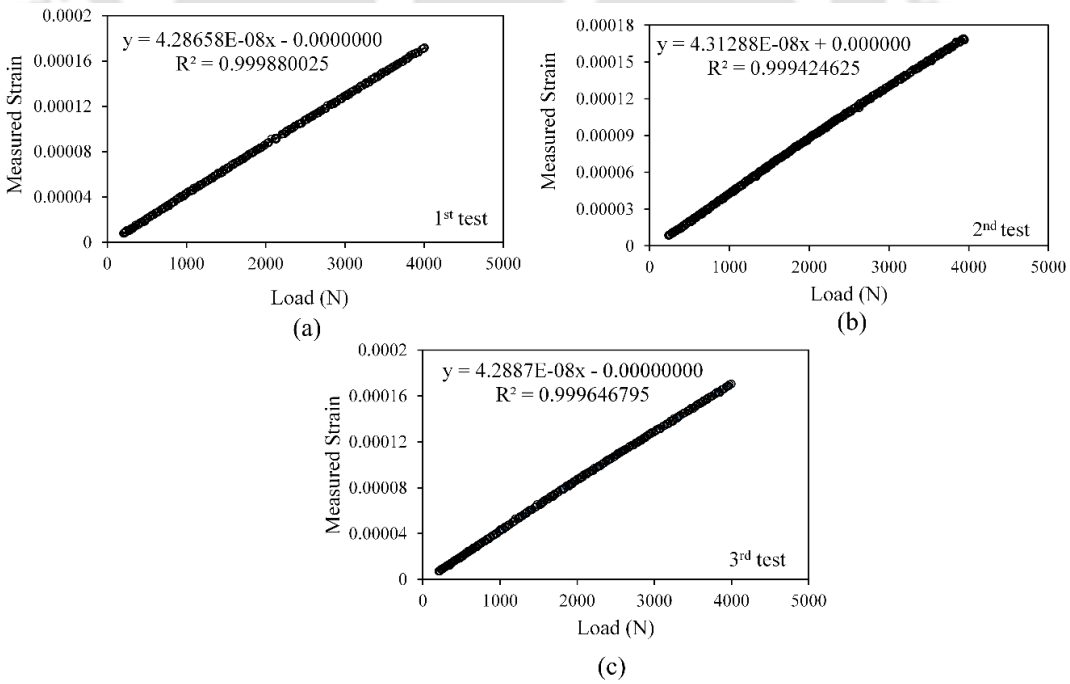

Figure 6.21 Measured strain (ε_{aa}) at $r_1 = 10$ mm for $a/b = 0.51$ for three repeated tests

Figure 6.21 also shows best-fit straight lines (solid lines) to the raw data with the corresponding slopes and the correction coefficients R^2. As expected, in all the repeated loads, the measured strains are linearly proportional to the applied load and slopes of best-fit lines in all the repeated tests are also nearly same, which yet again reinforces the excellent calibration of the entire experimental setup.

Figures 6.22 – 6.25 show the raw data of measured strains ε_{aa} (circled data points) versus applied load for the strain gages at r_2 = 19 mm, r_3 = 35 mm, r_4 = 60 mm and r_5 = 70 mm respectively for all the three repeated tests. The best-fit lines to the raw data (solid lines) along with their corresponding slopes and correlation coefficient R^2 are shown in Figs.6.22 – 6.25. Here also a perfectly linear trend between the measured strains and the applied load and similar slopes of best-fit lines in all the three repeated test have been observed as expected.

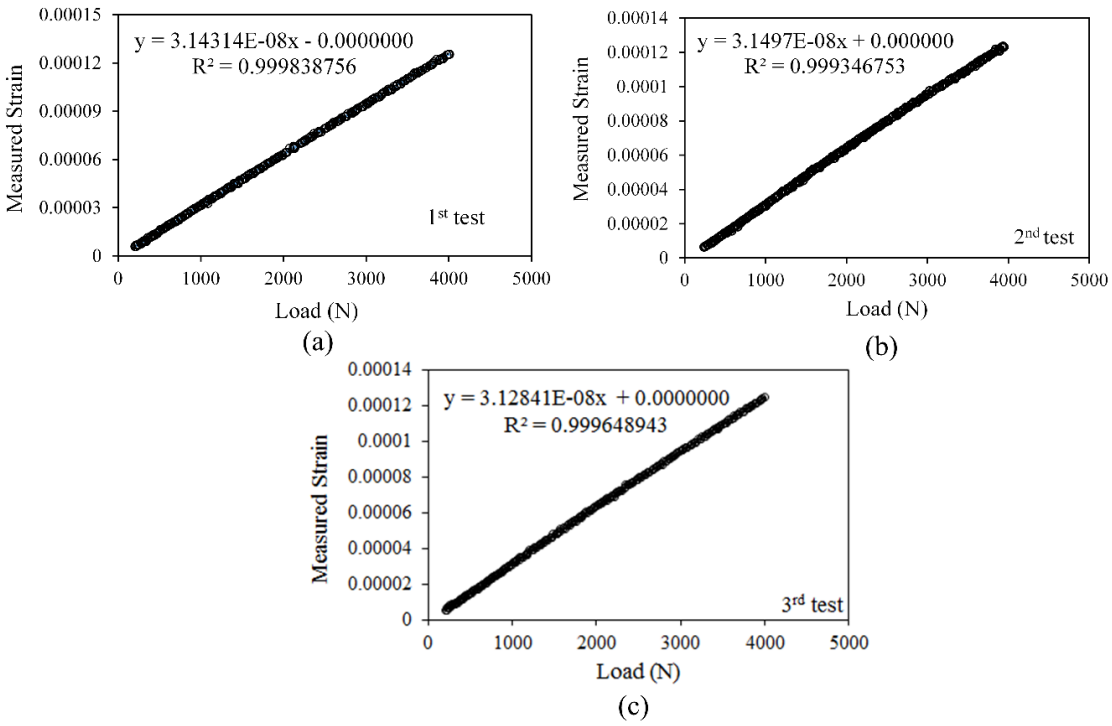

Figure 6.22 Measured strain (ε_{aa}) at $r_2 = 19\,\text{mm}$ for $a/b = 0.51$ for three repeated tests

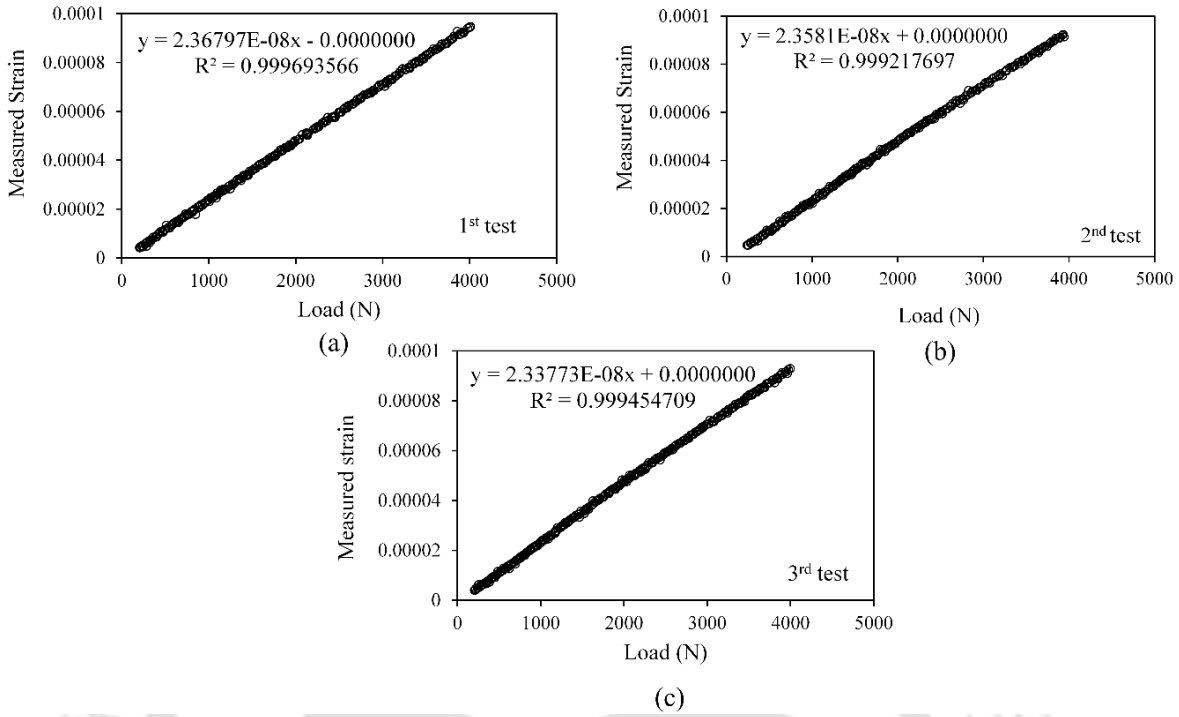

Figure 6.23 Measured strain (ε_{aa}) at $r_3 = 35\,\text{mm}$ for $a/b = 0.51$ for three repeated tests

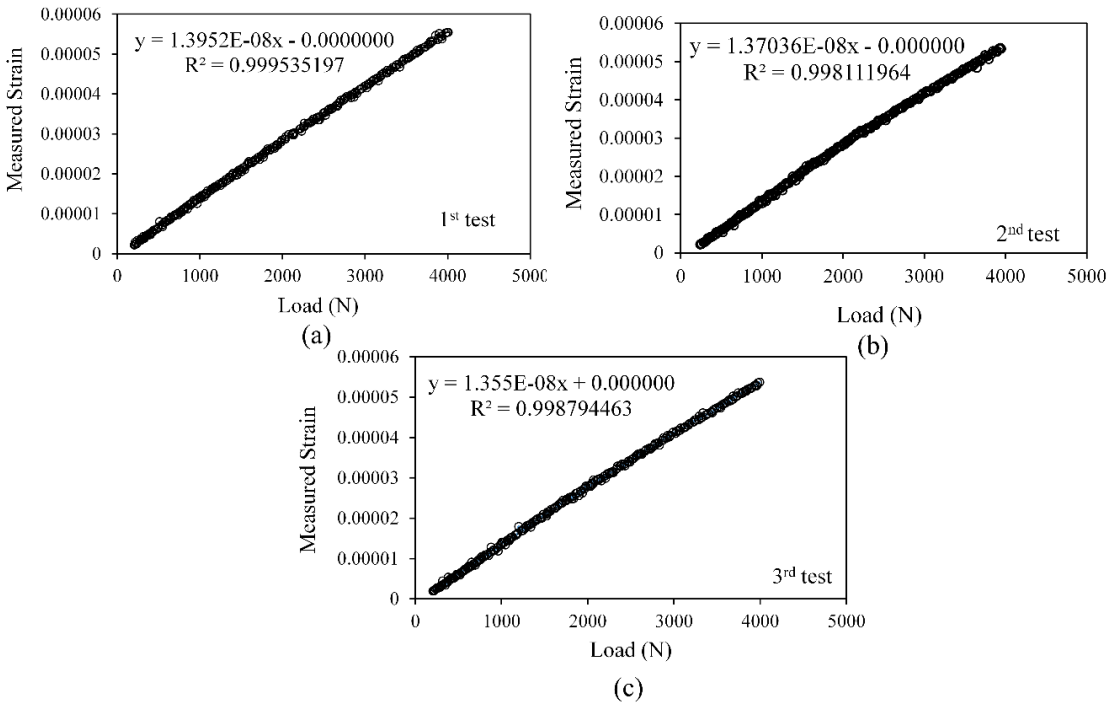

Figure 6.24 Measured strain (ε_{aa}) at $r_4 = 60\,\text{mm}$ for $a/b = 0.51$ for three repeated tests

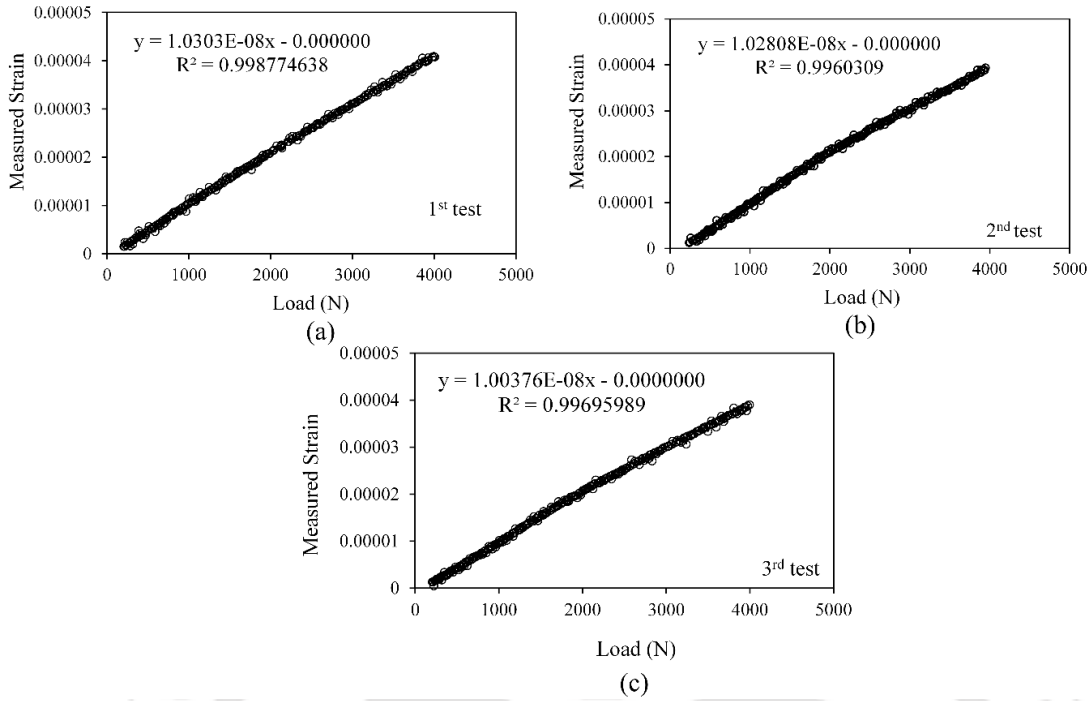

Figure 6.25 Measured strain (ε_{aa}) at $r_5 = 70\,\text{mm}$ for $a/b = 0.51$ for three repeated tests

Tables 6.15 – 6.19 show the measured strains ε_{aa} from the best-fit plots (Figs. 6.21 – 6.23) and the corresponding K_I and f_I determined (using Eqs. (3.58), (3.13) and (6.3), respectively) for strain gages located at r_1 = 10 mm, r_2 = 19 mm, $r_3 = 35$ mm, r_4 = 60 mm and $r_5 = 70$ mm, respectively for different values of applied load for the specimen with a/b = 0.51.

Table 6.15 Variation of K_I and f_I at $r_1 = 10\,\text{mm}$ with applied load in the 1st test $a/b = 0.51$

Load (N)	Measured strain, ε_{aa}	$K_I\left(\text{MPa}\sqrt{\text{mm}}\right)$	f_I
50	2.15644E-06	1.638	2.78
100	4.31288E-06	3.276	2.78
150	6.46932E-06	4.915	2.78
200	8.62576E-06	6.553	2.78
250	1.07822E-05	8.191	2.78
300	1.29386E-05	9.829	2.78

Table 6.16 Variation of K_I and f_I at $r_2 = 19\,\text{mm}$ with applied load in the 1st test $a/b = 0.51$

Load (N)	Measured strain, ε_{aa}	$K_I\left(\text{MPa}\sqrt{\text{mm}}\right)$	f_I
50	1.56755E-06	1.641	2.785
100	3.1351E-06	3.283	2.785
150	4.70265E-06	4.924	2.785
200	6.2702E-06	6.566	2.785
250	7.83775E-06	8.207	2.785
300	9.4053E-06	9.849	2.785

Table 6.17 Variation of K_I and f_I at $r_3 = 35\,\text{mm}$ with applied load in the 1st test $a/b = 0.51$

Load (N)	Measured strain, ε_{aa}	$K_I\left(\text{MPa}\sqrt{\text{mm}}\right)$	f_I
50	1.17297E-06	1.667	2.829
100	2.34594E-06	3.334	2.829
150	3.51891E-06	5.001	2.829
200	4.69188E-06	6.668	2.829
250	5.86485E-06	8.335	2.829
300	7.03782E-06	10.002	2.829

Table 6.18 Variation of K_I and f_I at $r_4 = 60\,\text{mm}$ with applied load in the 1st test $a/b = 0.51$

Load (N)	Measured strain, ε_{aa}	$K_I\left(\text{MPa}\sqrt{\text{mm}}\right)$	f_I
50	6.8518E-07	1.275	2.163
100	1.37036E-06	2.550	2.163
150	2.05554E-06	3.825	2.163
200	2.74072E-06	5.100	2.163
250	3.4259E-06	6.375	2.163
300	4.11108E-06	7.650	2.163

Table 6.19 Variation of K_I and f_I at $r_5 = 70\,\text{mm}$ with applied load in the 1st test $a/b = 0.51$

Load (N)	Measured strain, ε_{aa}	$K_I\left(\text{MPa}\sqrt{\text{mm}}\right)$	f_I
50	4.99219E-07	1.003	1.703
100	9.98437E-07	2.007	1.703
150	1.49766E-06	3.010	1.703
200	1.99687E-06	4.013	1.703
250	2.49609E-06	5.017	1.703
300	2.99531E-06	6.020	1.703

As in case of a/b = 0.39, here also K_I increases with increasing load but f_I being non-dimensional is independent of load as expected at all strain gage locations r_1, r_2, r_3, r_4 and r_5. Table 6.20 shows the f_I values obtained for all the strain gage readings on the specimen with a/b = 0.51 for all the three repeated tests and their corresponding average values. Once again it can be observed from Table 6.20 that, for a given radial location, the K_I values in all the repeated tests are almost same. This trend clearly substantiates the excellent repeatability of the present experimental procedure.

Table 6.20 Experimental values of f_I for three repeated tests for $a/b = 0.51$

Test	f_I				
	$r_1 = 10$ mm	$r_2 = 19$ mm	$r_3 = 35$ mm	$r_4 = 60$ mm	$r_5 = 70$ mm
1	2.763	2.792	2.855	2.203	1.757
2	2.780	2.785	2.843	2.163	1.702
3	2.764	2.779	2.812	2.139	1.687
Average	2.769	2.785	2.839	2.168	1.715

Table 6.21 shows the comparison of experimental values of the average f_I values obtained from the present experiments for a/b = 0.51 at all the strain gage locations (r_1, r_2, r_3, r_4 and r_5) with the reference solution obtained using DET (Table 6.6) in terms of % relative error.

Table 6.21 Experimental values of f_I for $a/b = 0.51$ at different gage locations

Location	f_I		% Relative Error
	Reference Solution (Table 6.6)	Experimental Value	
Optimal $(r_1 = 10\,\text{mm} < r_{max})$	2.768	2.769	0.04
Optimal $(r_2 = 19\,\text{mm} < r_{max})$		2.786	0.65
Optimal $(r_3 = 35\,\text{mm} < r_{max})$		2.839	2.57
Non-optimal $(r_4 = 60\,\text{mm} > r_{max})$		2.168	21.65
Non-optimal $(r_5 = 70\,\text{mm} > r_{max})$		1.715	38.02

It could be observed from these results that the % relative error in f_I calculated from the strain gage readings at the selected optimal locations r_1, r_2 and r_3 ($< r_{max}$) are as low as 0.04%, 0.65% and 2.57% respectively, while the error in f_I estimated from the strain gage readings

at the non-optimal location r_4 and r_5 ($> r_{max}$) is as high as 21% and 38%. These experimental observations once again substantiates the efficacy of the proposed single strain gage technique with optimal gage locations. Further, the present results also verifies the suggested procedures for r_{max} and its importance in deciding the optimal strain gage locations for accurate determination of mode I SIF of cracked orthotropic laminates. The results in Table 6.21 also indicate towards the high error in SIF if the gages are located at non-optimal locations provided r_{max} is not known prior to experiments.

6.6.3 Experimental results for $a/b = 0.61$

For the mode I orthotropic laminate with a/b =0.61 (Fig. 6.15 (c)), the r_{max} is 23 mm and two strain gage locations $(r_1 = 10 \text{ mm}$ and $r_2 = 18 \text{ mm})$ are selected at optimal locations and two other gage locations $(r_3 = 30 \text{ mm}$ and $r_4 = 40 \text{ mm})$ are selected outside the r_{max} (non-optimal locations) respectively for determination of K_I. Figures 6.26 and 6.27 show the raw data of measured strain ε_{aa} (circled data points) versus the applied load for all the three repeated tests at r_1 = 10 mm and r_2 = 18 mm respectively i.e. the strain gages within the optimal location. Figures 6.26 and 6.27 also show the best-fit straight lines to the raw data (solid lines) along with the corresponding slopes and the correction coefficients R^2. It may be observed that in all the repeated tests, the measured strains are linearly proportional to the applied load which follows from similar results conducted for other mode I configurations in the previous examples.

Figures 6.28 and 6.29 show the raw data of measured strains ε_{aa} versus applied load for the strain gages at the non-optimal locations (r_3 = 30 mm and r_4 = 40 mm) for all the three repeated tests. The best-fit lines to the raw data (solid lines) along with their corresponding slopes and correlation coefficient R^2 are also shown in the respective figures. Perfectly linear trends between the measured strains and the applied load with consistent repeatability (identical slopes of best-fit lines) across all the three repeated test at all the gage locations can be observed

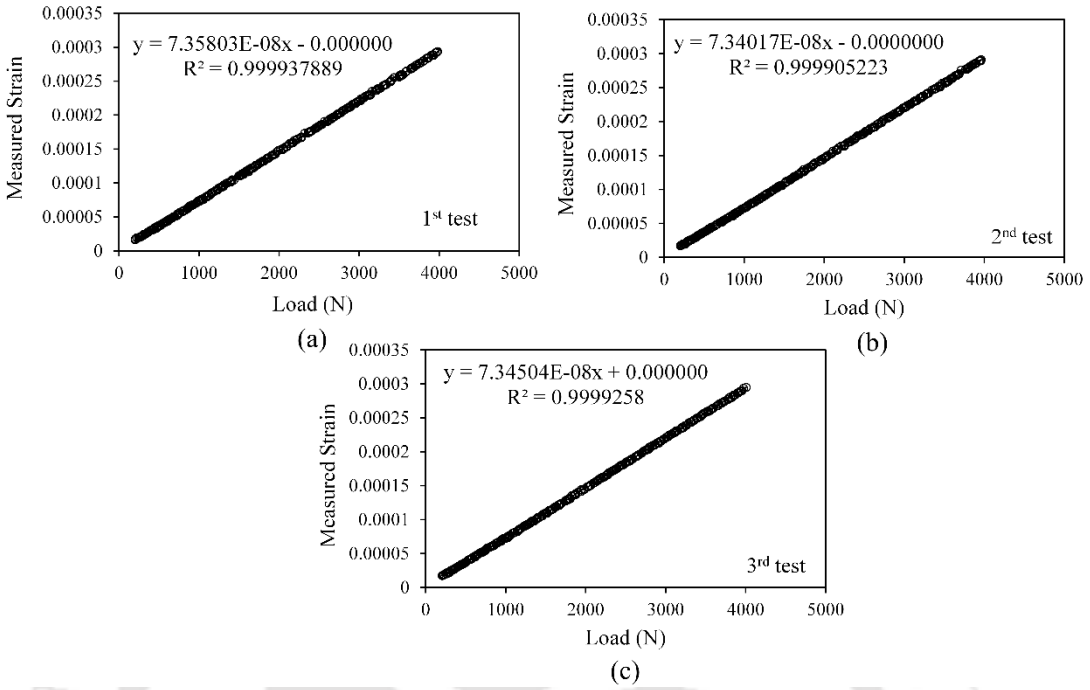

Figure 6.26 Measured strain (ε_{aa}) at $r_1 = 10\,\text{mm}$ for $a/b = 0.61$ for three repeated tests

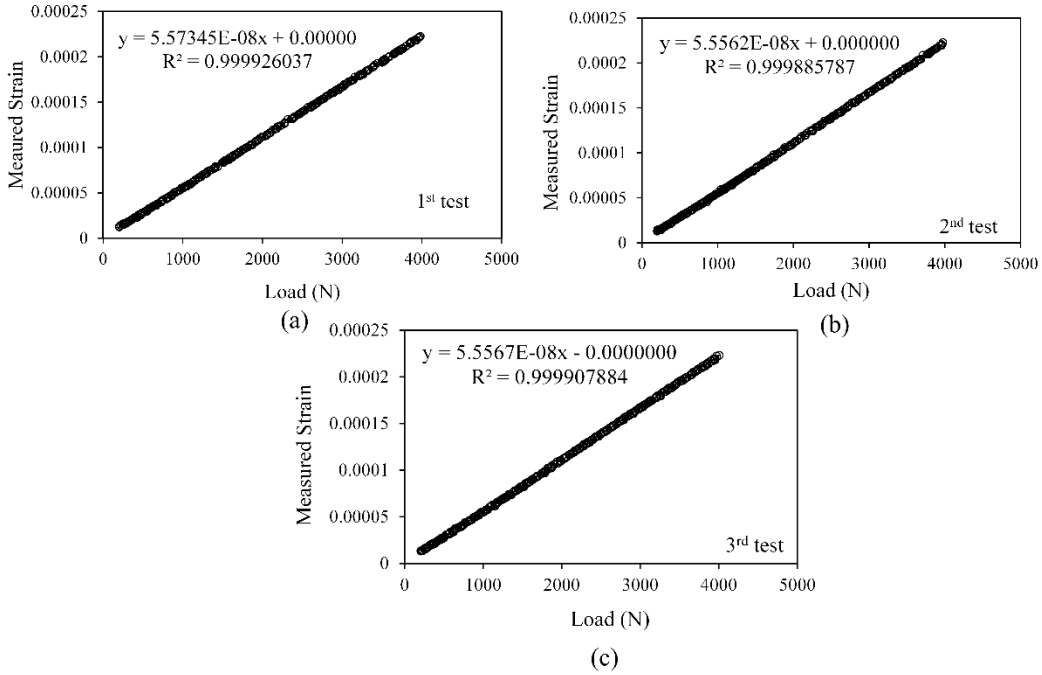

Figure 6.27 Measured strain (ε_{aa}) at $r_2 = 18\,\text{mm}$ for $a/b = 0.61$ for three repeated tests

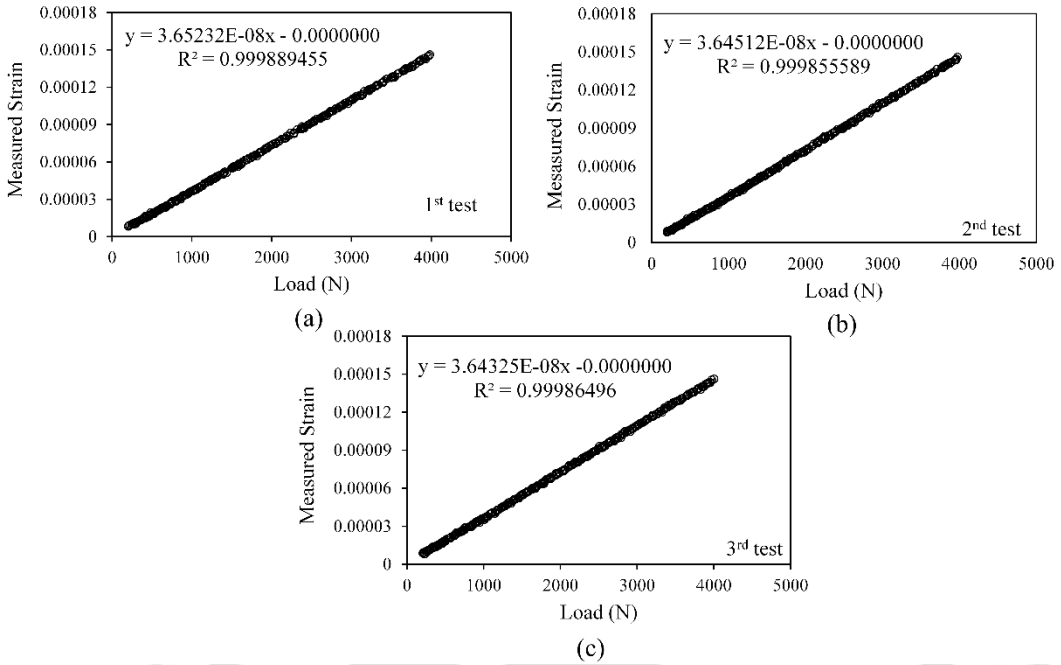

Figure 6.28 Measured strain (ε_{aa}) at $r_3 = 30\,\text{mm}$ for $a/b = 0.61$ for three repeated tests

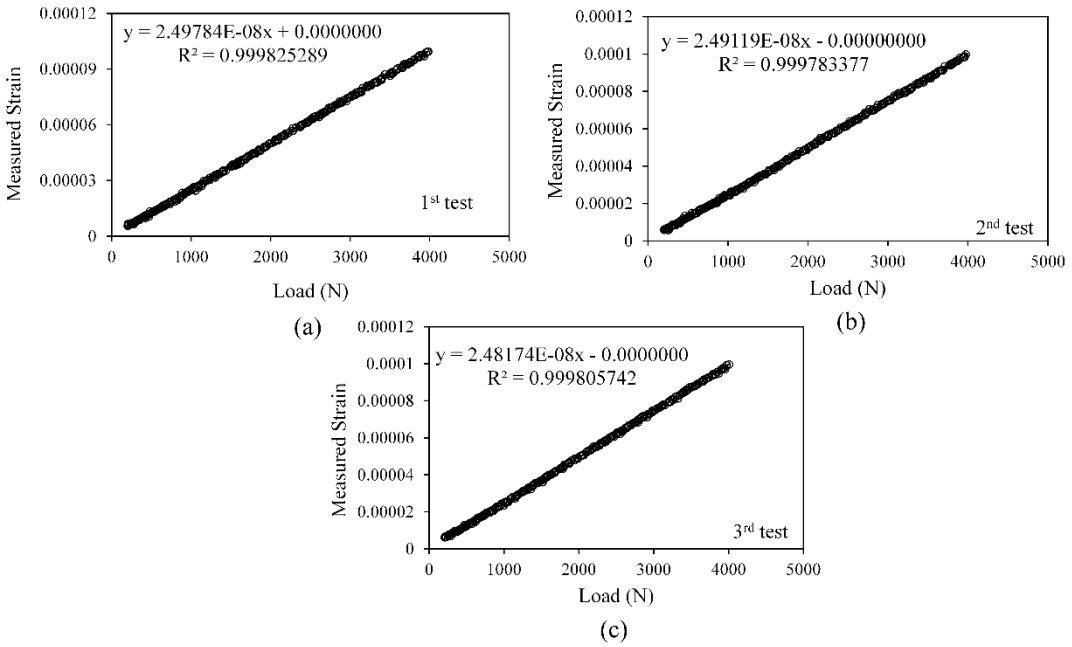

Figure 6.29 Measured strain (ε_{aa}) at $r_4 = 40\,\text{mm}$ for $a/b = 0.61$ for three repeated tests

Tables 6.22 – 6.25 show the measured strains obtained from the best-fit equations (Figs. 6.26 – 6.29) for different values of applied loads and for all the strain gages located at r_1 = 10 mm, r_2 = 18 mm, r_3 = 30 mm and r_4 = 40mm respectively. Using these strain values and material

properties in Eqs. (3.58) and (3.13), the experimental values of K_I have been computed corresponding to different load values. Normalized SIF, f_I is then computed using the experimental values of K_I by employing Eq. (6.1). The experimental values of K_I and f_I at different loads are also enlisted in Table 6.22 – 6.25. Results in these tables show that K_I increases with the increase in applied load and f_I remains constant irrespective of the applied load, similar to the results in previous sections.

Table 6.22 Variation of K_I and f_I at $r_1 = 10\,\text{mm}$ with applied load in the 1st test $a/b = 0.61$

Load (N)	Measured strain, ε_{aa}	$K_I\left(\text{MPa}\sqrt{\text{mm}}\right)$	f_I
50	3.67272E-06	2.768	4.697
100	7.34544E-06	5.537	4.697
150	1.10182E-05	8.305	4.697
200	1.46909E-05	11.073	4.697
250	1.83636E-05	13.842	4.697
300	2.20363E-05	16.610	4.697

Table 6.23 Variation of K_I and f_I at $r_2 = 18\,\text{mm}$ with applied load in the 1st test $a/b = 0.61$

Load (N)	Measured strain, ε_{aa}	$K_I\left(\text{MPa}\sqrt{\text{mm}}\right)$	f_I
50	2.77848E-06	2.81	4.768
100	5.55695E-06	5.62	4.768
150	8.33543E-06	8.429	4.768
200	1.11139E-05	11.239	4.768
250	1.38924E-05	14.049	4.768
300	1.66709E-05	16.86	4.768

Table 6.24 Variation of K_I and f_I at $r_3 = 30\,\text{mm}$ with applied load in the 1st test $a/b = 0.61$

Load (N)	Measured strain, ε_{aa}	$K_I\left(\text{MPa}\sqrt{\text{mm}}\right)$	f_I
50	1.82168E-06	2.378	4.035
100	3.64336E-06	4.757	4.035
150	5.46504E-06	7.135	4.035
200	7.28672E-06	9.513	4.035
250	9.1084E-06	11.891	4.035
300	1.09301E-05	14.27	4.035

Table 6.25 Variation of K_I and f_I at $r_4 = 40\,\text{mm}$ with applied load in the 1st test $a/b = 0.61$

Load (N)	Measured strain, ε_{aa}	$K_I\left(\text{MPa}\sqrt{\text{mm}}\right)$	f_I
50	1.24073E-06	1.870	3.174
100	2.48145E-06	3.741	3.174
150	3.72218E-06	5.611	3.174
200	4.9629E-06	7.482	3.174
250	6.20363E-06	9.352	3.174
300	7.44435E-06	11.222	3.174

The experimental values of f_I obtained at r_1, r_2, r_3 and r_4 for each of the three repeated experiments for a/b = 0.61 along with the average values of f_I are listed in Table 6.26. Excellent repeatability in measurement of f_I can be noticed from Table 6.26. Table 6.27 shows comparison of the average f_I obtained from the present experiments for a/b = 0.61 (Table 6.26) at all the gage locations (r_1, r_2, r_3 and r_4) with the reference solution obtained using DET (Table 6.6) in terms of the % relative error.

Table 6.26 Experimental values of f_I for three repeated tests for $a/b = 0.61$

Test	f_I			
	$r_1 = 10\,\text{mm}$	$r_2 = 18\ \text{mm}$	$r_3 = 30\,\text{mm}$	$r_4 = 40\ \text{mm}$
1	4.720	4.782	4.045	3.195
2	4.697	4.767	4.037	3.168
3	4.694	4.776	4.035	3.174
Average	4.7036	4.7751	4.0421	3.1789

Table 6.27 Experimental values of f_I for $a/b = 0.61$ at different gage locations

Location	f_I		% Relative Error
	Reference Solution (Table 6.6)	Experimental Value	
Optimal $(r_1 = 10\,\text{mm} < r_{\max})$	4.658	4.704	0.987
Optimal $(r_2 = 18\,\text{mm} < r_{\max})$		4.775	2.52
Non-optimal $(r_3 = 30\,\text{mm} > r_{\max})$		4.042	13.21
Non-optimal $(r_4 = 40\,\text{mm} > r_{\max})$		3.179	31.75

It could be observed once again from these results that the % relative error in f_I estimated from the strain gage readings at the selected optimal locations r_1, r_2 $(< r_{\max})$ is very less, of the order of 0.98%, while those determined using the strain gage reading at the non-optimal locations r_3, r_4 $(> r_{\max})$ are as high as 32%. These experimental observations yet again validates the proposed approach for determination of mode I SIF of orthotropic laminates using a single strain gage when placed with the optimal location.

6.6.4 Experimental results for $a/b = 0.71$

Finally, for the mode I orthotropic laminate with a/b =0.71 (Fig. 6.15 (d)), for which r_{max} is 18.8 mm, two optimal strain gage locations at r_1, r_2 = 9 mm, 17 mm and the other two non-optimal locations at r_3, r_4 = 35 mm, 45 mm (Table 6.7) respectively are selected for the purpose of experimental verification of optimal strain gage locations to be used in accurate determination of mode I SIF of the orthotropic laminates. The raw data of measured strain ε_{aa} (circled data points) versus the applied load for all the three repeated tests at r_1 = 9 mm and r_2 = 17 mm are shown in Figs. 6.30 and 6.31 respectively. The best-fit straight lines to the raw data (solid lines) along with the corresponding slopes and the correction coefficients R^2 are also shown in Figs. 6.30 an 6.31. The measured strains in all plots of Figs 6.30 and 6.31 for all the repeated tests are linearly proportional to the applied load thereby reinforcing the good calibration of the entire experimental setup.

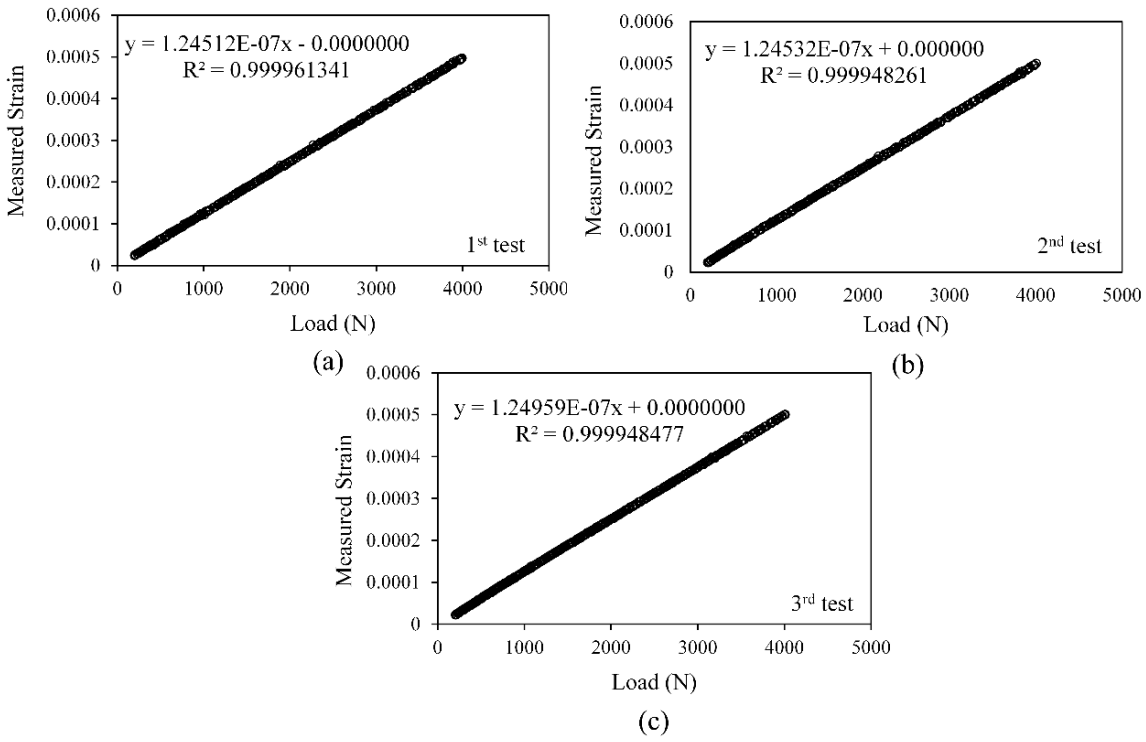

Figure 6.30 Measured strain (ε_{aa}) at $r_1 = 9\,\text{mm}$ for $a/b = 0.71$ for three repeated tests

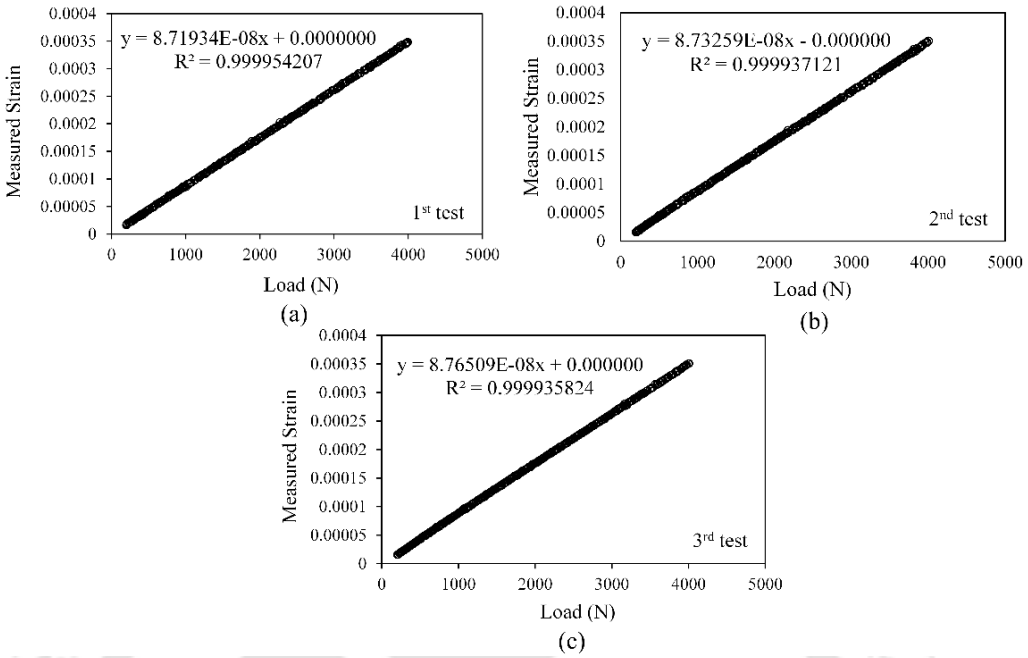

Figure 6.31 Measured strain (ε_{aa}) at $r_2 = 17\,\text{mm}$ for $a/b = 0.71$ for three repeated tests

Figures 6.32 and 6.33 show the raw data of measured strains ε_{aa} versus applied load for the strain gages located at the non-optimal locations r_3 = 35 mm and r_4 = 45 mm respectively, along with the best-fit lines to the raw data for all three repeated tests.

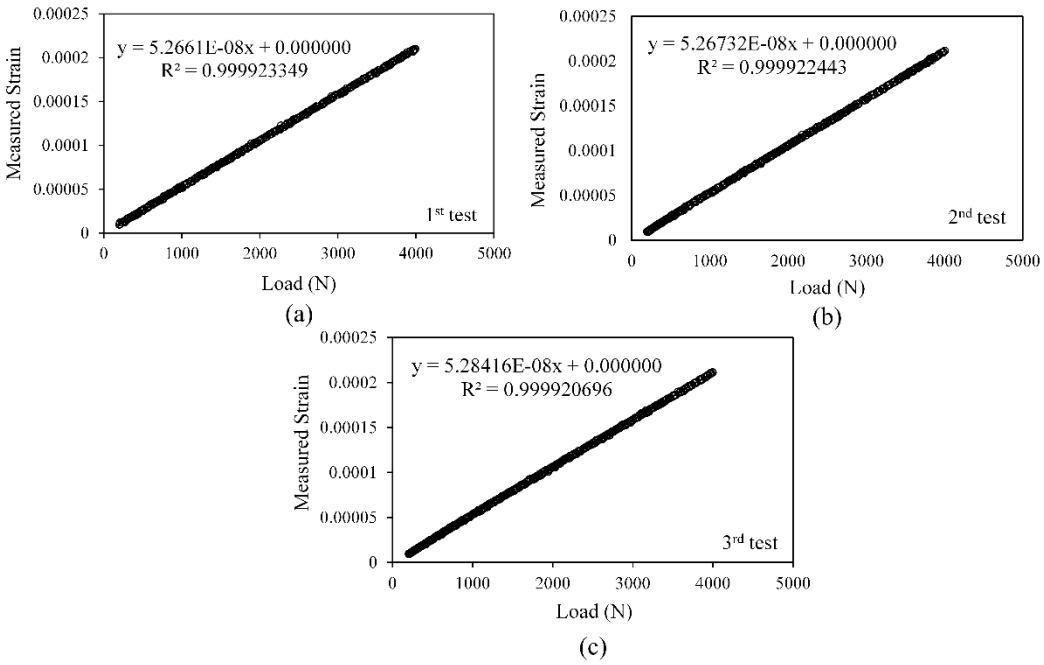

Figure 6.32 Measured strain (ε_{aa}) at $r_3 = 35\,\text{mm}$ for $a/b = 0.71$ for three repeated tests

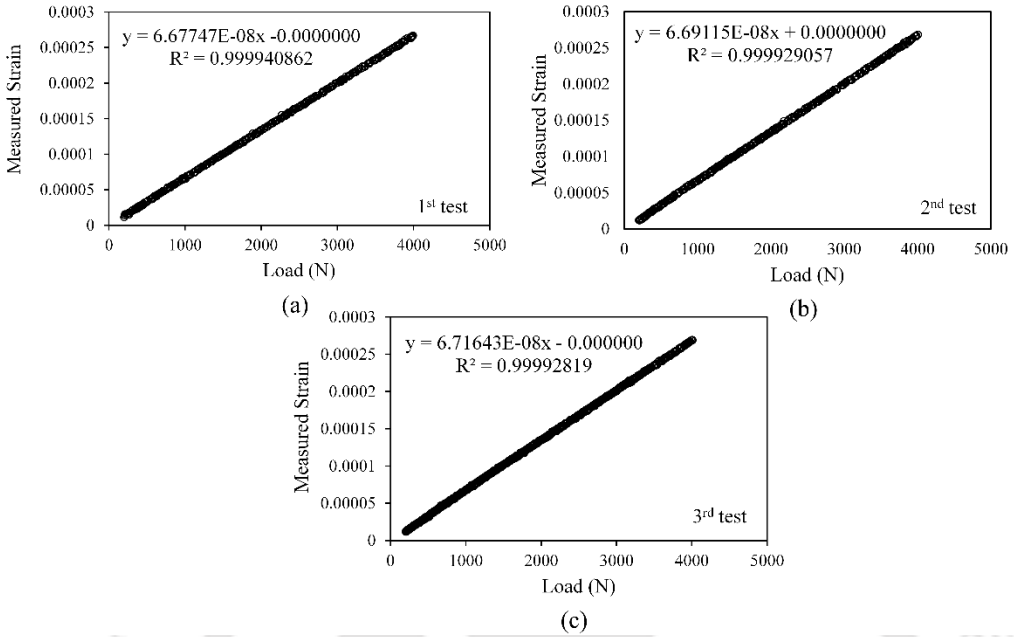

Figure 6.33 Measured strain (ε_{aa}) at $r_4 = 45$ mm for $a/b = 0.71$ for three repeated tests

The measured strains obtained from the best-fit equations at different values of applied load for the strain ages located at different radial locations, r_1 = 9 mm, r_2 = 17 mm, r_3 = 35 mm and r_4 = 45 mm are enlisted in Tables 6.28 – 6.31 respectively. The experimental values of K_I are computed at each load value for each radial position using Eqs. (3.58) and (3.13) employing the orthotropic material properties of the considered specimen (Table 6.1) and the respective strain values. Eq. (6.1) is employed to compute the non-dimensional SIF, f_I. The experimental values of K_I and f_I at different loads for the radial positions, r_1 = 9 mm, r_2 = 17 mm, r_3 = 30 mm and r_4 = 40 mm are also given in Tables 6.28 – 6.31 respectively. Analogous to previous examples, here also K_I increases with the increase in applied load, however f_I remains constant irrespective of the applied load as per the properties of non-dimensional SIF.

Table 6.28 Variation of K_I and f_I at $r_1 = 9\,\text{mm}$ with applied load in the 1st test $a/b = 0.71$

Load (N)	Measured strain, ε_{aa}	$K_I\left(\text{MPa}\sqrt{\text{mm}}\right)$	f_I
50	6.2266E-06	4.487	7.614
100	1.24532E-05	8.975	7.614
150	1.86798E-05	13.463	7.614
200	2.49064E-05	17.950	7.614
250	3.1133E-05	22.438	7.614
300	3.73596E-05	26.925	7.614

Table 6.29 Variation of K_I and f_I at $r_2 = 17\,\text{mm}$ with applied load in the 1st test $a/b = 0.71$

Load (N)	Measured strain, ε_{aa}	$K_I\left(\text{MPa}\sqrt{\text{mm}}\right)$	f_I
50	4.3663E-06	4.325	7.338
100	8.73259E-06	8.65	7.338
150	1.30989E-05	12.975	7.338
200	1.74652E-05	17.299	7.338
250	2.18315E-05	21.62	7.338
300	2.61978E-05	25.949	7.338

Table 6.30 Variation of K_I and f_I at $r_3 = 35\,\text{mm}$ with applied load in the 1st test $a/b = 0.71$

Load (N)	Measured strain, ε_{aa}	$K_I\left(\text{MPa}\sqrt{\text{mm}}\right)$	f_I
50	2.63366E-06	3.743	6.351
100	5.26732E-06	7.486	6.351
150	7.90098E-06	11.229	6.351
200	1.05346E-05	14.972	6.351
250	1.31683E-05	18.716	6.351
300	1.5802E-05	22.459	6.351

Table 6.31 Variation of K_I and f_I at $r_4 = 45\,\text{mm}$ with applied load in the 1st test $a/b = 0.71$

Load (N)	Measured strain, ε_{aa}	$K_I\left(\text{MPa}\sqrt{\text{mm}}\right)$	f_I
50	3.34558E-06	5.391	9.148
100	6.69115E-06	10.783	9.148
150	1.00367E-05	16.175	9.148
200	1.33823E-05	21.566	9.148
250	1.67279E-05	26.958	9.148
300	2.00735E-05	32.349	9.148

The experimental values of f_I obtained at r_1, r_2, r_3 and r_4 for each of the three repeated experiments for a/b = 0.71 along with the average values of f_I at each location are given in Table 6.32 and it may be observed that for a particular location f_I values across all the three tests are approximately the same showing the precision of the experimental results. The comparison of the average f_I values obtained from the present experiments for a/b = 0.71 (Table 6.33) at all the strain gage locations (r_1, r_2, r_3 and r_4) with the reference solution obtained using DET (Table 6.6) is shown in Table 6.33 in terms of the % relative error.

Table 6.32 Experimental values of f_I for three repeated tests for $a/b = 0.71$

Test	f_I			
	$r_1 = 9\,\text{mm}$	$r_2 = 17$ mm	$r_3 = 35\,\text{mm}$	$r_4 = 45$ mm
1	7.591	7.327	6.349	9.13
2	7.614	7.338	6.351	9.148
3	7.640	7.366	6.372	9.183
Average	7.615	7.344	6.357	9.154

Table 6.33 Experimental values of f_I for $a/b = 0.71$ at different gage locations

Location	f_I		% Relative Error
	Reference Solution (Table 6.6)	Experimental Value	
Optimal $(r_1 = 9\,\text{mm} < r_{\max})$	7.582	7.615	0.44
Optimal $(r_2 = 17\,\text{mm} < r_{\max})$		7.344	3.14
Non-optimal $(r_3 = 35\,\text{mm} > r_{\max})$		6.357	16.28
Non- optimal $(r_4 = 45\,\text{mm} > r_{\max})$		9.154	20.72

The results indicate that the % relative error in f_I at the selected optimal locations r_1, r_2 ($< r_{\max}$) is very less, of the order of 0.44% and 3.1% while the values of f_I estimated from the strain gage readings at the non-optimal locations r_3, r_4 ($> r_{\max}$) are highly erroneous, the error percent being as high as 16% and 21%. The estimation of mode I SIF of orthotropic laminates using a single strain gage and the existence of optimal locations for the strain gage is substantiated once again through these experimental observations.

6.6.5 Additional tests to substantiate accuracy and repeatability

In the previous sections four edge-cracked specimens with different a/b have been considered and each configuration is tested three times to examine the primary repeatability and accuracy of the proposed experimental technique. In this section, contrast to the previous sections, three identical specimens of $a/b = 0.51$ have been prepared and used to investigate the reproducibility and accuracy of the experimental procedure for determination of K_I of orthotropic laminates using the proposed single gage technique.

These additional test results are presented and discussed in this section. Figure 6.34 shows all the three specimens along with the gages pasted according to the radial locations mentioned in Table 6.7. Since, all the three specimens have $a/b = 0.51$, same gages locations on each specimen are maintained as in Table 6.7. Like in previous sections, three repeated tests have been conducted on each of these three specimens. The results for Specimen 1 are already presented in section 6.6.2 and therefore not repeated here.

(a) (b) (c)

Figure 6.34 Mode I specimens with $a/b = 0.51$

The best-fit plots and slopes for the raw data at different gage locations for all the repeated test for the other two specimens (Specimen 2 and Specimen 3) are found to be similar to that

has been observed for Specimen 1 with $a/b = 0.5$. Figures 6.35 and 6.36 show the raw data of measured strains versus applied load for the strain gages located at r_1 = 10 mm, r_2 = 19 mm, r_3 = 35 mm, r_4 = 60 mm and r_5 = 70 mm for Specimen 2 and Specimen 3 respectively for the 1st test conducted on each specimen. It may be observed from Figs. 6.35 and 6.36 and Figs. 6.21 – 6.25 in section 6.6.2 that the slopes are almost same at a particular gage location (r_1 = 10 mm, r_2 = 19 mm, r_3 = 35 mm, r_4 = 60 mm and r_5 = 70 mm) for all the three specimens with a/b = 0.51 thereby reinforcing the excellent repeatability of the proposed experimental procedure, even when the experiments are repeated on identical specimens of same a/b value.

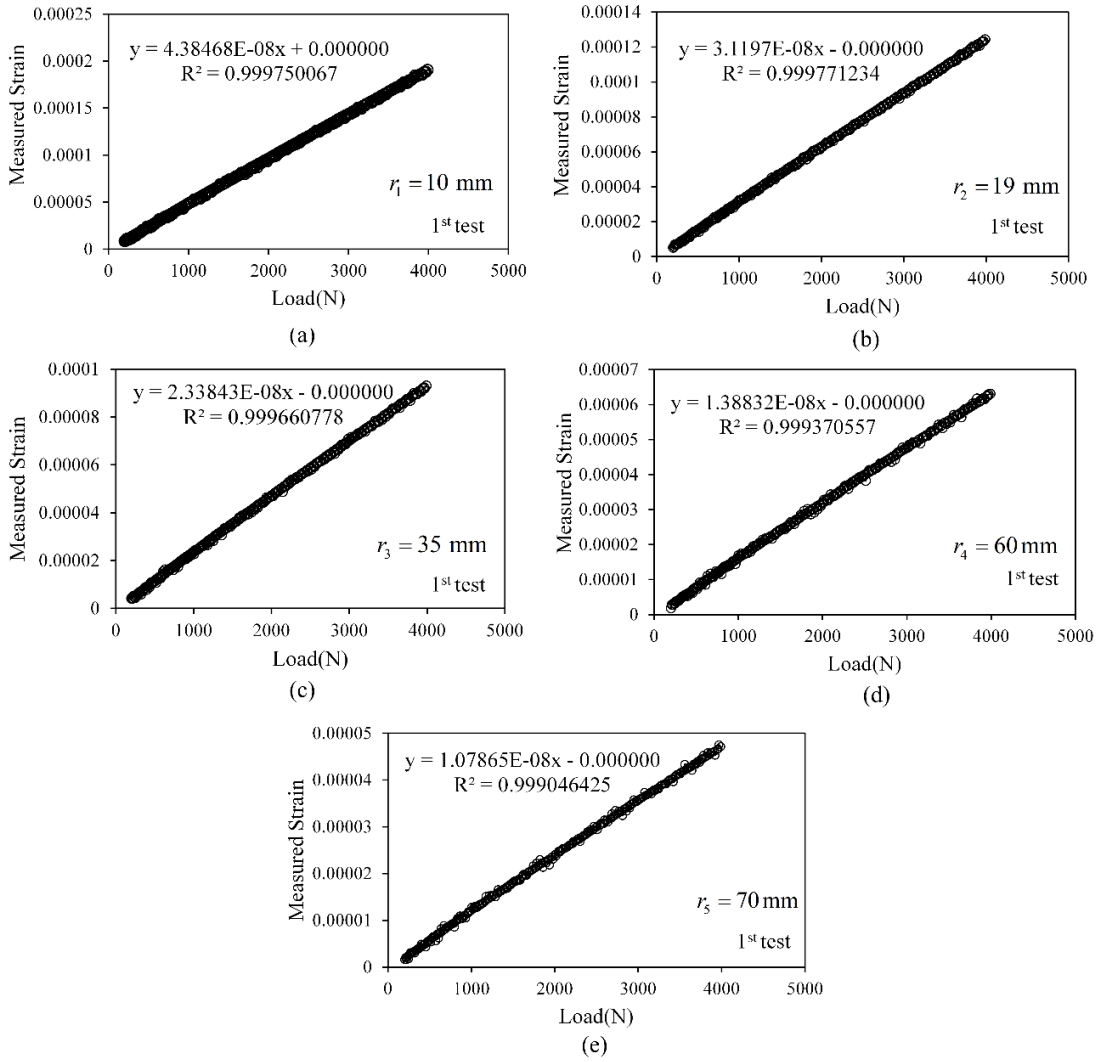

Figure 6.35 Measured strain (ε_{aa}) at various strain gage locations in a typical test on Specimen 2 with $a/b = 0.51$

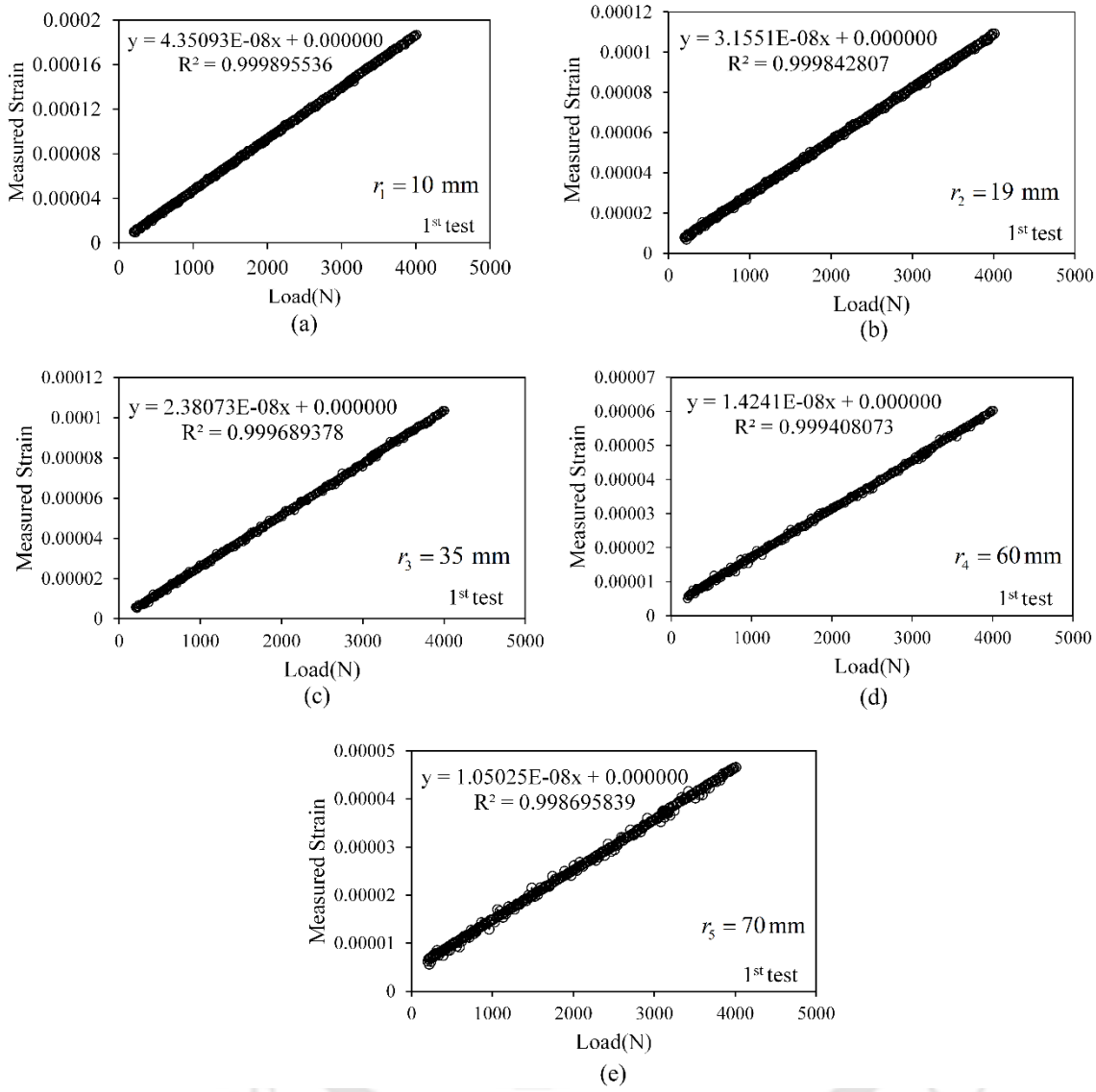

Figure 6.36 Measured strain (ε_{aa}) at various strain gage locations in a typical test on Specimen 3 with $a/b = 0.51$

Table 6.34 shows the measured normalized mode I SIF, f_I (using Eq. 6.1) at all the gage locations on all the three specimens with $a/b = 0.51$ (Fig. 6.21). Table 6.34 also presents average of measured f_I from all the nine tests (3 Specimen × 3 repeated tests) at all the gage locations and compares them with the reference value in Table 6.6. It may be pointed out from the results presented in Table 6.34 that nearly identical values of f_I have been obtained at a particular gage location (be it an optimal or a non-optimal location) for all three specimens with $a/b = 0.51$. Further, similar to the previous sections, here also for strain gage

placements at optimal locations very accurate values of mode I SIF are obtained as per the proposed single strain gage technique whereas for strain gages located at non-optimal locations the order of the error in estimated K_I and corresponding f_I is very high. The results in this section establish the repeatability and reproducibility of the experimental procedure for accurate determination of K_I of orthotropic laminates employing the single strain gage technique.

Table 6.34 Experimental values of f_I in all the repeated tests for all three specimens of $a/b = 0.51$ ($r_{max} = 51$mm) and accuracy of measured f_I

Specimen	Test	f_I				
		Optimal locations ($r_i < r_{max}$)			Non-optimal Locations ($r_i > r_{max}$)	
		$r_1 = 10$ mm	$r_2 = 19$ mm	$r_3 = 35$ mm	$r_4 = 60$ mm	$r_5 = 70$ mm
1	1	2.76	2.79	2.83	2.16	1.70
	2	2.78	2.78	2.84	2.15	1.74
	3	2.76	2.78	2.82	2.14	1.68
2	1	2.80	2.75	2.80	2.17	1.82
	2	2.78	2.72	2.76	2.14	1.79
	3	2.79	2.73	2.74	2.14	1.77
3	1	2.76	2.75	2.84	2.21	1.83
	2	2.79	2.78	2.83	2.19	1.81
	3	2.78	2.77	2.85	2.23	1.77
Average (f_I)		2.78	2.76	2.81	2.17	1.76
% Rel. Error*		0.36	0.36	1.44	21.67	36.86

* Ref. Value of $f_I = 2.77$ (Table 6.6)

6.7 Summary

This chapter presents the experimental determination of mode I SIF of $[90_2/0]_{10S}$ Carbon-epoxy laminates having edge cracked configuration with $a/b = 0.39$, 0.51, 0.61 and 0.71 using

the proposed single strain gage technique (section 3.5). The r_{max} values and hence the optimum gage locations for all the considered specimens have been determined using the present method by carrying out FEA using ANSYS® before conducting experiments. Depending upon the r_{max} values, strain gages were pasted at optimal and non-optimal locations to study the importance of radial location of a strain gage and the efficacy of the present method. An experimental set up was built for this purpose and optimized to take care of bending of the specimen and other factors.

Based on the strain readings at different locations on each specimen, the normalized SIFs (f_I) have been calculated. It was observed that the f_I values calculated from strain readings of gages placed at optimal locations $(r_{min} < r < r_{max})$ showed a very good agreement with the reference f_I values with error as low as 0.4%, whereas the f_I values calculated using strain gage readings placed beyond the r_{max} (non-optimal locations) showed an error as high as 49%. Experiments conducted on different specimens establishes the reproducibility of the proposed single strain gage technique. Additionally, experiments repeated on different specimens with same a/b also ensures a good repeatability of the experimental procedure.

Chapter 7

Comparison between Irwin's stress function and Liu's stress function

This chapter presents the numerical simulations conducted to verify the efficacy of the proposed displacement extrapolation technique (DET) as presented in Chapter 3 in estimation of SIFs of orthotropic laminates. In addition, the comparison of the Irwin [20] and Liu [74] proposed stress functions in terms of accuracy of the SIFs estimated using both the approaches is also presented here.

7.1 Stress functions proposed by Irwin and Liu

The stress function suggested by Liu [74] by employing Westergaard's approach [9] for orthotropic materials for mode I class of problems is

$$F_I = \frac{1}{2}\left(U_{11} + U_{12}\right) \tag{7.1}$$

where

$$\begin{aligned} U_{11} &= \mathrm{Re}\,\overline{\overline{Z_I}}\left(z_1\right) + \beta y\,\mathrm{Im}\,\overline{Z_I}\left(z_1\right) + Cy^2 \\ U_{12} &= \mathrm{Re}\,\overline{\overline{Z_I}}\left(z_2\right) + \beta y\,\mathrm{Im}\,\overline{Z_I}\left(z_2\right) + Cy^2 \end{aligned} \tag{7.2}$$

Also,

$$\begin{aligned} z_1 &= x_1 + iy_1 = (x + \alpha y) + i\beta y = r_1 e^{i\theta_1} \\ z_2 &= x_2 + iy_2 = (x - \alpha y) + i\beta y = r_2 e^{i\theta_2} \end{aligned} \tag{7.3}$$

and,

$$\begin{aligned} \tan\theta_1 &= \frac{\beta\sin\theta}{\cos\theta + \alpha\sin\theta} \qquad & \tan\theta_2 &= \frac{\beta\sin\theta}{\cos\theta - \alpha\sin\theta} \\ r_1 &= r\sqrt{\left(\beta\sin\theta\right)^2 + \left(\cos\theta + \alpha\sin\theta\right)^2} \qquad & r_1 &= r\sqrt{\left(\beta\sin\theta\right)^2 + \left(\cos\theta - \alpha\sin\theta\right)^2} \end{aligned} \tag{7.4}$$

The stress components for mode I loading of an orthotropic laminate obtained using Liu's stress function, F_1 using the Cauchy-Riemann equations (Eq. (3.6)) can be written as

$$\sigma_{xx} = \partial^2 F_I / \partial y^2 = \frac{\alpha^2+\beta^2}{2}\left[\mathrm{Re}\,Z_I(z_1)+\mathrm{Re}\,Z_I(z_2)\right]+\frac{\alpha^2-\beta^2}{2}\left[\mathrm{Im}\,Z_I'(z_1)+\mathrm{Im}\,Z_I'(z_2)\right]\beta y$$
$$+\alpha\beta^2 y\left[\mathrm{Re}\,Z_I'(z_1)-\mathrm{Re}\,Z_I'(z_2)\right]+2C$$

$$\sigma_{yy} = \partial^2 F_I / \partial x^2 = \frac{1}{2}\left[\mathrm{Re}\,Z_I(z_1)+\mathrm{Re}\,Z_I(z_2)\right]+\frac{\beta y}{2}\left[\mathrm{Im}\,Z_I'(z_1)+\mathrm{Im}\,Z_I'(z_2)\right] \tag{7.5}$$

$$\tau_{xy} = -\partial^2 F_I / \partial x\partial y = \frac{\alpha}{2}\left[\mathrm{Re}\,Z_I(z_2)-\mathrm{Re}\,Z_I(z_1)\right]+\frac{\alpha\beta y}{2}\left[\mathrm{Im}\,Z_I'(z_2)-\mathrm{Im}\,Z_I'(z_1)\right]$$
$$-\frac{\beta^2 y}{2}\left[\mathrm{Re}\,Z_I'(z_1)+\mathrm{Re}\,Z_I'(z_2)\right]$$

where $Z_I'(z_i)$ is the first derivative with respect to $z_i\,(i=1,2)$ of the complex function $Z_I(z_i)$ analogous to that for isotropic materials (Eqs. (3.4 – 3.5)) and α,β are given by the Eq. (3.26). Now, the strain field components for plane stress condition can be obtained by substituting Eq. (7.5) into Eq. (3.23) as

$$\varepsilon_{xx} = \frac{\left(\alpha^2+\beta^2\right)a_{11}+a_{12}}{2}\left[\mathrm{Re}\,Z_I(z_1)+\mathrm{Re}\,Z_I(z_2)\right]+\frac{\beta y}{2}\left[\mathrm{Im}\,Z_I'(z_1)+\mathrm{Im}\,Z_I'(z_2)\right]\left[\left(\alpha^2-\beta^2\right)a_{11}+a_{12}\right]$$
$$+a_{11}\alpha\beta^2 y\left[\mathrm{Re}\,Z_I'(z_1)-\mathrm{Re}\,Z_I'(z_2)\right]+2Ca_{11}$$

$$\varepsilon_{yy} = \frac{\left(\alpha^2+\beta^2\right)a_{12}+a_{22}}{2}\left[\mathrm{Re}\,Z_I(z_1)+\mathrm{Re}\,Z_I(z_2)\right]+\frac{\beta y}{2}\left[\mathrm{Im}\,Z_I'(z_1)+\mathrm{Im}\,Z_I'(z_2)\right]\left[\left(\alpha^2-\beta^2\right)a_{11}+a_{12}\right] \tag{7.6}$$
$$+a_{12}\alpha\beta^2 y\left[\mathrm{Re}\,Z_I'(z_1)-\mathrm{Re}\,Z_I'(z_2)\right]+2Ca_{12}$$

$$\gamma_{xy} = \frac{\alpha a_{66}}{2}\left[\mathrm{Re}\,Z_I(z_2)-\mathrm{Re}\,Z_I(z_1)\right]+\frac{\alpha\beta y a_{66}}{2}\left[\mathrm{Im}\,Z_I'(z_2)-\mathrm{Im}\,Z_I'(z_1)\right]$$
$$-\frac{\beta^2 y a_{66}}{2}\left[\mathrm{Re}\,Z_I'(z_1)+\mathrm{Re}\,Z_I'(z_2)\right]$$

The displacement components for mode I condition can now be obtained by integrating the strain components as

$$
\begin{aligned}
u_I &= a_{11}\left\{\frac{\alpha^2+\beta^2}{2}\operatorname{Re}\bar{Z}_I(z_1)+\frac{\alpha^2-\beta^2}{2}\beta\, y \operatorname{Im} Z_I(z_1)+\alpha\beta^2 y \operatorname{Re} Z_I(z_1)\right\} \\
&+ a_{11}\left\{\frac{\alpha^2+\beta^2}{2}\operatorname{Re}\bar{Z}_I(z_2)+\frac{\alpha^2-\beta^2}{2}\beta\, y \operatorname{Im} Z_I(z_2)-\alpha\beta^2 y \operatorname{Re} Z_I(z_2)\right\} \\
&+ \frac{a_{12}}{2}\left\{\operatorname{Re}\bar{Z}_I(z_1)+\beta y \operatorname{Im} Z_I(z_1)\right\}+\frac{a_{12}}{2}\left\{\operatorname{Re}\bar{Z}_I(z_2)+\beta y \operatorname{Im} Z_I(z_2)\right\}+2a_{11}C
\end{aligned}
\tag{7.7}
$$

$$
\begin{aligned}
v_I &= a_{12}\left\{\frac{\alpha}{2}\left[\operatorname{Re}\bar{Z}_I(z_1)+\beta y \operatorname{Im} Z_I(z_1)\right]+\frac{\beta}{2}\beta y \operatorname{Re} Z_I(z_1)\right\} \\
&+ a_{12}\left\{\frac{\alpha}{2}\left[\operatorname{Re}\bar{Z}_I(z_2)+\beta y \operatorname{Im} Z_I(z_2)\right]-\frac{\beta}{2}\beta y \operatorname{Re} Z_I(z_2)\right\} \\
&+ \frac{a_{22}}{2}\left\{\operatorname{Im}\bar{Z}_I(z_1)-y \operatorname{Re} Z_I(z_1)+\frac{1}{\beta}\operatorname{Im}\bar{Z}_I(z_1)\right\} \\
&+ \frac{a_{22}}{2}\left\{\operatorname{Im}\bar{Z}_I(z_2)-y \operatorname{Re} Z_I(z_2)+\frac{1}{\beta}\operatorname{Im}\bar{Z}_I(z_2)\right\}+2a_{12}C
\end{aligned}
$$

The displacements in the region very near to the crack tip i.e. the singularity dominated zone (SDZ) can be expressed by using a singular term representation in Eq. (7.7). The analytic functions in the displacement equations in Eq. (7.7) obtained can be written in terms of the coefficient A_0 to capture the singular solution as

$$
\begin{aligned}
&\operatorname{Re} Z_I(z_1)=\frac{A_0}{\sqrt{r_1}}\cos\frac{\theta_1}{2} \qquad \operatorname{Re} Z_I(z_2)=\frac{A_0}{\sqrt{r_2}}\cos\frac{\theta_2}{2} \\
&\operatorname{Im} Z_I(z_1)=-\frac{A_0}{\sqrt{r_1}}\sin\frac{\theta_1}{2} \qquad \operatorname{Im} Z_I(z_2)=-\frac{A_0}{\sqrt{r_2}}\sin\frac{\theta_2}{2} \\
&\operatorname{Re}\bar{Z}_I(z_1)=2A_0\sqrt{r_1}\cos\frac{\theta_1}{2} \qquad \operatorname{Re}\bar{Z}_I(z_2)=2A_0\sqrt{r_2}\cos\frac{\theta_2}{2} \\
&\operatorname{Im}\bar{Z}_I(z_1)=2A_0\sqrt{r_1}\sin\frac{\theta_1}{2} \qquad \operatorname{Im}\bar{Z}_I(z_2)=2A_0\sqrt{r_2}\sin\frac{\theta_2}{2}
\end{aligned}
\tag{7.8}
$$

Substituting Eq. (7.8) into Eq. (7.7) u_I, v_I obtained using Liu's stress functions can be written in terms of A_0 as

$$u_I = A_0 \left\{ \begin{array}{l} r_1^{\frac{1}{2}} \left[\begin{array}{l} \left(a_{11}\left(\alpha^2+\beta^2\right)+a_{12}\right)\cos\frac{\theta_1}{2} - \frac{\beta}{2}\left(a_{11}\left(\alpha^2-\beta^2\right)+a_{12}\right)\sin\frac{\theta_1}{2}\sin\theta_1 \\ +a_{11}\alpha\beta^2\cos\frac{\theta_1}{2}\sin\theta_1 \end{array} \right] \\ +r_2^{\frac{1}{2}} \left[\begin{array}{l} \left(a_{11}\left(\alpha^2+\beta^2\right)+a_{12}\right)\cos\frac{\theta_2}{2} - \frac{\beta}{2}\left(a_{11}\left(\alpha^2-\beta^2\right)+a_{12}\right)\sin\frac{\theta_2}{2}\sin\theta_2 \\ -a_{11}\alpha\beta^2\cos\frac{\theta_2}{2}\sin\theta_2 \end{array} \right] \end{array} \right\}$$

$$v_I = A_0 \left\{ \begin{array}{l} r_1^{\frac{1}{2}} \left[\begin{array}{l} a_{12}\alpha\cos\frac{\theta_1}{2} + \frac{1}{2}\left(\beta^2 a_{12} - a_{22}\right)\cos\frac{\theta_1}{2}\sin\theta_1 - a_{12}\frac{\alpha\beta}{2}\sin\frac{\theta_1}{2}\sin\theta_1 \\ +\left(1+\frac{1}{\beta}\right)a_{22}\sin\frac{\theta_1}{2} \end{array} \right] \\ r_2^{\frac{1}{2}} \left[\begin{array}{l} a_{12}\alpha\cos\frac{\theta_2}{2} + \frac{1}{2}\left(\beta^2 a_{12} - a_{22}\right)\cos\frac{\theta_2}{2}\sin\theta_2 - a_{12}\frac{\alpha\beta}{2}\sin\frac{\theta_2}{2}\sin\theta_2 \\ +\left(1+\frac{1}{\beta}\right)a_{22}\sin\frac{\theta_2}{2} \end{array} \right] \end{array} \right\} \tag{7.9}$$

Now, the DET formulations presented in Chapter 3 are applied to the displacement components obtained using Liu's stress functions. Along the crack faces ($\theta = \pm\pi$, $\theta_1 = \theta_2 = \pm\pi$ and $r_1 = r_2 = r$) the displacements for mode I conditions are given by

$$\begin{aligned} u_I^{+} &= u_I^{-} = 0 \\ v_I^{+} &= A_0 \left\{ r^{\frac{1}{2}} \left[\left(1+\frac{1}{\beta}\right)a_{22} \right] + r^{\frac{1}{2}} \left[\left(1+\frac{1}{\beta}\right)a_{22} \right] \right\} = 2A_0 \left\{ r^{\frac{1}{2}} \left(1+\frac{1}{\beta}\right)a_{22} \right\} \\ v_I^{-} &= -2A_0 \left\{ r^{\frac{1}{2}} \left(1+\frac{1}{\beta}\right)a_{22} \right\} \end{aligned} \tag{7.10}$$

where, u_I^{+}, v_I^{+} are the displacement components for $\theta = +\pi$ and u_I^{-}, v_I^{-} are the displacement components for $\theta = -\pi$. Therefore, the net displacement along the crack faces for mode I case is given by

$$\begin{aligned} \nabla u_I &= u_I^{+} - u_I^{-} = 0 \\ \nabla v_I &= v_I^{+} - v_I^{-} = 4A_0 \left\{ r^{\frac{1}{2}} \left(1+\frac{1}{\beta}\right)a_{22} \right\} = 4A_0 r^{\frac{1}{2}} f\left(\alpha, \beta, a_{22}\right) \end{aligned} \tag{7.11}$$

where, $f\left(\alpha, \beta, a_{22}\right)$ for Irwin's stress function is given by $2\beta a_{22} / \beta^2 - \alpha^2$ (Eq. (3.88)) and for Liu's stress function is given by $\left(1+\left(1/\beta\right)\right)a_{22}$ respectively. An orthotropic formulation boils down to isotropic case if $\beta = 1$; $\alpha = 0$ and $a_{22} = 1/E$. Incidentally, both Eqs. (3.88) and

(7.11) which are given by stress functions proposed by Irwin [20] and Liu [74] respectively boil down to the same isotropic expression given by

$$\nabla u_I = 0$$
$$\nabla v = 8A_0 r^{\frac{1}{2}} \frac{1}{E} \tag{7.12}$$

Eq. (7.12) shows that both the stress functions given by Irwin [20] and Liu [74] reduce to the same isotropic form after simplification. Therefore, though the stress function proposed by Irwin [20] does not reduce to Westergaard's solution under isotropic conditions as asserted by Liu [74], both the stress functions give the same final displacement equations as is evident from Eq. (7.12). Hence, estimation of SIFs using both the stress function approaches and their consequent degree of accuracy helps in ascertaining which stress function can be used for future works. Keeping this in mind numerical simulation of standard mode I configurations has been conducted to estimate the SIFs using both the stress function approach and the results are compared with handbook and other published results.

7.1.1 Numerical simulation of an edge cracked orthotropic plate

In this example, an orthotropic plate with an edge cracked configuration and subjected to pure tension has been considered to estimate K_I using the DET. Figure 7.1(a) shows the geometric, loading and boundary conditions and Fig. 7.1(b) shows the half plate symmetric model used for the FEA . The elastic properties of the plate are considered as $E_L = 3.5\text{GPa};\ E_T = 12\text{GPa};\ \nu_{LT} = 0.204$ and $G_{LT} = 3\text{GPa}$. Eight noded isoparametric elements (Q8) are used to model the meshes and collapsed quarter point elements are used to model the $\sqrt{r}$ singularity of the crack tip. Assuming symmetry it has been considered that displacement values, v_2, v_4 and v_3, v_5 in Eq. (3.86) across the opposite crack faces are equal and opposite in sign. The mode I SIFs are then calculated employing the DET using

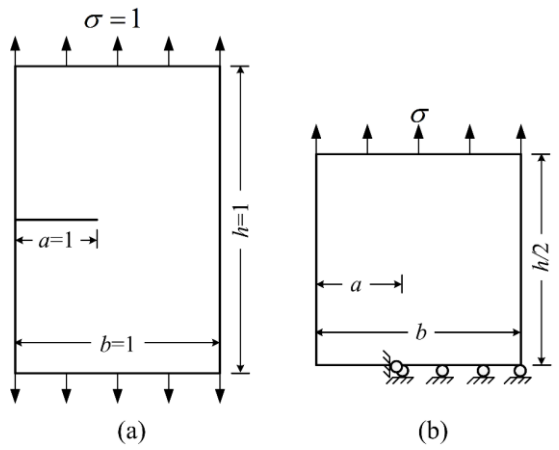

Figure 7.1 (a) Geometry, loading and boundary conditions for an edge cracked orthotropic plate (b) analysis domain used in FEA

displacement equations obtained from both Irwin and Liu's stress functions (Eq. (7.11) and Eq. (3.13) respectively).

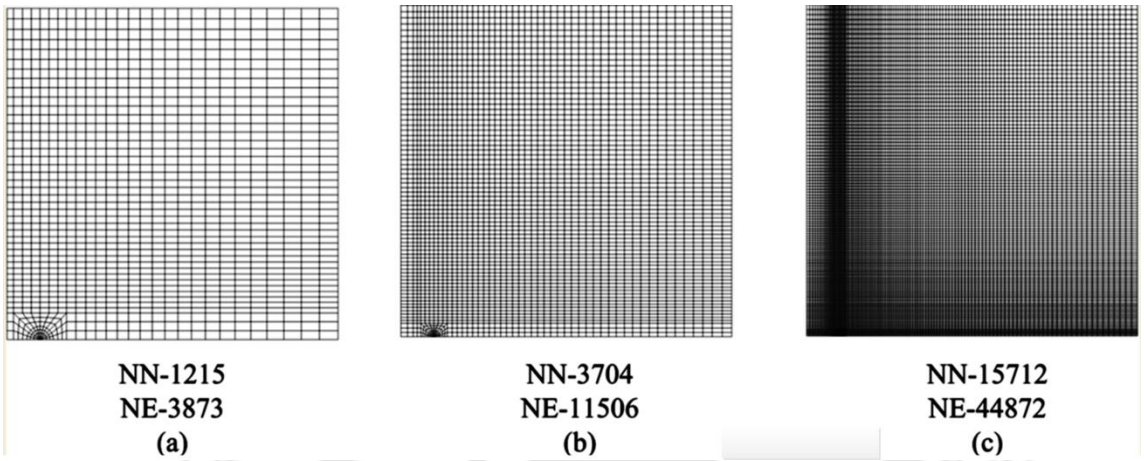

Figure 7.2 Different mesh densities for the edge cracked configuration used for numerical simulations

Figure 7.2 shows meshes employed in FEA with different mesh densities. Table 7.1 presents the K_I values estimated using DET employing both the Irwin's [20] and Liu's [74] displacement equations and compares them with handbook results. The analytical expression for mode I SIF of this configuration is given by Eq. (4.1), which gives the reference value of K_I as 2.103. It may be observed that the K_I calculated using the Liu's stress function approach gives much higher error as compared to the K_I calculated using the Irwin's stress function approach. Even there is no improvement in the K_I values obtained using Liu's [74] displacement equations with mesh refinement.

Table 7.1 Comparison of simulated K_I with already published results

Mesh	Computed K_I		Reference K_I	% Rel. error in Irwin K_I	% Rel. error in Liu K_I
	Irwin's formu-lation	Liu's formu-lation	Tada, Paris, Irwin [13]		
Coarse	2.071	1.88	2.103	1.52	10.6
Medium	2.076	1.886		1.28	10.31
Fine	2.081	1.89		1.04	10.16

7.1.2 Numerical simulation of a centre cracked orthotropic plate

In this example, an orthotropic plate with a central crack and subjected to pure mode I loading has been analysed. Figure 7.3(a) shows the geometry and Fig. 7.3(b) shows the quarter plate symmetry model used for the numerical studies in ANSYS® along with boundary conditions. The elastic properties of the plate composed of graphite-epoxy laminate are $E_L = 114.8\,\text{GPa};\ E_T = 11.7\,\text{GPa};\ \nu_{LT} = 0.21$ and $G_{LT} = 9.66\,\text{GPa}$. The domain has been modelled using eight noded isoparametric elements (Q8) and collapsed quarter point elements similar to that the edge cracked specimen. The mode I SIFs are calculated employing the same procedure used in the previous example. Figure 7.4 shows the sequence of meshes employed in FEA.

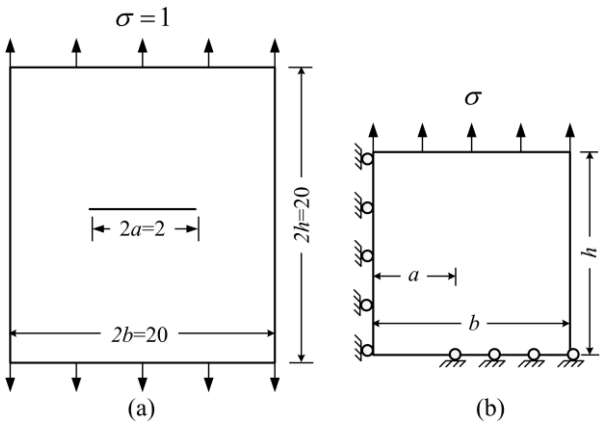

Figure 7.3 (a) Geometry, loading and boundary conditions for a center cracked orthotropic plate (b) analysis domain used in FEA

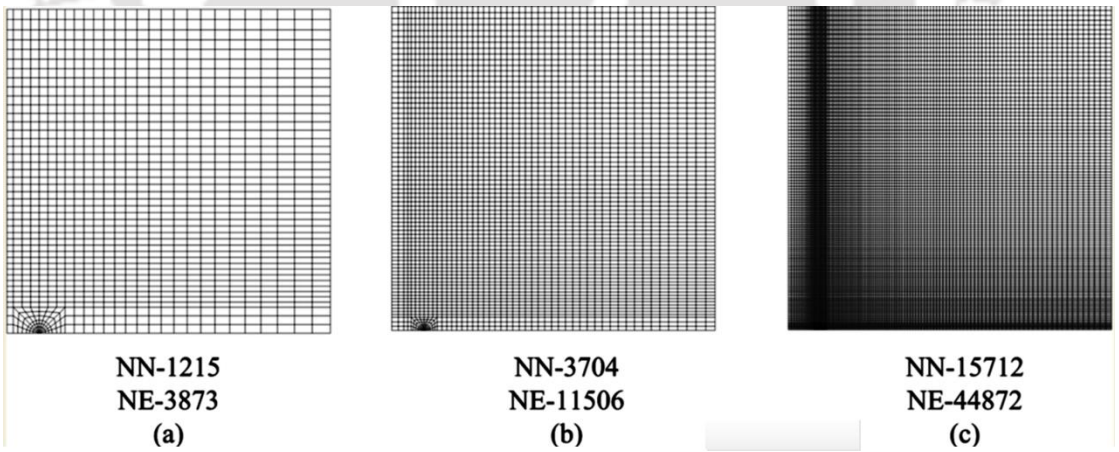

Figure 7.4 Different mesh densities for the center cracked configuration used for numerical simulations

Table 7.3 compares the K_I values for this configuration obtained using DET with both the Liu's [74]and Irwin's [20] displacement functions. Table 7.3 also shows published results provided by other researchers. The percentage relative error has been calculated using Asadpoure and Mohammadi results [36]. It is observed once again that the SIF calculated

using Liu's stress functions tends towards much higher error percentage than that determined using Irwin's stress function as in the previous problem.

Table 7.2 Comparison of simulated K_I with already published results

Mesh	Computed K_I		Published works			% Rel. error in Irwin K_I	% Rel. error in Liu K_I
	Irwin's formu-lation	Liu's formu-lation	Kim and Paulino [32]	Asadpoure and Mohammadi [36]	Ghorashi et al. [37]		
Coarse	1.7886	1.6267				0.427	8.66
Medium	1.7868	1.6284	1.767	1.781	1.780	0.325	8.56
Fine	1.785	1.63				0.224	8.47

The comparison of SIFs obtained using both the stress functions with handbook results and published works of other researchers shows that the mode I SIF obtained using the stress function proposed by Liu [74] gives higher error percent than that obtained using Irwin proposed stress function [20]. Thus, for the development of a strain gage technique for orthotropic laminates, it is prudent to proceed with Irwin proposed stress functions [20].

7.2 Numerical simulation to verify the displacement extrapolation technique (DET) for orthotropic materials

In this example the performance of the DET (section 3.8) has been studied for an orthotropic plate with a central inclined crack at an angle of 45° as shown in Fig. 7.5(a). The elastic properties of the plate are $E_L = 3.5\text{GPa}$; $E_T = 12\text{GPa}$ $\nu_{LT} = 0.204$ and $G_{LT} = 3\text{GPa}$. The same problem has been taken up by various other researchers in the past. Figure 7.5(b) shows the orthotropic plate with the loading and boundary conditions as used in FEA. The domain has been modelled using eight-noded isoparametric (Q8) elements and collapsed quarter point

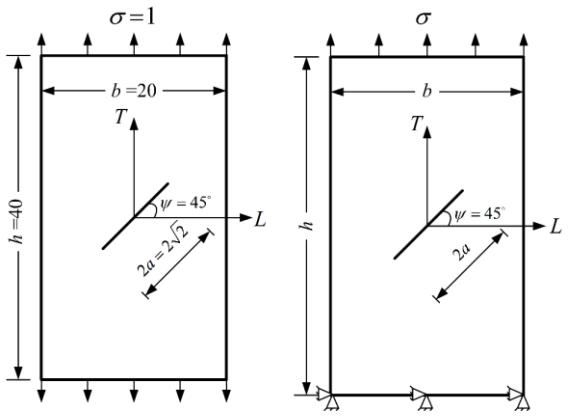

Figure 7.5 (a) Geometry, loading and boundary conditions for an slant centre cracked orthotropic plate (b) analysis domain used in FEA

elements have been used to model the $\sqrt{r}$ singularity of the crack tip. The finite element meshes with varying degrees of mesh densities considered are shown in Fig. 7.6

.

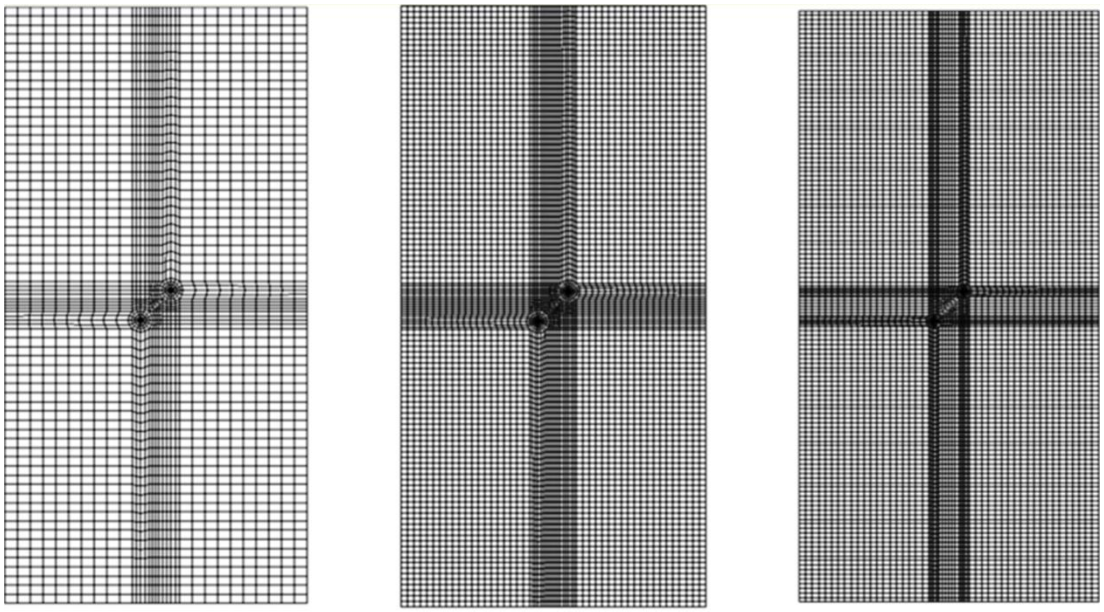

Figure 7.6 Different mesh densities for the slant center cracked configuration used for numerical simulations

Extracting the displacement values of the crack tip elements along the crack face, the mode I and mode II SIFs are calculated using Eqs. (3.88), (3.90), (3.103), (3.105) and (3.13). Table 7.3 presents the comparison of the present simulations with various available reference results.

Table 7.3 Comparison of simulated K_I, K_{II} with already published results

Mesh	Com-puted K_I	Com-puted K_{II}	Published works			% Rel. error in K_I	% Rel. error in K_{II}
				Sih et al. [22]	Kim and Paulino [32]	Asadpoure and Mohammadi [36]	
Coarse	1.042	1.027					1.12	2.57
Medium	1.045	1.029	K_I	1.054	1.067	1.084	0.81	2.34
Fine	1.052	1.035	K_{II}	1.054	1.044	1.095	0.22	1.76

The analytical solution obtained by Sih et al. [22] using a complex variable method has been used to predict the percentage relative error. It may be observed that for different mesh densities the proposed method gives fairly good result and the accuracy increases with mesh refinement.

7.3 Summary

The numerical analyses presented in section 7.1.1 and 7.1.2 show that the orthotropic SIFs for the mode I specimens estimated employing the Irwin proposed stress functions provide better solutions as compared to that using Liu's [74] stress functions. The proposed displacement extrapolation technique with displacement components obtained using Irwin [20] is found to estimate very accurate values of SIFs of orthotropic laminates. A mixed mode example shows the efficacy of the DET based on Irwin' [20] stress function.

Chapter 8

Conclusions and Scope of Future Work

The present works aims at developing proper theoretical framework for simple, robust and practicable experimental procedure for determining the mode I and mixed mode (I/II) SIFs of orthotropic laminates using strain gages. The proposed techniques for determination of mode I and mixed mode I/II SIFs are based on representing measured strains using a three parameter strain series. For accurate determination of SIFs, it is also necessary to know apriori the valid gage locations. Therefore, the present work also addresses the important issue of assessment of valid optimal gage locations supported by appropriate theory. The conclusions drawn from the present work have been presented categorically as general and specific conclusions.

8.1 General Conclusions

1. Starting with Generalized Westergaard approach, a theoretical framework has been developed for strain gage based determination of mode I and mixed mode I/II SIFs of orthotropic laminates.

2. The DS technique has been extended to orthotropic materials where only a single strain gage is required for determination of mode I SIF.

3. The proposed technique for determination of mode I SIF of orthotropic materials has been extended to mixed mode I/II cases of orthotropic materials where only four strain gages are required for determination of K_I and K_{II}.

4. Using strong theoretical background and a FE based methodology, a procedure has been developed for both mode I and mixed mode I/II cases for determination of $r_{\max}$ i.e. the upper bound on the radial location of the strain gage(s). This $r_{\max}$ is shown to be useful in assessing optimal radial gage locations for accurate determination of SIFs in orthotropic laminates which has been an unsolved issue hitherto.

5. Present theoretical development of single ended crack theory for orthotropic materials could be successfully applied to double ended cracks also for the range of a/b considered in the present study.

6. Numerical simulations have been performed to validate the proposed theory for strain gage based determination of mode I and mixed mode (I/II) SIFs and also to assess the existence and importance of optimal gage locations.

7. Results of numerical simulations show that accurate values of the SIFs can be obtained using the proposed techniques when the gage(s) are pasted within the estimated $r_{\max}$ for each configuration, thereby reinforcing the importance of knowing the optimal radial strain gage locations apriori.

8. Using numerical results, a sensitivity analysis for possible errors in estimated SIFs arising out of deviations in angular orientations of the strain gage has been done.

9. Experimental set up has been planned for experimental determination of mode I SIF of cracked orthotropic laminates. Edge cracked specimens having different a/b ratios have been prepared from $\left[90_2/0\right]_{10S}$ Carbon/Epoxy laminates, strain gages are pasted at optimal and non-optimal locations and repeated experiments have been conducted on each specimen to estimate mode I SIF for those specimen from the strain gage readings.

10. Effect of crack length to width ratio $\left(a/b\right)$ on the estimated $r_{\max}$ values of the experimental specimens have been studied and observed to agree well with that obtained from numerical simulations.

11. Comparison of experimentally determined mode I SIF values of various specimens with the reference solutions verifies that very accurate mode I SIF can be obtained using the proposed technique.

12. Comparison of experimentally determined SIF values obtained from the strain readings of the gages located at different locations also substantiate the importance of placing strain gages within the $r_{\max}$ for accurate determination of K_I.

13. The methodologies developed in the present work will be of immense help to experimentalists for accurate determination of K_I and mixed mode SIFs of orthotropic

laminates in view of the fact that strain gage based determination of K_I is sparse and for mixed mode cases, is not available till date.

8.2 Specific Conclusions

8.2.1 Numerical simulations of orthotropic laminates having mode I configuration

1. The proposed theoretical development and subsequent numerical investigations conducted show that it is possible to determine K_I for edge cracked orthotropic laminates using a single strain gage by choosing a specific angular location and orientation of the strain gage by extending DS technique to orthotropic materials considering three parameters strain series.

2. Strain variation along the gage line for all the configurations considered follow theoretical predictions made using three parameter strain series.

3. There exists an upper bound ($r_{\max}$) on the radial location of the strain gage up to which the three parameter strain series is valid.

4. The proposed method could accurately determine $r_{\max}$ values for a variety of cracked configurations having orthotropic properties and under mode I loading viz. edge cracked plate, center cracked plate, double edge cracked plate and eccentric center cracked plate.

5. The $r_{\max}$ is found to be dependent on the crack length to width ratio (a/b) of the cracked configurations. At low values of a/b, the crack length dominates the influence on $r_{\max}$, but at larger values of a/b, the net ligament length $(b-a)$ dominates the influence on the $r_{\max}$ value for the mode I configurations studied. The dependence of $r_{\max}$ on a/b may be attributed to the variation of magnitude of both the singular and nonsingular coefficients which is decided by the geometry and boundary conditions of the cracked configuration.

6. Numerical simulation of the proposed single strain gage technique shows that for both single-ended and double-ended cracked orthotropic laminates, accurate values of K_I

could be obtained only when the strain gage is placed at optimal locations i.e. within r_{max}. On the other hand, when the gage is placed outside r_{max} (non-optimal locations), highly inaccurate values of K_I for the mode I orthotropic laminate configurations are obtained.

7. Numerical results show that r_{max} is a useful parameter in assessing optimal gage locations for accurate determination of mode I SIFs.

8. Thus the present FE based method will be useful in knowing the r_{max} values apriori for conducting experiments for determination of accurate K_I using a single strain gage.

9. The sensitivity analysis for the variation of $\pm 0.5^{\circ}$ in strain gage orientation shows a moderate change in measured SIFs. However, precluding the chances of such deviations, it may be concluded that though a deviation of 0.5° in the angle may be viable, it would be judicious not to allow for such variations since during experiments various factors other than strain gage pasting may have direct or indirect impact on the output.

8.2.2 Numerical simulations of orthotropic laminates having mixed mode configuration

1. Variation of strains with the radial distance from the crack tip along the gage lines computed from the numerical simulations follow the theoretical predictions proposed in the present investigation.

2. Numerical results show that the extent of validity of the three parameter zone i.e. r_{max} which decides the upper bound of the valid strain gage locations in experimental determination of mixed mode I/II SIFs can be accurately determined using the proposed FE approach.

3. The variation of r_{max} with a/b ratio shows that similar to mode I cases, for mixed mode configurations also r_{max} value increases with increasing a/b, reaches a maximum and decreases as the crack tip approaches boundary.

4. Numerical simulation of the strain gage technique for estimation of mixed mode SIFs of orthotropic laminates shows that strain readings give accurate values of K_I and K_{II} only when all the four gage locations are within r_{max} i.e. at optimal locations.

5. The proposed strain gage approach for determination of mixed mode SIFs of orthotropic laminates stands true over a wide range crack inclination angle (ψ) as can be seen from the numerical investigations. Variations of K_I and K_{II} estimated using the proposed approach with respect to the crack inclination angle (ψ) follow an analogous trend as reported by previous researchers.

6. For slant edge cracked orthotropic laminate configurations, the dependence of r_{max} on the crack angle variation is noticeable only for higher values of angular orientations when the boundary effects come into the picture.

8.2.3 Experimental determination of K_I of edge cracked $[90_2/0]_{10S}$ Carbon-epoxy laminates

1. Measured strains from all the strain gages show a linear variation with the applied load for all the specimens tested and in all the repeated tests.

2. Mode I SIF has been determined using the strain data from the strain gages at different radial locations for all the configurations for each of the repeated test. An excellent repeatability in terms of SIF values has been achieved for all repeated tests at any given load.

3. Experimentally determined mode I SIF corresponding to all the configurations show excellent agreement with the reference SIF when the strain gages are located at optimal locations (i.e., within the r_{max}) as recommended by the present methodology. On the other hand, experimentally determined mode I SIF using the data obtained from strain gages placed outside the r_{max} (i.e., non-optimal location) show very high error. This observation is true for all mode I configurations tested in all the repeated tests.

4. The r_{max} values evaluated numerically are substantiated by the excellent agreement of experimentally determined mode I SIF values with the reference solution thereby reinforcing the dependence of r_{max} on a/b as obtained in the numerical studies.

5. Results from the present experimental investigation very well substantiate the proposed single strain gage technique for estimation of mode I SIF of orthotropic laminates and the associated theory for determination of optimal strain gage locations in determining mode I SIFs.

8.3 Scope of Future Work

1. Experiments could be performed on double ended cracked orthotropic laminates to validate the proposed single strain gage technique for determination of mode I SIFs.

2. Experiments could also be performed on specimens having different laminate compositions such as glass-epoxy.

3. Experiments could be performed for orthotropic laminates with mixed mode configuration to validate the proposed approach for determination of mixed mode SIFs of orthotropic laminates.

4. A methodology on the lines of the proposed single strain gage technique could be developed for estimation of dynamic SIFs of orthotropic laminates.

References

[1] **C. B. Smith,** Some new types of orthotropic plates laminated of orthotropic materials, *Journal of Applied Mechanics*, (1953), 20, 286-288.

[2] **K. S. Pister** and **S. B. Dong,** Elastic bending of layered plates, in *Proceedings of American Society of Civil Engineers (Journal of Engineering Mechanics Division)*, (1985),85, EM4, 1-10.

[3] **E. Reissner** and **Y. Starvksy**, Bending and stretching of certain types of heterogeneous aeolotropic elastic plates, *Journal of Applied Mechanics*, (1961), 28, 402-408.

[4] **S. G. Lehnitskii**, Anisotropic plates (translation from the 2d Russian ed.) in S. W. Tsai and T. Cheron eds. Gordon and Breach Publishers, New York (1968).

[5] **Y. Starvsky** and **N. J. Hoff**, *Mechanics of Composites Structures*, in A. G. H. Dietz ed., Composite Engineering Laminates (1969). MIT Press, Cambridge, MA.

[6] **C. E. Inglis**, Stresses in a plate due to the presence of cracks and sharp conners, *Transactions of the Royal Institute of Naval Architects* (1913), 60, 214-219.

[7] **A. A. Griffith**, The phenomenon of rupture and flow in solids, *Philosophical Transactions Series A* (1920), 221, 163–198.

[8] **S. Ya. Yarema**, On the contribution G. R. Irwin to fracture mechanics, *Materials Science* (1995), 31, 617-623.

[9] **H. M. Westergaard**, Bearing pressures and cracks, *Journal of Applied Mechanics* (1939), 61, 49-53.

[10] **M. L. Williams**, On the stress distribution at the base of a stationary crack, *Journal of Applied Mechanics*, (1957), 24, 109-114.

[11] **G. R. Irwin**, Fracture dynamics, Fracture of metals, *American Society for Metals*, Cleveland (1948), 147–166.

[12] **Y. Murakami**, *Stress Intensity Factors handbook*. England: Pergamon, (1987).

[13] **H. Tada, P. C. Paris and G. R. Irwin**, *The Stress Analysis of Cracks Handbook*. New York, ASME, (2000).

[14] **J. R. Rice**, A path independent integral and the approximate analysis of stress concentration by notches and cracks, *Journal of Applied Mechanics*, Transactions ASME (1968), 379–386.

[15] **J. R. Rice**, Mathematical analysis in the mechanics of fracture, Fracture A path independent integral and the approximate analysis of stress concentration by notches and cracks, *Journal of Applied Mechanics*, Transactions ASME (1968), 379–386.

[16] **A. A. Wells**, Unstable crack propagation in metals: cleavage and fast fracture, *Proceeding of the Crack Propagation Symposium*, Cranfield, U.K (1961), Paper 84.

[17] **R. J. Sanford**, *Principles of Fracture Mechanics*, Upper Saddle River, NJ: Prentice Hall, (2003).

[18] **A. J. Rosakis, A. T. Zehinder** and **R. Narashim**, Caustics by reflection and their application to elastic-plastic and dynamic fracture mechanics, *Optical Engineering* (1988), 27, 596–610.

[19] **E. A. Patterson** and **E. J. Olden**, Optical analysis of crack tip stress fields: a comparative study, *Fatigue and Fracture of Engineering Materials and Structures*, (2004), 27, 623–635.

[20] **G. R. Irwin**, Analytical aspects of crack stress field problems. T&AM Report No. 213, Urbana: University of Illinois; (1962).

[21] **E. M. Wu**, On the application of fracture mechanics to orthotropic plates. T&AM Report No. 248, Urbana: University of Illinois; (1963).

[22] **G. C. Sih, P. C. Paris** and **G. R. Irwin,** On cracks in rectilinearly anisotropic bodies. *International Journal of Fracture Mechanics* (1965), 1, 189-203.

[23] **C. K. H. Dharan**, Fracture Mechanics of Composite Materials. *Journal of Engineering Materials and Technology* (1978),100, 233-247.

[24] **Sharokh Parhizgar, Loren. W. Zachary** and **C. T. Sun**. Application of linear elastic fracture mechanics to composite materials. *International Journal of Fracture* (1982), 20, 3-15.

[25] **H. P. Rossmanith** and **H. N. Linsbauer**. Analysis of mode.1 crack-tip stress patterns in orthotropic materials. *Ing Arch* (1985), 55,258-66.

[26] **L. Nobile** and **C. Carloni**. Fracture analysis of orthotropic cracked plates. *Composite Structures* (2005), 68, 285-293.

[27] **T. Cruse**. Boundary Element Analysis in Computational Fracture Mechanics (1988), Kluwer, Dordrecht, The Netherlands.

[28] **M. H. Alibadi** and **P. Sollero**. Crack growth analysis in homogenous orthotropic laminates. *Composites Science and Technology* (1998), 58(10), 1697-1703.

[29] **F. Garcia-Sanchez, C. Zhang** and **A. Saez.** A two-dimensional time-domain bondary element method for dynamic crack problems in anisotropic solids. *Engineering Fracture Mechanics* (2008), 75, 1412-1430.

[30] **S. N. Atluri, A. S. Kobayashi and M. Nakagaki.** An assumed displacement hybrid finite element model for linear elastic fracture mechanics, *International Journal of Fracture* (1975), 11(2), 257-271.

[31] **S. Mohammadi**, Discontinuum Mechanics by Combined Finite/Discrete Elements, WIT Press (2003), UK.

[32] **J. H. Kim, G. H. Paulino**. Mixed-mode fracture of orthotropic functionally graded materials using finite elements and the modified crack closure method, *Engineering Fracture Mechanics* (2002c), 69, 1557-1586.

[33] **S. Mohammadi,** XFEM Fracture Analysis of Composites, Wiley & Sons, Ltd., Publication (2012), USA.

[34] **T. Belytschko** and **M. Tabbara**. Dynamic Fracture using element-free Galerkin methods. *International Journal for Numerical Methods in Engineering* (1996), 37, 923-938.

[35] **S. S. Ghorashi, S. Mohammadi** and **S. R. Sabbagh-Yazdi**, Orthotropic enriched element free Galerkin method for fracture analysis of composites. *Engineering Fracture Mechanics* (2011), 78, 1906-1927.

[36] **A. Asadpoure** and **S. Mohammadi,** A new approach to simulate the crack with the extended finite element method in orthotropic media. *International Journal for Numerical Methods in Engineering* (2007), 69, 2150-2172.

[37] **A. Asadpoure**, **S. Mohammadi** and **A. Vafai**, Modelling crack in orthotropic media using a coupled finite element and partition of unity methods. *Finite Elements in Analysis and Design* (2006), 42(13), 1165-1175.

[38] **S. S. Ghorashi, N. Valizadeh** and **S. Mohammadi**, Extended isogeometric analysis (XIGA) for analysis of stationary and propagating crack. *International Journal for Numerical Methods in Engineering* (2012), 89(9), 1069-1101.

[39] **M. C. Baik, S. H. Choi , J. S. Hawong** and **J. D. Kwon**. Determination of stress intensity factors by the method of caustics in anisotropic materials. *Experimental Mechanics* (1995); 35:137-43

[40] **X. Yao, J. Chen, G. Jin, K. Arakawa** and **K. Takahashi**. Caustic analysis of stress singularities in orthotropic composite materials with mode-I crack. *Composite Science and Technology* (2004), 64,917-24

[41] **M. Mojtahed** and **L. W. Zachary**. Use of photoelasticity to determine orthotropic K_I stress-intensity factor. *Experimental Mechanics* (1987), 27,184-89

[42] **S. H. Ju** and **S. H. Liu**. Determining stress intensity factors of composites using crack opening displacement. *Composite Structures* (2007), 81, 614-21.

[43] **S. K. Khanna, M. D. Ellingsen** and **R. M. Winter.** Investigation of fracture in transparent glass fiber reinforced polymer composites using photoelasticity. *Journal of Engineering Materials and Technology* (2004), 126, 1-7.

[44] **G. P. Mogadpalli** and **V. Parameswaran**. Determination of Stress Intensity Factor for Cracks in Orthotropic Composite Materials using Digital Image Correlation. *Strain* (2008), 44, 446-52.

[45] **G. R. Irwin**, Analysis of stresses and strains near the end of a crack traversing a plate, *Journal of Applied Mechanics* (1957), 24, 361–364.

[46] **D. Broek**, *Elementary Engineering Fracture Mechanics*, Martinus Nijhoff Publishers, Boston, (1987).

[47] **S. K. Bhandari**, Etude experimentale du factor d' intensine des contraintes au voisinage de la pointe d' une fissure de fatigue centrale dans une tole mince au moyen des measures extensometriques, *These, Ecole Nat Superiure de L' Aeronautique*, Paris (1969).

[48] **Monthulet, S. K. Bhandari** and **C. Riviere**, Methods pratiquess de determination du factor d'intensite des contraintes pour la propagation des fissures, *La recherché Aerospatiale* (1971), 297-303

[49] **J. Rosakis** and **K. Ravi-Chandar**, On crack-tip stress state: An experimental evaluation of three-dimensional effects. *International Journal of Solids and Structures* (1986), 22, 121–134.

[50] **J. W. Dally** and **R. J. Sanford**, Strain gage methods for measuring the opening mode stress intensity factor, *Experimental Mechanics* (1987), 27, 381–88.

[51] **A. Shukla, R. K. Agarwal** and **H. Nigam**, Dynamic fracture studies on 7075-T6 aluminum and 4340 steel using strain gages and photoelastic coating, *Engineering Fracture Mechanics* (1988), 31, 501–515.

[52] **J. R. Berger, J. W. Dally** and **R. J. Sanford**, Determining the dynamic stress intensity factor with strain gages using a crack tip algorithm, *Engineering Fracture Mechanics* (1990), 36, 145–156.

[53] **J. W. Dally** and **D. B. Barker**, Dynamic measurement of initiation toughness at high loading rates, *Experimental Mechanics* (1988), 298–303.

[54] **L. Parnas, O. G. Bilir** and **E. Tezcan**, Strain gage methods for measurement of opening mode stress intensity factor. *Engineering Fracture Mechanics* (1996), 55, 485–492.

[55] **S. Rizal** and **H. Homma**, Dimple fracture under short pulse loading, *International Journal of Impact Engineering* (2000), 24, 69-83.

[56] **P. R. Marur, R. C. Batra, G. Garcia** and **A. C. Loos**, Static and dynamic fracture toughness of epoxy/alumina composite with submicron inclusions, *Journal of Material Science* (2004), 39,1437–1440.

[57] **M. Kirugulige** and **H. V. Tippur**, Mixed-mode dynamic crack growth in a functionally graded particulate composite. *Experimental Mechanics* (2006), 46:269-281.

[58] **S. Shirley** and **H. Homma**, Approach to dynamic fracture toughness of GFRP from aspect of viscoelastic and debonding behaviors, *Journal of Solid Mechanics and Materials Engineering* (2007), 1, 275–286.

[59] **S. C. Wadgaonkar** and **V. Parameswaran**, Structure of near-tip stress field and variation of stress intensity factor for a crack in a transversely graded material, *Journal of Applied Mechanics* (2009), 76, 011014-1-011014-9.

[60] **H. Sarangi, K. S. R. K. Murthy** and **D. Chakraborty**, Radial locations of strain gages for accurate measurement of mode I stress intensity factor. *Materials and Design* (2010), 31, 2840-2850**.**

[61] **H. Sarangi, K. S. R. K. Murthy** and **D. Chakraborty**, Optimum strain Gage location for evaluating stress intensity factors in single and double ended cracked configurations. *Engineering Fracture Mechanics* (2010), 77, 3190- 3203.

[62] **H. Sarangi, K. S. R. K. Murthy** and **D. Chakraborty**, Extent of three parameter zone and optimum strain gage location for eccentric cracked configurations, *Applied Mechanics and Materials* (2012), 110-116,127-134.

[63] **H. Sarangi, K. S. R. K. Murthy** and **D. Chakraborty,** Experimental verification of optimal strain gage locations for the accurate determination of mode I stress intensity factors. *Engineering Fracture Mechanics* (2013), 110, 189-200.

[64] **J. W. Dally** and **J. R. Berger**, A strain gage method for determining K_I and K_{II} in a mixed mode stress field, *Proceeding of the 1986 SEM Spring Conference Experimental Mechanics* (1986), 603-612.

[65] **T. Kondo, M. Kobayashi** and **H. Sekine**, Strain gage method for determining stress Intensities of sharp-notched strips. *Experimental Mechanics* (2001), 41, 1–7.

[66] **A. Dorogoy** and **D. Rittel**, Optimum location of a three strain gauge rosette for measuring mixed mode stress intensity factors, *Engineering Fracture Mechanics* (2008), 75, 4127-4139.

[67] **H. Sarangi, K. S. R. K. Murthy** and **D. Chakraborty**, Optimum strain gage locations for accurate determination of the mixed stress intensity factors. *Engineering Fracture Mechanics* (2012), 88,63-78.

[68] **H. Sarangi, K. S. R. K. Murthy** and **D. Chakraborty**, Accurate measurement of mixed mode (I/II) SIFs using strain gages. *ASTM* (2017), 45,63-78.

[69] **A. Shukla, B. D. Agarwal** and **B. Bhushan**, Determination of stress intensity factor in orthotropic composite materials using strain gages, *Engineering Fracture Mechanics* (1989), 32, 469–477.

[70] **S. K. Khanna** and **A. Shukla**, Development of stress field equations and determination of stress intensity factor during dynamic fracture of orthotropic composite materials, *Engineering Fracture Mechanics* (1994), 47, 345–59.

[71] **S. K. Khanna** and **A. Shukla**, On the use of strain gages in dynamic fracture mechanics, *Engineering Fracture Mechanics* (1995), 51,933–948.

[72] **D. Cerniglia, V. Nigrelli** and **A. Pasta**. Experimental and numerical determination of stress intensity factor in composite material, *In: Conference proceedings ICCM-12*, paper 932, Europe; 1999.

[73] **R. J. Sanford**, A critical re-examination of the Westergaard method for solving opening mode crack problems, *Mechanics Research Communications* (1979), 6, 289-294.

[74] **C. D. Liu**, Analytical solution for orthotropic composite plate containing a mode I crack along principle axis, *International Journal of Fracture* (1996), 76, 21-38.

[75] **R. S. Barsoum**, On the use of isoparametric finite elements in linear fracture mechanics, *International Journal for Numerical Methods in Engineering* (1976), 10, 25-37.

[76] **R. D. Henshell** and **K. G. Shaw,** Crack tip finite elements are unnecessary, *International Journal for Numerical Methods* (1975), 9, 495-507.

[77] **A. O. Ayhan, A. C. Kaya, A. Loghin, J. H. Laflen, R. D. McClain RD, D. Slavik**, Fracture Analysis of cracks in orthotropic materials using ANSYS®, *In: Conference Proceedings GT 2006 (ASME Turbo Expo 2006: Power for Land, Sea and Air)*, Spain, 2006.

[78] **G. Dhondt**, Mixed mode K-calculations in anisotropic materials, *Engineering Fracture Mechanics* (2002), 69, 909-922.

[79] **R. D. Cook**, *Concepts and Application of Finite Element Analysis*, John Wiley & Sons Inc., Singapore, (2002)

[80] **R. Chona, G. R, Irwin** and **R. J. Sanford**, The influence of specimen size and shape on the singularity dominated zone (1983), *ASTM STP 791*, p.13-123.

[81] **N. T. Younis** and **B. Kang**, Averaging effects of a strain gage, *Journal of Mechanical Science and Technology* (2011), 25(1), 163-169.

[82] **N. T. Younis** and **J. Mize**, Discrete averaging effects of a strain gage at a crack tip, *Engineering Fracture Mechanics* (1996), 55, 147-153.

[83] **J. R. Berger** and **J. W. Dally**, An error analysis for a single strain gage determination of the stress intensity factor K_I, *Experimental Techniques* (1988), 12, 31-33.

List of Publications

International Journals

1. Debaleena Chakraborty, K. S. R. K. Murthy and D. Chakraborty, A new single strain gage technique and optimal gage locations for determination of mode I stress intensity factors in orthotropic composite materials, *Engineering Fracture Mechanics* (2014),124-125,142-154

2. Debaleena Chakraborty, K. S. R. K. Murthy and D. Chakraborty, Determination of K_I in orthotropic laminates with double ended cracks using a single strain gage technique, *Theoretical and Applied Fracture Mechanics* (2016), 82.96-106

3. Debaleena Chakraborty, D. Chakraborty and K. S. R. K. Murthy, Strain gage method for the determination of mixed mode stress intensity factors of orthotropic materials, *Composite Structures* (2017),160,185-194.

4. Debaleena Chakraborty, K. S. R. K. Murthy and D. Chakraborty, Experimental determination of mode I stress intensity factor in orthotropic materials using a single strain gage, *Engineering Fracture Mechanics* (2017),173,130-145

5. Debaleena Chakraborty, D. Chakraborty and K. S. R. K. Murthy, Choice of stress functions for estimation of mode I stress intensity factors in orthotropic materials, *Composites Communications,* Under Review

Conferences

1. Debaleena Chakraborty, D. Chakraborty and K. S. R. K. Murthy, Determination of Mode I Stress Intensity Factor for orthotropic laminates using a single strain gage, *Fifth International Congress on Computational Mechanics and Simulation (ICCMS-2014), CSIR-SERC, Chennai*

2. Debaleena Chakraborty, D. Chakraborty and K. S. R. K. Murthy, Mode I SIF determination of orthotropic laminates with double ended cracks using a single strain gage, *Proceedings of First Structural Integrity Conference and Exhibition (SICE-2016), Bangalore July 4-6, 2016*

3. D. Chakraborty, Debaleena Chakrabrorty and K. S. R. K Murthy, Optimal strain gage location for determination of mode I stress intensity factor for orthotropic laminates using a single strain gage, Accepted for publication in *17th International Conference on Experimental Mechanics (ICEM 17), July 3-7, 2016, Rhodes.*

About the Author

Ms. Debaleena Chakraborty was born to Mr. Hiren Chakraborty and Ms. Tinku Chakraborty in the year 1987. She completed her Class-X from Board of Secondary Education, Assam and Class-XII from Assam Higher Secondary Education Council in the years 2003 and 2005 respectively securing 1st division in both the examinations. She completed her Bachelor of Engineering in Mechanical Engineering securing 1st class with Honours from Dibrugarh University in the year 2010. She joined Mechanical Engineering Department at Indian Institute of Technology Guwahati as a regular Research Scholar in the year 2011 and has been a PhD student during 2011-2016. Her areas of academic interest are stress analysis of composite materials and fracture mechanics.